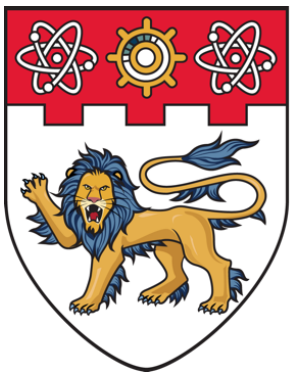

NANYANG TECHNOLOGICAL UNIVERSITY
SINGAPORE

THE STUDY OF THE INTRA-GOLGI TRAFFICKING AND MOLECULAR ORGANIZATION OF THE GOLGI

TIE HIENG CHIONG

SCHOOL OF BIOLOGICAL SCIENCES

2020

THE STUDY OF THE INTRA-GOLGI TRAFFICKING AND MOLECULAR ORGANIZATION OF THE GOLGI

TIE HIENG CHIONG

SCHOOL OF BIOLOGICAL SCIENCES

A thesis submitted to the Nanyang Technological University in partial fulfilment of the requirement for the degree of Doctor of Philosophy

2020

Statement of Originality

I hereby certify that the work embodied in this thesis is the result of original research done by me except where otherwise stated in this thesis. The thesis work has not been submitted for a degree or professional qualification to any other university or institution. I declare that this thesis is written by myself and is free of plagiarism and of sufficient grammatical clarity to be examined. I confirm that the investigations were conducted in accord with the ethics policies and integrity standards of Nanyang Technological University and that the research data are presented honestly and without prejudice.

22-August-2020

. . . . . .

Date

. . . . . .

Tie Hieng Chiong

Supervisor Declaration Statement

I have reviewed the content and presentation style of this thesis and declare it of sufficient grammatical clarity to be examined. To the best of my knowledge, the thesis is free of plagiarism and the research and writing are those of the candidate's except as acknowledged in the Author Attribution Statement. I confirm that the investigations were conducted in accord with the ethics policies and integrity standards of Nanyang Technological University and that the research data are presented honestly and without prejudice.

20-Aug-2020

Date

Dr. Lu Lei

Authorship Attribution Statement

This thesis contains materials from 2 papers published in the following peer-reviewed journals.

Chapter 3 and 6 contain results from the paper published as **Tie, H., Mahajan, D., Chen, B., Cheng, L., VanDongen, A., & Lu, L. (2016). A novel imaging method for quantitative Golgi localization reveals differential intra-Golgi trafficking of secretory cargoes. *Molecular biology of the cell, 27*(5), 848.**

The contributions of the co-authors are as follow:

- Assoc/Prof Lu Lei wrote the manuscript and I assisted in preparing figures and revising the manuscript.
- Assoc/Prof Lu Lei provided the project direction.
- I performed laboratory experiments and analysis on fluorescence microscopy data.
- Dr.Cheng Li wrote the Matlab code for the chromatic aberration correction for GLIM.

Chapter 4-6 contain results from the paper published as **Tie, H. C., Ludwig, A., Sandin, S., & Lu, L. (2018). The spatial separation of processing and transport functions to the interior and periphery of the Golgi stack. *Elife, 7*, e41301.**

The contributions of the co-authors are as follow:

- Assoc/Prof Lu Lei wrote the manuscript and I assisted in preparing figures and revising the manuscript.
- Assoc/Prof Lu Lei provided the project direction.
- Assoc/Prof Lu Lei wrote macros for the en face and side views averaging.
- Asst/Prof Alexander Ludwig performed the sectioning and imaging for EM samples. He guided me on EM samples preparation.
- I performed laboratory experiments and analysis on microscopy data.

22-August-2020

. . . . . .

. . . . . .

Date

Tie Hieng Chiong

Acknowledgements

I considered for a few years before finally committing myself to the four-year Ph.D. program and I have never felt regret since then. The journey has been challenging and full of uncertainties. However, I feel honoured to join the league of cell biologists in deciphering the fascinating Golgi apparatus.

I am grateful to my supervisor, Dr. Lei Lu, as I wouldn't be able to achieve thus far without his full support and guidance. He has inspired me with his enthusiasm in science and introduced me into the interesting microscopic world. His creative and adventurous ideas have spurred the development of my Golgi study.

My appreciation also goes to members of my Thesis Advisory Committee (TAC), including Dr. Cheng Gee Koh, Dr. Alexander Ludwig and Dr. Suet Mien Tan. I learnt a lot from their suggestions and critics during TAC meetings.

I would like to express my appreciation to my past and present laboratory members, including Dr.Divyanshu Mahajan and Miss Xiuping Sun. They have been helpful and generous in sharing laboratory experiences and precious reagents which have greatly smoothened my work progress. In particular, I would like to thank the late Miss Yan Zhou, who had helped me to settle down in this laboratory when I first joined. She was a great mentor and always being patience and kind to provide all forms of help.

I would like to thank my collaborators, Dr. Alexander Ludwig and Dr. Sara Sandin, for their help in EM experiments. I am grateful to Dr.Ludwig for his detail guidance in preparing EM samples.

Most importantly, I would like to thank my loving family who has shown me unconditional support and love whenever I feel insecure. I wouldn't be able to focus on my study without them. Lastly, I would like to thank my brothers and sisters in Christ

who have been keeping me in their prayers. I wish my research outcome could contribute to the scientific community and that would be the greatest reward to all my efforts. May all the glory be to my heavenly Father.

~SDG~

Tie Hieng Chiong

22 August 2020

Contents

Abbreviations

AA	amino acid
ACBD3	acyl-CoA-binding domain containing protein 3
AP	adaptor protein
APEX2	ascorbate peroxidase 2
Arf	ADP-ribosylation factor 1
Arl	ADP-ribosylation factor like
AU	airy unit
C2GNT1	core 2 beta1,6-N-acetylglucosaminyl transferase 1
cab45	45-kDa calcium-binding *protein*
CB	cacodylate buffer
CCV	clathrin coated vesicle
CD-MPR	cation-dependent mannose 6-phosphate receptor
center*mass*	center of fluorescence mass
CGN	*cis*-Golgi network
CI-MPR	cation-independent mannose 6-phosphate receptor
CLCB	clathrin light chain B
CLEM	correlative light electron microscopy
COPI	coat protein complex I
COPII	coat protein complex II
DMEM	Dulbecco's Modified Eagle's medium
DTT	dithiothreitol
ECM	extracellular matrix
EE	early endosome
EM	electron microscope
ER	endoplasmic reticulum
ERES	endoplasmic reticulum exit site
ERGIC	ER-Golgi intermediate compartment
ET	electron tomography
ExM	Expansion microscopy
FBS	fetal bovine serum
FIB	focused ion beam
FKBP12	12-kDa FK506-binding protein
FM	FKBP12 mutant
FP	fluorescent protein
Fuc	fucose
FWHM	Full width at half maximum
GaAsP	Gallium arsenide phosphide
GalNAc	acetylgalactosamine
GALNT	polypeptide N-acetylgalactosaminyltransferases
GalT	β1,4-galactosyltransferase
GCC185	185-kDa Golgi coiled-coil protein

GCC88	88-kDa Golgi coiled-coil protein
GFP	green fluorescent protein
GGA	Golgi associated, gamma adaptin ear containing, ARF binding
Glc	glucose
GlcNAc	N-acetylglucosamine
GLIM	Golgi proteins localization by imaging centers of mass
Golph3	Golgi phosphoprotein 3
GP73	73-KDa Golgi phosphoprotein
GPI	glycosylphosphatidylinositol
GPP130	130-KDa Golgi phosphoprotein
GRASP	Golgi reassembly stacking protein
GS	Golgi SNARE
HeLa	Henrietta Lacks
hr	hour
IPTG	Isopropyl β-D-1-thiogalactopyranoside
KDa	Kilodalton
KDEL	lysine-aspartic acid-glutamic acid-leucine
Lamp	lysosome associated membrane glycoprotein
LE	late endosome
LM	light microscopy
LQ	localization quotient
Man1B1	mannosidase alpha class 1b member 1
ManII	mannosidase alpha class 2A member 1
MDCK	Madin-Darby Canine Kidney
MGAT1	mannosyl(alpha-1,3-)-glycoprotein beta-1,2-N-acetylglucosaminyltransferase
MGAT2	mannosyl(alpha-1,6-)-glycoprotein beta-1,2-N-acetylglucosaminyltransferase
MGAT4B	alpha-1,3-mannosyl-glycoprotein 4-beta-N-acetylglucosaminyltransferase B
moxGFP	monomeric oxidizing environment optimized green fluorescent protein
MTOC	microtubule organizing centre
nm	nanometer
NPC	nucleopore complex
NRK	normal rat kidney
Nup133	Nucleoporin 133
PACS1	phosphofurin acidic cluster sorting protein 1
PALM	photoactivation localization microscopy
PBS	phosphate-buffered saline
PFA	paraformyldehyde
PM	plasma membrane
PMT	photomultiplier tube
POMGNT1	protein O-linked mannose N-acetylglucosaminyltransferase 1 (beta1,2-)

PVDF	polyvinylidene difluoride
Rab	Ras-related proteins in brain
RE	recycling endosome
ROI	region of interest
RUSH	retention using selective hook system
SBP	streptavidin binding peptide
sCMOS	scientific complementary metal oxide semiconductor
SDS-PAGE	sodium dodecyl sulphate-polyacrylamide gel electrophoresis
SIM	structured illumination microscopy
SLC35C1	solute carrier family 35 member C1
SNARE	soluble N-ethylmaleimide-sensitive factor attachment protein receptor
SNR	Signal-to-noise ratio
ST6Gal1	ST6 β -galactoside α2,6-sialyltransferase 1
ST6GalNAC6	ST6 N-acetylgalactosaminide alpha-2,6-Sialyltransferase 6
STED	stimulated emission depletion
STORM	stochastic optical reconstruction microscopy
TfR	transferrin receptor
TGN	*trans*-Golgi network
TNFα	Tumour necrosis factor α
TPST	tyrosylprotein sulfotransferase
Vamp	vesicle-associated membrane protein
Vip36/LMAN2	36kDa vesicular integral-membrane protein/ Lectin, mannose binding 2
Vps	vacuolar protein sorting
VSVG-tso45	Temperature sensitive vesicular stomatitis virus G protein
Vti	Vesicle transport through interaction with t-SNAREs
Ycenter*mass*	y coordinate of the center of fluorescence mass
β3GalT6	beta-1,3-galactosyltransferase 6
β4GalT3	beta-1,4-galactosyltransferase 3
β4GalT7	beta-1,4-galactosyltransferase 7
µm	micrometer

List of figures

List of tables

Abstract

The mammalian Golgi complex adopts a complicated architecture which is unresolvable under a conventional light microscope. Based on a previously developed method, Golgi protein localizations by imaging centers of mass (GLIM), we quantitatively mapped the axial localization of dozens of Golgi proteins along the Golgi axis in nocodazole-induced Golgi mini-stacks. In this study, we explored the lateral localization of Golgi proteins. Using Airyscan microscopy, we identified and validated that GPP130 and several Golgins, including Golgin84, Giantin and GCC185 exclusively localized to Golgi cisternal rims. Hence, they were used to discern the orientations (i.e. side and en face views) of Golgi mini-stacks. By systematically screening Golgi enzymes and components of trafficking machinery, we found that the former preferentially localized to the cisternal interior, whereas the latter was mostly found at the periphery or the rim of the Golgi mini-stack. In addition, after averaging large number of en face and side view images, we generated quantitative molecular organization maps, which summarize the axial and lateral localizations of Golgi proteins in the Golgi mini-stack.

For the first time, we provide imaging evidence on the spatial separation of the processing and transport domains to the cisternal interior and rim of the Golgi mini-stack, respectively. Notably, the TGN was observed to organize into a multi-tier architecture axially and demonstrate two types of molecular localization patterns, i.e. compact lump and scattered puncta, laterally.

To investigate intra-Golgi trafficking of secretory cargos, their lateral localizations were analysed. Conventional or small secretory cargos (<115 kDa), including GFP, mCherry-GPI, CD59, E-cadherin, VSVG, CD8a-Furin, Lamp1, TfR and CD-MPR, were

found to mainly localize in the cisternal interior. In contrast, bulky cargos (>20,000 kDa), including collagenX, FM4-CD8a and FM4-moxGFP aggregates, mainly localized at the cisternal rim.

Collectively, our imaging data suggest a size-dependent lateral partitioning model for secretory cargos, where bulky and small cargos preferentially localize to the cisternal rim and interior, respectively. Intriguingly, the synchronous cargo waves of VSVG and TfR were observed to progressively transit from the *cis*- to the *trans*-side of the Golgi mini-stack.

Furthermore, various secretory cargos were observed to exit the Golgi at either the *trans*-Golgi or the TGN. The cytosolic tail of Furin was found to be sufficient for VSVG-tso45-Furin to exit the Golgi at the TGN. Besides that, the tyrosine motif of Lamp1 could be important in guiding the protein to access and exit the Golgi at the TGN.

Hence, we propose that both the *trans*-Golgi and TGN can function as Golgi exit sites. Cargos harbouring the TGN targeting signal(s) can access and exit the Golgi at the TGN in a signal-dependent manner. In contrast, cargos without such a signal constitutively exit at the *trans*-Golgi by default.

Chapter 1: Introduction

1.1 The architecture of the mammalian Golgi complex

The ‘Golgi apparatus’ or ‘Golgi complex’ (hereafter Golgi), is a cellular organelle named after the Italian physician and pathologist Camillo Golgi. It was first described in 1898, when an unknown perinuclear basket-like structure was stained in Purkinje cells by a metal impregnation technique (Golgi, 1898). It was not until the 1950s that the ultrastructure of the Golgi was finally revealed using the newly-developed electron microscopy (EM) (Dalton and Felix, 1954; Farquhar and Rinehart, 1954). Since then, our understanding of the Golgi has grown concurrently with advances in EM techniques and other cutting-edge imaging technologies.

The mammalian Golgi is typically located at the perinuclear region and closely associated with the microtubule organizing centre (MTOC). The Golgi comprises hundreds of membrane stacks that are linked laterally into an elaborate continuous network. The lateral connections of Golgi stacks form Golgi ribbons (Figure 1A).

Almost one-third of eukaryotic proteins are targeted to the endoplasmic reticulum (ER) to enter the secretory pathway (Ghaemmaghami et al., 2003). In the conventional protein secretory pathway, newly synthesized proteins are co- or post-translational translocated into the ER lumen or inserted into the ER membrane. Secretory proteins are packaged in small coated vesicles called coat protein complex II (COPII)-coated vesicles and bud off from the ER via the ER exit sites (ERES) (Bannykh et al., 1996). COPII vesicles are normally 60–90 nm in diameter (Matsuoka et al., 1998). COPII-coated-tubules of approximately 200 nm long also bud from the ERES (Zanetti et al., 2013). COPII-coated vesicles and tubules, after uncoating, can fuse to form the endoplasmic reticulum (ER)-Golgi intermediate compartment (ERGIC) (Farquhar and

Hauri, 1997). It mediates anterograde transport from the ER to the Golgi and retrograde transport from the Golgi back to the ER.

1.1.1 The Golgi stack

A Golgi stack is highly compact and is therefore also referred to as the compact zone. Adjacent Golgi stacks are interconnected by a vesicular tubular membranous network that occupies the region known as the non-compact zone. Each Golgi stack comprises a few flattened membranous saccules called cisternae (singular: cisterna) (Figure 1B). The number of cisternae per Golgi stack ranges from four to eleven cisternae across mammalian cell types (Rambourg and Clermont, 1997). The diameter of a cisterna can range from 0.7 to 1.1 micrometers (μm); this, too, is dependent on organisms and cell types (Pelletier et al., 2002; Rabouille et al., 1995b). A cisterna is shaped into a densely packed central region with two dilated rims. Both intracisternal and intercisternal spaces at the central region are estimated to be approximately 10–20 nanometers (nm) (Engel et al., 2015; Klumperman, 2011). Golgi cisternae are fenestrated (Ladinsky et al., 1999), wherein numerous budding profiles and vesicles can be found (Ladinsky et al., 1999) (Figure 1A).

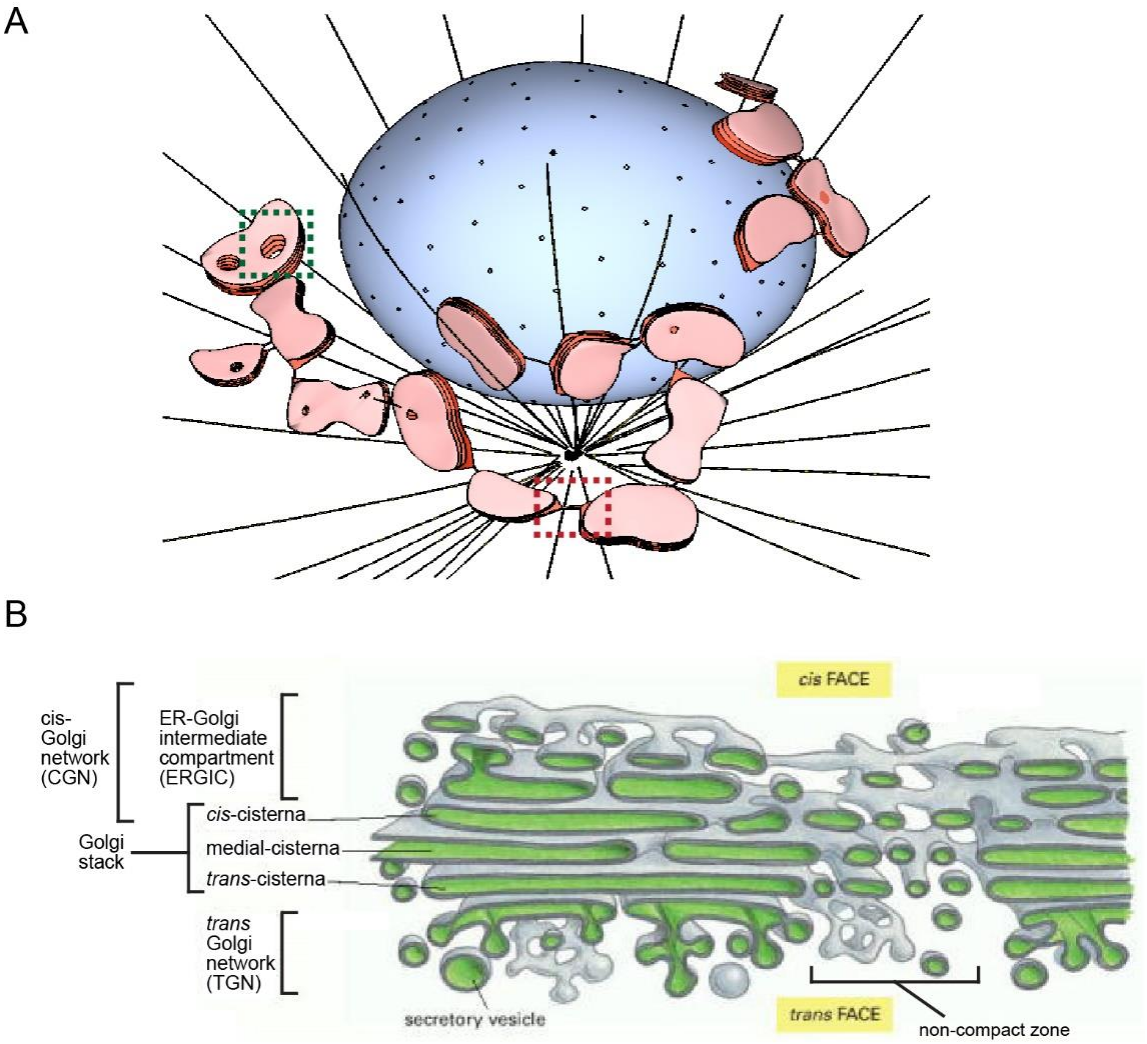

Figure 1: The schematic diagram of the mammalian Golgi.
(A) The mammalian Golgi is located at the perinuclear region and in adjacent to MTOC (dot of converged black lines), where microtubules (black lines) emanate. The Golgi consists of hundreds of Golgi stacks that are laterally linked to each other. The green dotted box represents the fenestrae in Golgi cisternae, whereas the red dotted box is enlarged and schematically shown in (B). The blue oval shape represents the nucleus, where nuclear pores (puncta) are found. (B) The architecture of the Golgi. The Golgi is divided into 4 regions, namely the *cis*-, medial-, *trans*-Golgi and the TGN. The *cis*-, medial- and *trans*-Golgi are collectively known as the Golgi stack. Golgi stacks are laterally linked by vesicular tubular network, which is known as the non-compact zone. The ERGIC and the *cis*-Golgi are collectively known as the *cis*-Golgi network (CGN). Secretory vesicles that are leaving the Golgi to their post-Golgi destinations can be found at the *trans*-face of the Golgi stack.

The Golgi is a polarized organelle that can be qualitatively divided into four regions: the *cis*-, medial-, and *trans*-Golgi and the *trans*-Golgi network (TGN) (Figure 1B). The polarity of the Golgi is characterized by different molecular and biochemical compositions across the four regions (Banfield, 2011). For instance, a pH gradient is

established across Golgi cisternal lumens, with the *cis*-Golgi (pH =6.7) and the TGN (pH =6.0) having the highest and lowest pH, respectively (Kellokumpu, 2019). In addition, a gradient of cholesterol and sphingolipids is established. These molecules are mostly concentrated at the *trans*-Golgi/TGN (Van Meer et al., 2008). In EM images, the *cis*-Golgi and ERGIC are frequently observed to associate closely; thus, they have been coined the *cis*-Golgi network (CGN; Figure 1B) (Mellman and Simons, 1992). A Golgi stack, including the *cis*-, medial- and *trans*-Golgi together with the TGN, is surrounded by numerous vesicles of 50–70 nm in diameter (Ladinsky et al., 1994; Ladinsky et al., 1999). Many of these are coated with coat protein complex I (COPI) coats. They are mostly found at the cisternal rim and occasionally at the ERGIC (Weidman et al., 1993). The majority of COPI-coated vesicles are observed at the *cis*-cisternae, and they gradually reduce in number toward the *trans*-cisternae (Ladinsky et al., 1999; Oprins et al., 1993).

1.1.2 The TGN

The TGN is responsible for sorting and packaging secretory cargos into transport carriers that are eventually delivered to post-Golgi destinations (De Matteis and Luini, 2008; Guo et al., 2014). It also receives molecules that move through endocytic trafficking routes, in which molecules that are endocytosed at the plasma membrane (PM) are either directly targeted to the TGN or indirectly to the TGN via endosomes. The morphology of the TGN is different from that of the other three Golgi subcompartments. The TGN is defined as a reticular tubular network that is continuous with the *trans*-most cisterna (Griffiths and Simons, 1986; Rambourg and Clermont, 1990) (Figure 1B). However, it was later observed that the penultimate cisterna also projected tubules into the *trans*-most region. Hence, Ladinsky et al. proposed that the TGN consists of the two *trans*-most cisternae together with their tubular projections

(Ladinsky et al., 1999; Mogelsvang et al., 2004). These projected tubules are anastomosed and associated with many budding profiles and vesicles. Of note, clathrin coats and clathrin-coated vesicles (CCVs) were observed to exclusively associate with the *trans*-most cisterna and its associated tubular projections, but not with preceding cisternae (Ladinsky et al., 1999).

Despite the distinct morphologies of the Golgi in different organisms and cell types, its two major functions, post-translational modification and protein sorting, remain conserved (Klute et al., 2011).

1.2 The Golgi functions as the protein processing centre

More than 300 Golgi enzymes have been identified in humans (Nilsson et al., 2009). These enzymes include glycosyltransferases, glycosidases and nucleotide sugar transporters, among others. Proteins and lipids that traverse the Golgi can undergo various post-translational modifications, with glycosylation being the most common (Stanley, 2011). Glycosylation generates a great diversity of glycans, which have important cellular functions. For instance, glycans can facilitate proper protein folding, serve as recognition markers on the cell surface and regulate protein turnover (Shental-Bechor and Levy, 2008).

It was believed that the localization of glycosylation enzymes in the Golgi followed the sequence of actions in the glycosylation pathway (Dunphy and Rothman, 1985; Roth, 2002). In brief, early- and late-acting enzymes localize to the *cis*- and *trans*-side of the Golgi, respectively. This notion was supported by a number of findings. First, membrane fractionation experiments suggested that N-linked glycosylation enzymes, such as mannosidases, were concentrated in the early Golgi, while galactosyltransferase and sialyltransferase were mainly found in the late Golgi

(Dunphy et al., 1981; Goldberg and Kornfeld, 1983). Second, EM studies mapped mannosyl(alpha-1,3-)-glycoprotein beta-1,2-N-acetylglucosaminyltransferase (MGAT1) and galactosyltransferase specifically to the medial- and *trans*-cisternae, respectively (Dunphy et al., 1985; Roth and Berger, 1982). However, the notion of distinct compartmental localization of Golgi enzymes has been challenged by gradient-like localization patterns exhibited by several N-glycosylation enzymes, such as MGAT1, mannosidase alpha class 2A member 1 (ManII), beta-1,4-galactosyltransferase (GalT) and ST6 beta-galactoside alpha-2,6-sialyltransferase 1 (ST6Gal1) (Nilsson et al., 1993; Rabouille et al., 1995a). A similar phenomenon was also observed for O-glycosylation enzymes, such as polypeptide N-acetylgalactosaminyltransferase-1, -2 and -3 (GalNAc-T1, -T2 and -T3) (Rottger et al., 1998), whose distribution gradients can significantly overlap with each other (Rabouille et al., 1995a). In addition, the distribution of Golgi enzymes could vary across cell types (Velasco et al., 1993). Therefore, the spatial relationship and cisternal organization of Golgi enzymes remain to be characterized. In this study, the localizations of various Golgi enzymes, especially those involved in glycosylation, are investigated.

There are two major types of glycosylation, namely N- and O-glycosylation. In the ER, N-glycosylation is initiated by the transfer of precursor polysaccharides en bloc to an asparagine residue in a conserved motif, N-X-S/T (N: asparagine; S: serine; T: threonine; X: any amino acid except proline), in newly synthesized proteins (Kelleher and Gilmore, 2006). The resulting high-mannose-modified glycoproteins could retain their high-mannose glycans in the Golgi and end up on the PM. However, most of them are trimmed by mannosidase alpha class 1 (ManI) in the *cis*-Golgi, after which, the trimmed intermediates become substrates for the medial-Golgi-localized MGAT1.

Glycans on the intermediates can be further modified by galactosyltransferases and sialyltransferases in the *trans*-Golgi and/or the TGN to become either hybrid or complex N-glycan forms (Stanley, 2011).

Moreover, several O-glycan species can be generated from O-glycosylation pathways. These include O-N-acetylgalactosamine (O-GalNAc), O-mannose (O-Man), O-N-acetylglucosamine (O-GlcNAc), O-fucose (O-Fuc) and O-glucose (O-Glc). They are differentiated by the first sugar added on to the S or T residue of newly synthesized proteins. O-GalNAc, also known as mucin-type O-glycosylation, is one of the most abundant O-glycan species. In general, it is initiated in the Golgi by the addition of GalNAc and galactose (Gal), followed by GlcNAc, sialic acid and fucose to form branched or linear O-glycan chains (Brockhausen et al., 2009). Apart from the Golgi, O-glycosylation could occur in the ER when high-level of invasion-promoting kinases EGF receptor, platelet-derived growth factor receptor and Src are activated in cells (Gill et al., 2013). Most of the O-glycosylation enzymes investigated in this study are involved in O-GalNAc formation.

Nucleotide sugar transporters are also required for the generation of glycan chains. They function to transport nucleotide sugar units into the Golgi lumen to provide building blocks for glycosylation (Freeze and Elbein, 2009).

1.3 The Golgi functions as the protein sorting centre

The Golgi constantly experiences membrane traffic from anterograde and retrograde trafficking. In anterograde trafficking, the Golgi receives newly synthesized proteins or lipids from the ER, whereas in retrograde trafficking, the Golgi receives deliveries from the PM or post-Golgi subcellular compartments, such as recycling endosome (RE), early endosome (EE) and late endosome (LE) (Figure 2). Therefore, the Golgi is the

central hub for sorting proteins coming from all directions. Protein sorting in the Golgi can occur at two levels. First, a great variety of cargos are segregated from each other and transported to different post-Golgi destinations. Second, Golgi resident proteins are retained or retrieved amid anterograde trafficking (Warren and Mellman, 1999).

Here, within the scope of membrane trafficking of the Golgi, I review three transport mechanisms by which secretory cargos can leave the Golgi: bulk flow transport, signal-mediated transport and lateral partition transport (Borgese, 2016; Pelham and Munro, 1993). The current understanding of cargo exit sites at the Golgi is also discussed.

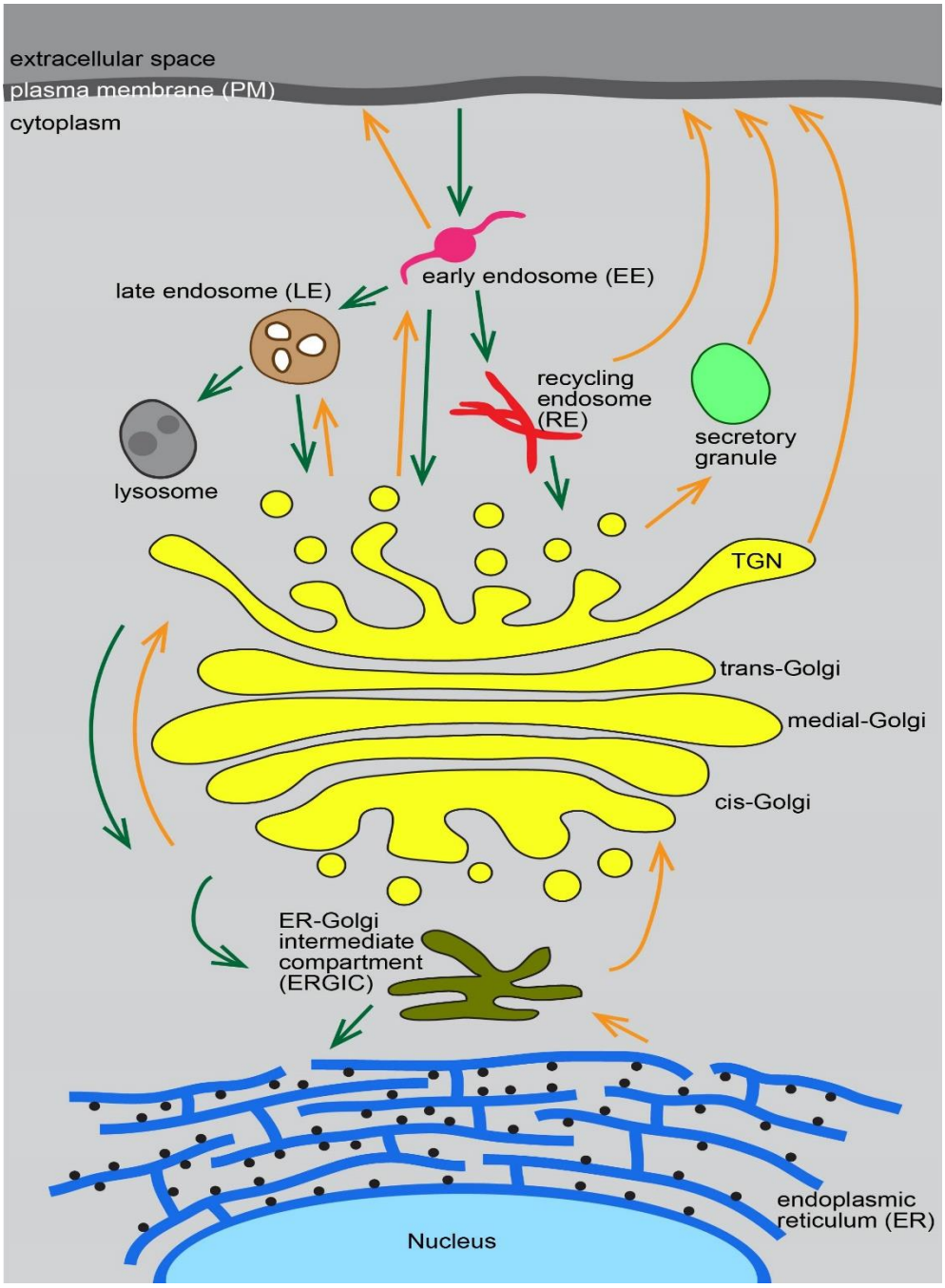

Figure 2: An overview of trafficking routes between subcellular membrane compartments in a nonpolarized cell.

Newly synthesized proteins and lipids are delivered from the ER to the ERGIC en route to the Golgi. In the Golgi, secretory and resident proteins undergo the intra-Golgi trafficking. Secretory cargos are delivered to either the PM or endosomal compartments, such as early- and late-endosomes. In addition, cargos can be targeted to secretory granules in specialized cells. On the other hand, endocytic molecules are delivered to endosomal compartments and eventually degraded in the lysosome or they can be recycled back to the PM directly from the early endosome or via the recycling endosome. Some endocytic molecules are targeted to the TGN. At the ERGIC and *cis*-Golgi interface, transport machineries that originate from the ER and ERGIC can be recycled back to their donor compartments. Orange and green arrows indicate anterograde and retrograde trafficking respectively.

1.3.1 Bulk flow transport

Bulk flow is a process in which a cargo moves down its concentration gradient from a donor compartment into an acceptor compartment, such that the cargo concentrations in both compartments are identical (Borgese, 2016). There are more studies on bulk flow in the context of ER to early Golgi trafficking (early secretory pathway)(Barlowe and Helenius, 2016; Borgese, 2016); its role in intra-Golgi trafficking and Golgi export is less understood. Cargos such as vesicular stomatitis virus G protein (VSVG), E-cadherin and N-Ras have been found in transport carriers generated from bulk flow, and they are usually targeted to the PM (Lock et al., 2005; Polishchuk et al., 2000). Using correlative light electron microscopy (CLEM), Polishchuk and colleagues described these transport carriers as pleiomorphic structures that could be as large as half the size of a Golgi cisterna (Polishchuk et al., 2000). In addition, it was once suggested that these transport carriers move from the Golgi to the PM without contacting with other membrane compartments (Polishchuk et al., 2003). However, they were later shown to access intermediate membrane compartments, such as the RE, before reaching the PM. This was observed in the post-Golgi trafficking of VSVG and E-cadherin (Ang et al., 2004; Lock and Stow, 2005) in Madin-Darby canine kidney (MDCK) and HeLa cells, respectively. The molecular mechanism of the post-Golgi carrier biogenesis from bulk flow remains elusive. Although it was reported that the process might be independent of adaptor proteins, coat proteins and cargo receptors, it likely relies on microtubules and microtubule-based motors (Polishchuk et al., 2003; Roux et al., 2002). The detachment of transport carriers originated from bulk flow at the Golgi could be dependent on actin (Hirschberg et al., 1998). Considering the great diversity of secretory cargos in the Golgi, the number of identified cargo receptors is too small to account for cargo sorting (Herzig et al., 2012). Therefore, many secretory

cargos might not require cargo receptors for their sorting and export. This leads to the speculation that receptor independent bulk flow could be indispensable for the sorting and export of most cargos at the Golgi. Another unresolved question pertaining to bulk flow is the origin of its transport carriers. Unlike clathrin-coated vesicles (CCVs) generated at the TGN, the transport carriers from bulk flow are non-coated. This suggests that they might originate from clathrin-free TGN subdomain(s) and/or preceding cisternae of the TGN in the Golgi stack.

1.3.2 Signal-mediated transport

Signal-mediated transport actively concentrates cargos in transport carriers (Borgese, 2016). This process is regulated by the interaction between sorting signals in cargos and their respective receptors. In general, sorting signals in cytosolic tails of transmembrane cargos can interact with adaptor proteins. Such interactions can result in the recruitment of coat proteins to generate membrane budding profiles and eventually lead to transport carrier formation and Golgi export. The clathrin coat is the major coat protein that exclusively localizes to the TGN (Ladinsky et al., 1999). In general, CCVs generated from the TGN can mediate cargo transport to endolysosomal compartments. This can occur either directly from the TGN to endolysosomes transport (Chen et al., 2017; Waguri et al., 2003) or indirectly from the TGN to the PM en route to endolysosomal stations (Chen et al., 2017). Cargo sorting at the TGN can be even more complicated in polarized epithelial cells due to the necessity to specifically target proteins to apical or basolateral domains in these cells (Fölsch et al., 2003; Gonzalez and Rodriguez-Boulan, 2009).

There are two types of cargo adaptor in the Golgi: one is monomeric and the other is heterotetrameric (Lu and Hong, 2014). Five heterotetrameric adaptor protein

complexes (APs), AP-1 to 5, have been reported in higher eukaryotes. Among them, AP-1, AP-3 and AP-4 are involved in cargo sorting and transport at the TGN. AP-1, but not AP-4, interacts with clathrin, whereas whether AP-3 associates with clathrin remains to be elucidated (Guo et al., 2014). AP-1 has two isoforms, AP-1A and AP-1B, which contain different medium (μ) subunits, namely μ1A and μ1B, respectively (Fölsch et al., 1999). While AP-1B is expressed only in polarized epithelial cells, AP-1A is expressed ubiquitously (Guo et al., 2014). They recognize YXXØ (Y: tyrosine, X: any amino acid, Ø: bulky hydrophobic amino acid) and [DE]XXXL[LI] (D: aspartic acid, E: glutamic acid, X: any amino acid, L: leucine, I: isoleucine) in the cytosolic tails of client proteins. These signal-adaptor interactions are important in targeting endolysosomal proteins (Traub and Bonifacino, 2013) and basolateral PM proteins in polarized cells (Stow and Murray, 2015). There also exist sorting signals other than those mentioned above. For instance, AP-1B can bind the GDNS motif-containing transferrin receptor (TfR) and sort it to the basolateral PM of polarized epithelial cells (Odorizzi and Trowbridge, 1997).

Another class of cargo adaptor is the ubiquitously expressed monomeric Golgi-localized, γ-ear-containing, Arf-binding proteins (GGAs). In mammalian cells, there are three types of GGAs: GGA1, GGA2 and GGA3. They regulate the transport of cargos to endolysosomal compartments through the interaction with the acidic cluster-dileucine motifs (DXXLL) in the cytosolic tails of cargos (Guo et al., 2014). Two of the most studied clients of GGAs are cation-dependent and cation-independent mannose-6-phosphate receptors (CD-MPR and CI-MPR, respectively). Mutation of the dileucine motif of CD-MPR can disable its export from the Golgi (Chen et al., 2017). Similarly, when a dominant-negative GGA1 mutant was introduced into cells, CD-MPR was found to be accumulated in the Golgi (Puertollano et al., 2001a). Hence, these

experiments highlight the importance of signal-adaptor interaction in facilitating the export of a cargo from the Golgi. EpsinR and yeast exomers are clathrin-associated adaptors that also localize to the TGN. The former regulates the transport between the TGN and endosomes, whereas the latter facilitates the trafficking from the TGN to the PM.

Despite the identification and characterization of signal-adaptor interactions, their functional role at the TGN is not always well understood. For example, the Golgi export of lysosome-associated membrane glycoprotein 1 (Lamp1) has been shown to be independent of its cytosolic YXXØ (i.e. YQTI) motif (Chen et al., 2017), although Lamp1 was observed in the AP-1/clathrin-positive TGN-derived vesicles (Höning et al., 1996). Nonetheless, it was reported that Lamp1 could adopt a clathrin-independent pathway involving vacuolar protein sorting-associated protein 41 (Vps41) and vesicle-associated membrane protein 7 (Vamp7) to be transported to the LE (Pols et al., 2013). In Chapter 6, the role of sorting signals of several secretory cargos is investigated.

1.3.3 Lateral partition transport

The third mechanism for cargo sorting in the Golgi proposes that cargos can be concentrated into subdomains or transport carriers in a signal-independent manner. This can be driven by the physico-chemical features of cargos and the surrounding lipid environments (Borgese, 2016; Kaiser et al., 2011). This mechanism is less often discussed and remains elusive, although it could offer explanations for some observations pertaining to the retrieval or retention of ER and Golgi proteins. For instance, the membrane of post-Golgi compartments is generally thicker than that of the ER and Golgi. This is caused by the asymmetric distribution of cholesterol, sphingolipid, sterol and other lipid components. In accordance with the trend of membrane thickness, a systematic analysis of transmembrane proteins revealed that

the length of the transmembrane domain of proteins that localize to post-Golgi compartments is generally longer than that of ER- and Golgi-localized proteins (Sharpe et al., 2010). Hence, Munro and colleagues proposed that membrane proteins could be preferentially sorted to compartments that best match with their transmembrane domain lengths (Sharpe et al., 2010). Other lipid bilayer features, such as membrane curvature, could also play a role in protein sorting in the Golgi. Recently, it was reported that palmitoylation of membrane proteins could induce small positive membrane curvatures that would favourably drive palmitoylated proteins laterally to the Golgi cisternal rim, which has a high membrane curvature that could favourably accommodate palmitoylated proteins and their associated subdomains (Ernst et al., 2018).

Both bulk flow and selective transports, whether signal- or non-signal-mediated, could coordinate to generate the specificity and efficiency of protein sorting in the Golgi. For instance, the signal-mediated concentration of proteins in a domain may create a favourable environment into which other proteins are allowed to diffuse (Barlowe and Helenius, 2016; Borgese, 2016). However, there remain research gaps in the understanding of molecular mechanisms that govern protein sorting in the Golgi and the extent of the contributions of the sorting mechanisms described above.

1.3.4 Golgi exit sites

Conventionally, the TGN is regarded as the main sorting site for various secretory cargos that are destined for post-Golgi destinations, such as the extracellular space, PM, endosomes, lysosomes and specialized compartments, including secretory granules. It is widely accepted that all cargos that traverse the Golgi stack end up in

the *trans*-most TGN to be exported from the Golgi. However, the following observations support alternative Golgi exit sites.

First, both the *trans*-most and penultimate cisternae were reported to project tubules into the TGN region (Ladinsky et al., 1999; Mogelsvang et al., 2004). Second, the three *trans*-most cisternae displayed bulging domains upon incubation at 20°C (Ladinsky et al., 2002), suggesting that multiple cisternae could function in exit from the Golgi. Third, some TGNs do not display tubular profiles, suggesting that tubular profiles might not be indispensable in generating budding carriers; hence, tubule-less early cisternae could also facilitate cargo export. Fourth, unlike CCVs generated at the TGN, a class of transport carriers generated from bulk flow are non-clathrin coated, suggesting that they could originate from subcompartments other than the TGN (Polishchuk et al., 2003). Fifth, Patterson et al. proposed that cargos could exit the Golgi at multiple cisternae, based on the measurement of cargo kinetics using fluorescence microscopy (Patterson et al., 2008). Sixth, Chen et al. have reported that secretory cargos, such as TfR and Lamp1, were segregated from CD-MPR in the preceding cisternae of the TGN. Furthermore, transport carriers for TfR and Lamp1 displayed tubular profiles, which were different from the GGA positive vesicular profiles exhibited by CD-MPR (Chen et al., 2017). Altogether, these observations suggest that multiple subdomains of the TGN and/or multiple cisternae at the *trans*-face could function as exit sites for distinct cargos (Chen et al., 2017; Klumperman, 2011).

Our laboratory has previously reported that the *trans*-Golgi could also function as a Golgi exit site. This was based on our observation that several PM-targeted secretory cargos, including CD59, E-cadherin and tumour necrosis factor α (TNFα) exited the Golgi at the *trans*-Golgi (Tie et al., 2016a). Since then, we have expanded our study

on Golgi exit sites by examining a repertoire of secretory cargos that are targeted to various subcellular compartments. These findings are reported in Chapter 6.

1.4 Intra-Golgi trafficking

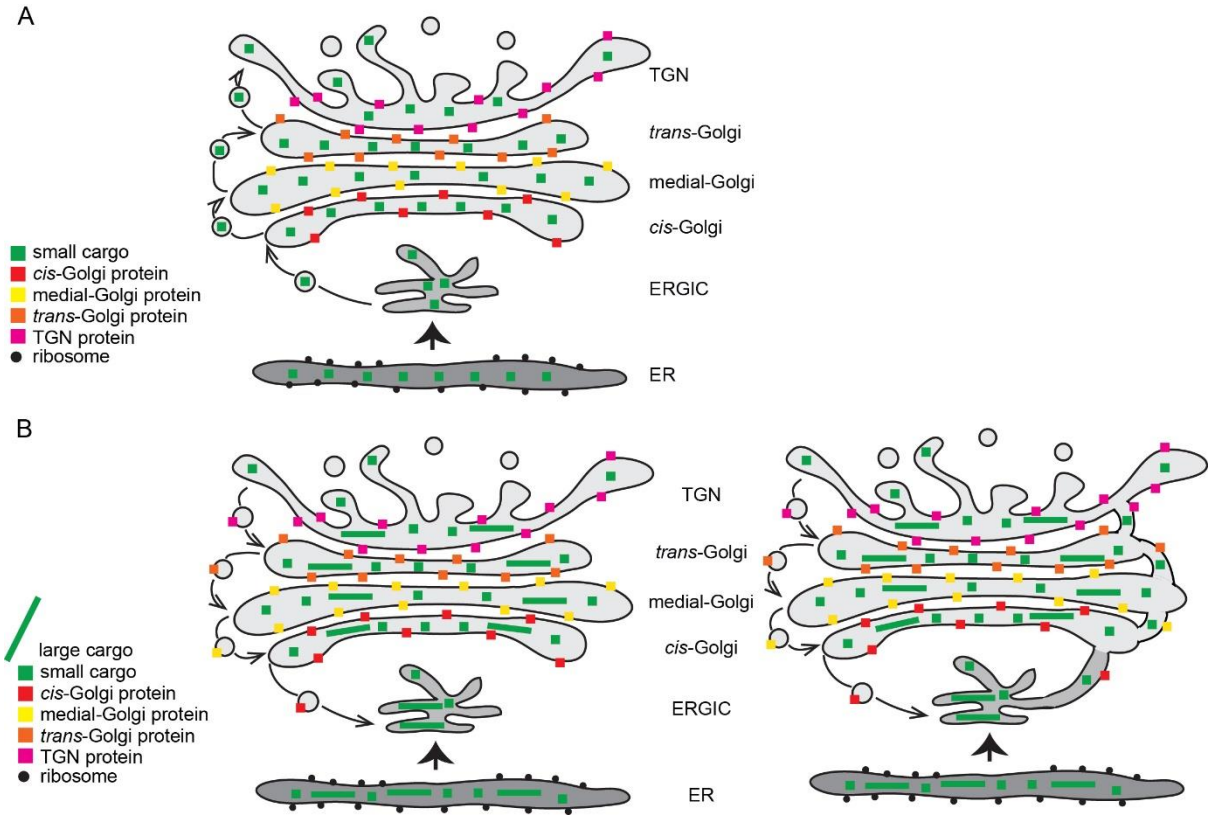

Figure 3: The three prevalent intra-Golgi trafficking models.
(A) Stable compartment model. Dissociative carriers from the ER are delivered to the ERGIC en route to the *cis*-Golgi. In the Golgi stack, the transport of molecules is mediated by COPI vesicles that bud from early cisternae and fuse with late cisternae, Golgi resident proteins are excluded from these vesicles. This model can't explain the transport of large cargos that are physically incompatible with COPI vesicles. (B, left) Cisternal maturation model. Dissociative carriers are delivered from the ER and coalesce to form the ERGIC, which matures into a nascent cisterna by receiving *cis*-Golgi resident proteins from a maturing *cis*-cisterna via COPI vesicles. The *cis*-cisterna then matures into an older cisterna by receiving Golgi resident proteins sequentially from medial-, *trans*-Golgi and the TGN while it is exporting *cis*-, medial-, and *trans*-Golgi proteins to younger cisternae. During the maturation, small and largo cargos are retained within Golgi cisternae and eventually the TGN can break down into post-Golgi carriers. (B, right) Cisternal maturation with intercisternal continuities. A Golgi cisterna matures in the same manner as described in the cisternal maturation model, except that this model introduces intercisternal continuities. These continuities or tubules facilitate anterograde trafficking of small secretory cargos while allowing Golgi resident proteins from older cisternae diffuse to younger ones. Adapted from (Glick and Luini, 2011).

The mechanism of intra-Golgi trafficking has been actively studied for several decades. However, it remains a topic of heated debate. Several prominent models have been proposed, but none can satisfactorily account for all reported observations.

Here, three major intra-Golgi trafficking models, namely 1) the cisternal maturation model, 2) the stable compartment model and 3) the cisternal maturation with intercisternal continuities trafficking model, are described and reviewed (Kurokawa et al., 2019) (Figure 3).

1.4.1 Cisternal maturation model

The cisternal maturation model views Golgi subcompartments as conveyor belts or transient membrane carriers. It predicts that secretory cargos remain in the same cisterna while it changes its molecular composition and sequentially matures into the *cis*-, medial- and *trans*-Golgi and the TGN. Although there is no direct evidence, the TGN is suggested to eventually dissipate into tubules and vesicles to serve as transport carriers to deliver cargos to their destinations (Glick and Luini, 2011; Nakano and Luini, 2010). During the maturation, Golgi resident proteins are recycled from older to younger cisternae by COPI vesicles (Rabouille and Klumperman, 2005), thereby maintaining the polarity of the Golgi (Figure 3B, left). This model is strongly supported by the observation in mammalian cells that supramolecules, such as procollagen I, were found residing in Golgi cisternae throughout their intra-Golgi trafficking (Bonfanti et al., 1998; Mironov et al., 2001). Similarly, algae scales were also reported to reside in Golgi cisternae as they traversed the Golgi (Becker et al., 1995).

The size of large cargos, such as procollagen I and algae, could range from a few hundred nm to several μm (Becker et al., 1995; Bonfanti et al., 1998). Therefore they cannot be accommodated within COPI vesicles of ~50 nm in diameter (Bykov et al.,

2017). Hence, intra-Golgi trafficking mediated by COPI vesicles, which is a hallmark of the stable compartment model, cannot explain the intra-Golgi transport of large cargos such as procollagen I. As a result, the cisternal maturation model has gained popularity and is more convincing than the stable compartment model (described below).

Additional monumental evidence came from the live cell imaging of yeast Golgi cisternae. This provided direct evidence for cisternal maturation, as resident proteins of a cisterna were observed to change gradually from those characteristic of early to late Golgi (Losev et al., 2006; Matsuura-Tokita et al., 2006). Other supporting evidence includes the observation of several Golgi resident proteins in COPI vesicles (Gilchrist et al., 2006; Martínez-Menárguez et al., 2001). Recently, the persistent residence of soluble or membrane cargos within maturing yeast Golgi cisternae has also been reported (Casler et al., 2019; Kurokawa et al., 2019).

Despite the accumulated evidence supporting the cisternal maturation model, the experimental observation of exponential export kinetics exhibited by secretory cargos contradict the model's prediction of linear export kinetics (Patterson et al., 2008). Moreover, although glycosylation enzymes are predicted to concentrate in COPI vesicles according to this model, such observations have rarely been obtained (Cosson et al., 2002; Kweon et al., 2004).

1.4.2 Stable compartment model

The stable compartment model views Golgi subcompartments as stable entities, with the stable characteristics of Golgi cisternae preserving the polarity of the Golgi. It proposes that COPI vesicles facilitate bi-directional trafficking in the Golgi. While the anterograde movement of COPI vesicles promotes cisternal transition of secretory

cargos, their retrograde movement retrieves components of trafficking machinery to their donor compartments, such as the ER and younger cisternae (Orci et al., 2000). However, the model is challenged for a number of reasons. First, COPI vesicles are too small to accommodate bulky secretory cargos such as procollagens and chylomicrons (Figure 3A). Second, secretory cargos are either not found or not enriched in COPI vesicles (Gilchrist et al., 2006; Martínez-Menárguez et al., 2001).

Nonetheless, to partially resolve the issues mentioned above, the Rothman laboratory has proposed a revised model–rim progression model, in which a Golgi cisterna is proposed to comprise a stationary central and mobile rim domain. It was suggested that dilated and dynamic rim domains could be large enough to accommodate bulky cargos and facilitate their anterograde transport (Lavieu et al., 2013).

1.4.3 Intercisternal continuities trafficking model

The intercisternal continuities trafficking model can be viewed as a revised cisternal maturation model, as basic features of the original model are retained. It also introduces heterotypic tubular connections across Golgi cisternae that function in intra-Golgi trafficking (Figure 3B, right). Intercisternal continuities have been observed in multiple EM tomographic studies (Beznoussenko et al., 2014; Han et al., 2013; Trucco et al., 2004). Beznoussenko and colleagues reported that albumin can traverse the Golgi via these tubular continuities at a fast rate, while procollagens remain in Golgi lumens and traverse the Golgi at a slower speed. Hence, this model may partially resolve the observation of different transport kinetics displayed by different cargos (Beznoussenko et al., 2014). However, the molecular mechanism by which the molecular and biochemical polarity of the Golgi is maintained in the presence of intercisternal continuities has not yet been established. It is also not clear whether

tubular connections are universal, persistent features or only induced in the presence of unusually busy traffic (Glick and Luini, 2011).

Notably, none of the models mentioned above can satisfactorily explain all experimental data reported thus far. In fact, there are other models proposed over the past decades, such as the rapid partitioning model (Patterson et al., 2008) and the Golgi progenitor model (Pfeffer, 2010). However, they are not discussed here due to their obvious flaws.

1.5 An overview of choices of microscopy, Golgi models and traffic synchronization methods in Golgi research

1.5.1 Light and electron microscopy

In the context of architecture and industrial design, 'form follows function' is widely accepted as a general principle to relate the shape of an object to its function or purpose (Sullivan, 1922). This is applicable to Golgi research as well. In recent decades, tremendous effort has been invested to decipher the architecture of the Golgi, which then serves as the framework to constrain models related to its functions (Ladinsky et al., 1999). In particular, the development of EM instruments and techniques has revealed unprecedented details of the Golgi architecture.

Despite the high resolution, one must be aware of the limitations of EM. Chemical fixation involved in conventional EM might take a few minutes to fix cellular processes completely. Distinct cellular components might also be immobilized at different rates (Gilkey and Staehelin, 1986). These issues could impair the reliability of EM in the study of dynamic structures such as the Golgi. In addition, the use of diaminobenzidine (DAB) in the cytochemical staining could be problematic, as it can be incorporated into lipid bilayers and artificially expand the membrane (Boos and Stachelin, 1981). Moreover, the imaging on thin sections of EM samples is severely under-sampled

given the huge volume and structural complexity of the native Golgi. Furthermore, membrane profiles from EM thin sections could lead to ambiguous interpretations. For instance, a round membrane profile could be interpreted as a vesicle or a longitudinal section of a tubule. The requirement of special labelling techniques for EM samples and the tremendous cost of EM instruments have also made it impractical for most laboratories (Tie et al., 2016a).

Collectively, these limitations highlight the need for improvements in EM sample preparation protocols and the necessity to image a large volume of the Golgi. Combining the fast-frozen/freeze substitution protocol and cryo-electron tomography (ET), several early EM tomographic studies of the mammalian Golgi have provided new insights for the tubular or vesicular profiles associated with Golgi cisternae. For instance, the TGN has been re-defined based on the observation that tubular extensions were found associated not only with the *trans*-most cisterna but also with the penultimate cisterna, in NRK cells (Ladinsky et al., 1999). Besides that, direct continuities between Golgi cisternae have been observed in glucose-stimulated pancreatic cells (Marsh et al., 2004). Similar phenotype was also observed in nocodazole-induced Golgi mini-stacks of NRK cells when mini-stacks were loaded with synchronous traffic waves (Trucco et al., 2004).

Recently, Engel and colleagues have reported the application of the state-of-the-art techniques, cryo-focused ion beam (cryo-FIB) and cryo-ET. After immobilizing *Chlamydomonas* cells in vitreous ice, they utilized cryo-FIB and cryo-ET to reconstruct the Golgi architecture in its native form, in which, molecular details were successfully revealed (Engel et al., 2015). Using similar methods, Bykov et al. have successfully revealed the COPI coat structure and arrangement in greater details (Bykov et al., 2017). These improved sample preparation protocols and EM techniques provide

images of large-volume 3D organization of the Golgi and its associated budding profiles and minimize the introduction of artefacts into samples.

On the other hand, light microscopy (LM) and genetically encoded fluorescent proteins allow us to study the molecular organization and dynamic of the Golgi in living cells. In general, fluorescence microscopy generates images with a high signal-to-noise ratio (SNR) that are suitable for various quantitative studies. In recent years, the advent of super-resolution light microscopic instruments and techniques has broken the resolution barriers (~200–250 nm and 450–700 nm in the x-y and z directions, respectively) of conventional LM (Galbraith and Galbraith, 2011).

In general, there are two types of super-resolution imaging techniques. The ensemble-based imaging techniques, such as structured illumination microscopy (SIM), stimulated emission depletion (STED) microscopy, Airyscan microscopy and the single-molecule-based imaging techniques, such as stochastic optical reconstruction microscopy (STORM) and photoactivation localization microscopy (PALM), have been gaining popularity in cell biology research (Galbraith and Galbraith, 2011). The fluorescent probes that are used in SIM and Airyscan microscopy are conventional fluorescent proteins and dyes. In contrast, special fluorescent probes, such as inorganic photoswitchable dyes (for STORM), photoswitchable probes (for STED) and photoactivatable probes (for PALM), are required for these imaging techniques (Galbraith and Galbraith, 2011). Due to its simplicity and versatility, Airyscan microscopy was chosen for the super-resolution imaging in this study. The principle of Airyscan microscopy involves the projection of 1.25 Airy unit (AU) onto a 32-channel gallium arsenide phosphide (GaAsP) photomultiplier tube (PMT) detector. This ensures that signal collection efficiency is maintained while every detector serves as a pinhole of 0.2 AU. This improves the resolution dramatically and the theoretical

resolution could reach 120 nm and 350 nm laterally and axially, respectively (Huff et al., 2017). Another advantage of Airyscan microscopy is its relatively fast acquisition speed compared to single-molecule-based techniques and SIM. It is also more versatile than STED for multicolour imaging (Thorley et al., 2014) because samples generated from conventional staining protocols are perfectly compatible with the Airyscan microscope. Therefore, it is suitable for our study of Golgi molecular organization and dynamics in both fixed and living cells. The results of these studies are presented in Chapters 4, 5 and 6.

1.5.2 The Golgi model

1.5.2.1 The organization of the Golgi in different organisms

The Golgi adopts various architectures across different organisms. Some of them are structurally simpler than the mammalian architecture. For instance, in plants, Golgi stacks are dispersed throughout the cytoplasm (Staehelin and Moore, 1995); in *Drosophila*, Golgi stacks are mostly discontinuous. However, pair-wise Golgi stacks have been observed under EM in *Drosophila* spermatids. 3D tomography study has also revealed a shared tubular network at the *cis*-face of these adjacent Golgi stacks (Kondylis and Rabouille, 2009; Kondylis et al., 2007); and in microsporidia, the Golgi appears as a branching tubular network (Beznoussenko et al., 2007). In the budding yeast *Pichia pastoris*, the Golgi is in stacked form (Mogelsvang et al., 2003); in contrast, in *Saccharomyces cerevisiae (S. cerevisiae)*, Golgi cisternae are unstacked and dispersed throughout the cytoplasm (Preuss et al., 1992). These simplified Golgi architectures have provided insights for our understanding of the mammalian Golgi. For instance, experiments conducted in *S. cerevisiae* have provided some of the most convincing evidence for the cisternal maturation model (Losev et al., 2006; Matsuura-

Tokita et al., 2006). Researchers in the Nakano and Glick laboratories have observed the gradually changing in the characteristics of Golgi resident proteins from those of early Golgi to become those of late Golgi in *S. cerevisiae*. In addition, they reported that both soluble and membrane cargos stay in a Golgi cisterna during its early-to-late maturation (Casler et al., 2019; Kurokawa et al., 2019), providing further support for the cisternal maturation model.

1.5.2.2 Nocodazole-induced mammalian Golgi mini-stacks

The architecture of a mammalian Golgi is too complicated to be resolved under LM. Although EM imaging on thin sections from small-volume samples can resolve the Golgi in detail, it is not an ideal method to obtain a grand view of the Golgi due to its enormous structure and volume. It is also almost impossible to reconstruct the native Golgi using electron tomography (Mogelsvang et al., 2003).

To partially resolve these issues, the nocodazole-induced Golgi mini-stack could be a good system to study the mammalian Golgi. Nocodazole is a microtubule-depolymerizing drug, and its effect on the Golgi is reversible. Nocodazole treatment can lead to the breakdown of Golgi ribbons and the redistribution and incorporation of Golgi proteins and membranes into the ER. Golgi elements can then reappear adjacent to ERES and eventually reassemble into functional Golgi mini-stacks (Cole et al., 1996). The structure and functions of Golgi mini-stacks were examined and shown to be similar to those of the native Golgi (Trucco et al., 2004). It was observed that Golgi mini-stacks remained polarized and allowed normal trafficking for both VSVG and procollagen I (Trucco et al., 2004). Moreover, the post-translational modification function of these Golgi mini-stacks was also unaffected (Xiang et al.,

2013). In this study, the majority of experiments were conducted using Golgi mini-stacks as the model.

1.5.3 The principle of Golgi protein localizations by imaging centers of mass

Our laboratory previously developed the method Golgi protein localizations by imaging centers of mass (GLIM), which allows us to quantitatively study the subcompartmental localization of Golgi proteins, based on the imaging of three-colour-labelled nocodazole-induced Golgi mini-stacks (Tie et al., 2016a). After the correction of chromatic aberration in a microscope system, more than 20 Golgi proteins were successfully mapped for their subcompartmental localizations along the Golgi axis with submicron accuracy. The Golgi axis is defined as the vector from the center of fluorescence mass (center^{mass}) of a *cis*-Golgi marker (e.g. GM130) to that of a *trans*-Golgi marker (e.g. GalT). The center^{mass} of a fluorescent object is defined as the average position of all component fluorescent signals or all component pixels of the object, weighted according to their fluorescence intensities. In our method, three-colour-labelled Golgi mini-stacks are imaged using a wide-field fluorescence microscope. Endogenous GM130 and exogenous GalT-mCherry are used as two reference markers that have localization quotients (LQs) of 0.00 and 1.00, corresponding to the *cis*- and *trans*-Golgi, respectively. The LQ denotes the quantitative localization of a Golgi protein. It is calculated from d_x/d_1, where d_x is the projected distance to the image plane from the center^{mass} of a test protein to that of GM130 and d_1 is the projected distance to the image plane from the center^{mass} of GM130 to that of GalT-mCherry. To correlate the qualitative localization of Golgi proteins with our LQs, the ranges of LQ were defined as follows: LQ<-0.25 (ERES/ERGIC), LQ=0.00±0.25 (*cis*-Golgi), LQ=0.50±0.25 (medial-Golgi), LQ=1.00±0.25 (*trans*-Golgi) and LQ>1.25 (TGN) (Tie et al., 2016a).

GLIM is ideal for most laboratories because it: 1) is compatible with conventional staining protocols; 2) requires only a conventional wide-field fluorescence microscope; 3) can complete the image acquisition and analysis within hours; 4) reaches submicron accuracy (~30 nm); 5) generates reproducible quantitative results; and 6) is applicable to both fixed and living cell samples (Tie et al., 2017; Tie et al., 2016a).

1.5.4 The synchronization of secretory proteins

It is critical to study the trafficking of secretory cargos when they are synchronized so that the unidirectional trafficking history of the cargos can be monitored and tracked over time during their intra-Golgi trafficking. Cell biologists have developed handy fluorescence-based tools and protocols to synchronize secretory cargos, and several of them are discussed in this section.

Temperature-sensitive VSVG (VSVG-tso45) is a classic tool in the study of the anterograde trafficking pathway. Under the restrictive temperature, 40°C, VSVG-tso45 can be arrested in the ER. The arrest is reversible after incubation at the permissive temperature, 32°C, at which it can resume anterograde trafficking (Kreis and Lodish, 1986; Lafay, 1974). However, the use of non-physiological temperatures, 40°C and 32°C, could disturb the mammalian cellular system. Furthermore, its application in the study of secretory cargos other than VSVG-tso45 is limited (Boncompain et al., 2012; Boncompain and Perez, 2013).

Another classic method is based on the use of two temperatures, 15°C and 20°C, that are much lower than the physiological 37°C. By incubating cells at 15°C and 20°C, secretory cargos can be arrested in the ERGIC and Golgi, respectively (Matlin and Simons, 1983; Saraste and Kuismanen, 1984). Although the effect is reversible, the reduced temperatures broadly affect almost all biosynthetic pathways temporarily

(Boncompain et al., 2012). Therefore, this method is not ideal to be generally applied in most experimental setups.

A third method is a conditional protein aggregation system. It takes advantage of a monomeric human protein, 12-kDa FK506-binding protein (FKBP12), by turning it into a dimerizing mutant (FM) through a mutation of phenylalanine^{36} to methionine (Rivera et al., 2000). Usually, multiple FMs are fused with a test protein. By default, the inter-molecular interaction between FMs can occur in the ER after expression of the protein. This leads to the formation of protein aggregates that are too large to be transported in COPII vesicles from the ERES, resulting in the arrest of protein aggregates in the ER. However, they can be de-aggregated by synthetic ligands, such as the D/D solubilizer used in our study (Figure 4A) (Rivera et al., 2000). Therefore, by genetically engineering fusion proteins that contain FMs and secretory cargos of interest, the secretory pathway of various cargos can be studied. An advantage of this method over previous ones is that non-physiological temperatures are not used. A drawback associated with this method is the possibility of generating inhomogeneous de-aggregated proteins (Boncompain and Perez, 2013). A mixture that contains both monomers and oligomeric protein aggregates might be induced in the presence of solubilizing ligands. The mixture might access different secretory pathways after ER export (Boncompain and Perez, 2013; Lavieu et al., 2014; Lavieu et al., 2013) and could complicate the interpretation of results.

Thus far, the retention using selective hook (RUSH) system appears to be the most versatile method and can be conducted at the physiological temperature (Boncompain et al., 2012). It is based on the co-expression of two fusion proteins from a bicistronic expression plasmid. To arrest a secretory cargo in the ER, the first fusion protein functions as an ER hook that contains an ER-retention signal, such as KDEL (lysine-

aspartic acid-glutamic acid-leucine) or invariant chain (Ii), and a hook, such as streptavidin. The second fusion protein contains a test secretory cargo that is fused with a streptavidin-binding peptide (SBP) and a fluorescent protein or non-fluorescent tag, which allows the tracking of the secretory cargo in living and fixed cells. A secretory cargo can be arrested in the ER via the streptavidin–SBP interaction. The arrest can be reversed by supplying cells with biotin which competes off the SBP, disrupting the interaction between SBP and streptavidin. Secretory cargos can then be released into the anterograde trafficking pathway from the ER (Figure 4B). This method can be applied to a diverse range of secretory cargos, including both membrane and soluble cargos (Boncompain et al., 2012). Theoretically, the synchronization can be achieved not only in the ER, but also in subcompartments of the Golgi if an ideal compartment-specific hook is available. RUSH and the conditional protein aggregation system have been utilised extensively in the study of intra-Golgi trafficking of various secretory cargos. These results are presented in Chapter 6.

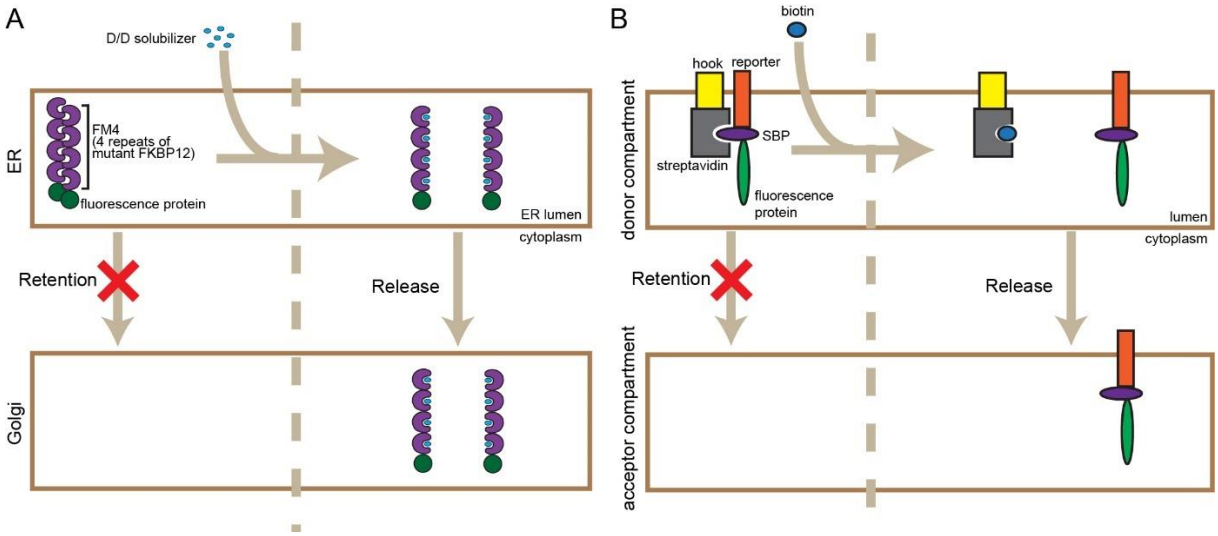

Figure 4: Basic principles of conditional protein aggregation and RUSH systems. (A) Conditional protein aggregation system. Four repeats of FM (FM4) are fused with a fluorescent protein (FP). FM4-FP can interact with each other via FMs to form large protein aggregates, which are unable to be exported from the ER. In the presence of the D/D solubilizer, a protein aggregate is de-aggregated, constituent cargos then resume their anterograde trafficking into the Golgi and subsequently to post-Golgi destinations. (B) RUSH system. A bicistronic expression plasmid expresses two fusion proteins, namely the hook-streptavidin and reporter-SBP-FP. They interact with each other via the streptavidin-SBP interaction, leading to the arrest of the reporter-SBP-FP in the donor compartment. Biotin competes off the SBP by binding to streptavidin, releasing the reporter-SBP-FP from a donor compartment to an acceptor compartment. Adapted from (Boncompain et al., 2012).

1.6 Objectives of the study

1) To investigate the molecular organization of Golgi mini-stacks by localizing Golgi proteins axially and laterally.

2) To investigate the intra-Golgi trafficking of various secretory cargos and their Golgi exit sites.

Chapter 2: Materials and methods

2.1 Construction of DNA plasmids

All constructs made in this thesis were sequences verified.

2.1.1 Vectors

pDMyc-N1: A pair of oligonucleotides (5’-TCG ACC CCG GGC CGC GGG GCC GGC CAG AAC AAA AAC TCA TCT CAG AAG AGG ATC TGG AAC AAA AAC TCA TCT CAG AAG AGG ATC TGT AAG C-3’ and 5’-GGC CGC TTA CAG ATC CTC TTC TGA GAT GAG TTT TTG TTC CAG ATC CTC TTC TGA GAT GAG TTT TTG TTC TGG CCG GCC CCG CGG CCC GGG G-3’) was annealed and ligated into SalI/NotI digested pCI-neo (Promega).

pmCherry-C2: A pair of oligonucleotides (5'- GAT CAC AGA TCT CGA GCT CAA GCT TCA GCG GCC GCG-3' and 5'-AAT TCG CGG CCG CTG AAG CTT GAG CTC GAG ATC TGT-3') were annealed and ligated into Bgl II/EcoRI digested pmCherry-C1.

These plasmids were previously described: **pDMyc-neo**(Lu and Hong, 2003), **pGEB**(Lu et al., 2001), **pA2E-N1**(Ludwig et al., 2016).

2.1.2 Constructs of Golgi enzymes and a nucleotide sugar transporter

MGAT1-AcGFP1: The coding sequence of human MGAT1 was PCR amplified from an IMAGE clone (GenBank Accession No. M61829) using a pair of oligonucleotides (5’-AGT GAC GAA TTC ATG CTG AAG AAG CAG TCT G-3’ and 5’-AGT GAC GGA TCC CGA TTC CAG CTA GGA TCA TAG CC-3’). The PCR product was digested by EcoRI/BamHI and ligated into the pAcGFP-N1 (Clontech) using the same restriction sites.

MGAT2-AcGFP1: The coding sequence of human MGAT2 was PCR amplified from an IMAGE clone (GenBank Accession No. BC006390) using a pair of oligonucleotides (5'-AGT GAC GAA TTC ATG AGG TTC CGC ATC TAC-3' and 5'-AGT GAC GGA TCC CGC TGC AGT CTT CTA TAA CT-3'. The PCR product was digested by EcoRI/BamHI and ligated into the pAcGFP-N1 (Clontech) using the same restriction sites.

MGAT4B-AcGFP1: The coding sequence of human MGAT4B was PCR amplified from an IMAGE clone (GenBank Accession No. AB000624) using a pair of oligonucleotides (5'-AGT GAC CTC GAG ATG AGG CTC CGC AAT GGC-3' and 5'-AGT GAC AAG CTT GTC GGC CTT TTT CAG GAA G-3'). The PCR product was digested by XhoI/HindIII and ligated into the pAcGFP1-N1 (Clontech) using the same restriction sites.

ST6Gal1-AcGFP1: The coding sequence of human ST6Gal1 was PCR amplified from a cDNA clone (GenBank Accession No. BC040009) using a pair of oligonucleotides (5'- AGT GAC CTC GAG ATG ATT CAC ACC AAC CTG-3' and 5'- AGT GAC GGA TCC CGG CAG TGA ATG GTC CGG AAG-3'). The PCR product was digested by XhoI/BamHI and ligated into the pAcGFP-N1 (Clontech) using the same restriction sites.

Man1B1-Myc: The coding sequence of Man1B1 was PCR amplified from a cDNA clone (GenBank Accession No. BC006079.1) using a pair of oligonucleotides (5'-AGT GAC CTC GAG GCC ACC ATG GCT GCC TGC GAG GGC AGG AGA AGC-3' and 5'- AGT GAC TCT AGA GGC AGG GGT CCA GAT AGG CAG-3'). The PCR product was digested by XhoI/XbaI and ligated into the pDMyc-N1 using the same restriction sites.

MGAT1-Myc: The coding sequence of human MGAT1 was PCR amplified from a cDNA clone (GenBank Accession No. M61829) using a pair of oligonucleotides (5'-AGT GAC CTC GAG GCC ACC ATG CTG AAG AAG CAG TCT G-3' and 5'-AGC GAC TCT AGA ATT CCA GCT AGG ATC ATA GCC C-3'). The PCR product was digested by XhoI/XbaI and ligated into the pDMyc-N1 using the same restriction sites.

MGAT2-Myc: The coding sequence of human MGAT2 was PCR amplified from a cDNA clone (GenBank Accession No. BC006390) using a pair of oligonucleotides (5'-AGT GAC GAA TTC GCC ACC ATG AGG TTC CGC ATC TAC-3' and 5'- AGT GAC TCT AGA CTG CAG TCT TCT ATA ACT-3'). The PCR product was digested by EcoRI/XbaI and ligated into the pDMyc-N1 using the same restriction sites.

ST6Gal1-Myc: The coding sequence of human ST6Gal1 was PCR amplified from a cDNA clone (GenBank Accession No. BC040009) using a pair of oligonucleotides (5'-AGT GAC CTC GAG GCC ACC ATG ATT CAC ACC AAC CTG-3' and 5'- AGT GAC TCT AGA GCA GTG AAT GGT CCG GAA GC-3'). The PCR product was digested by XhoI/XbaI and ligated into the pDMyc-N1 using the same restriction sites.

β4GalT3-Myc: The coding sequence of human β4GalT3 was PCR amplified from a cDNA clone (GenBank Accession No. BC009985.2) using a pair of oligonucleotides (5'-AGT GAC TCT AGA GCC ACC ATG TTG CGG AGG CTG CTG GAG-3' and 5'-AGT GAC GTC GAC GTG TGA ACC TCG GAG GGC TGT G-3'). The PCR product was digested by XhoI/XbaI and ligated into the pDMyc-N1 using the same restriction sites.

C2GNT1-GFP: The coding sequence of human C2GNT1 was PCR amplified from an IMAGE clone: 30915474 (GenBank Acc. No.: BC074886) using a pair of oligonucleotides (5'-GAT GCA CTC GAG GCC ACC ATG CTG AGG ACG TTG CTG-

3’ and 5’-GAT GCA GGA TCC GCG TGT TTT AAT GTC TCC AAA G-3’). The PCR product was digested by XhoI/BamHI and ligated into the pEGFP-N1 (Clontech) using the same restriction sites.

GALTNT8-GFP: The coding sequence of human GALNT8 was PCR amplified from an IMAGE clone: 9021756 (GenBank Acc. No.: NM_017417.2) using a pair of oligonucleotides (5’-GAT GCA CTC GAG GCC ACC ATG ATG TTT TGG AGG AAA C-3’ and 5’-GAT GCA GGA TCC GCC TGG CTG TTG GTC TGA CC-3’). The PCR product was digested by XhoI/BamHI and ligated into the pEGFP-N1 using the same restriction sites.

GALNT4-GFP: The coding sequence of human GALNT4 was PCR amplified from an IMAGE clone: 263604 (GenBank Acc. No.: NM_003774.5) using a pair of oligonucleotides (5’- GAT GCA CTC GAG GCC ACC ATG GCG GTG AGG TGG ACT TG-3’ and 5’-GAT GCA GGA TCC GCT TTC TCA AAA CTC CAA ATT TG-3’). The PCR product was digested by XhoI/BamHI and ligated into the pEGFP-N1 (Clontech) using the same restriction sites.

GalT-mCherry was previously described (Tie et al., 2016a). These plasmids were purchased from OriGene Technologies Inc.: **SLC35C1-myc** (RC200101), **β3GalT6-myc**(MR204731), **β4GalT7-myc** (RC200258), **POMGNT1-myc** (RC200176), **ST6GalNAC6-myc** (RC200218). These plasmids were generous gifts: **TPST1-GFP** (Addgene #66617) and **TPST2-GFP** (Addgene #66618)(Spooner et al., 2008)(D. Stephens lab).

2.1.3 Constructs of trafficking machinery components

Rab1a-GFP: The coding sequence of human Rab1a was PCR amplified from a cDNA clone (GenBank Accession No: DQ894084.2) using a pair of oligonucleotides (5’-GAT

GCA CTC GAG ACT CCA GCA TGA ATC CCG AAT ATG-3' and 5'-GAT GCA GTC GAC TTA CAA GCA GCA ACC TCC ACC-3'). The PCR product was digested by XhoI/SalI and ligated into the pEGFP-N1 (Clontech) using the same restriction sites.

Furin-GFP: The coding sequence of human Furin was PCR amplified from a cDNA clone (GenBank Accession No. BC012181.1) using a pair of oligonucleotides (5'-CAG ATC TCG AGC TCA AGC TTC GAA TTC GCC ACC ATG GAG CTG AGG CCC TGG-3' and 5'- GAT CCC GGG CCC GCG GTA CCG TCG ACC CGA GGG CGC TCT GGT CTT TG-3'). The PCR product was digested by EcoRI/SalI and ligated into the pEGFP-N1 (Clontech) using the same restriction sites.

Furin-Myc: The coding sequence of human Furin was PCR amplified from a cDNA clone (GenBank Accession No. BC012181.1) using a pair of oligonucleotides (5'-CAG ATC TCG AGC TCA AGC TTC GAA TTC GCC ACC ATG GAG CTG AGG CCC TGG-3' and 5'- GAT CCC GGG CCC GCG GTA CCG TCG ACC CGA GGG CGC TCT GGT CTT TG-3'). The PCR product was digested by EcoRI/SalI and ligated into the pDMyc-N1 using the same restriction sites.

GFP-GCC185: The coding sequence of GFP was PCR amplified from pEGFP-C1 using a pair of oligonucleotides (5'-GAA CTG GCT AGC ATG GTG AGC AAG GGC GAG-3' and 5'-GTA CTG CTC GAG GCA ATA CCG CGG CTT GTA CAG CTC GTC CAT GC-3'). The PCR product was digested by NheI/XhoI and ligated into the pDMyc-neo using the same sites. The intermediate construct was digested by XhoI/NotI and ligated with a fragment encoding full length GCC185, which was released from XhoI/NotI digested pDMyc-GCC185 (a gift from W. Hong lab).

GFP-GCC185-mCherry: GFP-GCC185 was digested by XmaI and the digested vector backbone was dephosphorylated by calf intestinal alkaline phosphatase.

mCherry was PCR amplified from pmCherry-N1 (Clontech) using a pair of oligonucleotides (5’-GAT GAC CCC GGG ACG TGA GCA AGG GCG AGG AG-3’ and 5’-GAT GAC CCC GGG AAG TCA GTC GAC TCT TGT ACA GCT CGT CCA T-3’). The PCR product was digested by XmaI and ligated into the XmaI digested GFP-GCC185 vector backbone described above. The clone with the correct mCherry orientation was screened.

GFP-ACBD3: The IMAGE clone 5259930 (GeneBank Acc. No.: BC045533) was digested by SpeI, end-blunted by T7 DNA polymerase and digested by EcoRI to release the fragment containing the coding sequence of ACBD3. The fragment was then ligated with pEGFP-C2, which was sequentially digested by BamHI, end-blunted by T7 DNA polymerase, digested by EcoRI and treated by calf intestinal alkaline phosphatase.

GFP-Rab6: The coding sequence of Rab6 was PCR amplified from an IMAGE clone: 2124966 (Genbank Acc. No.: AI435940) using a pair of oligonucleotides (5'-GTA CCT GAA TTC ATG TCC ACG GGC GGA GAC TTC G-3' and 5'-CAA GTC GGA TCC TTA GCA GGA ACA GCC TCC TTC AC-3'). The PCR product was digested by EcoRI/BamHI and ligated into the pEGFP-C2 (Clontech) using the same restriction sites.

mCherry-Golgin84: The coding sequence of Golgin84 was PCR amplified from the GFP-Golgin84 using a pair of oligonucleotides (5’-GAT GCA GTC GAC TCT TGG TTT GTT GAT CTT G-3’ and 5’-GAT GCA GGA TCC TCA TTT GCC ATA TGG TTG-3’). The PCR product was digested by SalI/BamHI and ligated into the pmCherry-C1 (Clontech) using the same restriction sites.

GFP-GGA1: The coding sequence of human GGA1 was released from the GGA1-pGAD-T7 (Lu et al., 2003) by EcoRI/BamHI digestion. The GGA1 fragment was ligated into the pEGFP-C2 using the same restriction sites.

mCherry-GM130: The coding sequence of GM130's C-terminus was released from GFP-GM130 by BamHI digestion and ligated into the pmCherry-C2 using the same restriction site. The clone with the correct orientation was screened to obtain an intermediate construct. The N-terminus of GM130 was PCR amplified from GFP-GM130 using a pair of oligonucleotides (5'-AGT GAC CTC GAG CAT GTC GGA AGA AAC CCG AC-3' and 5'-GAC CCG AAG CTT CTC TTC C-3'). The PCR product was digested by XhoI/HindIII and ligated into the intermediate construct using the same restriction sites.

GFP-Golph3: The coding sequence of Golph3 was PCR amplified from pDONR223-GOLPH3 (Addgene #21688) using a pair of oligonucleotides (5’-GAT GCA GAA TTC TAC CTC GCT GAC CCA GCG CAG CTC C-3’and 5’- GAT GCA GGA TCC TTA CTT GGT GAA CGC CGC CAC CAC CGC-3’). The PCR product was digested by EcoRI/BamHI and ligated into the pEGFP-C1 (Clontech) using the same restriction sites.

Vip36-GFP: The coding sequence of human Vip36 was PCR amplified from an IMAGE clone: 4135210 (Genbank Acc. No.: NM_006816.3) using a pair of oligonucleotides (5’-GAT GCA CTC GAG GCC ACC ATG GCG GCG GAA GGC TGG-3’ and 5’-GAT GCA GGA TCC GC GTA GAA GCG CTT GTT CCG-3’). The PCR product was digested by XhoI/BamHI and ligated into the pEGFP-N1 (Clontech) using the same restriction sites.

GFP-GCC88 was previously described (Tie et al., 2016a). **cab45-myc** (GenBank Acc. No.: NM_011341; cat #: MR205523) was purchased from OriGene Technologies Inc. **GP73-myc** (GenBank Acc. No.: NM_016548.3; cat# HG13066-CM) was purchased from Sino Biological Inc. These plasmids were generous gifts: **Arf1-GFP** (Wessels et al., 2006), **Arf4-GFP** and **Arf5-GFP** (F.J.M. van Kuppeveld lab), **GFP-ERGIC53** (Ben-Tekaya et al., 2005)(H.Hauri lab), **GFP-GM130** (Marra et al., 2001)(M. De Matties lab), **GFP-Golgin84** (Diao et al., 2003)(M. Lowe lab), **pmScarlet-Giantin-C129** (Bindels et al., 2017)(Addgene #85048, D. Gadella lab), **GPP130-GFP** (Linstedt et al., 1997)(A. Linstedt lab), **GRASP55-GFP** and **GRASP65-GFP** (Y. Wang lab), **GFP-Golgin97**, **DMyc-GCC185**, **Sec23a-mCherry**, **Sec31a-GFP** (Tang et al., 2000), **Vamp4-GFP** (Tran et al., 2007), **Myc-Sec34** (Loh and Hong, 2002) and **Myc-Sec13** (Niu et al., 2012) (W. Hong lab).

2.1.4 Constructs of RUSH reporters

Ii-Streptavidin(Strep)_ss-SBP-GFP: Two intermediate PCR products were PCR amplified from Ii-Strep_ss-SBP-EGFP-Ecadherin and pEGFP-C1, respectively, using two pair of oligonucleotides (5’-GAT GCA CCC GGG AGG CGC GCC ATG-3’ and 5’-CTC CTC GCC CTT GCT CAC ACC TGC AGG TGG TTC ACG-3’); (5’-CGT GAA CCA CCT GCA GGT GTG AGC AAG GGC GAG GAG-3’ and 5’-GAT GCA TCT AGA TTA CTT GTA CAG CTC GTC CAT-3’). The two intermediate PCR products were used as templates and the first and fourth primers were used to PCR amplify the final PCR product. The final PCR product was digested by XmaI/XbaI and ligated into the Ii-Strep_ss-SBP-EGFP-Ecadherin using the same restriction sites.

Strep-Ii_VSVG-SBP-Flag: To obtain a fragment encoding SBP-Flag, SBP was PCR amplified from the Strep-Ii_VSVG-SBP-EGFP using a pair of oligonucleotides (5'-GAA

AGC TGA ATT CCA TGG ACG AGA A-3' and 5'- GAT GCA GGC CGG CCT TAC TTA TCG TCG TCG TCT TTG TAG TCC TTA TCG TCG TCA TCC TTG TAA TCT GGT TCA CGT TGA CCT TG-3'), where two Flag coding sequences were incorporated in the reverse primer, to obtain a PCR product of SBP-Flag. The PCR product was digested by EcoRI/FseI and ligated into the Strep-Ii_VSVG-SBP-EGFP using the same restriction sites.

Strep-KDEL_Vamp4-SBP-APEX2-Dmyc: To obtain a fragment encoding Vamp4-SBP-APEX2-(dual Myc)Dmyc, two intermediate products were PCR amplified from Strep-KDEL_Vamp4-SBP-EGFP (unpublished construct) and pCI-neo-VSVGtsO45-APEX2-Dmyc (unpublished construct), respectively, using two pairs of oligonucleotides (5'-TAC TGC GAA TTC CAT GGA C-3' and 5'-GTA AGA CTT TCC CAT GGT GGC CAT ACC TGC AGG TGG TTC ACG TTG ACC TTG-3'); (5'-CAA GGT CAA CGT GAA CCA CCT GCA GGT ATG GCC ACC ATG GGA AAG TCT TAC-3' and 5'-GAT GCA CTC GAG TTA CAG ATC CTC TTC TGA G-3'). The two intermediate PCR products were used as templates and the first and fourth primers were used to PCR amplify the final PCR product. The final PCR product was digested by EcoRI/XhoI and ligated into the Strep-KDEL_Vamp4-SBP-EGFP using the same restriction sites.

Strep-KDEL_ss-SBP-Lamp1: Lamp1 was PCR amplified from Lamp1-GFP (a gift from T. Kirchhausen lab) using a pair of oligonucleotides (5'-GAT GCA GGC CGG CCA GAC GCA ATG TTT ATG GTG AAA AAT G-3' and 5'-GAT GCA CTC GAG CTA GAT AGT CTG GTA GCC-3'). The PCR product was digested by FseI/XhoI and ligated into the Strep-KDEL_ss-SBP-GFP-E-cadherin using the same restriction sites.

Strep-KDEL_ss-SBP-Lamp1^{Y404A}: A pair of oligonucleotides (5'-GAT GCA GGC CGG CCA GAC GCA ATG TTT ATG GTG AAA AAT G-3' and 5'-GAT GCA CTC GAG CTA GAT AGT CTG TGC GCC TGC GTG ACT CCT CTT CC-3') were designed such that the Y404A mutation was incorporated into the reverse primer. The Lamp1 ^{Y404A} was PCR amplified from the Lamp1-GFP using above-mentioned primers. The PCR product was digested by FseI/XhoI and ligated into the Strep-KDEL_ss-SBP-GFP-Lamp1 using the same restriction sites.

These plasmids were previously described: **ss-Strep-KDEL_ss-SBP-GFP-CD8a-Furin** and **ss-Strep-KDEL_ss-SBP-GFP-CD59** (Tie et al., 2016a). These plasmids were generous gifts: **Strep-KDEL_TfR-SBP-GFP**, **Strep-KDEL_ss-SBP-GFP-CD-MPR** and **Strep-KDEL_ss-SBP-GFP-CD-MPR$^{L274A/L275A}$** (Chen et al., 2017)(J. Bonifacino lab), **Strep-Ii_VSVG-SBP-EGFP**, **ss-Strep-KDEL_ManII-SBP-GFP**, **ss-Strep-KDEL_ss-SBP-GFP-E-cadherin**, **ss-Strep-KDEL_ss-SBP-mCherry-GPI**, (Boncompain et al., 2012) and **ss-Strep-KDEL_ss-SBP-GFP-collagenX** (F. Perez lab).

2.1.5 Constructs of FM4-fusion conditional protein aggregation reporters

FM4-moxGFP: The moxGFP coding sequence was PCR amplified from moxGFP (Addgene #68070) using a pair of oligonucleotides (5'-GAT GCA ACT AGT GTG TCC AAG GGC GAG GAG-3' and 5'-GAT GCA GGA TCC TTA CTT GTA CAG CTC GTC-3'). The PCR product was digested by SpeI/ BamHI and ligated into the backbone obtained from SpeI/ BamHI digested pC4S1-FM4-FCS-hGH (J. Rothman lab).

GFP-FM4-CD8a (Lavieu et al., 2013) was a generous gift from J. Rothman lab.

2.1.6 Constructs for APEX2-EM

MGAT2-APEX2-GFP: The coding sequence of human MGAT2 was PCR amplified from an IMAGE clone (GenBank Accession No. BC006390) using a pair of oligonucleotides (5'-AGT GAC CTC GAG ATG AGG TTC CGC ATC TAC-3' and 5'-AGT GAC AAG CTT CTG CAG TCT TCT ATA ACT TTT AC-3'). The PCR product was digested by XhoI/HindIII and ligated into the pA2E-C1 (A. Ludwig lab) using the same restriction sites.

GPP130-APEX2-GFP: The coding sequence of APEX2 was PCR amplified from the pA2E-N1 (Ludwig et al., 2016) using a pair of oligonucleotides (5'-GAT GCA CCG CGG GCG GAA AGT CTT ACC CAA CTG-3' and 5'-GAT GCA GGA TCC GGC ATC AGC AAA CCC AAG-3'). The PCR product was digested by SacII/BamHI and ligated into the GPP130-GFP (Linstedt et al., 1997) using the same restriction sites.

2.1.7 Constructs for Giantin antibody production

His-Giantin (3131-3201aa): The coding sequence 3131-3201 amino acids (aa) of human Giantin (NP_004478.3) was PCR amplified from pmScarlet-Giantin-C129 (Addgene #85048)(Bindels et al., 2017) using a pair of oligonucleotides (5'-GAT GCA GGA TCC GAA CCG CAG CAA AGC TTT TC-3' and 5'-GAT GCA CTC GAG TCT CCT GAG TGC CAC AGG AG-3'). The PCR product was digested by BamHI/ XhoI and ligated into the pET30a (Novagen) using the same restriction sites.

GST-Giantin (3131-3235aa): The coding sequence 3131-3235 aa of human Giantin (NP_004478.3) was PCR amplified from pmScarlet-Giantin-C129 (Addgene #85048)(Bindels et al., 2017) using a pair of oligonucleotides (5'- GAT GCA GAA TTC GAA CCG CAG CAA AGC TTT T C-3' and 5'-GAT GCA GGA TCC TCA TCG GGT CCG TGA ATG ACA G-3'). The PCR product was digested by EcoRI/ BamHI and ligated into the pGEB using the same restriction sites.

2.1.8 Other constructs

tsO45-VSVG-Furin-GFP: Two intermediate PCR products were PCR amplified from tsO45-VSVG-GFP (Presley et al., 1997) and CD8a-Furin (Mahajan et al., 2013) using two pairs of oligonucleotides (5'-AGT CAA GA ATT CAT GAA GTG CTT TTT GTA C-3' and 5'-CTA AAG CCA GAG CGC AGC TGA ATG CAA AGA TAA ATA CCA A-3'); (5'-TTG GTA TTT ATC TTT GCA TTC AGC TGC GCT CTG GCT TTA G-3' and 5'-AGT CAA GGA TCC GCG AGG GCG CTC TGG TCT TTG AT-3'). The two intermediate PCR products were used as templates and the first and fourth primers were used to PCR amplify the final PCR product. The final PCR product was digested by EcoRI/BamHI and ligated into the pEGFP-N1 (Clontech) using the same restriction sites.

These plasmids were generous gifts: **tsO45-VSVG-GFP**(Presley et al., 1997)(J. Lippincott-Schwartz lab), **Streptavidin-His** (Howarth et al., 2006) (T.Alice lab). These plasmids were constructed in our lab and previously described: **GFP-Nup133-mut** and **shNup133-1** (Tie et al., 2016b), **CD8a-Furin** and **CD8a-CI-MPR** (Mahajan et al., 2013).

2.2 Cell lines

Cell line	Species
HeLa	Homo sapiens
Normal rat kidney (NRK) fibroblast cell	Rattus norvegicus
293FT	Homo sapiens

Table 1: List of cell lines.

2.3 Commercial kits

Commercial kit	Source	Catalog number
APEX Alexa Fluor 647 Antibody labelling kit	Thermo Fisher Scientific	A10475
APEX Alexa Fluor 488 Antibody labelling kit	Thermo Fisher Scientific	A10468

Table 2: List of commercial kits.

2.4 Software/algorithm

Software/Algorithm	Source	Purpose
Fiji	https://fiji.sc/	Image processing
ImageJ	https://imagej.nih.gov/ij/	Image processing
Chromatic aberration correction (For GLIM)	(Tie et al., 2016a)	To correct the chromatic aberration induced by the microscope system
Normalization and Giantin alignment for en face Golgi mini-stacks.ijm (Appendix 1)	This thesis	To translate Golgi images to the image center and normalize their gyradii followed by generating trimmed image and normalizing intensity of each channel image
Radial mean intensity profile.ijm (Appendix 2)	This thesis	To measure radial mean intensity of averaged en face view image
Rotation _resize_normalization for side view averaging.ijm (Appendix 3)	This thesis	To translate, rotate, normalize sizes of side view images of Golgi proteins, followed by generating trimmed image and normalizing intensity of each channel image

Table 3: List of software/algorithm.

2.5 Chemicals/recombinant proteins.

Chemical	Source	Catalogue No.	Working concentration
Biotin	IBA	21016002	40 µM
Biotin phenol	Iris Biotech GmbH	LS3500	500 µM
Nocodazole	Merck	487928	33 µM
D/D solubilizer	Clontech	635054	1 mM
Cycloheximide	Sigma-Aldrich		10 µg/mL
Streptavidin-His	Purified in the lab		100ng/mL

Table 4: List of chemicals/recombinant proteins.

2.6 Antibodies

Antibody	Source	Clone/catalogue No.	Purpose	Working dilution
GM130 C-terminus (mouse monoclonal)	BD Bioscience	610823	IF	1:500
GM130 N-terminus (rabbit monoclonal)	Abcam	Ab52649	IF	1:500
Golgin245 (mouse monoclonal)	BD Bioscience	611280	IF	1:100
GGA2 (mouse monoclonal)	BD Bioscience	612612	IF	1:200
GS15 (mouse monoclonal)	BD Bioscience	610960	IF	1:250

GS27 (mouse monoclonal)	BD Bioscience	611034	IF	1:250
GS28 (mouse monoclonal)	BD Bioscience	611184	IF	1:250
Syntaxin6 (mouse monoclonal)	BD Bioscience	610635	IF	1:250
Vti1a (mouse monoclonal)	BD Bioscience	611220	IF	1:500
Myc (mouse monoclonal)	Santa Cruz Biotechnology	9E10	IF	1:200
CLCB (mouse monoclonal)	Santa Cruz Biotechnology	SC-376414	IF	1:200
γCOP (mouse monoclonal)	Santa Cruz Biotechnology	SC-393977	IF	1:200
Furin (rabbit polyclonal)	Thermo Fisher Scientific	PA1062	IF	1:100
CI-MPR	Thermo Fisher Scientific	MA1-066	IF	1:200
Alexa Fluor 594 conjugated streptavidin	Thermo Fisher Scientific	S11227	IF	1:500
βCOP (mouse monoclonal)	Sigma-Aldrich	maD	IF	1:200
Flag (mouse monoclonal)	Sigma-Aldrich	F1804	IF	1:200
Giantin N-terminus (rabbit polyclonal)	BioLegend	924302	IF	1:1000
Giantin C-terminus (rabbit polyclonal)	this thesis	–	IF; WB; IP	1:500; 1:1000; 1 µg/mL
KDEL receptor (mouse monoclonal)	Enzo Life Sciences	KR-10	IF	1:250
GALNT1 (mouse monoclonal)	H. Clausen lab	–	IF	1:10
GALNT2 (mouse monoclonal)	H. Clausen lab	–	IF	1:10
Arl1 (rabbit polyclonal)	(Lu et al., 2001)	–	IF	1:100
Golgin97 (rabbit polyclonal)	(Lu and Hong, 2003)	–	IF	1:1000
Dopey1 (rabbit polyclonal)	(Mahajan et al., 2019)	–	IF	1:500
γ-adaptin (mouse monoclonal)	Sigma-Aldrich	A4200	IF	1:250
GPP130 (rabbit polyclonal)	BioLegend	Poly19238	IF	1:1000
TGN46 (rabbit monoclonal)	Abcam	Ab50595	IF	1:1000

CD8a (mouse monoclonal)	Developmental Studies Hybridoma Bank (DSHB)	OKT8	IF	1:200
Goat anti-rabbit IgG conjugated with hoseradish peroxidase (HRP)	Bio-Rad	1706515	WB	1:5000

Table 5: List of antibodies.

2.7 The production of antibody against Giantin C-terminus 3131 to 3201 aa

2.7.1 The preparation of the Giantin C-terminus antigen and the immunization of rabbits

BL21 DE3 *Escherichia coli* (*E.coli)* bacteria were transformed with His-Giantin(3131-3201). The expression of His-Giantin (3131-3201) was induced by 0.25 mM Isopropyl β-D-1-thiogalactopyranoside (IPTG) for 18 hours (hrs). The bacteria were pellet down and lysed in 8 M urea and went through 3 cycles of freeze-and-thaw. The cell lysate was pellet down, and the supernatant was incubated with Ni-NTA agarose beads for about 18 hrs at 4°C. The agarose beads were washed with 8 M urea containing 20 mM imidazole. The His-Giantin (3131-3201) was eluted from beads by incubating with 8 M urea containing 250 mM imidazole for 1 hr at the room temperature. The elute was dialyzed in phosphate-buffered saline (PBS) and served as the antigen to be injected into rabbits to produce serum that contained antibody against Giantin C-terminus (3131-3201). The immunization procedures were performed by Genemed Synthesis Inc. In brief, the antigen was properly diluted and mixed with the appropriate adjuvant to form a stable emulsion. The resulting mixture was injected subcutaneously into rabbits. 5 immunizations were performed on rabbits over 63 days. The antiserum was collected and prepared from the clarified blood from immunized rabbits.

2.7.2 The purification of the Giantin C-terminus antibody

The cross-linked GST-Giantin (3131-3235 aa) beads were incubated with the anti-serum for 1 hr at the room temperature. The serum was drained and recycled for incubation with beads for another hour. Beads were washed with PBS and incubated with 100 mM glycine, pH 2.8 for 10 min at the room temperature. The elute was collected and added with 1 M Tris, pH 8.0. The elute which contained the polyclonal Giantin C-terminus antibody, was concentrated and ready for use.

2.7.3 The characterization of the Giantin C-terminus antibody

The purified Giantin C-terminus antibody was characterized for its specificity by using immunoprecipitation and immunofluorescence assays, which were described in Section 2.10 and 2.11.

2.8 Cell Culture, transfection and induction of Golgi mini-stacks formation

HeLa and normal rat kidney fibroblast (NRK) cells were cultured in the Dulbecco's Modified Eagle's Medium (DMEM) supplemented with 10% fetal bovine serum (FBS) in a 37°C incubator with the supply of 5% CO_2. 293FT cells were cultured under the same conditions as HeLa and NRK cells, except that 0.5mg/mL of G418 (Promega) was added into its culture medium. Cells were transfected with DNA plasmids by using Lipofectamine 2000 (Invitrogen) according to the manufacturer's manual. In the live-cell imaging, cells grown on 35 mm glass-bottom petri dish (MatTek) were cultured in CO_2-independent medium (Invitrogen) supplemented with 4 mM glutamine and 10% FBS at 37°C. To induce the formation of Golgi mini-stacks, cells were incubated with the medium containing 33 µM nocodazole for 2 to 3 hrs at 37°C.

2.9 Fluorescence microscopy

Cells were imaged under a wide-field microscope system comprising an Olympus IX83 equipped with an oil objective lens (100x, NA 1.40), motorized filter cubes/wheels, a motorized stage, a scientific complementary metal oxide semiconductor (sCMOS) camera (Neo; Andor), and a 200-W metal halide excitation light source (Lumen Pro 200; Prior Scientific). Dichroic mirrors and filters were optimized for GFP/Alexa Fluor (AF) 488, mCherry/AF594, AF647 and AF680. Only the central quadrant of the camera sensor was used for imaging. Camera settings were rolling shutter, 200-MHz digitizer, and 16 bit (low noise, high well capacity). The pixel size of images under the 100x objective lens was measured as 64 nm. The microscope system was controlled by the Metamorph software.

Cells were also imaged under the Airyscan super-resolution confocal microscopy system (Carl Zeiss) comprising a Zeiss LSM710 confocal microscope equipped with an oil objective lens (α-plan apochromat 100x, NA 1.46), a motorized stage and an Airyscan module. Three laser lines of 488, 561 and 640 nm were used to excite fluorophores and their emission filter bandwidths were 495-550 nm, 595-620 nm and long pass 645 nm, respectively. The microscope system is controlled by the ZEN software (Carl Zeiss). The pixel size of images ranged between 40 to 54 nm. The z-step size was 170 nm. In the ZEN software, image stacks were subjected to Airyscan processing followed by maximal intensity projection (MIP).

2.10 Immunoprecipitation

293FT cells were lysed in the chilled lysis buffer containing 40 mM HEPES pH7.3, 100 mM NaCl, 1% TX-100 and protease inhibitor cocktail (Roche). The cell lysate was incubated for 30 mins with rotation. Then, it was pellet down. The supernatant was added with 1 μg/mL antibody and allowed for 18 hrs rotating incubation in a cold room.

40 µl protein A/G bead slurry was added into the supernatant-antibody mixture and allowed for 3 hrs incubation with rotation in a cold room. Protein A/G beads were washed with the lysis buffer for 4 times. After that, 1X sodium dodecyl sulphate (SDS) loading buffer was added into samples and boiled for 10 mins. Protein samples were ready for the SDS-polyacrylamide gel electrophoresis (PAGE) gel loading.

2.11 Immunofluorescence

HeLa or NRK cells were grown on No.1.5 12mm-diameter glass cover slips. Cells were washed once with PBS and fixed in 4% paraformyldehyde (PFA) for 20 mins at the room temperature. Cells were then washed with PBS and 100 mM NH_4Cl. Cells were subsequently processed for immunofluorescence labelling by primary antibodies, followed by AF488-, AF647- or AF680-conjugated goat anti-mouse or anti-rabbit secondary antibodies (Invitrogen). Both primary and secondary antibodies were diluted in PBS containing 5% FBS, 2% bovine serum albumin, and 0.1% saponin (Sigma-Aldrich). Cells were mounted onto glass slides in Mowiol mounting medium containing 12% Mowiol 4-88 (EMD Millipore, Billerica, MA), 30% glycerol, and 100 mM Tris pH 8.5.

2.12 Western blot

Protein samples were prepared from cell lysates that were lysed in 1X SDS loading buffer containing 250 mM Tris-Cl pH 6.8, 8% SDS, 400 mM dithiothreitol (DTT), 0.4% bromophenol blue and 40% glycerol. Boiled and denatured protein samples were loaded and resolved in an SDS-PAGE gel. Proteins samples were then electro-blotted onto a polyvinylidene difluoride (PVDF) membrane (Bio-Rad) for 2-3 hrs at 4°C. Then, the PVDF membrane was blocked by 5% fat-free milk in PBS for 1 hr, followed by the primary antibody solution incubation for 1hr at the room temperature or more than 16

hrs at 4°C. The PVDF membrane was washed with PBS and incubated with the secondary antibody for 1 hr at the room temperature. Both primary and secondary antibodies were diluted in 5% fat-free milk in PBS. After washing off unbound secondary antibodies, the PVDF membrane was ready for exposure using chemiluminescence reagents, such as Luminol Enhancer and hydrogen peroxide solution (Advansta). The chemiluminescence signal was detected by ImageQuant LAS-4000 (GE healthcare Life Sciences).

2.13 Measuring the localization quotient (LQ) of Golgi resident protein and Golgi-transiting cargo by using GLIM

The detail protocol was previously described (Tie et al., 2017; Tie et al., 2016a). In brief, TetraSpeck beads (110 nm in diameter; Invitrogen) and nocodazole-treated HeLa cells were imaged under green, red and far-red channels. It is assumed that the center^{mass} of red fluorescence is the true position of a bead. Center^{mass}s of green, red, and far-red fluorescence of beads were measured using FIJI and fitted by a first-order polynomial function in MATLAB (MathWorks) for the microscope calibration and an algorithm was generated. The algorithm was later used to correct chromatic shifts in Golgi markers imaged in the same imaging session. All Golgi mini-stacks are three-color labelled, which represents endogenous GM130, transiently expressing GalT-mCherry and a test protein. A test protein could be either fused with a fluorescent protein or immunolabeled by an antibody. Three-color labelled Golgi mini-stacks were chosen as regions of interest (ROIs). Chromatic shifts in ROIs were corrected by the algorithm mentioned above. ROIs that fulfilled three criteria were used in LQ measurement. These criteria include 1) the total intensity of ROI $\geqslant$ 30 times of the standard deviation (SD) of the background; 2) the projected distance between the GM130 and GalT-mCherry to the image plane $\geqslant$ 70 nm; 3) the tangent of the axial

angle between the Golgi axis to test protein ⩽ 0.3. The axial angle is defined as the angle between the image plane and the test protein. Using OriginPro, corrected center^{mass}s were used to calculate the LQ of a test protein. LQ is defined as d_x/d_1, where d_x is the projected distance from center^{mass} of the test protein to that of GM130 and d_1 is the projected distance from center^{mass} of the GM130 to that of GalT-mCherry.

To measure the LQ plateau from the LQ vs time plot of a secretory cargo, the plot was fitted by a single exponential function, $y = y_0 + A_1\, e^{[-(x-x0)/t1]}$, where y_0 is the LQ plateau. The adjusted R^2 resulted from the fitting was indicated in each plot. The fitting was done by using OriginPro.

2.14 Measuring LQ$^{side\text{-}view}$s, lateral sizes of Golgi proteins and axial distance between GM130 and GalT-mCherry or Giantin from side view images

The LQ$^{side\text{-}view}$ is defined as the axial localization of a Golgi protein along the Golgi axis and its measurement is based on the averaged side view image of the protein (see Section 2.17). $\mathrm{LQ}^{\mathrm{side-view}} = \frac{d_{x,GM130}}{d_{GalT-mCherry,GM130}}$,where $d_{x,GM130}$ is defined as the axial distance from the center^{mass} of test protein x to that of GM130, whereas $d_{GalT-mCherry,GM130}$ is defined as the axial distance from the center^{mass} of the GalT-mCherry to that of GM130 (Figure 5A).

To measure the lateral size of the distribution of a Golgi protein, a thick line that incorporated the entire signal in the averaged side view was drawn orthogonally to the Golgi axis (Figure 5B). The line intensity profile was measured and subjected to either 1) super-Gaussian fitting (O. Burri, R. Guiet, EPFL-SV-BIOP), if it displays none or single peak or 2) multi-peak fitting (OriginPro), if it displays multiple peaks. In a fitted curve, the distance between two boundaries at half-maximum-intensity points of outer

slopes (Figure 5B, indicated by crosses on fitted curves) is defined as the lateral size of the Golgi protein. The lateral size of a test protein is normalized by that of Giantin.

To measure the axial distance from GM130 to GalT-mCherry or Giantin, a thick line that incorporated the entire side view-oriented Golgi mini-stack that was positive for GM130, Giantin and GalT-mCherry, was drawn in the direction of the Golgi axis (Figure 5C). Line intensity profiles were plotted and Gaussian fitted in OriginPro. The axial distance between two Golgi proteins is defined as the distance between the two half-maximum-intensity points at outer slopes of their fitted curves (Figure 5C, eg. the distance between the blue and red crosses represents the axial distance between GM130 and GalT-mCherry). The axial distance from GM130 to GalT-mCherry or Giantin is calculated by the following,

$$Axial\ distance_{GM130\ to\ GalTmCherry} = Xc_{GalT-mCherry} - Xc_{GM130} + 0.5 \times (w_{GalT-mCherry} + w_{GM130})\ ;$$

$$Axial\ distance_{GM130\ to\ Giantin} = Xc_{Giantin} - Xc_{GM130} + 0.5 \times (w_{Giantin} + w_{GM130}),$$

where Xc and w denote the x-axis value corresponding to the Gaussian peak and the full width at half maximum (FWHM) of the fitted curve respectively (Figure 5C, eg. FWHM of Giantin is indicated as w). As GM130 and GalT localize almost to two ends of the Golgi stack, the axial distance between them should indicate the axial size of the Golgi mini-stack (Figure 5C, indicated by the distance between blue and red crosses).

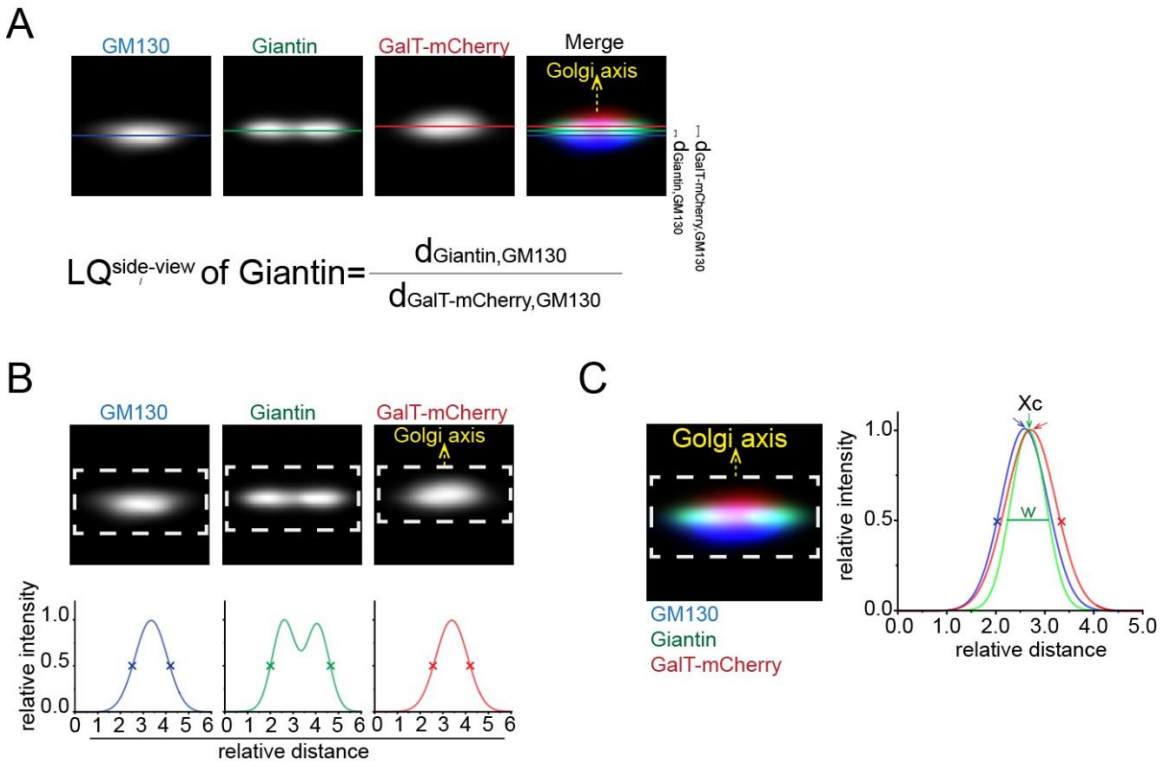

Figure 5: The measurements of $LQ^{side\text{-}view}$, lateral sizes of Golgi proteins and axial distance between GM130 and Giantin or GalT-mCherry.
Averaged side view images of GM130, Giantin and GalT-mCherry were obtained as described in Section 2.17. (A) An example of the measurement of the $LQ^{side\text{-}view}$ of Giantin. The blue, green and red lines indicate center^{mass}s along the Golgi axis of corresponding proteins. The $LQ^{side\text{-}view}$ of a Golgi protein, eg. Giantin, is calculated from the formula at the side. (B) An example of the lateral size measurement of Golgi proteins, such as GM130, Giantin and GalT-mCherry. Lines indicated by dotted boxes were drawn orthogonally to the Golgi axis. Line intensity profiles were fitted. Fitted curves were shown below and color-coded according to colours assigned to different proteins. Crosses on each curve indicate half-maximum-intensity points of slopes. (C) The measurement of axial distance. Averaged side views of GM130, Giantin and GalT-mCherry were merged. A thick line indicated by a dotted box was drawn in the direction of the Golgi axis. Line intensity profiles were fitted and color-coded according to colours assigned to different proteins. Xc indicates x-position corresponding to the peak. w indicates the FWHM of a fitted curve. The w (FWHM) of Giantin was indicated as an example.

2.15 Estimating diameters of Giantin-rings

A line was drawn across the center of the Giantin-ring and the line intensity profile was measured using FIJI. The diameter of Giantin-ring is defined as the distance between the two half-maximum-intensity points at outer slopes.

2.16 Averaging en face view-oriented Golgi mini-stack images and acquiring their radial mean intensity profiles

The detailed protocol is discussed in Section 4.6.1. In brief, en face view images of Golgi mini-stacks were identified in multi-colour labelled images, where Giantin must be immuno-labelled. They were cropped and subjected to background subtraction. A Golgi mini-stack was manipulated by the Giantin image. The gyradius of the Giantin-ring was calculated as follow,

$$\sqrt{\frac{\sum(I_i \cdot r_i^2)}{\sum I_i}}$$

, with i represents the pixel number, I_i represents the pixel intensity and r_i represents the distance of a pixel to the center^{mass} of Giantin. The Golgi mini-stack image was translated so that the center^{mass} of Giantin coincided with the image center. The Golgi mini-stack image was resized so that the gyradius of the Giantin-ring is 100 pixels. The image set was trimmed into 701×701 pixels. The total intensity of each channel image was normalized to 2×10^8. These steps can be done semi-automatically by using the macro 'Normalization and Giantin alignment for en face Golgi mini-stacks' (Appendix 1). Lastly, en face view images from each channel were averaged to generate an averaged en face view image. A radial mean intensity profile was plotted by using the macro 'Radial mean intensity profile' (Appendix 2). The radius of a Golgi protein was extracted from the profile and normalized against that of Giantin.

2.17 Averaging side view oriented Golgi mini-stack images

The detailed protocol is discussed in Section 4.6.2. In brief, side view images of Golgi mini-stacks were identified in multi-colour labelled images, where Giantin must be immuno-labelled. They were cropped and subjected to background subtraction. A Golgi mini-stack image was translated so that the center^{mass} of Giantin coincided with

the image center. The Giantin double-punctum was rotated so that it is parallel to the x-axis, while the *trans*-most protein was always positioned up. The axial and lateral sizes of a Golgi mini-stack were expanded and the image was trimmed to 701×701 pixels. The total intensity of each channel image was normalized to 5×10^7. Lastly, Golgi protein images were averaged to generate the averaged side view images. These procedures can be done semi-automatically by using the macro 'Rotation_resize_normalization for side view averaging' (Appendix 3).

2.18 Streptavidin-His purification

BL21 DE3 *E.coli* bacteria were transformed with streptavidin-His. Transformed bacteria were inoculated to 200 mL LB broth and cultured overnight at 37°C with constant shaking. After 15 hrs, LB broth volume was topped up to 1 L and IPTG was added into the bacteria culture to the final concentration of 0.5mM. The bacteria culture was incubated at the room temperature overnight. Then, the cell lysate was pellet down and lysed in 8M urea for 1.5 hrs at the room temperature with constant rotation. The cell lysate was subsequently pellet down and its supernatant was incubated with urea-equilibrated Ni-NTA beads at the room temperature for 2 hrs. Beads were then washed by 8M urea containing 20mM imidazole (Sigma-Aldrich). The streptavidin-His was eluted from beads by incubating with 8M urea containing 250mM imidazole (Sigma-Aldrich). The elute was dialyzed in PBS and eventually added with glycerol to the final concentration of 50%. The purified streptavidin-His was stored in -20°C for later use.

2.19 Anterograde trafficking assay

HeLa or NRK cells that were transfected with cargo reporters were subjected to either one of the following three methods to arrest reporters in the ER. In all scenarios,

cycloheximide was added into cell culture medium before reporters were released from their arrest.

2.19.1 RUSH reporters

HeLa cells transiently expressing RUSH reporters were cultured in DMEM, supplemented with 10% FBS, in the presence of 100ng/mL streptavidin-His to neutralize free biotin in the cell culture medium. RUSH reporters that were arrested in the ER were released into the secretory pathway in the presence of 40 µM biotin. In some experiments, 15°C or 20°C temperature block for 1.5 to 2 hrs was introduced to arrest reporters in either the ERGIC or Golgi, respectively.

2.19.2 FM4-fusion reporters

FM4-fusions that were transiently expressed in NRK cells would be trapped in the ER by default due to their formation of large protein aggregates. These protein aggregates were solubilized in the presence of 1mM D/D solubilizer (Clontech) and released into the secretory pathway.

2.19.3 VSVG-tso45 chimeras

HeLa cells transiently expressing VSVG-tso45-GFP or VSVG-tso45-Furin-GFP were cultured at 40°C to arrest misfolded VSVG-tso45 chimeras in the ER. The ER arrested chimeras were released into the secretory pathway after being incubated at 32°C.

2.20 APEX2 reaction and fluorescence labelling

HeLa cells transiently expressing MGAT2-ascorbate peroxidase 2 (APEX2)-GFP were treated with nocodazole for 2-3 hrs, followed by incubation with 500 µM biotin phenol for 30 mins at 37°C. Cells were chilled on ice and treated with 1 mM H_2O_2 for 1 min with brief agitation. Cells were then extensively washed with PBS containing 10 mM

sodium ascorbate (Sigma-Aldrich), 5 mM Trolox (Sigma-Aldrich), and 10 mM sodium azide (Sigma-Aldrich). Lastly, cells were fixed and processed for immunofluorescence. The biotin-phenol covalently modified products were labeled by AF594-conjugated streptavidin.

2.21 APEX2-EM

NRK cells were seeded onto 35 mm glass bottom petri dish (MatTek). Cells transiently expressing MGAT2-APEX2-GFP or GPP130-APEX2-GFP were fixed in 0.1 M sodium cacodylate buffer (CB) pH 7.4 containing 2 % glutaraldehyde (Electron microscopy Sciences) at the room temperature for 5 min. Cells were then incubated with fresh 2 % glutaraldehyde in CB buffer containing 2 mM $CaCl_2$, on ice for 1 hr. All subsequent steps were performed on ice until the resin infiltration. After 1 hr, cells were sequentially washed with CB buffer and CB buffer containing 50 mM glycine to quench unreacted glutaraldehyde. Cells were then incubated with diaminobenzidine (DAB, Sigma Aldrich) solution containing 0.14 mM DAB, 0.01 M HCl and 0.03 % H_2O_2 in CB buffer. The DAB polymerization reaction was halted by discarding DAB solution and washing cells with chilled CB buffer. The post-fixation staining was done on ice in dark by incubating cells in CB buffer containing 1 % osmium tetroxide (Electron Microscopy Sciences), 1% potassium ferricyanide and 2 mM $CaCl_2$ for 1 hr. Cells were then washed with chilled water, followed by the dehydration using a series (20 %, 50 %, 70%, 90 %, 100 %) of chilled ethanol. Cells were washed twice with anhydrous ethanol at the room temperature. Cells were infiltrated stepwise by the Durcupan ACM resin (Electron Microscopy Sciences) using 1:3, 1:1, 3:1 (v/v) resin:anhydrous ethanol for 30 min each, followed by infiltration of 100 % resin overnight. Next day, the 100 % resin exchange was performed for 3 to 6 rounds, with 1 hr incubation at 45 °C every time. Finally, cells were incubated at 60 °C for 48 hrs to allow the resin polymerization.

Samples were further processed as described previously (Ludwig et al., 2016). After image acquisition, Golgi stacks with long axis >500 nm were analyzed.

2.22 Fluorophore-conjugation of Giantin antibodies

The Alexa fluorophore conjugation onto the antibody was conducted by using the APEX Antibody Labeling Kit (Invitrogen) according to the manufacturer's manual. AF647 and AF488 were conjugated onto a commercial polyclonal Giantin N-terminus antibody (BioLegend) and our in-house polyclonal Giantin C-terminus antibody respectively. In brief, two APEX antibody labeling tips were first hydrated by wash buffer and two antibodies were loaded into tips. The reactive dyes that contained either AF488 or AF647 were added into tips for incubation with antibodies for 2 hrs at the room temperature. Tips were washed and neutralized by respective buffers. Finally, fluorophores conjugated antibody solutions were eluted and ready for use in the immunofluorescence labeling.

2.23 Estimating the stoichiometry and molecular weight of fluorescent protein aggregates

This was done by using a previously established protocol. To generate a fluorescence standard, in brief, HeLa cells were co-transfected with shNup133-1 and GFP-Nup133-mut to achieve the knock down of endogenous Nup133 and the substitution of which by the shRNA-resistant GFP-Nup133-mut respectively. The resulting nuclear pore complex which contains ~16 copies of GFP-Nup133-mut (Tie et al., 2016b), was used as the fluorescence standard to quantify the copy numbers of GFP-collagenX, GFP-FM4-CD8a and FM4-moxGFP aggregates. GFP-Nup133-mut and fluorescent protein aggregates were imaged under the Airyscan microscope using identical imaging conditions. Circular ROIs were drawn upon GFP-Nup133-mut positive nuclear pore complex and Golgi-associated fluorescent protein aggregates, their total intensity

within ROIs were denoted as I_{Nup} and $I_{punctum}$, respectively. The copy number of GFP-tagged protein aggregates, such as GFP-collagenX and GFP-FM4-CD8a were calculated as 16 x $I_{punctum}$ / I_{Nup}, whereas the copy number of FM4-moxGFP aggregates was calculated as 10.9 x $I_{punctum}$ / I_{Nup} because it was assumed that moxGFP is 1.47-fold brighter than the EGFP (https://www.addgene.org/fluorescent-proteins/plasmid-backbones/).

The molecular weight (MW) of a fluorescent protein aggregate was measured as follows $\text{MW per punctate aggregate} = \text{copy number per aggregate} \times MW\ per\ molecule$. It is assumed that every amino acid weighs 110 Dalton in average.

2.24 Statistical analysis

The statistical analysis in Figure 9B was performed using the student's t-test in Microsoft Excel. The rest of the statistical analysis were performed in OriginPro. Error bars represent standard deviations (SDs) or standard error of means (SEMs), as indicated in the main text or figure legends.

Chapter 3: Using GLIM to localize Golgi proteins axially in nocodazole-treated HeLa cells

To understand the biology of the Golgi, one key piece of information required is the localization of Golgi proteins. It can be interpreted from two aspects. First, the axial localization (or distribution), which is defined as the protein localization along the Golgi axis; second, the lateral localization (or distribution), which is defined as the protein localization orthogonal to the Golgi axis (discussed in Chapter 4). Although these localizations are essential for revealing the molecular organization of the Golgi, they have largely remained qualitative. For instance, the axial localization of Golgi proteins is vaguely described as the *cis*-, medial-, *trans*-Golgi or the TGN localization. These categories might not be detailed enough to reveal the spatial relationships among the hundreds of proteins found in the Golgi.

Although LM has been widely used in many Golgi localization studies, EM remains the standard because it produces results of the highest resolution. However, EM studies are beyond the capability of many laboratories, partly due to a lack of instruments, technical trainings and the time required to obtain high-quality and reliable results.

In order to accurately localize Golgi proteins using LM, GLIM has been developed to acquire the quantitative axial localization of Golgi proteins in nocodazole-treated mammalian cells (Tie et al., 2016a). The method is ideal for large-scale localization studies of Golgi proteins (see Section 1.5.3).

3.1 Using GLIM to establish a useful quantitative localization map of Golgi proteins

As a hub for post-translational modification and intracellular trafficking of proteins and lipids, the Golgi relies on more than 2000 proteins to carry out its functions (Gannon et al., 2011; Gilchrist et al., 2006). Here, 75 proteins that localize to the ERES, ERGIC,

cis-, medial-, *trans*-Golgi or the TGN, are reported (Figure 6; Table 6). They are expressed either endogenously or exogenously. The specificity of 17 out of 25 primary antibodies that target endogenous Golgi proteins has been confirmed by either gene knockdown or knockout experiments, and they were documented in literatures. Some of the tested proteins have been previously qualitatively localized using either LM or EM, and the comparison between these results and those obtained using GLIM is listed in Table 6.

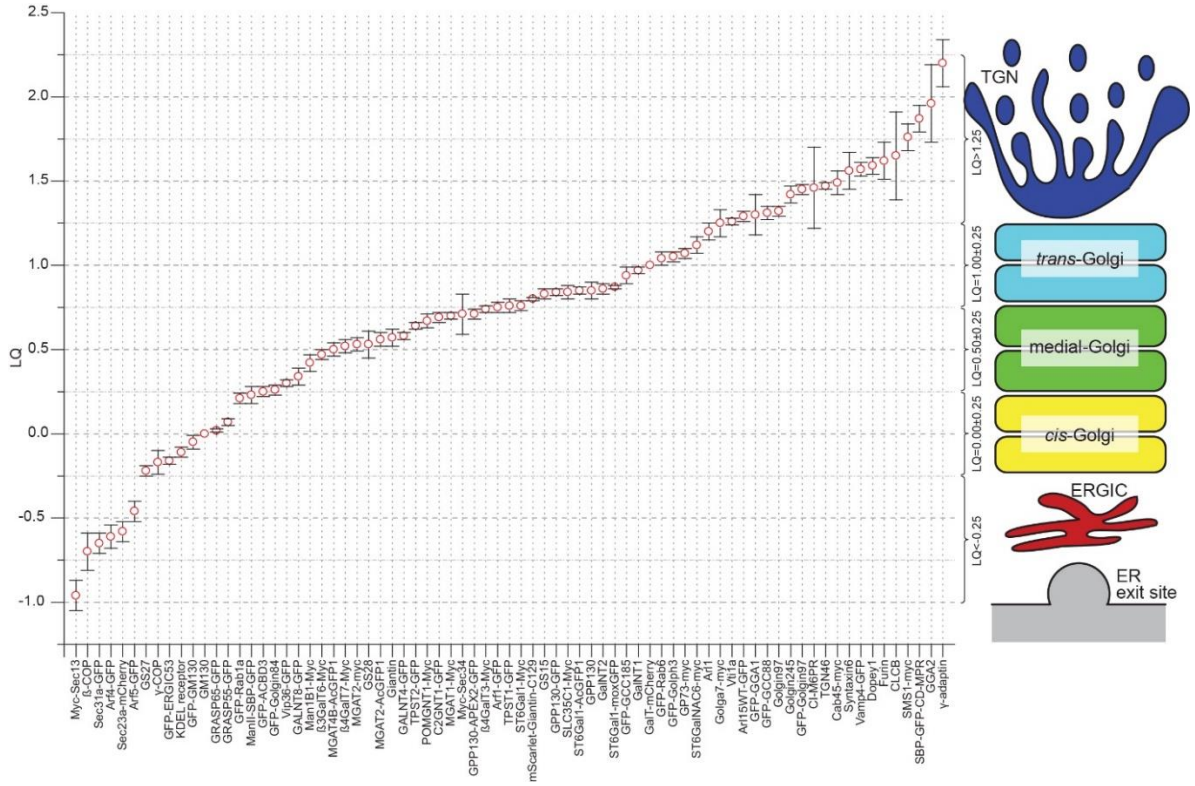

Figure 6: The mapping of Golgi proteins using GLIM.
The LQ plot maps the axial localization of various Golgi proteins according to their LQs. The range of LQ is defined as ERES/ERGIC (<-0.25), *cis*-Golgi (0.00±0.25), medial-Golgi (0.50±0.25), *trans*-Golgi (1.00±0.25) and the TGN (>1.25). The LQs of endogenous GM130 and exogenous GalT-mCherry are defined as 0.00 and 1.00, respectively (Tie et al., 2016a). Error bars, SEMs.

Name	LQ	SEM	n	Localization region	Reported localization
Myc-Sec13	-0.96	0.09	39	ERES/ERGIC	ERES (Shaywitz et al., 1995)
β-COP	-0.70	0.11	74	ERES/ERGIC	ERES/*cis* (Oprins et al., 1993)
Sec31a-GFP	-0.65	0.06	37	ERES/ERGIC	ERES/ERGIC (Tang et al., 2000)

Arf4-GFP	-0.61	0.07	51	ERES/ERGIC	ERGIC (Chun et al., 2008)
Sec23a-mCherry	-0.58	0.06	121	ERES/ERGIC	ERES (Paccaud et al., 1996)
Arf5-GFP	-0.46	0.06	42	ERES/ERGIC	ERGIC (Chun et al., 2008)
GS27*	-0.22	0.03	101	*cis*	ERGIC/*cis* (Hay et al., 1998)
γ-COP	-0.17	0.07	106	*cis*	*cis* (Moelleken et al., 2007)
GFP-ERGIC53*	-0.16	0.02	198	*cis*	ERGIC/*cis* (Hauri et al., 2000)
KDEL receptor*	-0.11	0.03	130	*cis*	ERGIC/*cis* (Griffiths et al., 1994)
GFP-GM130*	-0.05	0.04	93	*cis*	*cis* (Nakamura et al., 1995)
GM130*	0.00	-	-	*cis*	*cis* (Nakamura et al., 1995)
GRASP65-GFP	0.02	0.01	198	*cis*	*cis* (Barr et al., 1997)
GRASP55-GFP	0.07	0.02	140	*cis*	medial (Short et al., 2001)
GFP-Rab1a	0.21	0.03	154	*cis*	ERGIC/*cis* (Saraste et al., 1995)
ManII-SBP-GFP	0.23	0.05	53	*cis*	medial/*trans* (Rabouille et al., 1995a)
GFP-ACBD3	0.25	0.03	132	medial	Golgi stack (Sohda et al., 2001)
GFP-Golgin84*	0.26	0.03	108	medial	*cis* (Diao et al., 2003)
Vip36-GFP	0.30	0.02	134	medial	ERGIC/*cis* (Fullekrug et al., 1999)
GalNT8-GFP	0.34	0.05	73	medial	N.A.
Man1B1-Myc	0.42	0.05	88	medial	*cis*/medial (Dunphy and Rothman, 1983; Marra et al., 2001)
β3GalT6-Myc	0.47	0.03	97	medial	medial (Bai et al., 2001)
MGAT4B-AcGFP1	0.50	0.04	23	medial	N.A.
β4GalT7-Myc	0.52	0.04	110	medial	medial (Pinhal et al., 2001)
MGAT2-myc	0.53	0.04	136	medial	medial (Opat et al., 2001)
GS28*	0.53	0.08	125	medial	*cis*/medial/*trans* (Volchuk et al., 2004)
MGAT2-AcGFP1	0.56	0.04	110	medial	medial (Opat et al., 2000)
Giantin	0.57	0.05	103	medial	medial (Martínez-Menárguez et al., 2001)
GalNT4-GFP	0.58	0.02	163	medial	N.A.
TPST2-GFP*	0.64	0.02	154	medial	*trans* (Baeuerle and Huttner, 1987)
POMGNT1-Myc	0.67	0.04	87	medial	medial (Pereira et al., 2014)
C2GNT1-GFP	0.69	0.03	167	medial	*cis*/medial (Skrincosky et al., 1997)
MGAT1-Myc	0.70	0.02	141	medial	medial/*trans* (Rabouille et al., 1995a)
Myc-Sec34	0.71	0.12	27	medial	*cis*/medial (Suvorova et al., 2001)
GPP130-APEX2-GFP	0.71	0.03	100	medial	*cis*/medial (Linstedt et al., 1997)
β4GalT3-Myc	0.74	0.02	149	medial	N.A.
Arf1-GFP	0.75	0.03	87	*trans*	*trans*/TGN (Puertollano et al., 2001b)
TPST1-GFP*	0.76	0.04	111	*trans*	*trans* (Baeuerle and Huttner, 1987)

ST6Gal1-Myc	0.76	0.03	154	*trans*	*trans*/TGN (Rabouille et al., 1995a)
mScarlet-Giantin-C129	0.80	0.01	161	*trans*	N.A.
GS15	0.83	0.03	150	*trans*	medial (Xu et al., 2002)
GPP130-GFP*	0.84	0.02	168	*trans*	*cis*/medial (Linstedt et al., 1997)
SLC35C1-Myc	0.84	0.04	85	*trans*	*trans* (Zhang et al., 2012)
ST6Gal1-AcGFP1	0.85	0.02	138	*trans*	*trans*/TGN (Rabouille et al., 1995a)
GPP130	0.85	0.05	106	*trans*	*cis*/medial (Linstedt et al., 1997)
GalNT2	0.86	0.03	107	*trans*	Golgi stack/trans (Rottger et al., 1998)
ST6Gal1-moxGFP	0.87	0.01	183	*trans*	*trans*/TGN (Rabouille et al., 1995a)
GFP-GCC185	0.94	0.05	122	*trans*	TGN (Derby et al., 2004)
GalNT1	0.97	0.02	90	*trans*	Golgi stack (Rottger et al., 1998)
GalT-mCherry*	1.00	-	-	*trans*	*trans* (Roth and Berger, 1982)
GFP-Rab6*	1.04	0.04	262	*trans*	medial/*trans* (Goud et al., 1990)
GFP-Golph3	1.05	0.03	99	*trans*	*trans*/TGN (Snyder et al., 2006; Wu et al., 2000)
GP73-myc	1.07	0.03	75	*trans*	*cis* (Puri et al., 2002)
ST6GalNAC6-myc	1.12	0.05	96	*trans*	N.A.
Arl1*	1.20	0.05	26	*trans*	*trans*/TGN (Lu et al., 2001)
Golga7-myc	1.25	0.08	51	TGN	N.A.
Vti1a*	1.26	0.02	162	TGN	TGN (Kreykenbohm et al., 2002)
Arl15WT-GFP	1.29	0.03	104	TGN	TGN (Rocha et al., 2017)
GFP-GGA1	1.30	0.12	33	TGN	TGN (Dell'Angelica et al., 2000)
GFP-GCC88	1.31	0.04	62	TGN	*trans*/TGN (Luke et al., 2003)
Golgin97	1.32	0.03	174	TGN	TGN (Lu and Hong, 2003)
Golgin245*	1.42	0.05	126	TGN	TGN (Brown et al., 2001)
GFP-Golgin97*	1.45	0.03	161	TGN	TGN (Lu and Hong, 2003)
CI-MPR*	1.46	0.24	42	TGN	TGN (Brown, 1990)
TGN46	1.47	0.02	203	TGN	TGN (Luzio et al., 1990)
Cab45-myc	1.49	0.07	96	TGN	TGN (Crevenna et al., 2016)
Syntaxin6*	1.56	0.11	84	TGN	TGN (Bock et al., 1997)
Vamp4-GFP*	1.57	0.04	157	TGN	TGN (Steegmaier et al., 1999)
Dopey1	1.59	0.05	81	TGN	Late Golgi (Mahajan et al., 2019; Tanaka et al., 2014)
Furin*	1.62	0.11	43	TGN	TGN (Molloy et al., 1994)
CLCB	1.65	0.26	37	TGN	TGN (Puertollano et al., 2001b)
SMS1-myc	1.76	0.08	105	TGN	*trans* (Halter et al., 2007)
SBP-GFP-CD-MPR	1.87	0.08	74	TGN	TGN (Klumperman et al., 1993)

GGA2*	1.96	0.23	33	TGN	TGN (Hirst et al., 2000)
γ-Adaptin	2.20	0.14	43	TGN	TGN (Doray et al., 2002)

Table 6: LQs of Golgi proteins.
The table corresponds to the LQ plot in Figure 6. The comparison between reported localizations and results obtained from GLIM is listed. The LQs of endogenous GM130 and exogenous GalT-mCherry are defined as 0.00 and 1.00, respectively (Tie et al., 2016a). *, previously published data (Tie et al., 2016a); the rest were obtained during the course of this study.

Golgi enzymes were found mainly concentrate in the medial- (0.50±0.25) and *trans*-Golgi (1.00±0.25), except for sphingomyelin synthase 1 (SMS1; LQ=1.76) which is a lipid-modifying enzyme that localizes to the TGN (LQ>1.25). Interestingly, LQs of Golgi enzymes seemed not to strictly follow the order of glycosylation reactions. For instance, to generate the complex N-glycan, several enzymes are supposed to function in the following order: ManI (LQ=0.42), MGAT1 (LQ=0.7), ManII (LQ=0.23), MGAT2 (LQ=0.56), GalT (LQ=1.00) and ST6Gal1 (LQ=0.76 or 0.85, for ST6Gal1-myc or ST6Gal1-AcGFP1, respectively; Table 6) (Wildt and Gerngross, 2005).

In general, Golgi proteins that localize to the TGN tend to have large localization variances, as suggested by their larger SEMs (Table 6). Unlike the tightly-packed Golgi stack region, the TGN is generally portrayed as a region comprising pleiomorphic elements, such as vesicles and anastomosed tubules. Localization to these structures could result in the large variance in localization observed.

Importantly, the quantitative localization map allows us to unambiguously compare the axial localization of Golgi proteins. For instance, although both Giantin (LQ=0.57) and MGAT1 (LQ=0.70) localize to the medial-Golgi, their LQs suggest that Giantin might localize closer to the *cis*-face than MGAT1.

Chapter 4: Development of methods to discern Golgi mini-stack orientations and localize Golgi proteins laterally

Under a wide-field fluorescence microscope, blurry crescent and ring staining patterns are frequently observed in nocodazole-induced Golgi mini-stacks. It is thought that this is not due to artefacts, as such phenomena have been observed in many previous reports (Koreishi et al., 2013; Linstedt et al., 1997; Rizzo et al., 2013; Satoh et al., 2003). However, there has not yet been any detailed study of these observations.

In this section, the biological implications of the ring staining pattern are established. Moreover, its application in deciphering Golgi mini-stack orientations (i.e. en face and side views) is validated. A mini-stack can orient randomly in the cytoplasm. Its orientation is referred to as en face or side view when its Golgi axis is orthogonal or parallel to the image plane, respectively. These two views are crucial because the lateral localization of a Golgi protein can best be revealed under these views. This section also includes the introduction and validation of the concept of averaging en face or side view images in order to faithfully represent the lateral localization of Golgi proteins.

4.1 Giantin, GPP130 and Golgin84 serve as markers for the orientation of Golgi mini-stacks

Under the Airyscan microscope, the staining pattern of Giantin, GPP130 and Golgin84 consistently displayed circular rings, oval rings and double-puncta in nocodazole-treated HeLa cells (Figure 7A). Assuming that Golgi proteins are organized with rotational symmetry around the Golgi axis, the circular ring staining pattern might suggest that Giantin, GPP130 and Golgin84 localize to cisternal rims. The staining pattern of a Golgi cisternal-rim marker could facilitate the discernment of the orientation of the Golgi stack under fluorescence microscopy (Figure 7B), which was

previously almost impossible. The circular ring, oval ring and double-punctum staining patterns of a cisternal rim-localized protein were proposed to indicate en face, oblique and side views of the Golgi mini-stack, respectively (Figure 7B). Notably, a previous EM study has demonstrated the rim localization of Giantin (Koreishi et al., 2013).

We attempted to validate potential cisternal-rim markers, including Giantin, Golgin84 and GPP130, in Sections 4.3 and 4.4.

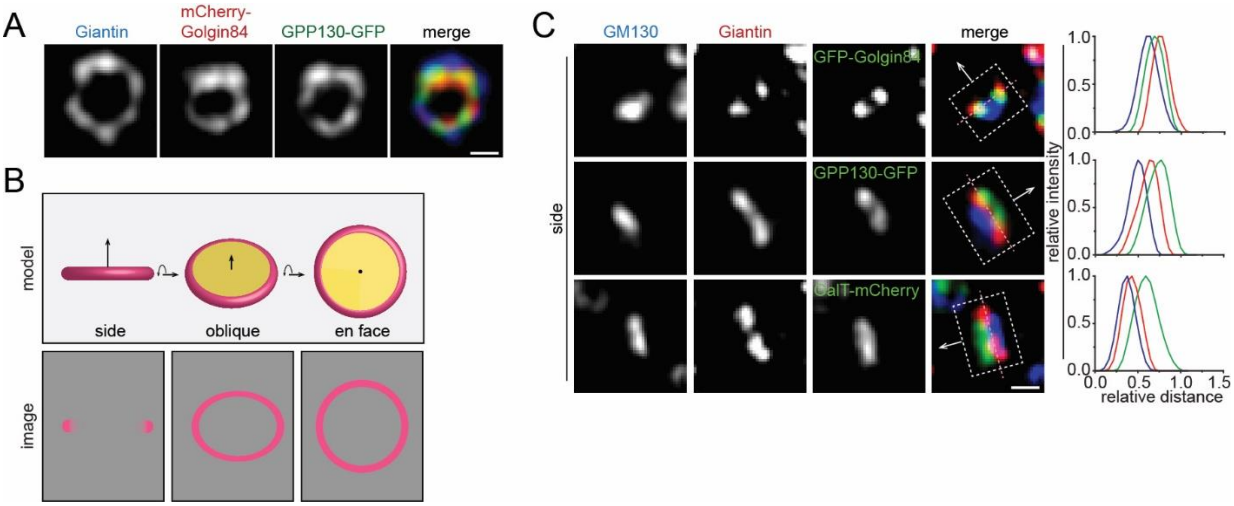

Figure 7: Giantin, GPP130 and Golgin84 are potential cisternal rim markers that might help to discern the orientation of a Golgi mini-stack.
Throughout this thesis, nocodazole-treated HeLa cells were imaged under the Airyscan microscope unless stated otherwise. In general, non-tagged proteins are endogenously stained by their antibodies while tagged-proteins are transiently transfected. (A) Giantin, Golgin84 and GPP130 appear as concentric rings. (B) The schematic representation of possible orientations (side, oblique and en face) of a Golgi cisterna and their corresponding predicted images of staining patterns under the fluorescence microscope. The arrows in the side and oblique views and the dot in the en face view indicate the Golgi axis at corresponding orientations. (C) The side views of Giantin, Golgin84 and GPP130 appear as double-punctum while that of GM130 and GalT appear as bar shape. In each merged image, the line intensity profile was generated from a thick line represented by a dotted box. The line was drawn along the direction indicated by an arrow. The same scheme is applied throughout this thesis. The direction of the line is following the Golgi axis from the *cis*- to *trans*-face, where the GM130 is at the *cis*-most in this case. The double-punctum is connected by a dotted pink line and it is almost orthogonal to the Golgi axis. The normalized intensity plot is color-coded according to colours assigned to different proteins. n, number of analysed Golgi mini-stacks. Scale bar, 500 nm.

4.2 The purification and characterization of a Giantin C-terminus antibody

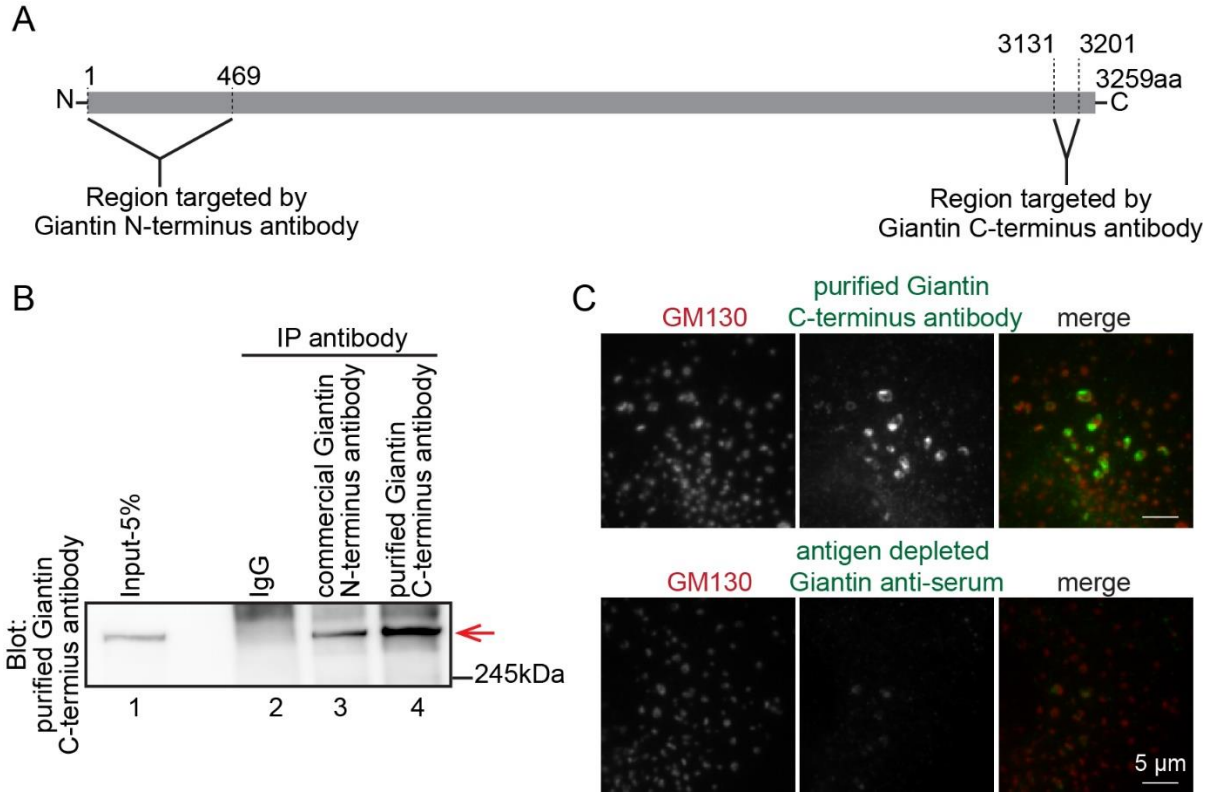

Figure 8: The characterization of the in-house purified Giantin C-terminus antibody using IP and IF assays.
(A) The schematic representation of the human Giantin coding sequence, 1-3259 aa. The regions demarcated by dotted lines, 1-469 aa and 3131-3201 aa, represent epitopes targeted by Giantin N- and C-terminus antibodies, respectively. (B) The in-house purified Giantin C-terminus antibody can immunoprecipitate the endogenous Giantin. The western blot shows the immunoprecipitation of 293FT cell lysates by three antibodies, IgG (negative control), commercial Giantin N-terminus antibody (positive control) and in-house purified Giantin C-terminus antibody (test antibody). The blot was detected by the Giantin C-terminus antibody. Lane1, 5% input from 293FT cell lysates; Lane 2-4, immunoprecipitated products from corresponding antibodies as indicated. Red arrow indicates the endogenous Giantin. (C) The in-house purified Giantin C-terminus antibody can immuno-stain the endogenous Giantin. Nocodazole-treated HeLa cells were immuno-stained by GM130 and Giantin C-terminus antibodies or antigen-depleted Giantin anti-serum. Scale bar, 5 μm.

In order to conduct the experiments described in the next section, a polyclonal Giantin C-terminus antibody was generated. First, His-tagged Giantin C-terminus containing aa 3131-3201 was purified as the antigen for the immunization of rabbits (Figure 8A). After obtaining the anti-serum, the affinity purification approach was adopted to purify the antibody against the Giantin C-terminus. The specificity of the antibody was

validated using an immunoprecipitation (IP) assay, which revealed that, like the commercial Giantin N-terminus antibody that was raised against Giantin aa 1-469, the antibody we generated can immunoprecipitate endogenous Giantin from 293FT cell lysates (Figure 8B, lanes 3-4). In an immunofluorescence (IF) assay, the Giantin C-terminus antibody could detect endogenous Giantin, and the staining could be blocked by its antigen (Figure 8C). Therefore, the specificity of in-house purified Giantin C-terminus antibody was validated.

4.3 N- and C-termini of Golgins coincide on cisternal membranes

Giantin, Golgin84 and GCC185 are members of the Golgin family, which are known to localize to Golgi cisternae via their carboxyl termini (Bascom et al., 1999; Linstedt et al., 1995; Munro, 2011). Members of the Golgin family share a common feature: a large percentage of their protein structures are coiled-coil domains (Muschalik and Munro, 2018). The length of these coiled-coil domains is predicted to reach a few hundred nm when fully extended. Every 500 aa of coiled-coils is calculated to have a length of 75 nm (Munro, 2011); therefore, fully extended Giantin and GCC185 molecules were estimated to have lengths of approximately 450 nm and 200 nm, respectively (Cheung et al., 2015; Munro, 2011).

According to our measurement, the diameter of the Giantin ring could reach approximately 950±10 nm (mean±SEM; Figure 15E). As the ring staining patterns of Giantin and Golgin84 were observed using a Giantin N-terminus antibody and N-terminus FP-tagged Golgin84, respectively, it is unclear whether their ring staining patterns truly indicate physical diameters of en face-oriented cisternae or are due to fully extended conformations of Golgins. They can be validated as cisternal rim markers only if the former is true.

If a Golgin molecule adopts an extended conformation *in vivo*, a significant difference in ring-diameters generated from the staining patterns of their respective N- and C-terminus-targeted antibodies should be revealed under Airyscan microscopy, which has a practical spatial resolution of 140 nm in the x-y plane (Huff, 2015). Hence, experiments were designed to test this idea on three Golgins, namely Giantin, GM130 and GCC185.

Due to the unavailability of a commercial antibody against the C-terminus of Giantin, an in-house antibody was prepared. Its production and validation are described in Section 4.2. Since our commercial N- and in-house C-terminal antibodies were both raised in rabbits, the two antibodies were covalently conjugated with the fluorophores AF647 and AF488, respectively, for co-staining. Using this method, the endogenous Giantin N- and C-termini on the same Golgi mini-stack can be immuno-labelled and differentiated using two rabbit antibodies. It was observed that the ring staining patterns generated from the two antibodies were highly colocalized. Quantitative analysis revealed that the ring-diameter observed with the N-terminus antibody ring was only ~50 nm larger than that observed with the C-terminus antibody (calculated from 0.95×950 nm; Figure 9A-B). This is far less than 900 nm (calculated from 450×2 nm), which is the predicted difference in ring-diameters if the molecule were fully extended *in vivo*. As a control, the Giantin N-terminus antibody was conjugated with AF647 and AF488 individually, and the ring-diameters obtained using these conjugated antibodies were almost identical, as the measured N-to-N diameter ratio was 1.0 (Figure 9B).

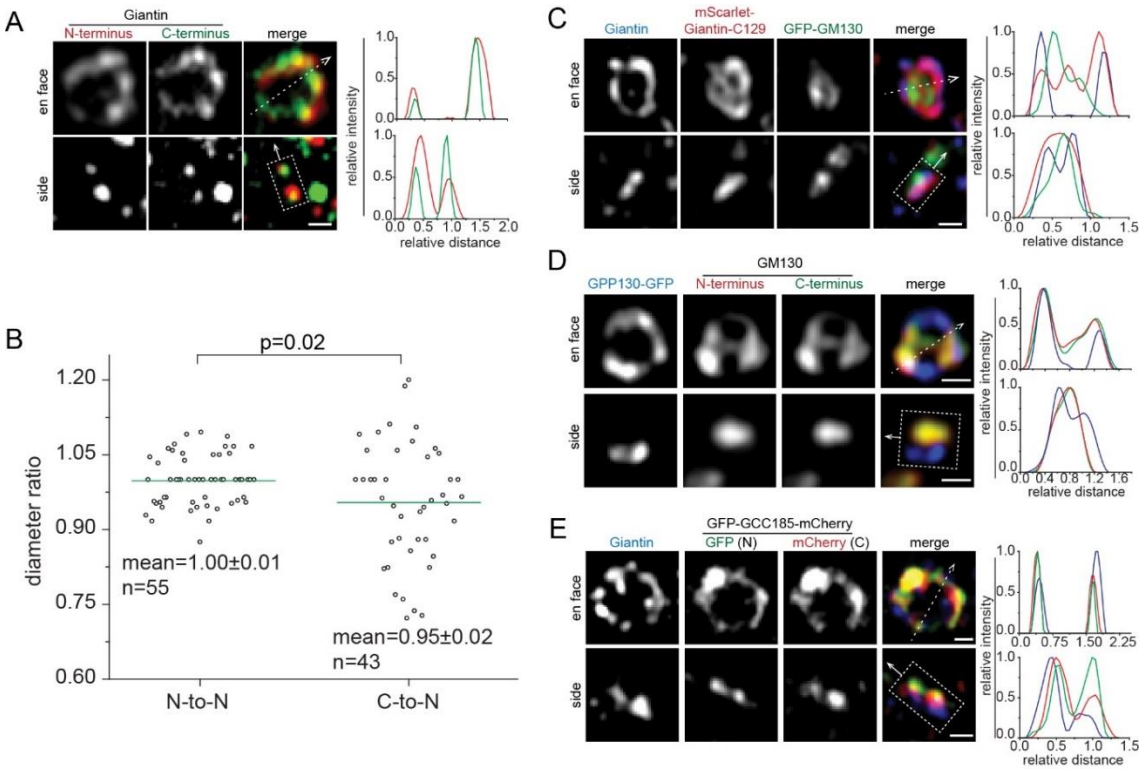

Figure 9: N- and C- termini of Giantin, GM130 and GCC185 coincide on the Golgi cisternal membrane.

(A-C) N- and C-termini of Giantin coincide on the cisternal membrane. (A) The endogenous Giantin was immuno-stained by N- and C-termini Giantin antibodies, which were conjugated with AF647 and AF488, respectively. (B) The ratio of Giantin-ring diameters obtained from the Giantin N-terminus antibody (N-N; Giantin N-terminus antibody was conjugated with AF647 and AF488) or Giantin C-terminus antibody (C-N; Giantin N- and C-termini antibodies were conjugated with AF647 and AF488, respectively) to that of the Giantin N-terminus antibody. The green line represents the mean of diameter ratios and the p-value is from the Student's t-test. (C) Cells transiently expressing mScarlet-Giantin-C129 and GFP-GM130 were immuno-stained by the Giantin N-terminus antibody. (D) N- and C-termini of GM130 coincide on the cisternal membrane. N- and C-termini of GM130 were immuno-stained by the corresponding antibodies, followed by secondary antibodies conjugated with AF594 and AF647, respectively. (E) N- and C-termini of GCC185 coincide on the cisternal membrane. N- and C-termini of GCC185 were tagged with GFP and mCherry, respectively. Endogenous Giantin was immuno-stained by its N-terminus antibody. In en face views of (A,C-E), dotted arrows represent lines (width=1 pixel), that were drawn to generate line intensity profiles, whereas in side views of (A,C-E), dotted boxes that represent lines drawn in the direction of arrows, were used to generate line intensity profiles. Line profiles were color-coded according to colours assigned to different proteins. n, number of analysed Golgi mini-stacks. Scale bar, 500 nm.

As an alternative method, HeLa cells transiently expressing mScarlet-Giantin-C129,

which contains 129 aa of the Giantin C-terminus, were stained using the Giantin N-

terminus antibody. The LQ (0.8) of mScarlet-Giantin-C129 is similar to that of endogenous Giantin (0.57; Table 6). Moreover, its ring staining pattern was almost identical to that observed with the Giantin N-terminus antibody (Figure 9C). Of note, it exhibited significant localization within the ring staining pattern of the Giantin N-terminus antibody.

Similarly, there was no difference in ring-diameters revealed by N- and C-terminus antibodies against GM130 or N- and C-terminally tagged and exogenously expressed GCC185 (Figure 9D-E).

Together, the investigation of Giantin, GM130 and GCC185 suggest that their N- and C-termini might predominantly collapse on Golgi cisternae *in vivo*, instead of adopting an extended conformation. This may also be true for Golgin84, as its ring staining patterns were similar to those of Giantin and GCC185 (Figure 7A,9E). In addition, GCC185 was suggested to crumble on the Golgi membrane (Cheung et al., 2015), as a difference of ~40 nm was measured between the N- and C-termini of GCC185.

Collectively, Giantin, GCC185 and Golgin84 were validated as Golgi cisternal rim markers. GM130 is not considered here because it did not exhibit exclusive ring and double-punctum in its en face and side view images, respectively (Figure 9D).

4.4 EM confirms the cisternal rim localization of GPP130

Like the Golgins mentioned above, GPP130 also consistently displays double-punctum, circular ring and oval ring staining patterns under Airyscan microscopy. This suggests that it is likely a cisternal rim-localized protein. GPP130 is a type II transmembrane protein that possesses a short N-terminal cytosolic tail, a transmembrane domain and a large luminal domain (Linstedt et al., 1997).

EM has been adopted to verify the rim localization of GPP130 at the ultra-structural level. The C-terminus of GPP130 was fused with GFP and APEX2, a hydrogen peroxidase that functions as an EM tag (Lam et al., 2015). In the presence of H_2O_2, APEX2 can catalyse the polymerization of DAB in its vicinity, giving rise to an electron-dense contrast. Therefore, cisternal rims are expected to accumulate electron density in GPP130-APEX2-GFP-expressing cells. In the native Golgi from 25 NRK cells transiently expressing GPP130-APEX2-GFP (Figure 10A, B), it was found that 68% of the 57 analysable Golgi stacks displayed electron density enrichment at the cisternal rim (Figure 10C, D). Hence, this result verified that GPP130 is indeed a cisternal rim marker. It also indicated that our data from LM and EM are consistent for GPP130.

Thus, Giantin, Golgin84, GCC185 and GPP130 are validated as cisternal rim markers and can be used to discern the orientation of Golgi mini-stacks. Their circular ring, oval ring and double-punctum staining patterns should correspond to en face, oblique and side views of the Golgi mini-stack, respectively (Figure 7B). In subsequent studies of the lateral localization of Golgi proteins, one of these markers (usually Giantin) is always present in the multi-colour labelling in order to identify the orientation. Notably, only en face and side views of Golgi mini-stacks are analysed because they can be easily identified under LM and are the best orientations to reveal the lateral localization of a Golgi protein.

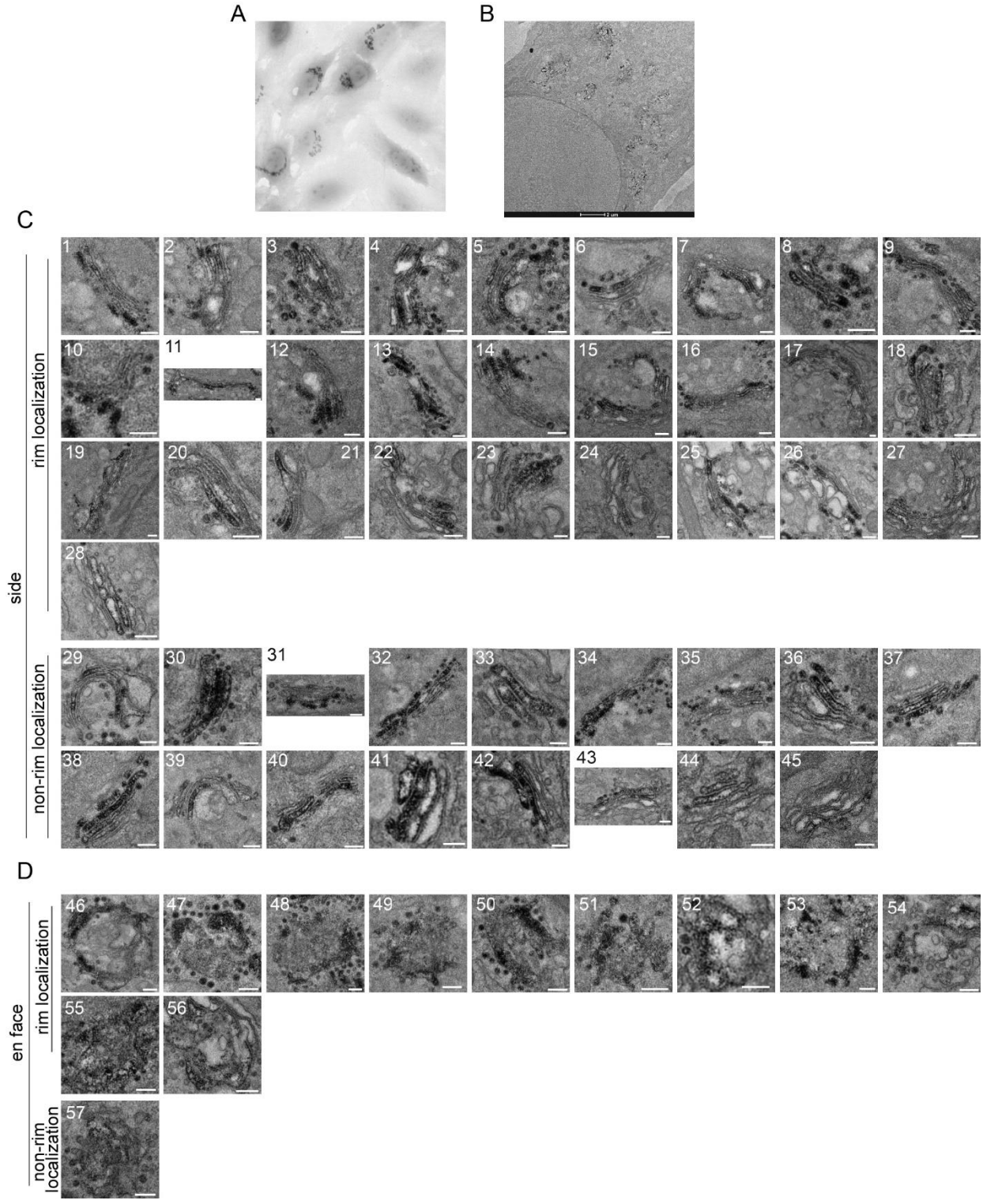

Figure 10: The EM imaging on GPP130-APEX2-GFP demonstrates its preferential localization at the rims of Golgi cisternae.

(A) NRK cells transfected with GPP130-APEX2-GFP were imaged under transmitted light after APEX2-labeling reaction and resin embedding. (B) An EM image showing the overview of an NRK cell positive for GPP130-APEX2-GFP transfection and APEX2-labeling reaction. (C-D) The categorization of interior or non-interior localization for side and en face view Golgi stacks. Golgi stacks of native Golgi from 25 cells were imaged and analysed. Scale bar, 200nm.

4.5 MGAT2 localizes to the cisternal interior

In addition to the rim localization, some Golgi proteins appear in the interior of the Giantin ring. MGAT2, an enzyme involved in the modification of N-glycosylation, is one such protein. It appeared as a short bar and a disk in side and en face views, respectively (Figure 11A). The line Intensity profile of the side and en face views of MGAT2 indicated that its signals were bound by that of Giantin (Figure 11A). Two strategies were devised to confirm our observation that MGAT2 is localized to the cisternal interior.

First, an APEX2-catalyzed reaction was performed in MGAT2-APEX2-GFP-transfected cells. In the presence of H_2O_2, APEX2 can catalyse biotin-phenol to covalently modify proteins in its immediate vicinity (Lam et al., 2015). Proteins that were covalently modified by the biotin-phenol were fluorescently labelled by AF594-conjugated streptavidin. Indeed, these proteins were also found within the Giantin ring (Figure 11B).

Second, EM study of MGAT2-APEX2-GFP-transfected cells was performed to investigate its lateral distribution (Figure 12). The analysis, which included 58 Golgi stacks from native Golgi in 14 cells, indicated that 93% of Golgi stacks demonstrated an enrichment in electron density in the cisternal interior (Figure 12D, E). This supports our LM observation, indicating that MGAT2 preferentially localizes to the cisternal interior.

To this end, two phenotypes of lateral localization, cisternal interior and rim, were identified. These were exemplified by MGAT2 and Giantin, respectively.

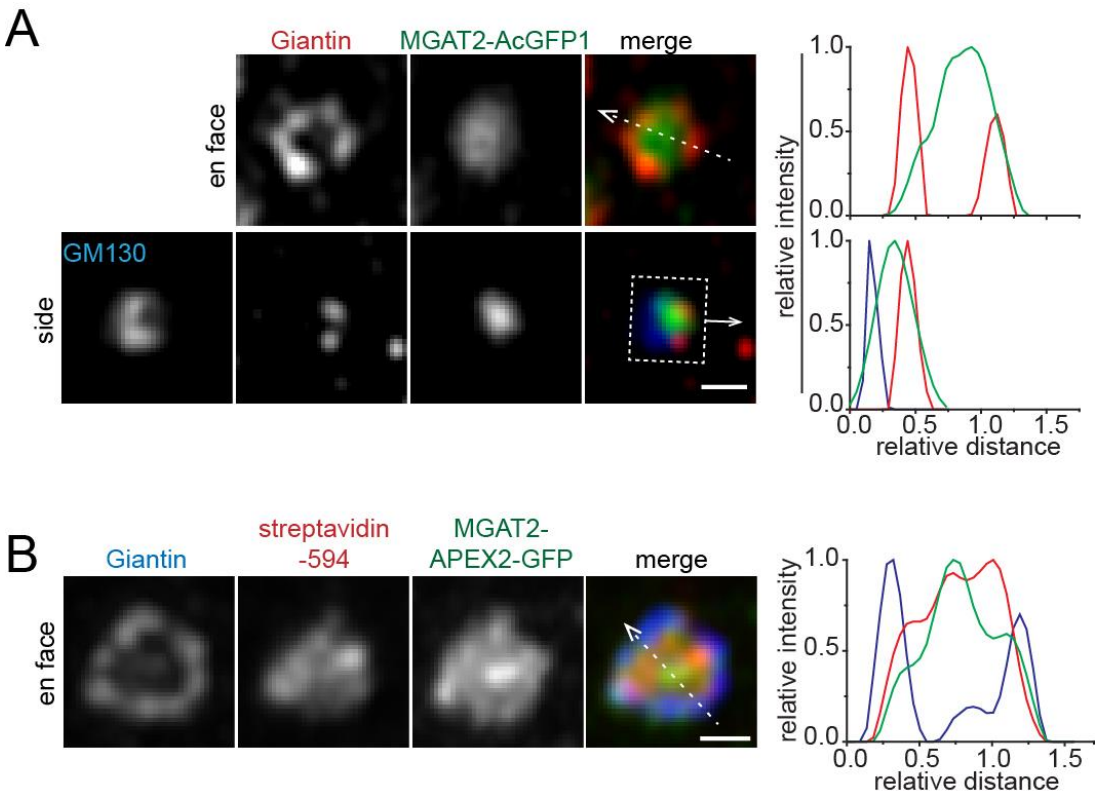

Figure 11: MGAT2 and biotin-phenol covalently modified products localize to the cisternal interior.

(A) MGAT2 localizes to the interior of Golgi cisternae. En face and side view images of MGAT2-AcGFP1 and their corresponding line intensity profiles were shown. These line intensity profiles were generated as described in Figure 9A and 7C. They were color-coded according to colours assigned to different proteins. (B) The biotin-phenol covalently modified products generated from the APEX2-labeling reaction, were found in the cisternal interior. HeLa cells transiently expressing MGAT2-APEX2-GFP were subjected to the APEX2-catalyzed reaction to label its neighbouring proteins with biotin-phenol. The biotin-phenol covalently modified products were detected by the AF594-conjugated streptavidin (streptavidin-594). The line intensity profile was generated as described in Figure 9A. It was color-coded according to colours assigned to different proteins. Scale bar, 500 nm.

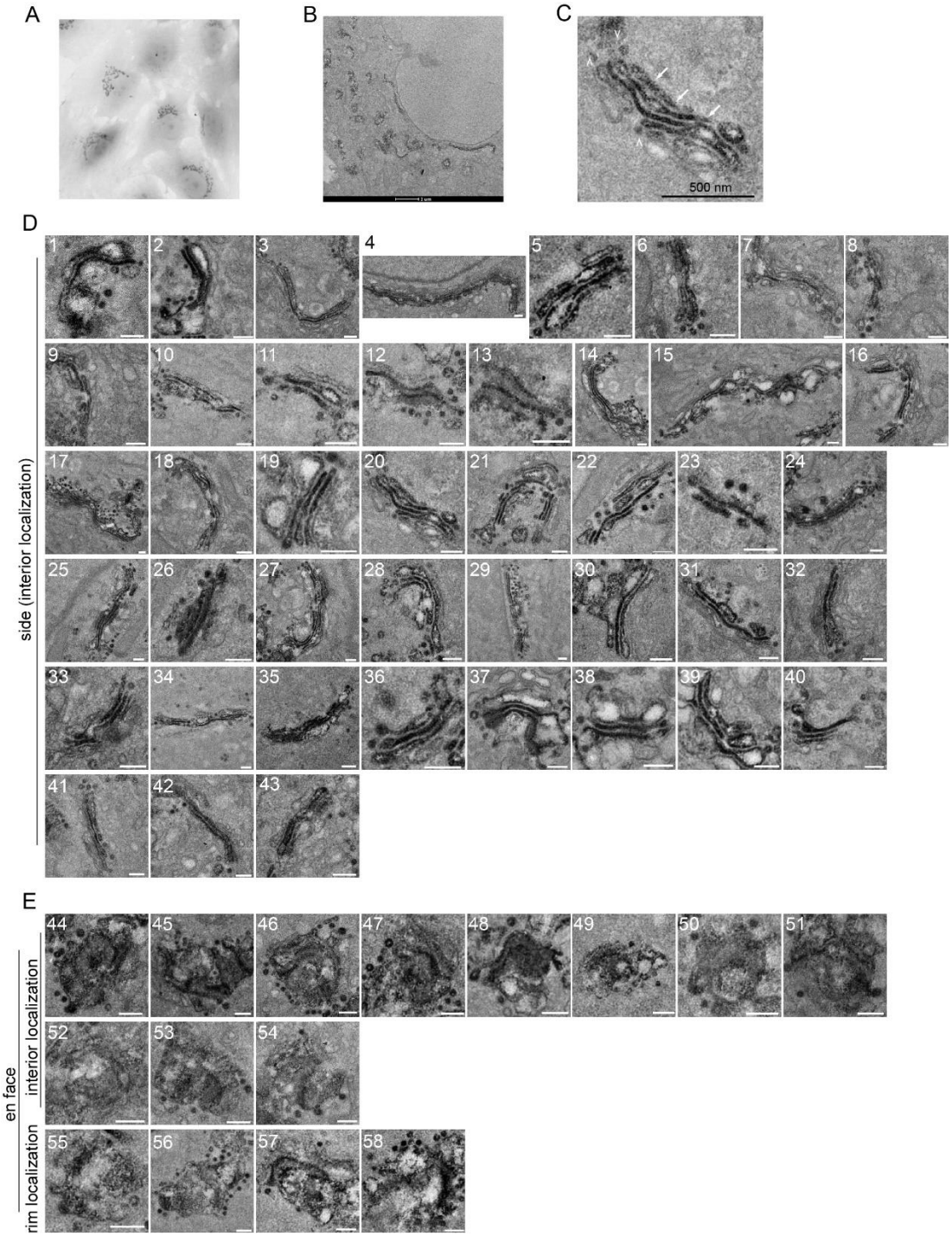

Figure 12: The EM imaging on MGAT2-APEX2-GFP demonstrates its preferential localization at the Golgi cisternal interior.

(A) NRK cells transiently expressing MGAT2-APEX2-GFP were imaged under transmitted light after the APEX2-catalyzed reaction and resin embedding. (B) An EM image showing the overview of an NRK cell positive for MGAT2-APEX2-GFP transfection and APEX2-catalyzed reaction. (C) The thin section of a side view Golgi stack which is positive for APEX2-catalyzed reaction. The MGAT2-APEX2 positive budding profiles and cisternal interior are indicated by arrow heads and arrows, respectively. (D-E) The categorization of interior or non-interior localization for side and en face view Golgi stacks. Golgi stacks of native Golgi from 14 cells were imaged and analysed. Scale bar, 200nm.

4.6 Generation of averaged en face and side view images of Golgi proteins

The cisternal rim markers that were identified and validated in Sections 4.1–4.4 can be used to discern the orientation of Golgi mini-stacks (i.e. en face and side views). These two views are exploited to study the lateral localization of Golgi proteins. Before delving into the detailed study, four concerns must be addressed. First, morphological variance in Golgi mini-stack images is always observed due to the differences in the size of Golgi mini-stacks. Second, the inconsistent antibody staining of endogenous proteins or the inhomogeneous expression of exogenous proteins in Golgi mini-stacks might result in inhomogeneous staining. Third, Golgi mini-stacks can orient randomly in the cytoplasm. Fourth, human bias in image analysis may be unavoidable. Therefore, conclusions about the lateral localization of Golgi proteins based on a limited number of IF images might be subjective and not credible enough. Hence, two methods were devised to mitigate the concerns mentioned above. These methods are based on the averaging of en face and side view images because lateral localization is best demonstrated when mini-stacks are in these orientations. The methods aim to enhance the feature(s) of a Golgi protein and suppress non-specific staining patterns.

4.6.1 Averaging en face view images

Under the en face view, the lateral localization of a Golgi protein, which is the distribution of the protein orthogonal to the Golgi axis, can be quantitatively represented by the metric gyradius. In fluorescence imaging, the gyradius of an object is defined as the root mean square distance of every pixel of the object, weighted by pixel intensity, to the center^{mass} of the object. Assuming that the distribution of a Golgi protein has rotational symmetry around the Golgi axis (Figure 13A) and that its lateral localization is independent of cisternal diameters, the intensities and diameters of en

face view images of a Golgi protein can be normalized. The resulting images can then be combined to produce its representative averaged image. Our newly developed image processing and analysis procedures were exemplified by immuno-labelled Giantin (Figure 13B-C).

For this analysis, an image of an en face view Golgi mini-stack was cropped and subjected to background subtraction. Signals that did not belong to the Golgi mini-stack were manually removed (indicated by yellow arrows in Figure 13C). The Golgi mini-stack was manipulated according to the Giantin image. First, the Golgi mini-stack was translated so that the center^{mass} of Giantin coincided with the image center. Next, the Golgi mini-stack image was expanded or shrunk so that the gyradius of Giantin was 100 pixels. The total intensity of each channel image was normalized to 2×10^8 and the Golgi mini-stack image was trimmed to 701×701 pixels. Finally, multiple en face view images of the same channel were averaged to generate an averaged en face view image (Figure 13B-C). Notably, the averaged en face view of Giantin was indeed rotationally symmetrical around the Golgi axis (Figure 13C, 15A). A radial mean intensity profile was also plotted (Figure 13B-C). This was calculated by averaging intensities of all pixels that have the same distance from the center^{mass}. It is plotted against the distance from the center, which is the radius of the circle (ranging from 1 to 350). The radius of a Golgi protein is defined as the distance between its center^{mass} and the outer slope at the half-maximum-intensity point in the radial mean intensity profile (Figure 13B). In subsequent en face view analyses for Golgi proteins, their radii were normalized to that of Giantin.

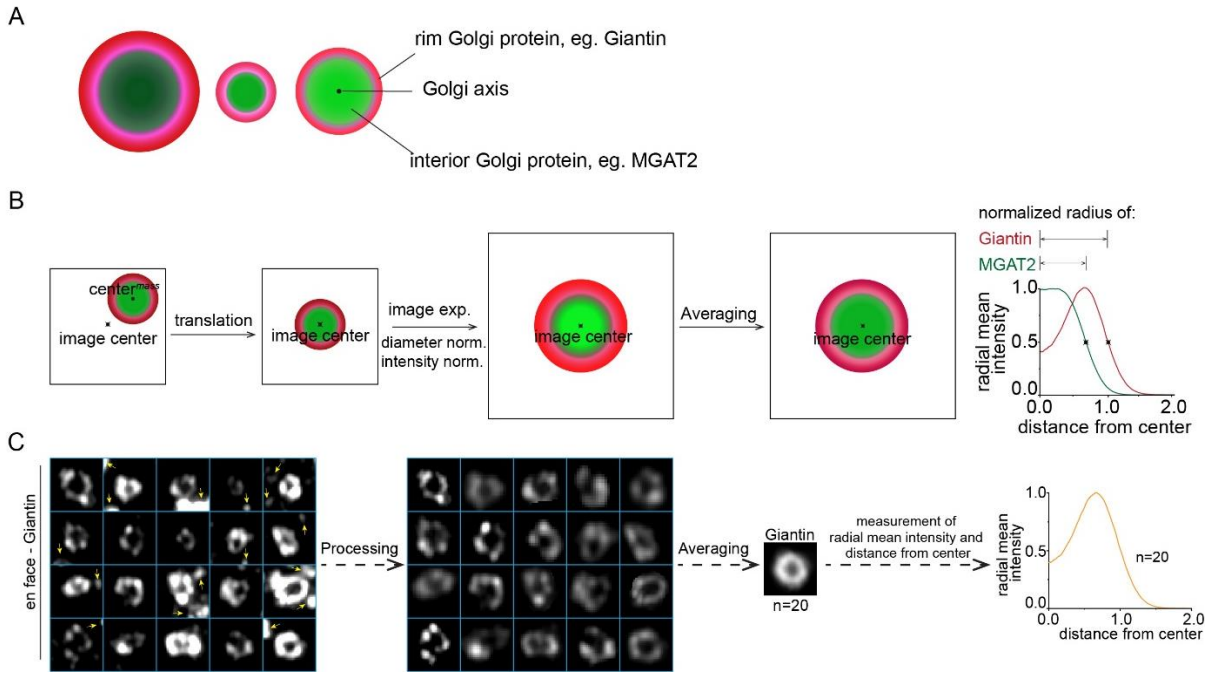

Figure 13: Generation of averaged en face view images of Golgi proteins.
(A) The schematic representation of three en face view Golgi ministacks of different diameters and intensities, positively stained for Giantin (red) and MGAT2 (green). (B) The schematic representation of procedures of generating averaged en face view images for Giantin (red) and MGAT2 (green). A Golgi mini-stack image is manipulated according to the Giantin image. Multiple en face view images of the same channel are combined to generate the averaged en face view. Its radial mean intensity vs. distance from center is plotted. The radius of Giantin is defined as 1.00 and the radius of other Golgi protein (MGAT2 in this example) is normalized against that of Giantin. Exp., expansion; norm., normalization (C) An experimental example of 20 en face view images of Giantin that were processed as described in (B). Yellow arrows indicate signals that do not belong to Golgi mini-stacks of interest.

4.6.2 Averaging side view images

To average side view images, it is assumed that the axial size of Golgi mini-stacks is constant, whereas their lateral sizes vary extensively (Figure 14A). The axial size of a Golgi mini-stack is defined as the spatial distance occupied by two Golgi markers, GM130 and GalT, which localize to the *cis*- and *trans*-most region of the Golgi stack, respectively, along the Golgi axis (see Section 2.14 for the calculation; Figure 14A). The lateral size of a Golgi mini-stack is defined as the spatial distance occupied by the two Giantin puncta, which is evident in the side view of a Golgi mini-stack (see Section 2.14 for the calculation; Figure 14A).

The axial size of Golgi stacks (or the axial distance from GM130 to GalT-mCherry) was relatively constant and seemed to converge at 588±106 nm (mean±SD; Figure 14B). However, the lateral size of Golgi mini-stacks (or the lateral size of Giantin double-puncta) varied extensively from 400 nm to 1000 nm. The axial size from GM130 to Giantin was also constant at 410±79 nm (mean±SD; Figure 14C). Previously, the LQs of Golgi proteins were verified to be highly reproducible (Tie et al., 2016a). This indirectly suggests that the axial relationship between Golgi proteins might remain the same in Golgi mini-stacks, which are constant in axial size. Interestingly, the lateral size of GM130 increased proportionally with that of Giantin (Figure 14D), suggesting that the ratio of the lateral sizes of Golgi cisternae could be constant. Collectively, the morphometric analyses on Golgi mini-stacks suggest that the axial size of Golgi mini-stacks and the ratio of the lateral sizes between cisternae are conserved.

To obtain averaged side view images, Golgi mini-stacks must be multi-labelled, with one labelled protein being Giantin. A Golgi mini-stack was manipulated based on the Giantin image. After background subtraction, a side view Golgi mini-stack image was cropped and translated so that the center^{mass} of Giantin coincided with the image center. The side view image of Giantin, which appears as a double-punctum, was rotated and aligned parallel to the x-axis (Figure 14E-F). The *trans*-most protein (GalT-mCherry in the example) was always positioned up. The Golgi mini-stack image was then horizontally expanded so that the lateral size of Giantin (the distance between the center^{mass}s of two Giantin puncta) reached 160 pixels. The image was vertically expanded by 8-fold. Next, the image was trimmed to the same size, 701×701 pixels, and the total intensity of each channel was normalized to 5×10^7. Finally, these processed images were averaged to generate averaged side view images (Figure

14E-F). In some cases, the y-coordinate of the center^{mass} (Ycenter^{mass}) of a Golgi protein was axially translated by 3-fold along the y-axis with respect to GM130 (Figure 14E, axial translation) in order to clearly demonstrate the axial relationship between proteins.

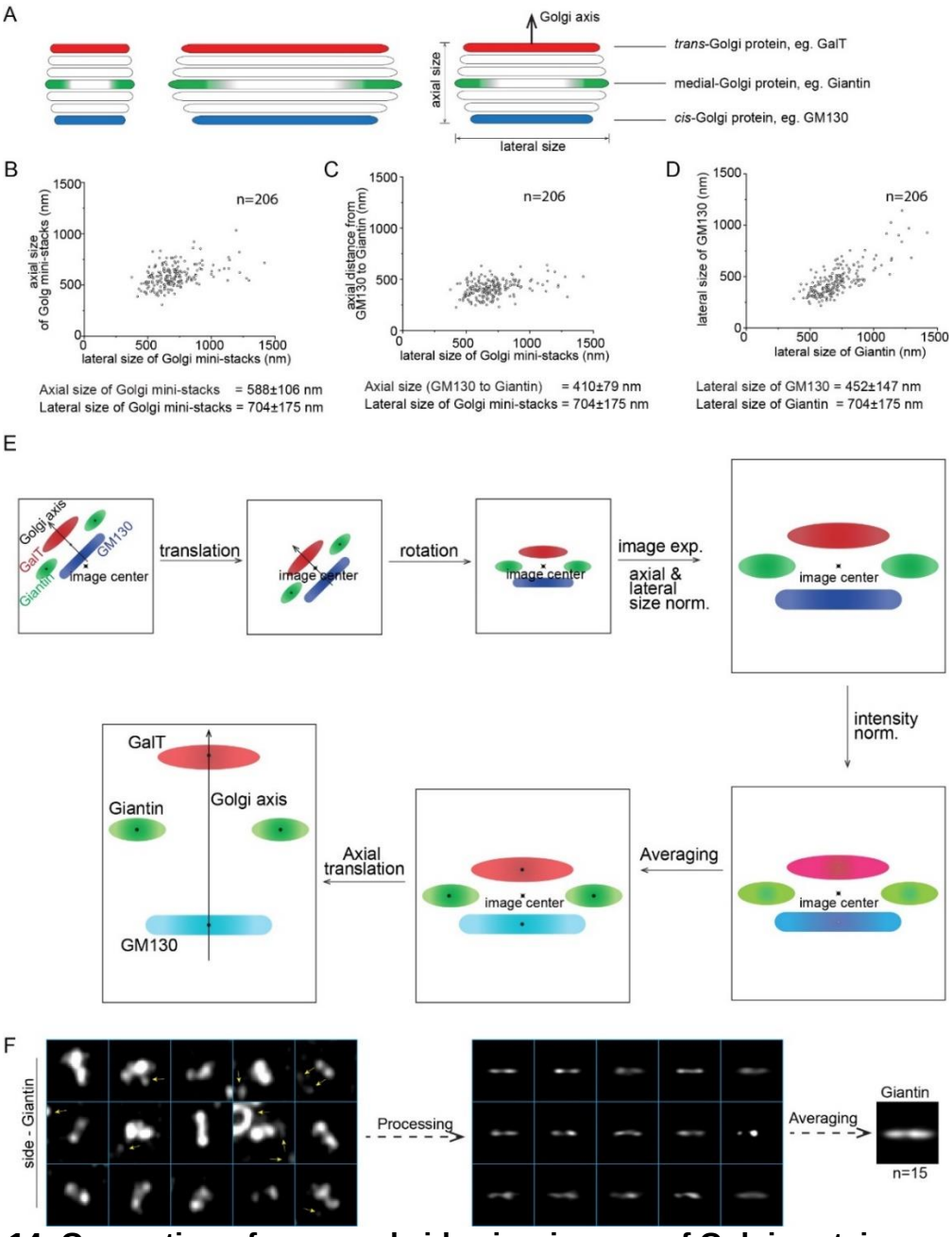

Figure 14: Generation of averaged side view images of Golgi proteins.
(A) The schematic representation of the side view of three Golgi mini-stacks with different lateral sizes and intensities, positively stained for GM130 (blue), Giantin (green) and GalT (red). (B-D) Morphometric analyses of Golgi mini-stacks. Golgi mini-stacks with three-colour labelling for endogenous GM130, Giantin and GalT-mCherry, were analysed. Statistics, mean±SD. n, number of analysed Golgi mini-stacks. (B) The axial size of mini-stacks are constant, whereas their lateral sizes vary extensively. (C) The axial size between GM130 and Giantin is constant. (D) The lateral size of GM130 increases proportional to that of Giantin. (E) The schematic representation of procedures of generating averaged side view images for GM130 (blue), Giantin (green) and GalT (red). A Golgi mini-stack image is manipulated according to Giantin image. Exp., expansion; norm., normalization. (F) An experimental example of 15 side view images of Giantin that were processed as described in (E). Yellow arrows indicate signals that do not belong to Golgi mini-stacks of interest.

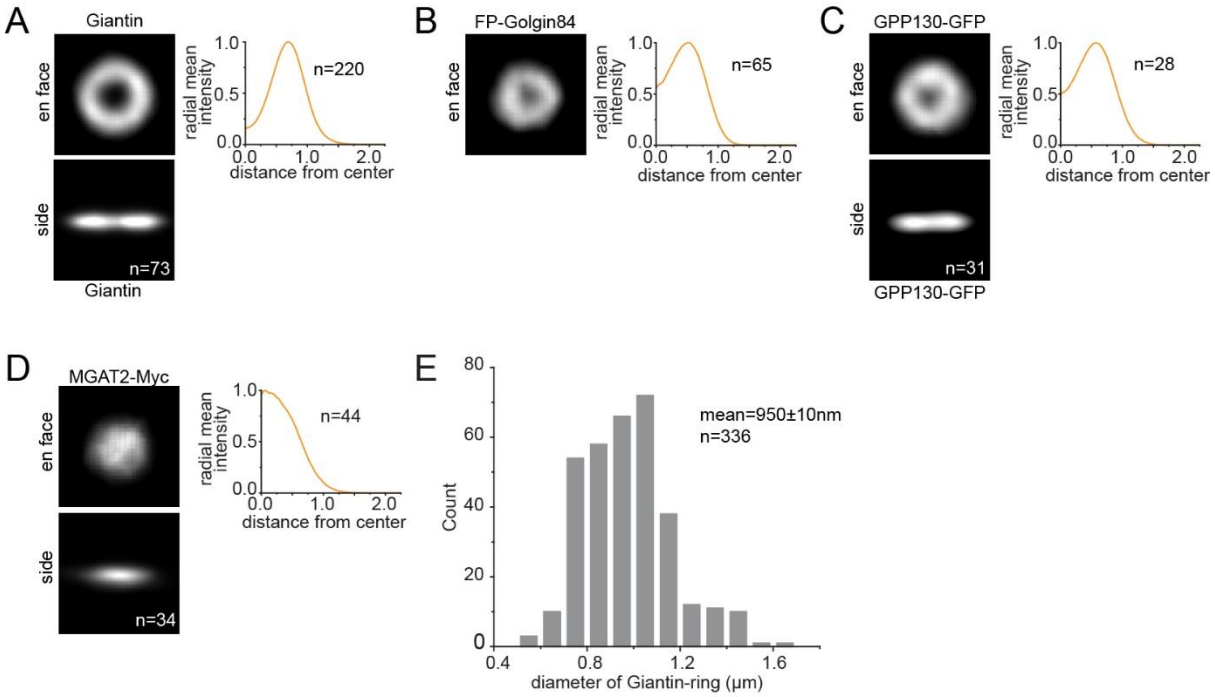

Figure 15: The averaged images of Giantin, GPP130, Golgin84 and MGAT2 confirm their rim and interior localizations, respectively.
(A-C) The averaged images of Giantin, GPP130 and Golgin84 demonstrate that they mainly localize to the cisternal rim. (D) The averaged image of MGAT2 demonstrates that it mainly localizes to the cisternal interior. (A-D) The averaged en face and side view images for Giantin, GPP130-GFP, fluorescent protein (FP)-tagged Golgin84 and MGAT2-Myc. Radial mean intensity profiles were plotted at the side of corresponding averaged en face view images. n, number of averaged Golgi mini-stacks. (E) The histogram displays the distribution of diameter of Giantin rings. n, number of analysed Golgi mini-stacks. Statistics, mean±SEM.

Thus, using methods described in Figures 13 and 14, the lateral localization of Giantin, Golgin84, GPP130 and MGAT2, was analysed (Figure 15). Consistent with our previous observations, averaged en face and side views demonstrated that Giantin, Golgin84 and GPP130 preferentially localize to the cisternal rim. Their en face and side views displayed ring and double-punctum patterns, respectively (Figure 15A-C). In contrast, MGAT2 mainly localizes to the cisternal interior. Its en face and side views displayed disk and bar shapes, respectively (Figure 15D).

4.7 The averaged side view of Golgi proteins reveals their axial localizations

GLIM has been successfully employed to quantitatively determine the axial localization of Golgi proteins (Figure 6, Table 6). The result indirectly suggests that the axial localization of Golgi proteins is constant. Likewise, our morphometric analyses demonstrated that the axial sizes of Golgi mini-stacks are constant (Figure 14B-C). Furthermore, averaged side view images of stack region-localized Golgi proteins mostly displayed the staining pattern of a single, compact bar shape or a double-punctum along the Golgi axis (averaged side view images presented in Chapter 5). Based on these collective results, I reasoned that the averaged side view image of Golgi proteins could be used to map their axial localizations. The LQ calculated from an averaged side view image is denoted as $LQ^{side\text{-}view}$. Like GLIM, GM130 and GalT-mCherry are used as reference markers and their $LQ^{side\text{-}view}$s are 0.0 and 1.0, respectively. Therefore, $LQ^{side\text{-}view} = \frac{d_{x,GM130}}{d_{GalT-mCherry,GM130}}$, with $d_{x,GM130}$ defined as the axial distance from the center^{mass} of the test protein, x, to that of GM130 and $d_{GalT-mCherry,GM130}$ defined as the axial distance from the center^{mass} of GalT-mCherry to that of GM130. As shown in Table 7, $LQ^{side\text{-}view}$s are similar to the LQs acquired using GLIM (LQ^{GLIM}s) though the former could be more error-prone due to the much smaller sample sizes. Indeed, in Airyscan imaging, the number of side views of Golgi proteins was noticeably reduced. Nonetheless, the consistency between $LQ^{side\text{-}view}$ and LQ^{GLIM} validated that the averaged side view image could faithfully demonstrate the axial localization of a Golgi protein.

	$LQ^{side\text{-}view}$	n	LQ^{GLIM}	n
Sec23a-mCherry	-1.15	37	-0.58	121
γ-COP	-0.19	26	-0.17	106
GM130	0.00	43	0.00	--
GFP-ACBD3	0.47	32	0.25	132
MGAT2-myc	0.47	34	0.53	136
Giantin	0.63	73	0.57	103
TPST2-GFP	0.77	47	0.64	154
GPP130-GFP	0.76	31	0.84	168
ST6Gal1-GFP	0.88	35	0.85	138
GalT-mCherry	1.00	40	1.00	--
GFP-Golph3	1.07	20	1.05	99
GGA2	2.43	20	1.96	33
γ-Adaptin	2.67	18	2.20	43

Table 7: The comparison between $LQ^{side\text{-}view}$s and LQ^{GLIM}s.
$LQ^{side\text{-}view}$ is directly measured from averaged side view images. LQ^{GLIM} is measured using GLIM (Table 6). The LQs of endogenous GM130 and exogenous GalT-mCherry are defined as 0.00 and 1.00, respectively. n, number of analyzed Golgi mini-stacks.

Chapter 5: The spatial molecular organization of the Golgi mini-stack

To date, there has not yet been any systematic study of the spatial molecular organization of the Golgi. To address this research gap, GLIM was applied to study the axial localization of Golgi proteins (see Chapter 3). The approaches described in Chapter 4 were adopted to systematically determine the lateral localization of Golgi proteins, which can best be demonstrated by the en face and side views of mini-stacks. In this chapter, the lateral localization of Golgi proteins is investigated. The proteins studied are involved in the two major Golgi functions, processing and trafficking.

5.1 Lateral localizations of components of trafficking machinery

5.1.1 ERES, ERGIC and *cis*-Golgi (LQ<0)

COPII coat subunits (e.g. Sec23a and Sec13), COPI coatomers (e.g. β-COP and γ-COP), ERGIC53, KDEL receptor, Arf4, Arf5 and GS27 exhibited lumps and puncta around Giantin rings in en face views and on one side of Giantin double-puncta in side views (Figure 16). These proteins function in the early secretory pathway, from the ER to the *cis*-Golgi. The ring pattern exhibited by the averaged γ-COP (Figure 16F) suggested that its budding and fusion sites might predominantly localize to the rim of Golgi mini-stack. In contrast, the averaged en face view of Sec23a (Figure 16H) indicated that COPII tend to organize into a ring pattern, suggesting a complex organization of the ERES. Of note, the averaged side views of Sec23a, ERGIC53 and GS27 displayed compact bar shape, suggesting that their axial distributions are concentrated at the ERES, ERGIC or *cis*-cisternae.

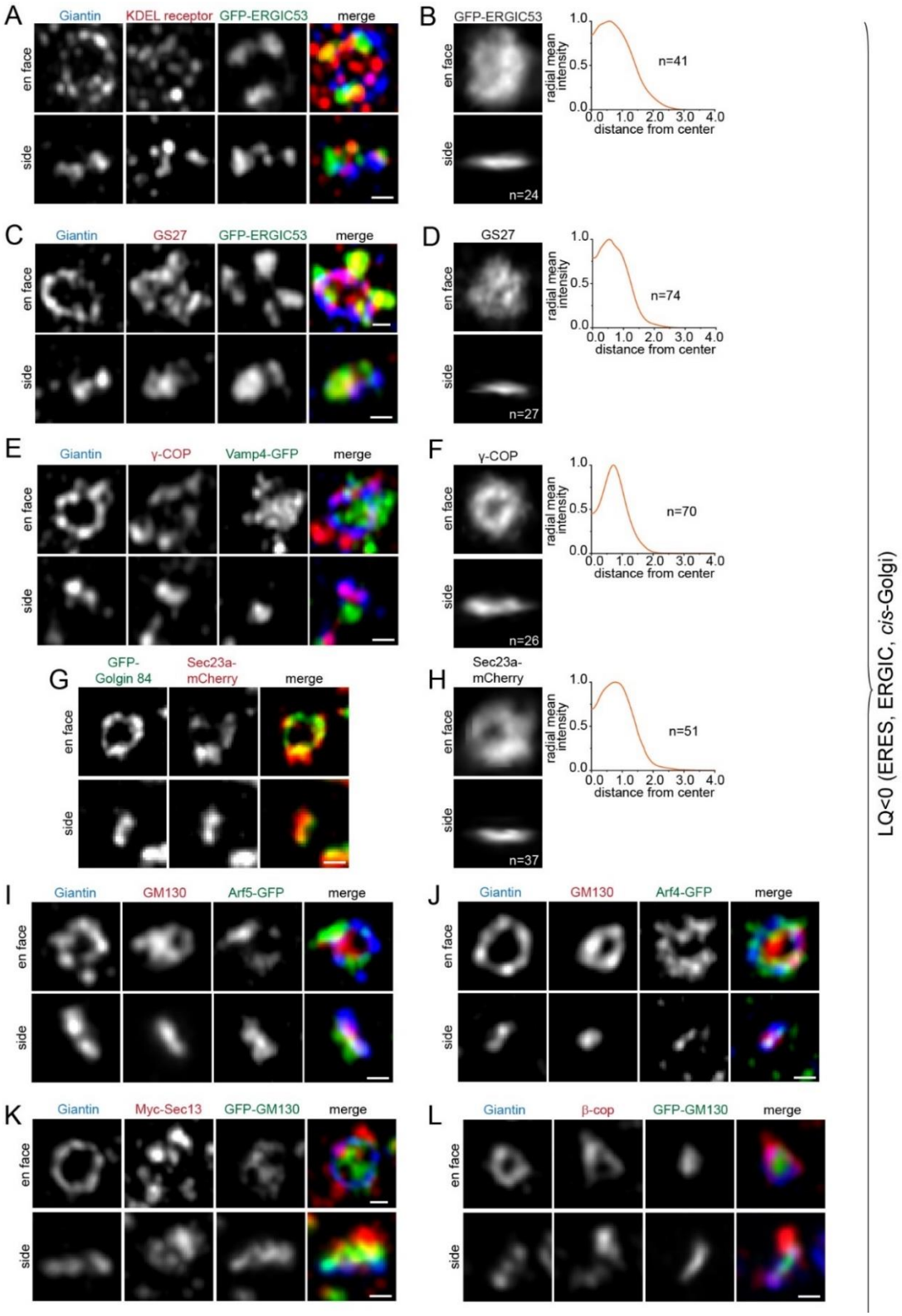

Figure 16: Components of transport machinery at the ERES, ERGIC and *cis*-Golgi primarily localize to the periphery of the Golgi mini-stack.

(A-L) ERES, ERGIC and *cis*-Golgi proteins (LQ<0). (A, C, E, G, I-L) Typical en face and side view images of components of transport machinery of the ERES, ERGIC and *cis*-Golgi. (B, D, F, H) The averaged side and en face view images of the ERES, ERGIC and *cis*-Golgi proteins and their radial mean intensity profiles. n, number of averaged Golgi mini-stacks. Scale bar, 500 nm.

5.1.2 *cis*-Golgi (0≤LQ<0.25)

GRASP65, GRASP55, Rab1a and GM130 appeared as central disks and bars in en face and side views, respectively (Figure 17). While there were usually some sheets or interior tubular connections in their en face views, their side views displayed compact bar shapes. These observations suggest that they might be distributed throughout the *cis*-cisternae.

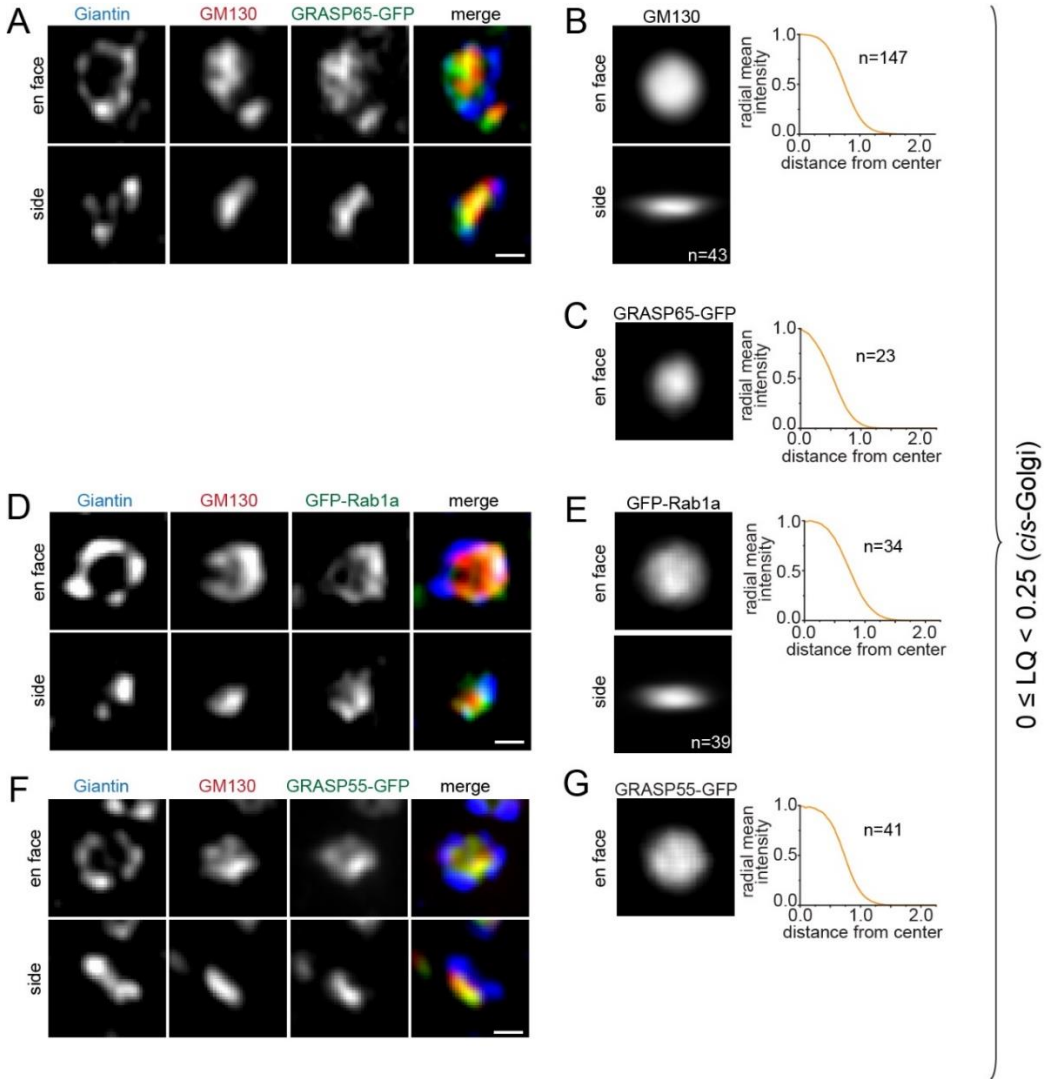

Figure 17: Components of transport machinery at the *cis*-Golgi localize throughout the *cis*-cisternae.
(A-G) *cis*-Golgi proteins (0≤LQ<0.25). (A, D, F) Typical en face and side view images of components of transport machinery of the *cis*-Golgi. (B, C, E, G) The averaged side and en face view images of *cis*-Golgi proteins and their radial mean intensity profiles. n, number of averaged Golgi mini-stacks. Scale bar, 500 nm.

5.1.3 Medial-Golgi (0.25≤LQ<0.75)

Giantin, ACBD3, Vip36, Sec34 (Cog3) and GS28 function in Golgi structure maintenance, ER-to-Golgi trafficking, intra-Golgi trafficking and/or vesicular transport (Hara-Kuge et al., 1999; Lesa et al., 2000; Sohda et al., 2001; Subramaniam et al., 1996; Suvorova et al., 2002). They displayed ring staining patterns in en face views, suggesting preferential localizations at the cisternal rims of medial-Golgi cisternae (Figure 18). Sec34 is one of the subunits of hetero-octameric COG complex. The COG complex is a peripheral membrane tethering complex that is suggested to facilitate the retrograde trafficking of Golgi enzymes (Smith and Lupashin, 2008). The en face view of Sec34 displayed scattered punctate profiles around the Giantin ring (Figure 18E).

The side views of ACBD3 and GS28 demonstrated double-puncta, consistent with the ring appearance of their en face views (Figure 18A-B, G-H). The averaged side view of Vip36 demonstrated a bar shape, instead of a double-punctum, possibly because a significant amount of the protein localizes to the cisternal interior, as suggested by its averaged en face view (Figure 18C-D).

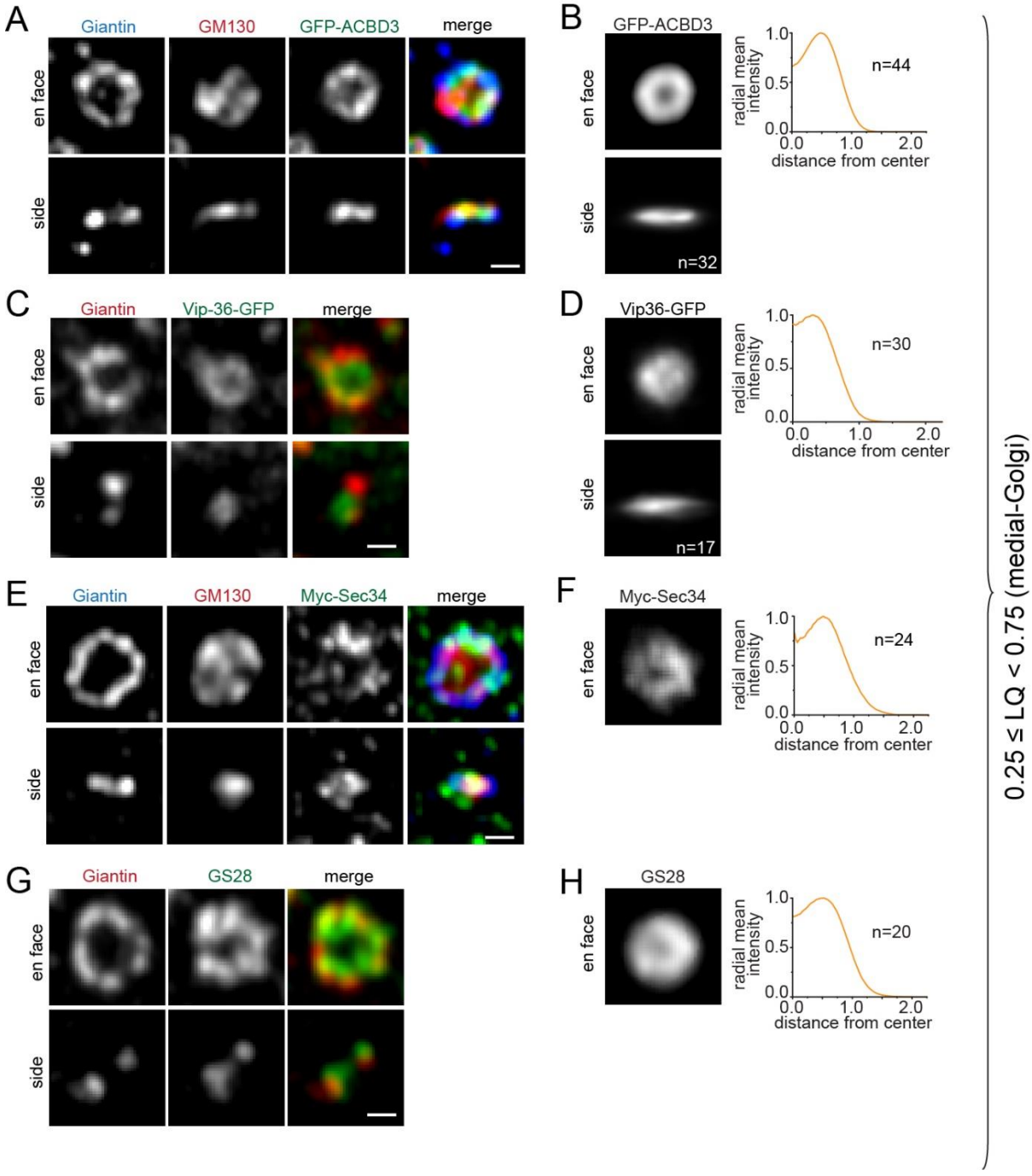

Figure 18: Components of transport machinery at the medial-Golgi primarily localize to rims of medial-cisternae.
(A-H) Medial-Golgi proteins (0.25≤LQ<0.75). (A, C, E and G) Typical en face and side view images of components of transport machinery of the medial-Golgi. (B, D, F, H) The averaged side and en face view images of medial-Golgi proteins and their radial mean intensity profiles. n, number of averaged Golgi mini-stacks. Scale bar, 500 nm.

5.1.4 *trans*-Golgi (0.75≤LQ<1.25)

Among the *trans*-Golgi proteins, GS15 is a v-SNARE that facilitates the fusion of vesicles to the Golgi membrane (Xu et al., 2002), GCC185 functions as a vesicle tether

that captures vesicles incoming toward the Golgi (Brown et al., 2011) and Golph3 recycles glycosylation enzymes between Golgi cisternae (Eckert et al., 2014; Pereira et al., 2014). GS15, GCC185 and Golph3 mostly appeared at the cisternal rim in their en face views (Figure 19A-F). Consistent with the en face views, their side views clearly displayed double-puncta. The functional role of GP73 at the Golgi is elusive. Although a significant amount of GP73 was observed in the cisternal interior, its averaged en face view showed a slight tendency toward rim localization (Figure 19H).

Rab6, Arl1 and Arf1 are small GTPases that function as molecular switches. Once activated, Rab6 and Arl1 recruit downstream effectors that function in membrane trafficking between the *trans*-Golgi/TGN and post-Golgi subcellular compartments (Crottet et al., 2002; Grigoriev et al., 2007; Lu et al., 2004). Arf1 recruits vesicular coats such as COPI and clathrin coats (Serafini et al., 1991; Stamnes and Rothman, 1993). Rab6, Arl1 and Arf1 each appeared as a homogenous disk and as a compact bar in their en face and side views, respectively (Figure 19I-N), suggesting that they might localize to the cisternal interior. Interestingly, Arf1 (LQ =0.75) was found to distribute into two pools, which might correspond to the *cis*/medial and *trans*/TGN compartments, as demonstrated by its side view (Figure 19M, side view). This observation is consistent with the idea that Arf1 plays a role in the assembly of COPI and clathrin coats at the *cis*-Golgi and TGN, respectively (Gillingham and Munro, 2007).

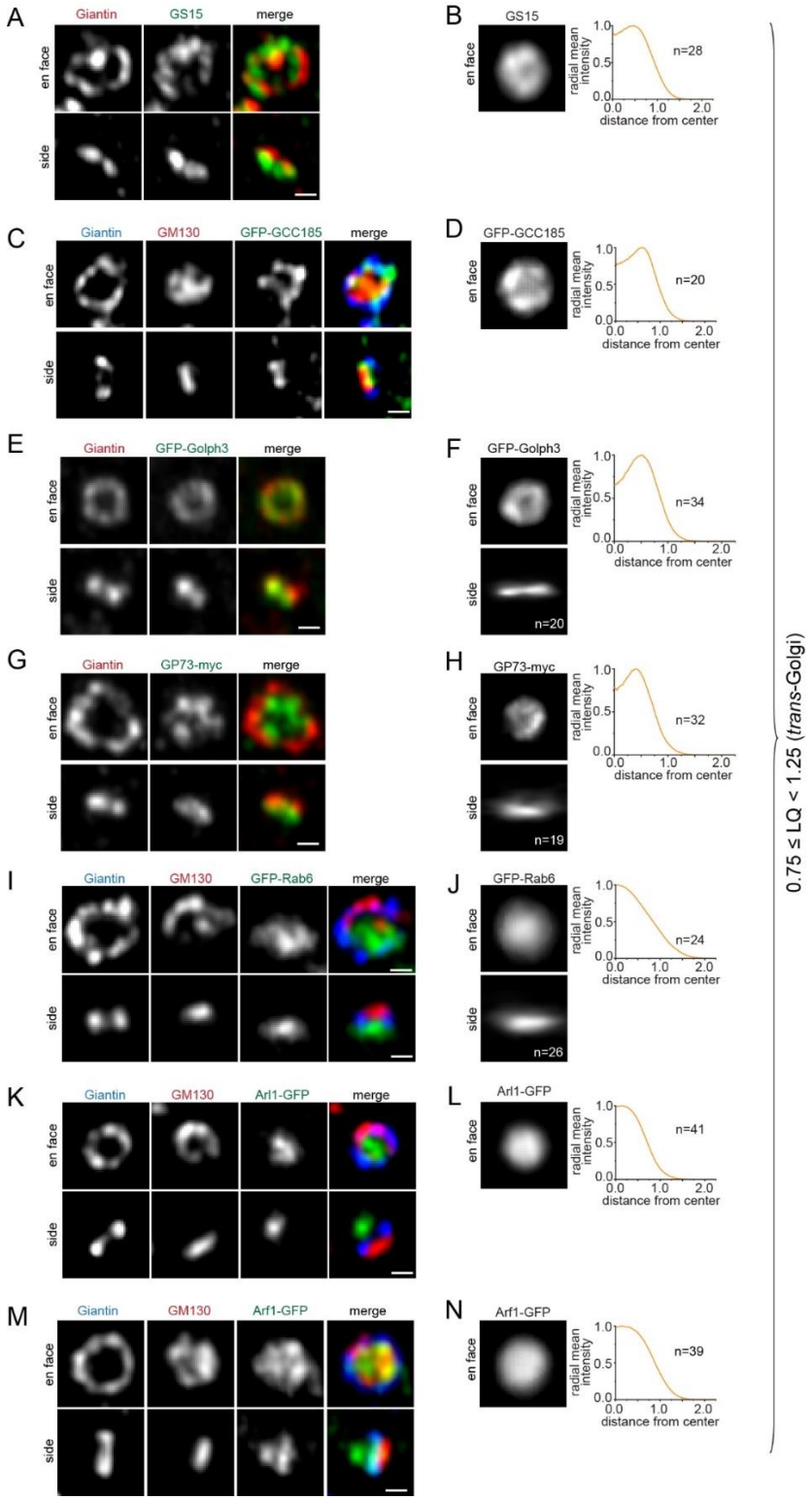

Figure 19: Components of trafficking machinery at the *trans*-Golgi localize to the rim and interior of the Golgi mini-stack.

(A-N) *trans*-Golgi proteins (0.75≤LQ<1.25). (A,C,E,G) Typical en face and side view images of components of transport machinery that localize to the rim of Golgi cisternae. (I,K,M) Typical en face and side view images of components of transport machinery that localize to the interior of Golgi cisternae. (B,D,F,H,J,L,N) The averaged side and en face view images of *trans*-Golgi proteins and their radial mean intensity profiles. n, number of averaged Golgi mini-stacks. Scale bar, 500 nm.

5.1.5 *trans*-Golgi network (LQ≥1.25)

Under Airyscan microscopy, two major distribution patterns were demonstrated by TGN proteins. The first is the compact lumps demonstrated by Golgin97, CD-MPR, Furin and Vamp4 (Figure 20A-J). In general, their averaged side views displayed compact bar shapes, whereas their averaged en face views showed inhomogeneous compact distribution due to insufficient sample sizes. The second pattern is the scattered puncta demonstrated by CI-MPR, GGA2, GGA1, clathrin light chain B (CLCB), γ-Adaptin, Vti1a, Syntaxin6 and Golgin245 (Figure 21A-N). In general, their en face and side views exhibited scattered punctate profiles. Of note, TGN proteins seemed to occupy larger areas both axially and laterally (Table 8-9). Occasionally, short tubule-like profiles were observed for TGN proteins, including Golgin245 and γ-Adaptin.

Although these Golgi proteins localize to the TGN, they did not co-localize significantly under the Airyscan microscope. For instance, Vamp4 did not overlap significantly with CI-MPR, GGA2, Vti1a and Furin (Figure 20E, H-J). On the other hand, CLCB seemed to furnish tubular and punctate profiles for Furin and Vamp4 outside the stacked cisternal membrane (arrows; Figure 21G, K). This is consistent with the functional role of clathrin in cargo recruitment and carrier biogenesis (Peden et al., 2001; Teuchert et al., 1999).

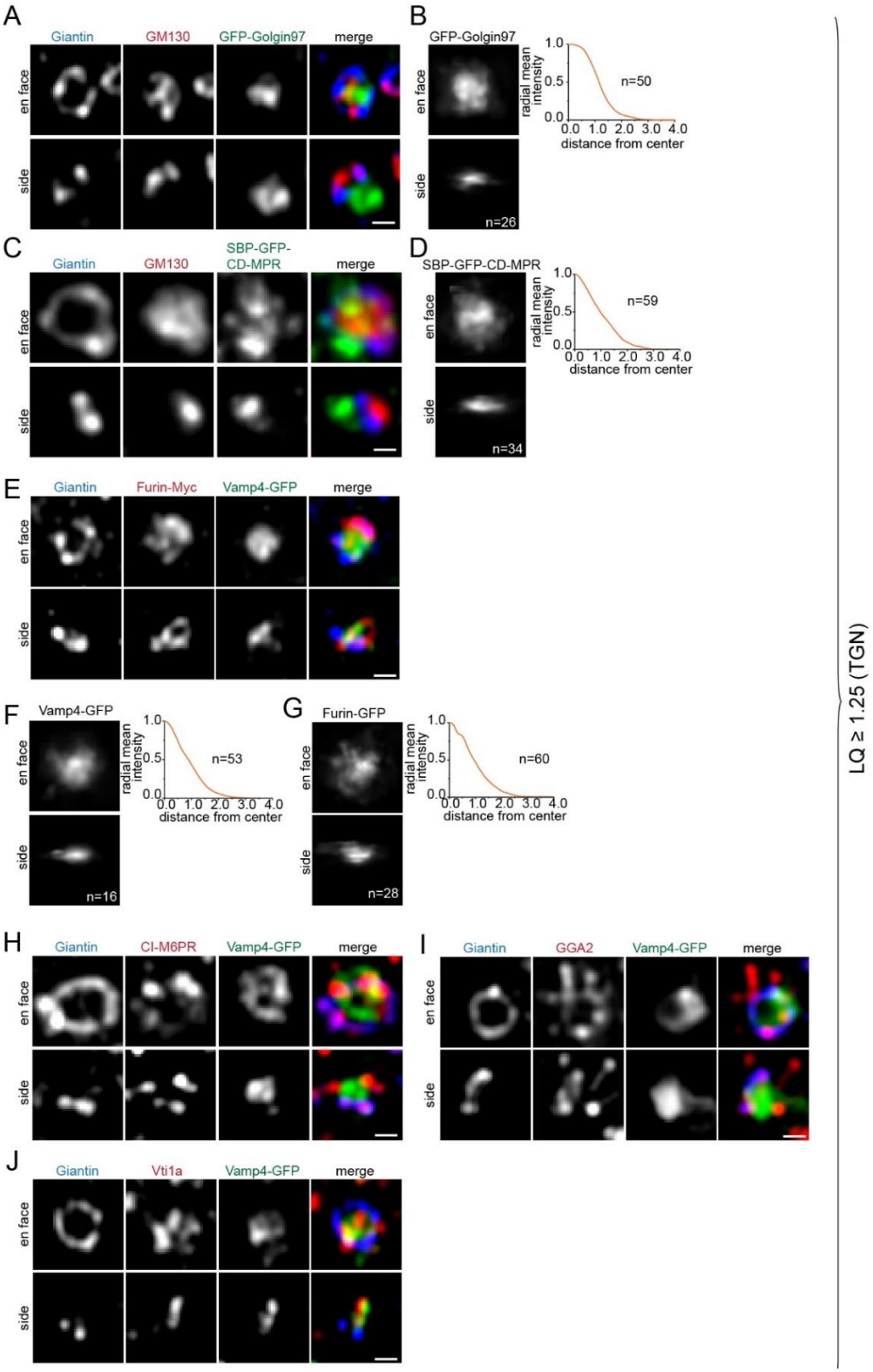

Figure 20: Components of trafficking machinery at the TGN display compact lump.

(A-J) TGN proteins (LQ≥1.25) that display compact lumps in their en face and side views. (A, C, E, H, I, J) Typical en face and side view images of components of trafficking machinery at the TGN. (B, D, F, G) The averaged side and en face view images of TGN proteins and their radial mean intensity profiles. n, number of averaged Golgi mini-stacks. Scale bar, 500 nm.

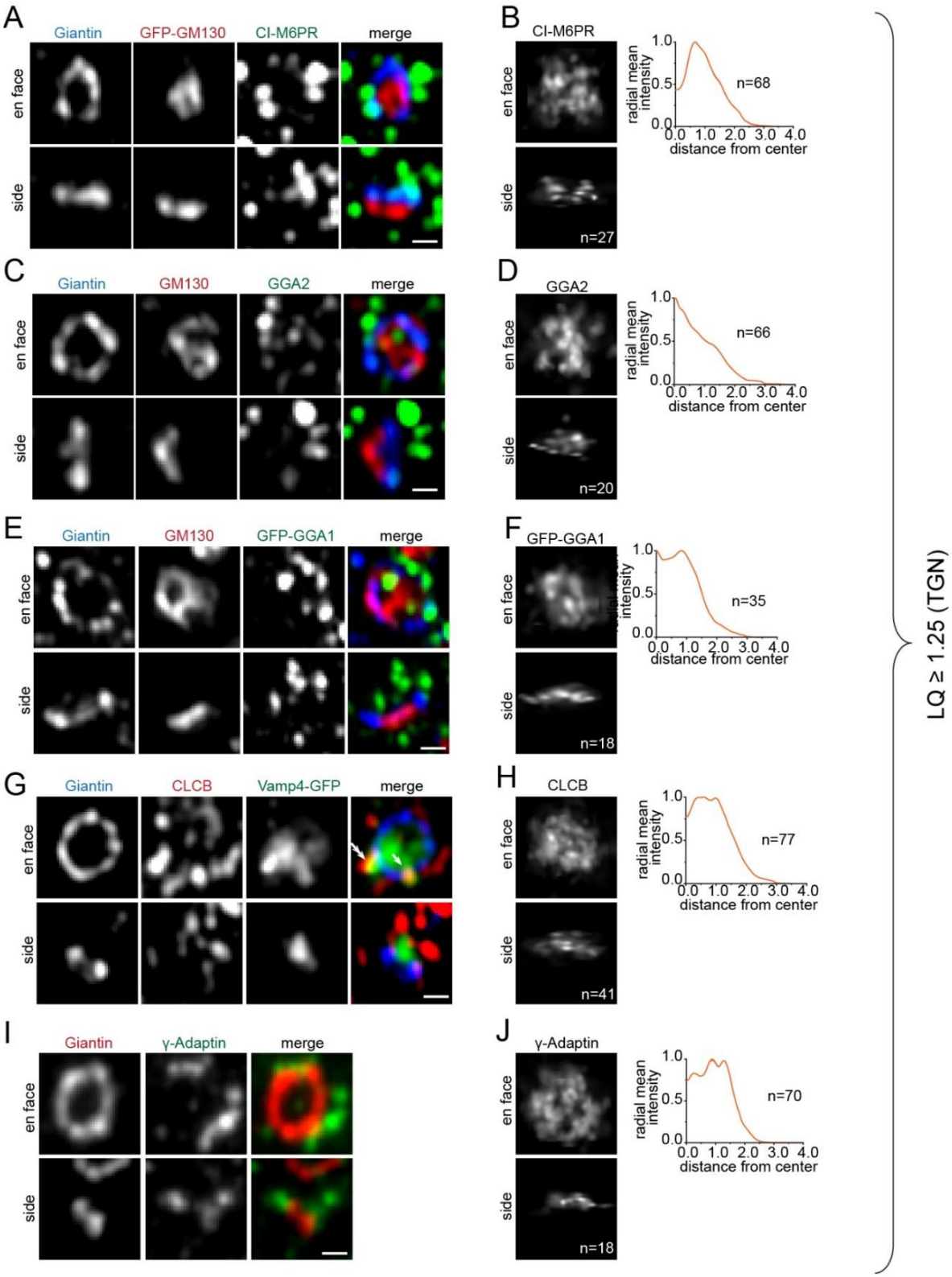
A
Giantin
GFP-GM130
CI-M6PR
merge
en face
side
B
CI-M6PR
radial mean intensity
distance from center
n=68
n=27
C
Giantin
GM130
GGA2
merge
D
GGA2
n=66
n=20
E
Giantin
GM130
GFP-GGA1
merge
F
GFP-GGA1
n=35
n=18
G
Giantin
CLCB
Vamp4-GFP
merge
H
CLCB
n=77
n=41
I
Giantin
γ-Adaptin
merge
J
γ-Adaptin
n=70
n=18
LQ ≥ 1.25 (TGN)

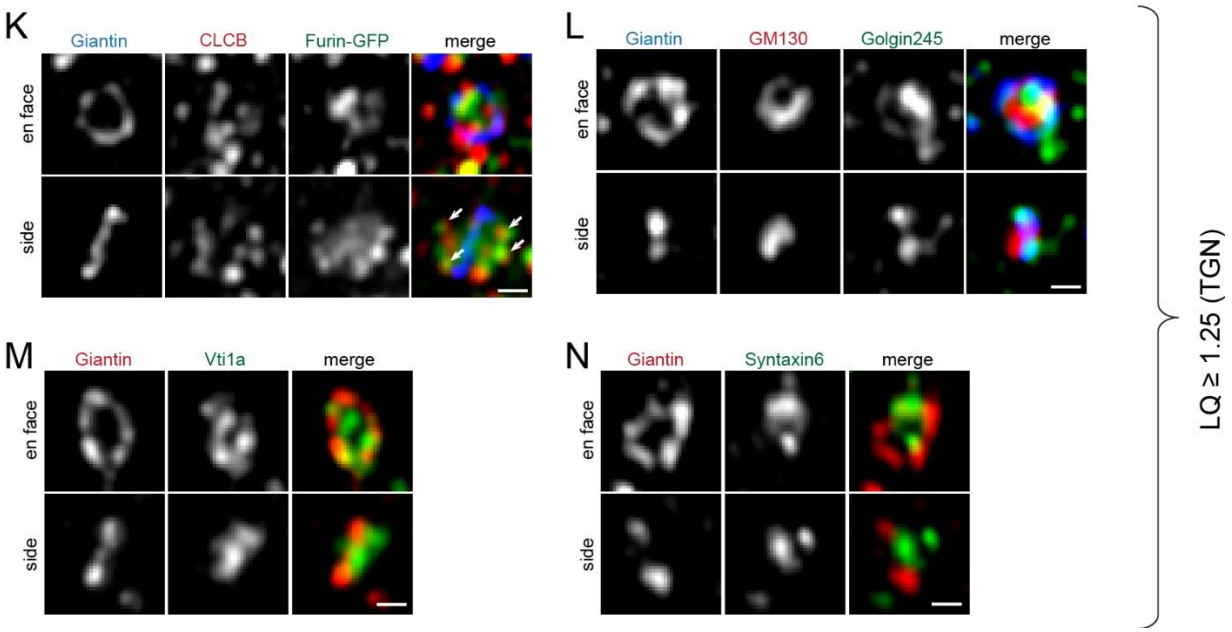

Figure 21: Components of trafficking machinery at the TGN display punctate or tubular profiles.
(A-N) TGN proteins (LQ≥1.25) that display tubular or punctate profiles in their en face and side views. (A, C, E, G, I, K-N) Typical en face and side view images of components of trafficking machinery at the TGN. (B, D, F, H, J) The averaged side and en face view images of TGN proteins and their radial mean intensity profiles. (G, K) Arrows in the side view images indicate that Vamp4 and Furin are decorated by CLCB puncta. n, number of averaged Golgi mini-stacks. Scale bar, 500 nm.

5.2 The averaged side views of TGN proteins reveal the TGN organization

The existence of multiple domains in the TGN has been proposed (Brown et al., 2011; Derby et al., 2004; Fölsch et al., 2003; Gleeson et al., 2004; Ladinsky et al., 1999), but this idea lacks of morphological evidence. In this section, several observations regarding TGN organization are reported.

First, TGN proteins did not co-localize significantly, as demonstrated by the lack of co-localization between Vamp4 and CI-MPR, GGA2, Vti1a or Furin (Figure 20E, H-J), suggesting that the TGN is not a single-mixed subcompartment.

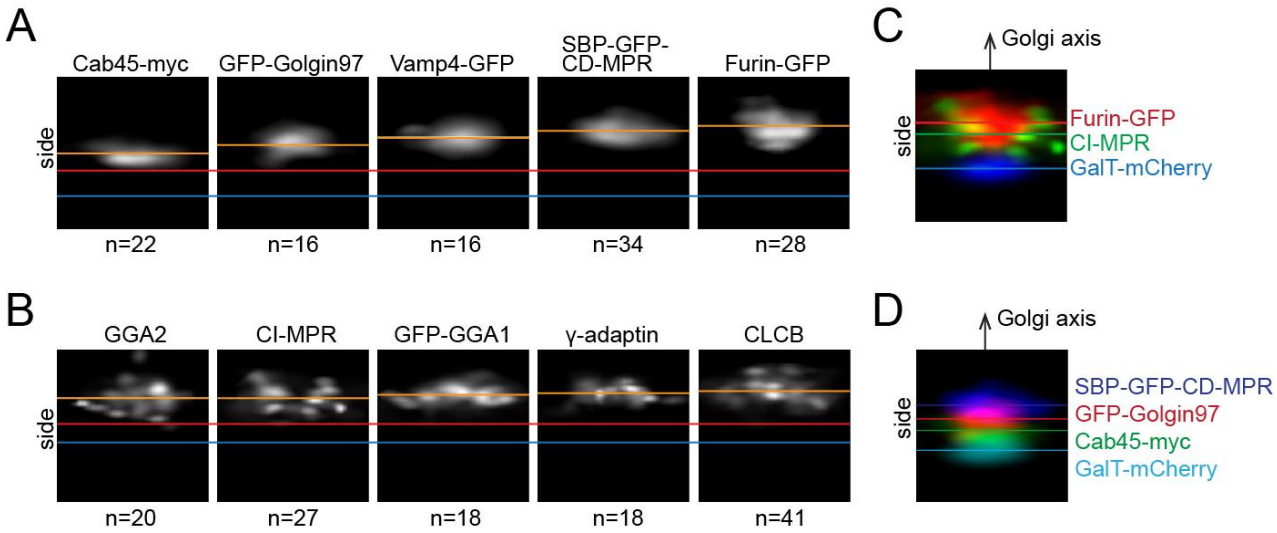

Figure 22: The averaged side view of TGN proteins reveals the molecular organization of the TGN.
(A-B) The averaged side view images of TGN proteins display (A) compact lumps or (B) scattered puncta. The y-coordinate of the center^{mass} (Ycenter^{mass}) of an averaged side view image was translated along the y-axis by 3-fold with reference to that of GM130 (indicated by the blue line, its corresponding image is from Figure 17B). The red and orange lines indicate Ycenter^{mass}s of GalT-mCherry and TGN proteins, respectively, after translation. (C) The colocalization of GalT, Furin and CI-MPR reveals the complementary organization of Furin and CI-MPR at the TGN. The red, green and blue lines indicate Ycenter^{mass}s of Furin-GFP, CI-MPR and GalT-mCherry, respectively. (D) The colocalization of CD-MPR, Golgin97, Cab45 and GalT reveal multi-tier organization at the TGN. The blue, red, green and cyan lines indicate Ycenter^{mass}s of SBP-GFP-CD-MPR, GFP-Golgin97, Cab45-myc and GalT-mCherry, respectively. (C-D) The Ycenter^{mass} of GalT-mCherry was measured from its averaged side view image taken from Figure 24J. Ycenter^{mass}s of proteins were translated as described in (A-B). n, number of averaged Golgi mini-stacks.

Second, the TGN displayed two molecular distribution patterns: compact lumps and scattered puncta (Figure 20-22). Notably, the proteins that displayed punctate profiles are either components of the clathrin coat (e.g. CLCB), clathrin adaptors (e.g. GGA2, GGA1 and γ-Adaptin) or known to be concentrated in CCVs (e.g. CI-MPR, Vti1a and Syntaxin 6). Hence, scattered puncta could represent budding, fusing or isolated CCVs at the TGN. Interestingly, CI-MPR was observed to preferentially localize to regions that are complementary to that of Furin (Figure 22C). Proteins that displayed compact lumps, on the other hand, were organized into a multi-tier structure along the Golgi axis, as demonstrated by the co-localization of CD-MPR, Golgin97 and Cab45

(Figure 22D). In contrast, the non-layered zones at the TGN might be occupied by dissociative tubular and punctate transport carriers, including clathrin-coated and non-clathrin-coated nascent transport carriers. Collectively, our imaging data suggest that TGN subdomains might adopt different membrane architectures. They could organize into distinct zones at the macro scale. Such a molecular organization of the TGN has never before been revealed under LM.

5.3 Lateral localizations of Golgi enzymes

The Golgi houses many enzymes that are involved in diverse post-translational modifications, including glycosylation. This lateral localization study focuses on glycosylation enzymes, including those involved in N- and O-glycosylation. In humans, there are more than 300 glycosylation enzymes (Cantarel et al., 2009). They are mostly type II transmembrane proteins and have similar domain organization. In general, a glycosylation enzyme consists of a short N-terminal cytosolic tail, a single-pass transmembrane domain, a stem region and a luminal catalytic domain (Lairson et al., 2008). It was observed from LM and EM imaging that the Golgi enzyme MGAT2 mainly localizes to the cisternal interior (Figure 11-12). How do other Golgi enzymes laterally organize in Golgi cisternae? In the following sections, N-glycosylation enzymes (Man1B1, MGAT1, ManII, MGAT2, MGAT4B, GalT and ST6Gal1), O-glycosylation enzymes (GALNT1, GALNT2, GALNT4, GALNT8, C2GNT1 and POMGNT1), protein sulfation enzymes (TPST1 and TPST2), glycosaminoglycan synthesis enzymes (β3GalT6 and β4GalT7) and a poly-N-acetyllactosamine synthesis enzyme (β4GalT3) are analysed. A GDP-fucose transporter, SLC35C1, is also analysed.

5.3.1 Lateral localizations of medial- (0.25≤LQ<0.75) and *trans*-Golgi (0.75≤LQ<1.25) enzymes

Medial-Golgi enzymes, including MGAT1, β4GalT7, β3GalT6, POMGNT1, GALNT4 and β4GalT3, were mainly found in the cisternal interior (Figure 23). Similarly, *trans*-Golgi enzymes, including TPST1, GALNT1, GALNT2, ST6Gal1, GalT and the *trans*-Golgi nucleotide sugar transporter SLC35C1, were also mainly found in the cisternal interior (Figure 24). Their side views displayed a bar shape flanked by the Giantin double-punctum (Figure 23-24).

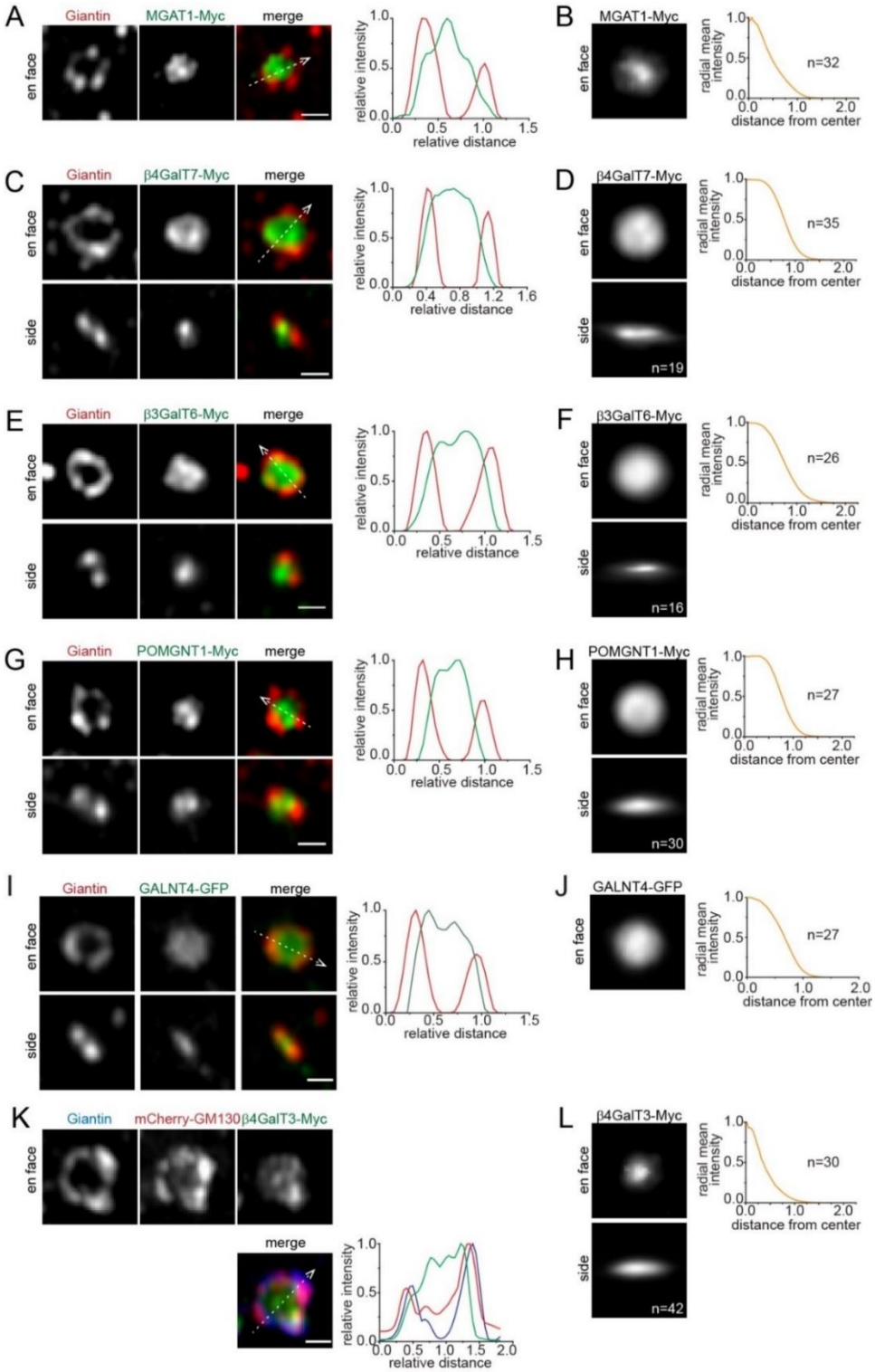

Figure 23: Golgi enzymes at the medial-Golgi primarily localize to the Golgi cisternal interior.

(A-L) Golgi enzymes that localize to the medial-Golgi. (A, C, E, G, I, K) Typical en face and side view images of medial-Golgi enzymes and their line intensity profiles. Line intensity profiles for the en face view images were generated as described in Figure 9A. Scale bar, 500 nm. (B, D, F, H, J, L) The averaged side and en face view images of medial-Golgi enzymes and their radial mean intensity profiles. n, number of averaged Golgi mini-stacks.

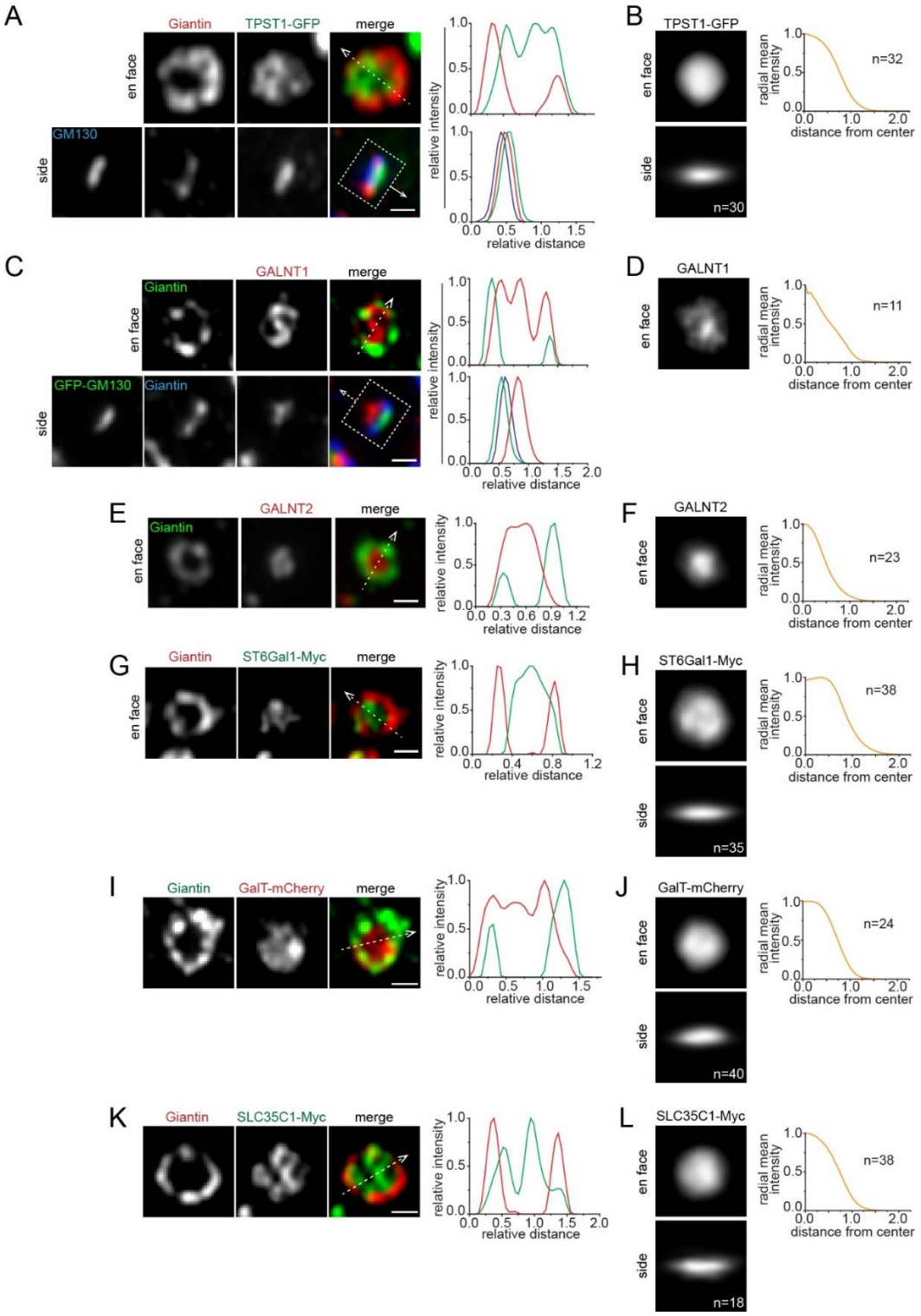

Figure 24: Golgi enzymes at the *trans*-Golgi primarily localize to the Golgi cisternal interior.

(A-L) Golgi enzymes that localize to the *trans*-Golgi. (A, C, E, G, I, K) Typical en face and side view images of *trans*-Golgi enzymes and their line intensity profiles. Line intensity profiles for the en face and side view images were generated as described in Figure 9A and 7C. Scale bar, 500 nm. (B, D, F, H, J, L) The averaged side view and en face view images of *trans*-Golgi enzymes and their radial mean intensity profiles. n, number of averaged Golgi mini-stacks.

5.3.2 The organization of Golgi enzymes in the cisternal interior

Most Golgi enzymes displayed an interior-disk pattern in their en face views. However, a few enzymes exhibited an inner-ring pattern, including ManII, Man1B1, GALNT8, MGAT4B, TPST2 and C2GNT1 (Figure 25A-L). Nonetheless, their averaged side views displayed a bar shape (Figure 25F,J,L), possibly due to their significant localization in the cisternal interior and/or the inability of the Airyscan microscope to resolve the interior.

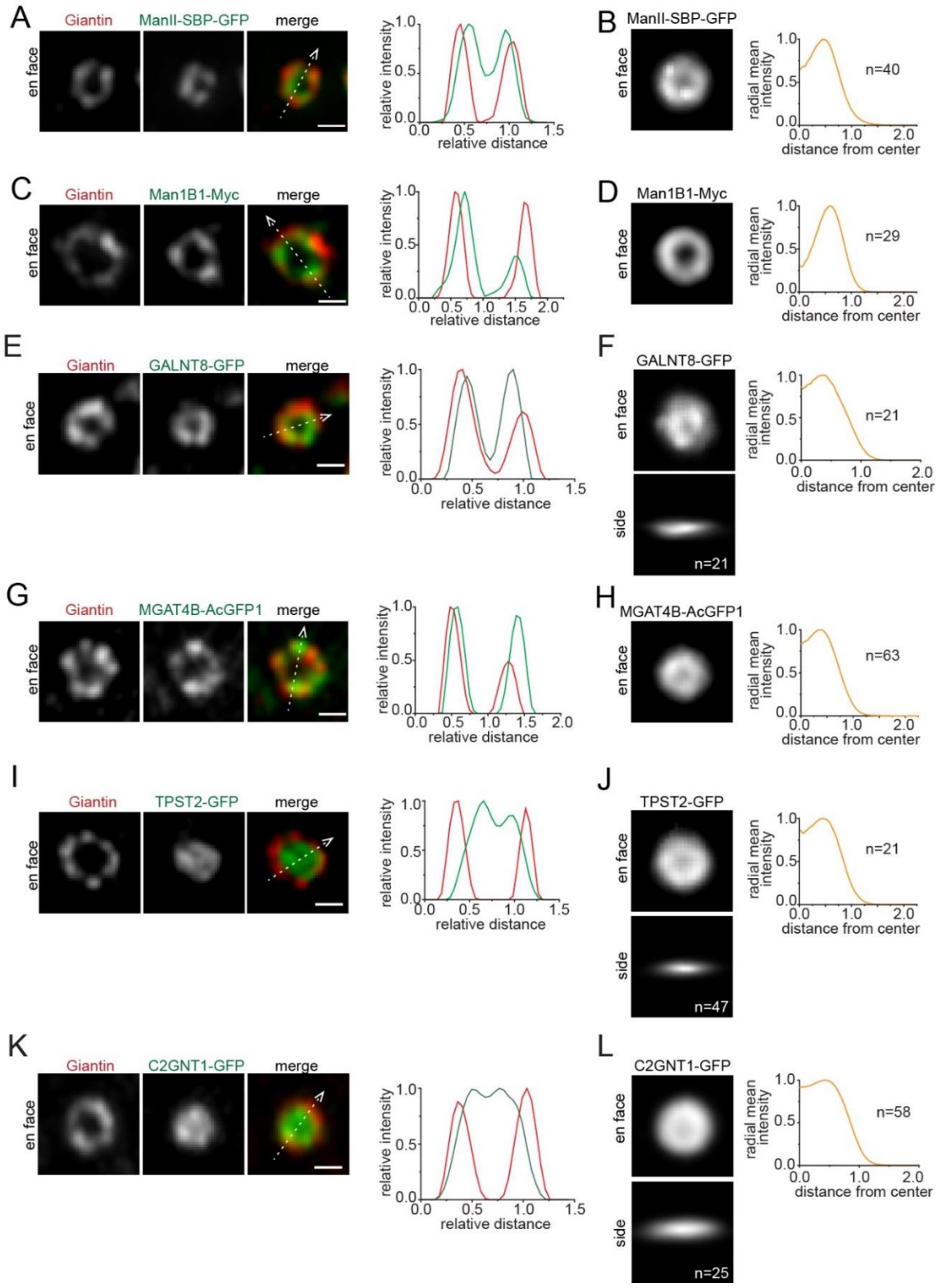

Figure 25: Golgi enzymes display the inner-ring appearance.
(A-B) ManII localizes to the *cis*-Golgi. (C-L) Golgi enzymes that localize to the medial-Golgi. (A, C, E, G, I, K) Typical en face view images of Golgi enzymes and their line intensity profiles. Line intensity profiles were generated as described in Figure 9A. Scale bar, 500 nm. (B, D, F, H, J, L) The averaged side and en face view images of Golgi enzymes and their radial mean intensity profiles. n, number of averaged Golgi mini-stacks.

Most Golgi enzymes display cisternal interior localization, but their spatial relationships are not known. Since MGAT2 (LQ=0.53), MGAT4B (LQ=0.50) and Giantin (LQ=0.57) have similar LQs (Table 6), they might largely reside in the same cisternae. Therefore, their averaged en face view images were merged to investigate their spatial relationships (Figure 26A). Giantin was observed to mark the rim of cisternae, while MGAT4B formed a concentric inner ring with respect to Giantin. MGAT2 filled the cisternal interior and significantly overlapped with MGAT4B (Figure 26A). Another pair of Golgi enzymes with similar LQs, β4GalT3 (LQ=0.73) and ST6Gal1 (LQ=0.85), localized to both shared (arrows in Figure 26B) and distinct domains within the Giantin ring (Figure 26B).

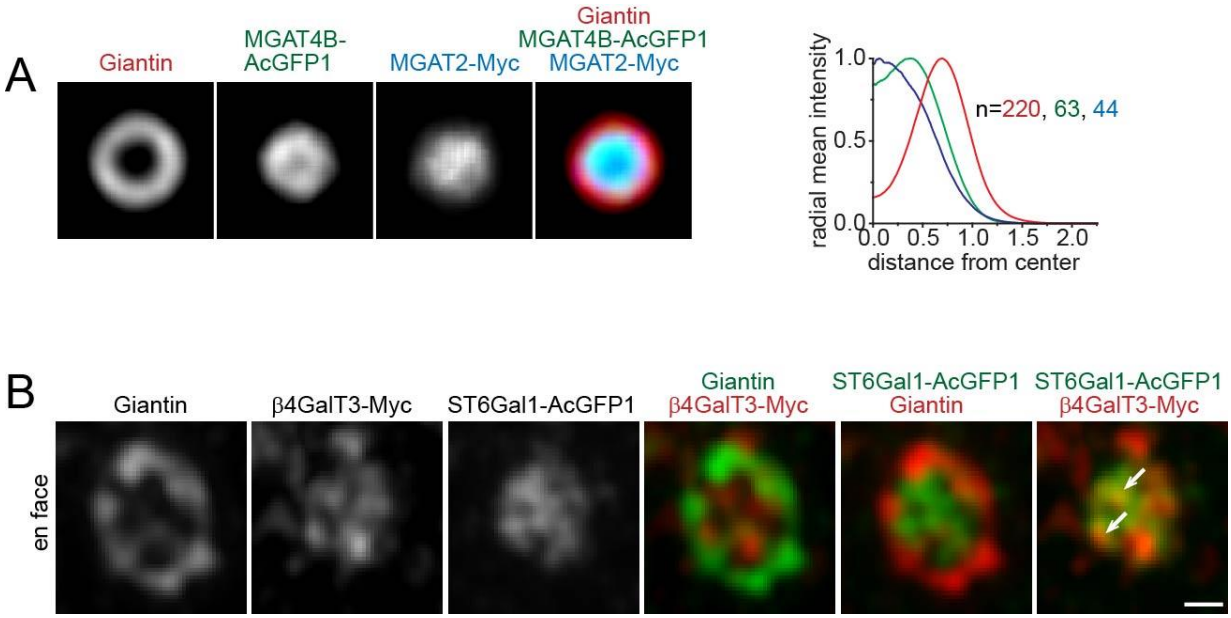

Figure 26: The organization of Golgi enzymes within Golgi cisternae.
(A) MGAT4B and MGAT2 display inner ring and disk-like patterns, respectively, whereas Giantin displays the outer-ring pattern. The averaged en face views of Giantin, MGAT4B-AcGFP1 and MGAT2-myc were merged and their respective radial mean intensity profiles were shown at the side. n, number of averaged Golgi mini-stacks. (B) ST6Gal1 and β4GalT3 can localize to distinct and shared (arrow) domains within the cisternal interior. HeLa cells transiently expressing β4GalT3-Myc and ST6Gal1-AcGFP1 were treated with nocodazole and immuno-stained by Myc and Giantin antibodies. Golgi proteins were merged in different combinations to reveal their spatial relationships. Scale bar, 500 nm.

5.4 Analysing the cisternal organization of the native Golgi

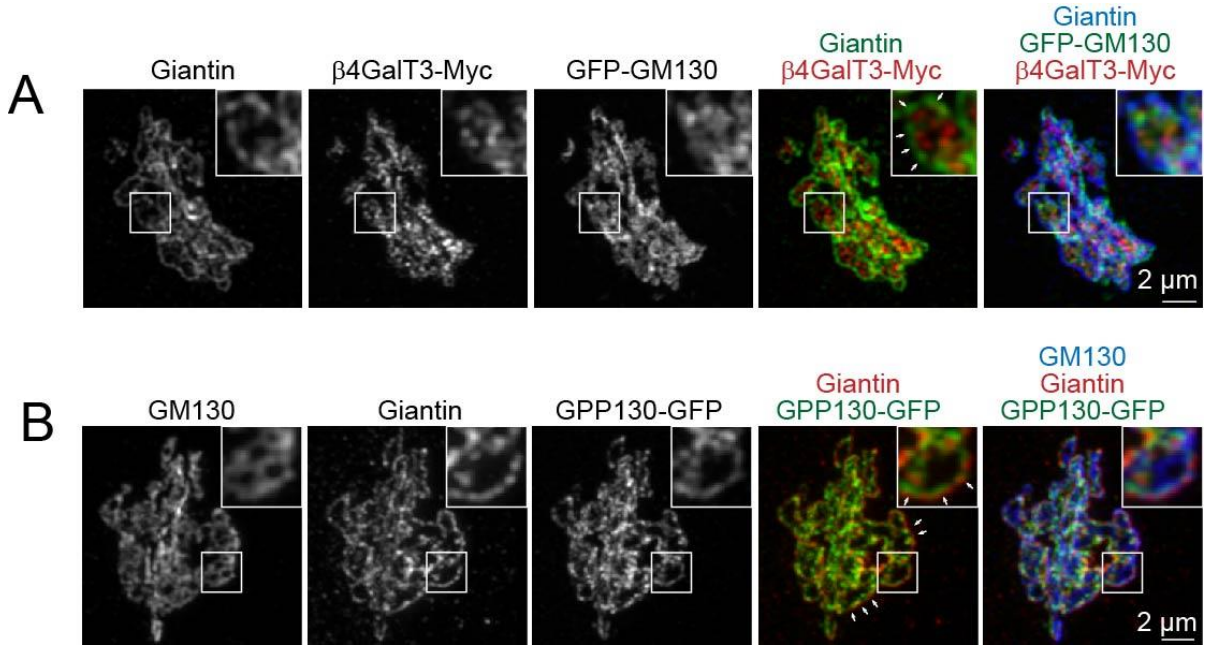

Figure 27: The identification of cisternal rim and interior in the native Golgi. (A) Giantin localizes to the cisternal rim, whereas β4GalT3 and GM130 localize to the cisternal interior and periphery of the native Golgi stack. HeLa cells transiently expressing β4GalT3-Myc and GFP-GM130 were immuno-stained by Myc and Giantin antibodies. Arrows indicate the cisternal rim, where Giantin is localized. The interior of Giantin ring is occupied by β4GalT3-Myc. (B) GPP130 and Giantin curvy lines represent the cisternal rim. They do not represent the side views of Golgi stacks. HeLa cells transiently expressing GPP130-GFP were immuno-stained by GM130 and Giantin antibodies. Arrows indicate the cisternal rims but not the side view of Golgi stacks. (A-B) Note that cells were not treated with nocodazole. Scale bar, 2 μm.

The study of native Golgi organization under LM is hampered by the resolution limit of LM and the inherent complexity of the Golgi architecture. For instance, the orientation of the Golgi stack was not discernible previously. However, it is now possible to assess Golgi architecture by taking advantage of the staining patterns of Giantin and Golgi enzymes. With these proteins labelled in a native Golgi, one could discern the orientation of convoluted Golgi stacks, especially in the less-dense region. For instance, Giantin and GPP130 appeared as loops or distinctive rings, while GM130 and β4GalT3 filled the interior regions (Figure 27). The sheet-like pattern occupied by GM130 and β4GalT3 may correspond to en face views of stacked Golgi cisternae (Figure 27A, arrows). Giantin- and GPP130-positive curvy lines likely represented the

rim of cisternae oriented in the en face or oblique view (Figure 27B, arrows). Therefore, with the help of Golgi rim and interior markers, we can decipher not only the orientation of nocodazole-induced Golgi mini-stacks, but also that of Golgi stacks in a native Golgi.

5.5 Quantitative molecular organization maps of the Golgi mini-stack

After examining the lateral localization of dozens of Golgi proteins, a quantitative molecular organization map of the Golgi mini-stack was plotted. It quantitatively describes the lateral (y-axis) and axial localizations (x-axis) of Golgi proteins (Figure 28). The former can be measured using the radial mean intensity profile as the radial mean radius, whereas the latter can be measured by GLIM as the LQ. Therefore, the plot summarized the morphological observation of disk and ring distributions of Golgi proteins along the Golgi axis. In addition, the lateral size of Golgi proteins was plotted against their corresponding LQs (Figure 29). The lateral size of a Golgi protein is defined as the distance between the two half-maximum-intensity points at the outer slopes of its averaged side view image (see Section 2.14). The two plots mentioned above model the Golgi mini-stack from two perspectives: the en face and side views, respectively. As expected, they share many similarities.

Most Golgi enzymes localized to the cisternal interior in the medial- and *trans*-Golgi (Figure 28-29, red closed circles), and they appeared as concentric disks or inner rings with respect to the Giantin rings. The cisternal rim and periphery of the Golgi stack were mainly occupied by components of trafficking machinery (Figure 28-29, red open circles). Regardless of whether they are enzymes or components of trafficking machinery, proteins that localize to the Golgi stack region generally appeared more confined and compact. This is suggested by their smaller radii and lateral sizes compared to those of Giantin (Figure 28-29, Table 8-9). In contrast, proteins that localize to the ERES/ERGIC and the TGN appeared more expansive and could spread

to regions where their radii and lateral sizes were 1.5 times larger than those of Giantin (Figure 28-29, green and purple open circles). Another common feature between the two plots was that *cis*-cisternae appeared smaller than medial-cisternae (Figure 28, blue lines connect GM130 with rim-localized proteins, namely Golgin84, Giantin and GCC185 at the *cis*-, medial- and *trans*-Golgi, respectively; Figure 29, blue lines connect GM130 with rim-localized proteins, namely ACBD3, Giantin, GPP30 and Golph3, from the *cis*- to *trans*-face). This is consistent with the measurement of the lateral size of GM130 and Giantin (Figure 14D), which were measured to be 452±147 nm and 704±175 nm (mean±SD), respectively. This observation was supported by some EM thin sections and 3D tomograms (Bykov et al., 2017; Engel et al., 2015; Staehelin and Kang, 2008), but its significance remains unknown.

Of note, the lateral localization of ERES- and ERGIC-localized proteins appeared different between the two plots. Sec23a, GS27 and ERGIC53 appeared less expansive in the lateral size plot, although γCOP remained almost the same in both plots. The discrepancy could be explained by the small number of side view images analysed in the lateral size plot, which could make artefacts more prominent. The ERES, ERGIC and TGN are generally less symmetrical around the Golgi axis; therefore, proteins in these regions might require a large number of images for averaging in order to generate non-biased views of these proteins.

Collectively, by combining GLIM and Airyscan imaging of the en face and side views of Golgi proteins, two quantitative molecular organization maps of the Golgi mini-stack were established. They are highly consistent with each other and with our current understanding of the Golgi.

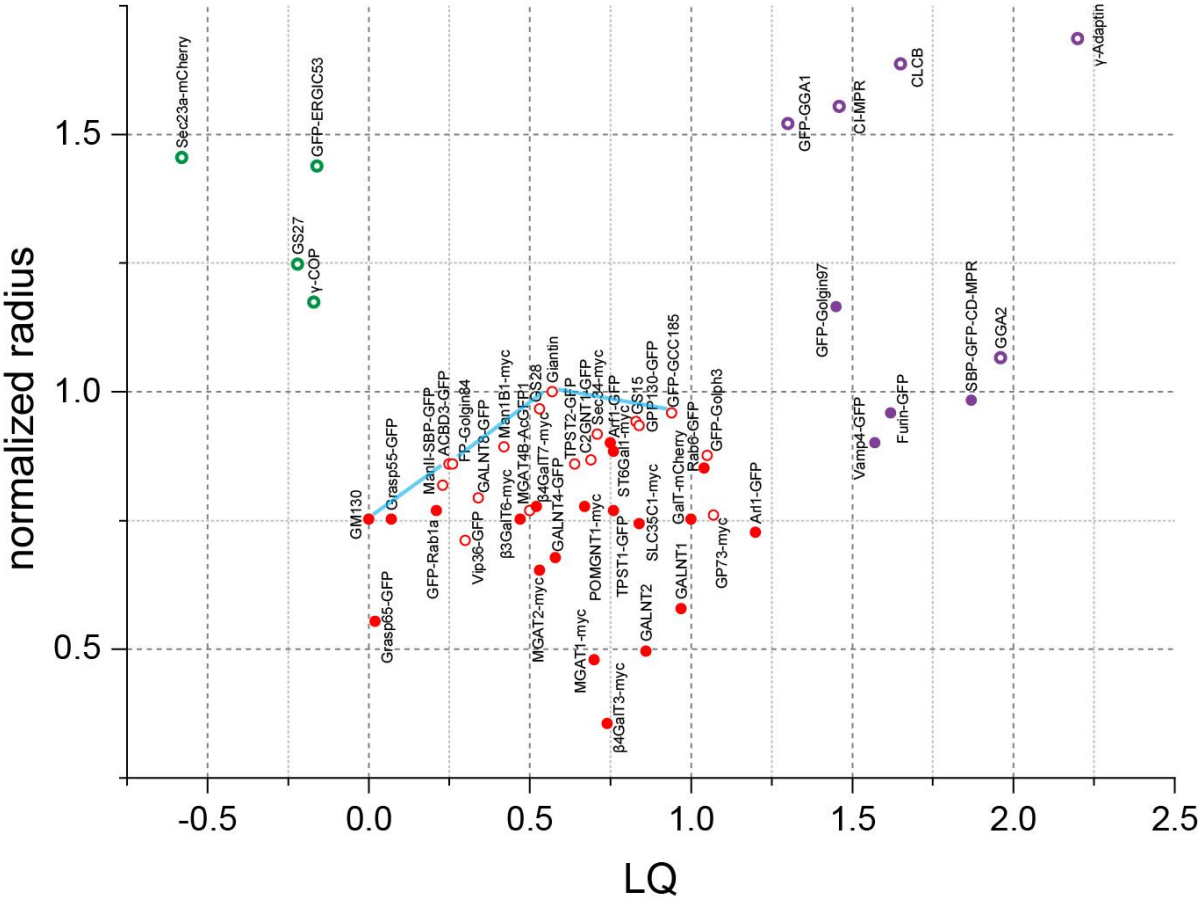

Figure 28: The quantitative molecular map of the Golgi mini-stack based on the radii of Golgi proteins.

The radii of Golgi proteins are plotted against their corresponding LQs (Table 8). Red open and closed circles denote the lateral localization patterns (ring and disk, respectively). Green open circles denote Golgi proteins that localize to the ERES and ERGIC. Purple open and closed circles denote TGN-localized proteins that exhibit scattered puncta and compact lumps, respectively. Blue lines connect GM130 and several rim-localized Golgi proteins, including FP-Golgin84, Giantin and GFP-GCC185, from the *cis*- to *trans*-face.

Name	n	normalized radius	LQ
Sec23a-mCherry	51	1.45	-0.58
GS27	74	1.25	-0.22
γCOP	70	1.17	-0.17
GFP-ERGIC53	41	1.44	-0.16
GM130	147	0.75	0.00
Grasp65-GFP	23	0.55	0.02
Grasp55-GFP	41	0.75	0.07
GFP-Rab1a	34	0.77	0.21
ManII-SBP-GFP	40	0.82	0.23
ACBD3-GFP	44	0.86	0.25
FP-Golgin84	65	0.86	0.26
Vip36-GFP	30	0.71	0.30

GALNT8-GFP	21	0.79	0.34
Man1B1-myc	29	0.89	0.42
β3GalT6-myc	26	0.75	0.47
MGAT4B-AcGFP1	63	0.77	0.50
β4GalT7-myc	35	0.78	0.52
MGAT2-myc	44	0.65	0.53
GS28	20	0.97	0.53
Giantin*	220	1.00	0.57
GALNT4-GFP	27	0.68	0.58
TPST2-GFP	21	0.86	0.64
POMGNT1-myc	27	0.78	0.67
C2GNT1-GFP	58	0.87	0.69
MGAT1-myc	32	0.48	0.70
Sec34-myc	24	0.92	0.71
β4GalT3-myc	30	0.36	0.74
Arf1-GFP	39	0.90	0.75
ST6Gal1-myc	38	0.88	0.76
TPST1-GFP	32	0.77	0.76
GS15	28	0.94	0.83
GPP130-GFP	28	0.93	0.84
SLC35C1-myc	38	0.74	0.84
GALNT2	23	0.50	0.86
GFP-GCC185	20	0.96	0.94
GALNT1	11	0.58	0.97
GalT-mCherry	24	0.75	1.00
Rab6-GFP	24	0.85	1.04
GFP-Golph3	34	0.88	1.05
GP73-myc	32	0.76	1.07
Arl1-GFP	41	0.73	1.20
GFP-GGA1	35	1.52	1.30
GFP-Golgin97	50	1.17	1.45
CI-MPR	68	1.55	1.46
CLCB	77	1.64	1.65
Vamp4-GFP	53	0.90	1.57
Furin-GFP	60	0.96	1.62
SBP-GFP-CD-MPR	59	0.98	1.87
GGA2	66	1.07	1.96
γ-Adaptin	70	1.69	2.20

Table 8: Normalized radii of Golgi proteins and their LQs.
This table corresponds to Figure 28. The radius of a Golgi protein is normalized against that of Giantin. LQs in this table are from Table 6. n, number of averaged Golgi mini-stacks. *The radius of Giantin is defined as 1.00.

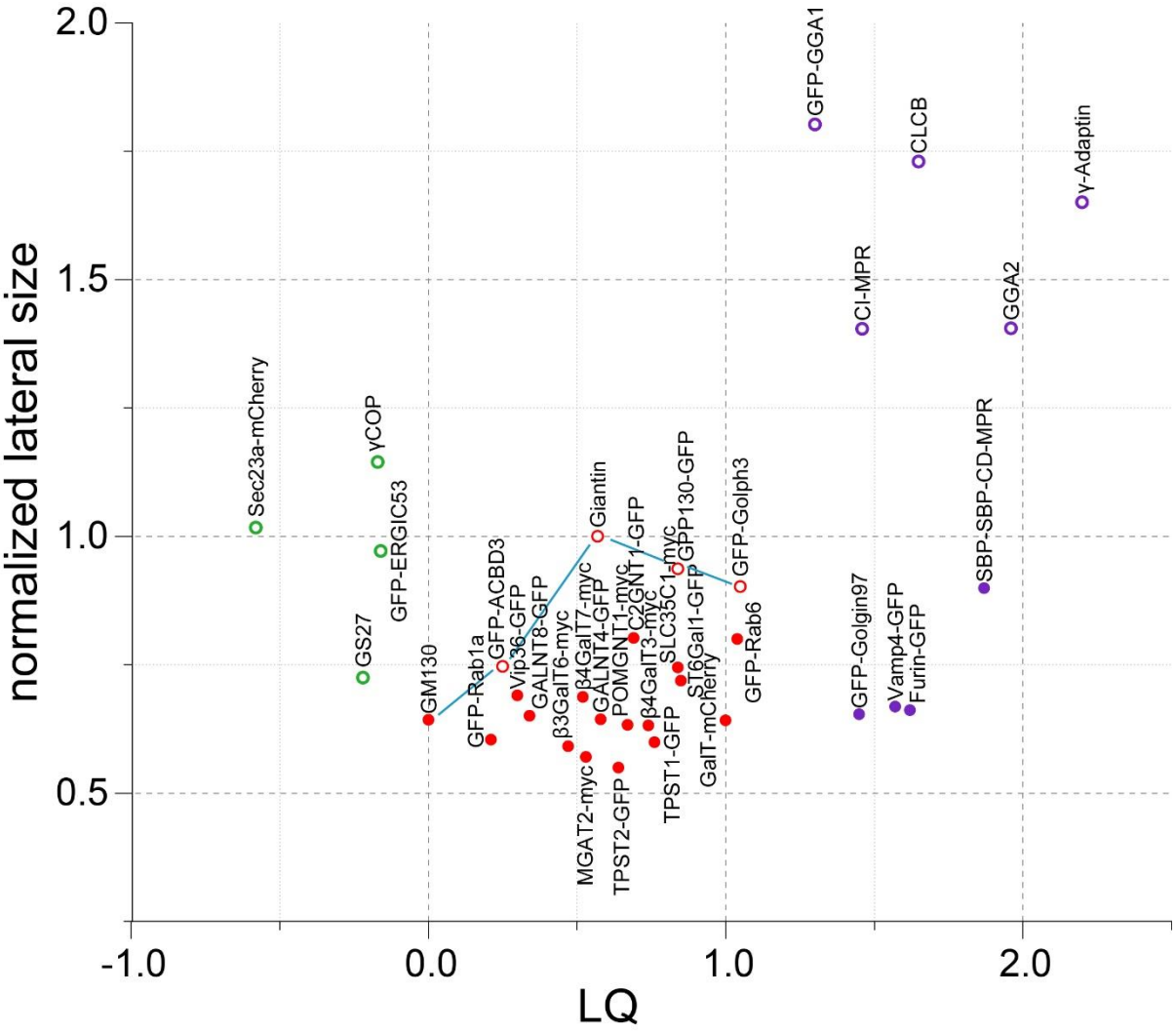

Figure 29: The quantitative molecular map of the Golgi mini-stack based on the lateral sizes of Golgi proteins.

The lateral sizes of Golgi proteins are plotted against their corresponding LQs (Table 9). Red open and closed circles denote the lateral localization patterns of double-punctum and bar-shape, respectively. Green open circles denote Golgi proteins that localize to the ERES and ERGIC, respectively. Purple open and closed circles denote TGN-localized proteins that exhibit scattered puncta and compact lumps, respectively. Blue lines connect GM130 and rim-localized Golgi proteins, including GFP-ACBD3, Giantin, GPP130-GFP and GFP-Golph3, from the *cis*- to *trans*-face.

Name	n	normalized lateral size	LQ
Sec23a-mCherry	37	1.02	-0.58
GS27	27	0.72	-0.22
γ-COP	26	1.14	-0.17
GFP-ERGIC53	24	0.97	-0.16
GM130	43	0.64	0.00
GFP-Rab1a	39	0.60	0.21
GFP-ACBD3	32	0.75	0.25
Vip36-GFP	17	0.69	0.30
GALNT8-GFP	21	0.65	0.34
β3GalT6-myc	16	0.59	0.47
β4GalT7-myc	19	0.69	0.52
MGAT2-myc	34	0.57	0.53
Giantin*	73	1.00	0.57
GALNT4-GFP	38	0.64	0.58
TPST2-GFP	47	0.55	0.64
POMGNT1-myc	30	0.63	0.67
C2GNT1-GFP	25	0.80	0.69
β4GalT3-Myc	42	0.63	0.74
TPST1-GFP	30	0.60	0.76
GPP130-GFP	31	0.94	0.84
SLC35C1-myc	18	0.74	0.84
ST6Gal1-GFP	35	0.72	0.85
GalT-mCherry	40	0.64	1.00
GFP-Rab6	26	0.80	1.04
GFP-Golph3	20	0.90	1.05
GFP-GGA1	18	1.80	1.30
GFP-Golgin97	26	0.65	1.45
CI-MPR	27	1.40	1.46
Vamp4-GFP	16	0.67	1.57
Furin-GFP	28	0.66	1.62
CLCB	41	1.73	1.65
SBP-SBP-CD-MPR	34	0.90	1.87
GGA2	20	1.40	1.96
γ-Adaptin	18	1.65	2.20

Table 9: Normalized lateral sizes of Golgi proteins and their LQs.
This table corresponds to Figure 29. The lateral size of a Golgi protein is normalized against that of Giantin. LQs in this table are from Table 6. n, number of averaged Golgi-mini-stacks. *The lateral size of Giantin is defined as 1.00.

A schematic model that summarizes the organization of a Golgi mini-stack was constructed (Figure 30). In summary, a Golgi mini-stack can organize into processing and transport domains (orange- and blue-shaded regions, respectively; Figure 30). These are predominantly found at the interior (orange-shaded regions) and the periphery (blue-shaded regions) of a Golgi mini-stack, respectively. The processing

domain is characterized by the preferential localization of Golgi enzymes, whereas the transport domain contains components of trafficking machinery.

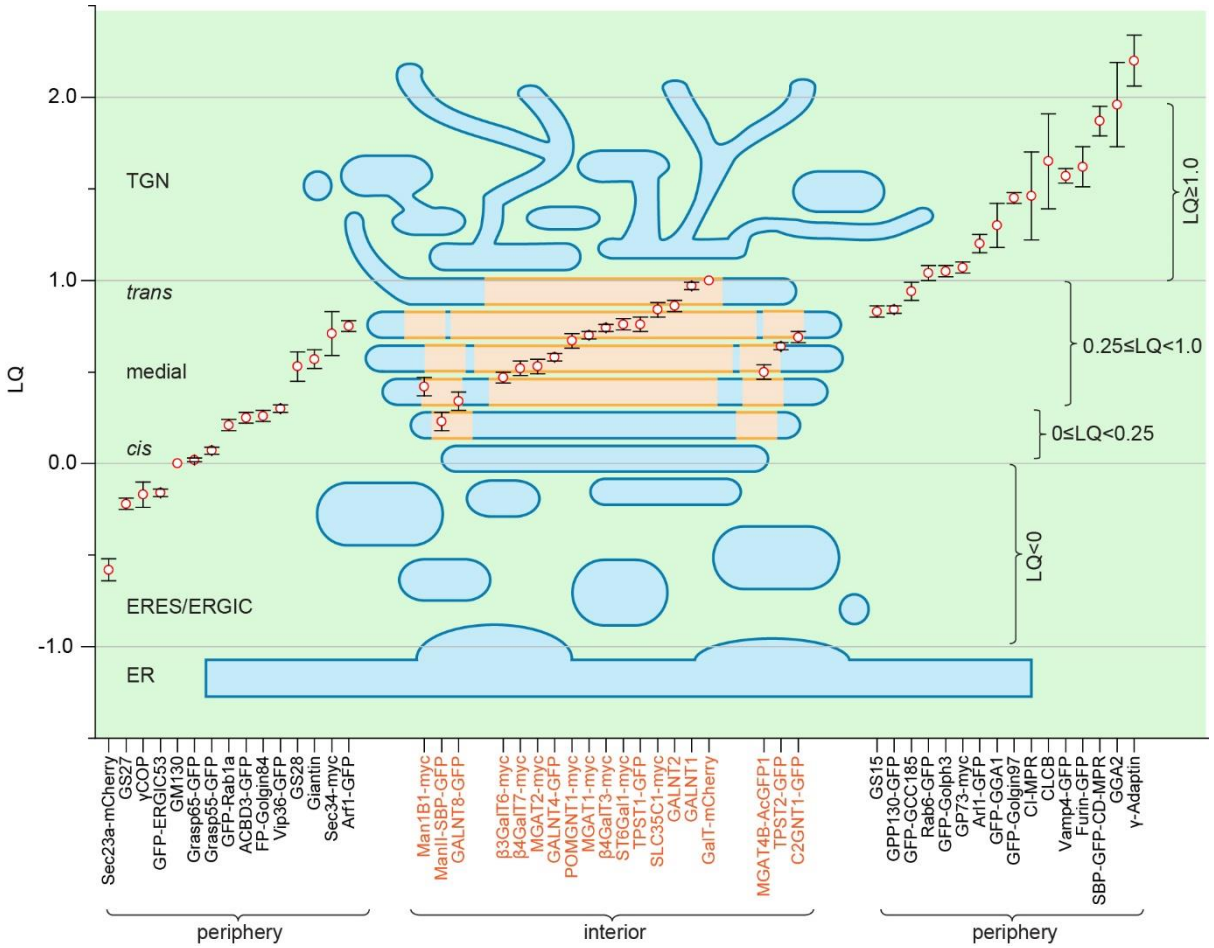

Figure 30: A schematic model that summarizes the organization of a Golgi mini-stack.

A schematic diagram of a Golgi mini-stack together with the ERES and ERGIC is overlaid by the LQs (see Table 6) of Golgi resident proteins. Golgi enzymes are localized to the interior (orange-shaded regions) of a Golgi mini-stack, they appear either as inner rings or disks. In contrast, components of trafficking machinery are localized to the ERES, ERGIC, Golgi cisternal rims, *cis*- and *trans*-most cisternae (blue-shaded regions). Red circles represent LQs and error bars indicate SEMs.

Chapter 6: Investigating the intra-Golgi trafficking of secretory cargos

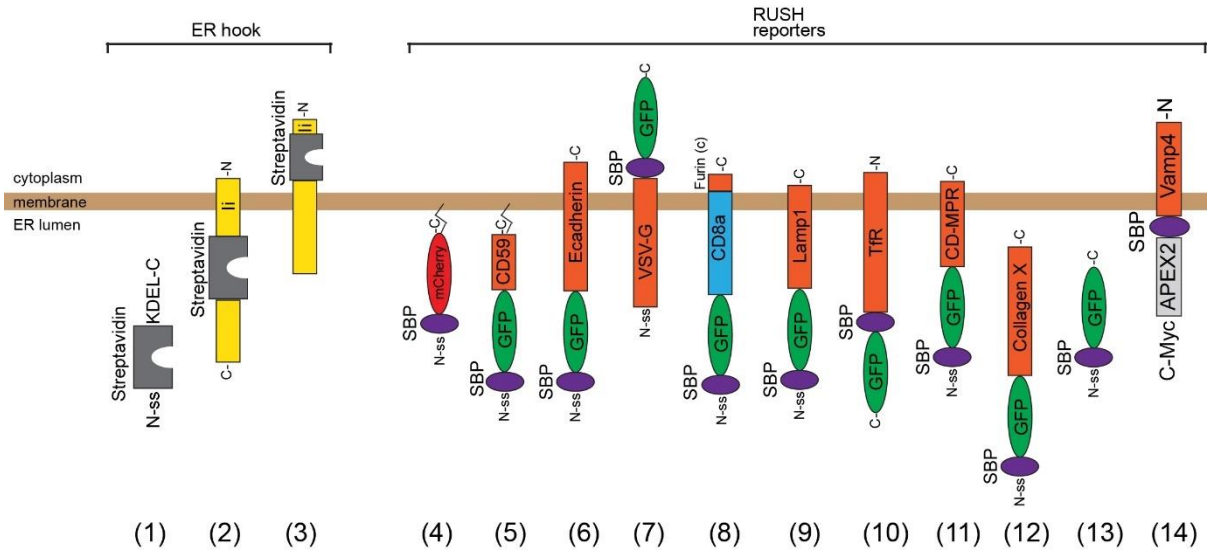

Figure 31: ER hooks and reporters in the RUSH system.
The schematic diagram shows ER hooks and reporters that are used in Figure 32-33, 36-38 and 41: 1) Strep-KDEL (soluble hook), 2) Ii-strep (membrane hook), 3) Strep-Ii (membrane hook), 4) ss-SBP-mCherry-GPI, 5) ss-SBP-GFP-CD59, 6) ss-SBP-GFP-E-cadherin, 7) VSVG-SBP-GFP, 8) ss-SBP-GFP-CD8a-Furin, 9) ss-SBP-GFP-Lamp1, 10) TfR-SBP-GFP, 11) ss-SBP-GFP-CD-MPR, 12) ss-SBP-GFP-collagen X, 13) ss-SBP-GFP, 14) Vamp4-SBP-APEX2-Myc. KDEL, an ER-retention signal that is encoded by lysine (K), aspartic acid (D), glutamic acid (E), leucine (L). Ii, invariant chain; ss, signal sequence; SBP, streptavidin-binding peptide.

Although a few major frameworks of intra-Golgi trafficking have been proposed, none can satisfactorily explain all observations (see Section 1.4). In addition, our previous work suggested alternative Golgi exit sites other than the TGN (see Section 1.3.4). This was supported by several EM studies and high-resolution fluorescence live cell imaging of endolysosomal-targeted proteins (see Section 1.3.4). Therefore, we decided to investigate the intra-Golgi trafficking and Golgi exit site of secretory cargos by inspecting their axial and lateral localizations. These secretory cargos include soluble proteins (GFP and collagen X), glycosylphosphatidylinositol (GPI)-anchored proteins (mCherry-GPI and CD59) and single-pass transmembrane proteins (E-cadherin, VSVG, Vamp4, CD8a-Furin, Lamp1, TfR and CD-MPR). In addition, two FM4-chimeras, FM4-moxGFP and GFP-FM4-CD8a, are also included in our study.

Among all membrane cargos, Lamp1, TfR and several TGN resident proteins, including Vamp4, CD8a-Furin and CD-MPR, cycle between the TGN, endosomes and the PM, while the rest are constitutive secretory cargos that are targeted to the PM.

6.1 Small cargos preferentially localize to the cisternal interior

The retention using selective hook (RUSH) system was used to synchronize ER-to-Golgi trafficking. Two experiments were performed in parallel for each cargo reporter in order to investigate LQ and lateral localization separately, thereby allowing us to correlate the axial and lateral localizations of cargos concurrently (Figure 32). When cargos were chased in the presence of biotin, the LQs of most secretory cargos (GFP, CD59, E-cadherin, VSVG and TfR) increased from values corresponding to the *cis*-Golgi to values corresponding to the *trans*-Golgi, following an exponential decay relationship, and eventually plateaued at around 1 (Figure 32D-F, L, P). In contrast, the LQs of CD8a-Furin, Lamp1 and CD-MPR increased up to approximately 1.5, corresponding to the TGN (Figure 32J-K, O). When the cargos reached late subcompartments, such as the *trans*-Golgi and the TGN, tubular or vesicular profiles were observed (indicated by arrows in Figure 32A-C, G-I, M-N). These were likely post-Golgi exocytic transport carriers.

In general, the lateral distribution of various cargos displayed interior localization during their intra-Golgi trafficking (Figure 32A-C, G-I, M-N), as they appeared within Giantin rings. Similarly, in Airyscan live cell imaging, mCherry-GPI appeared in the cisternal interior after 6 mins of biotin chase. It appeared in the interior of Golgi cisternae for more than 30 mins and eventually disappeared due to the post-Golgi exocytic transport (Figure 32Q, arrowheads indicate interior localizations), whereas Golgin84 appeared as a ring or double-punctum throughout the imaging period. Altogether, our imaging data demonstrated that conventional or small secretory cargos

(<115 kDa; 115 kDa is the MW of TfR-SBP-GFP, which is the largest cargo reporter analysed in this section), regardless of whether they are soluble or membrane-localized, appear in the cisternal interior during their intra-Golgi trafficking.

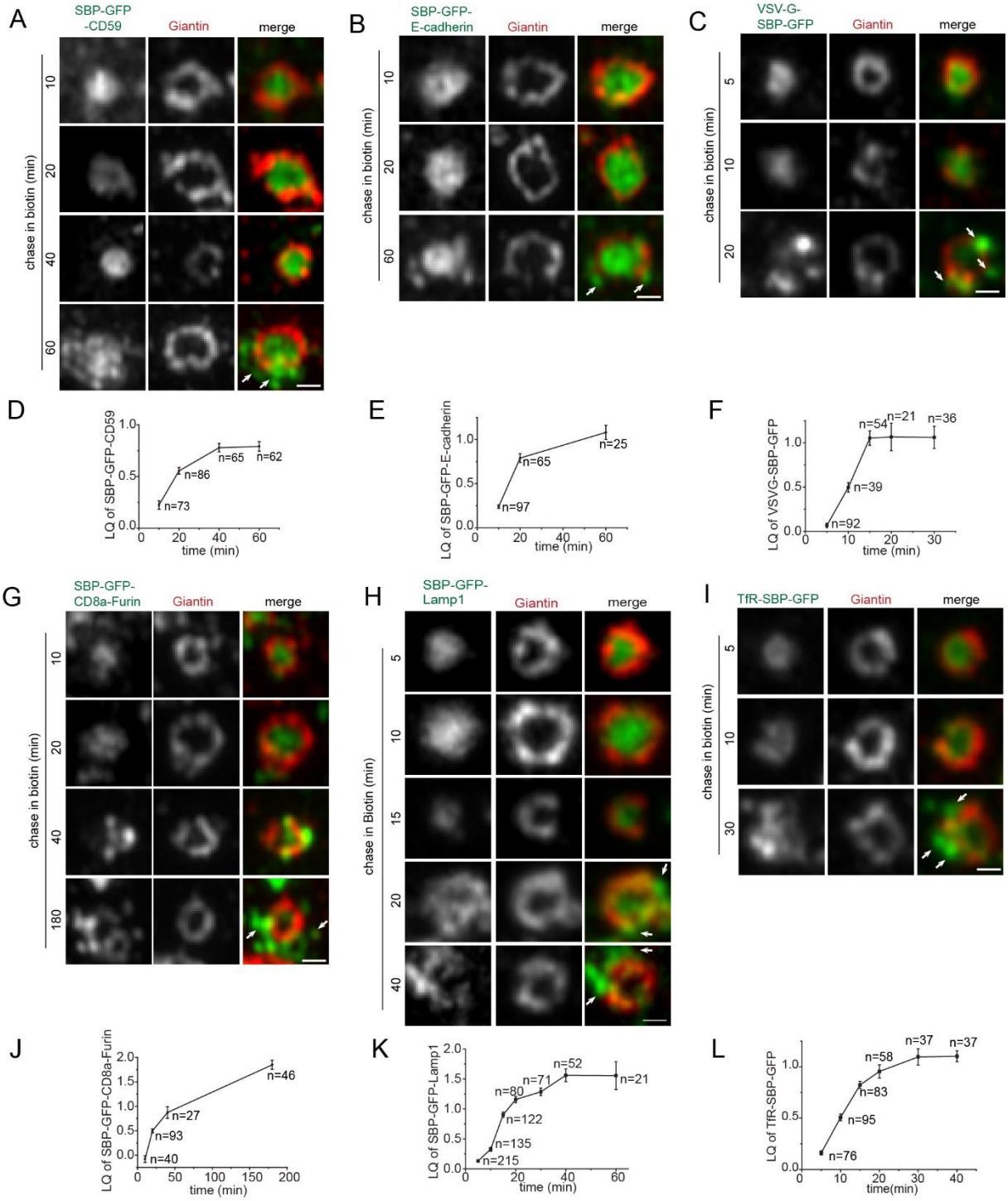

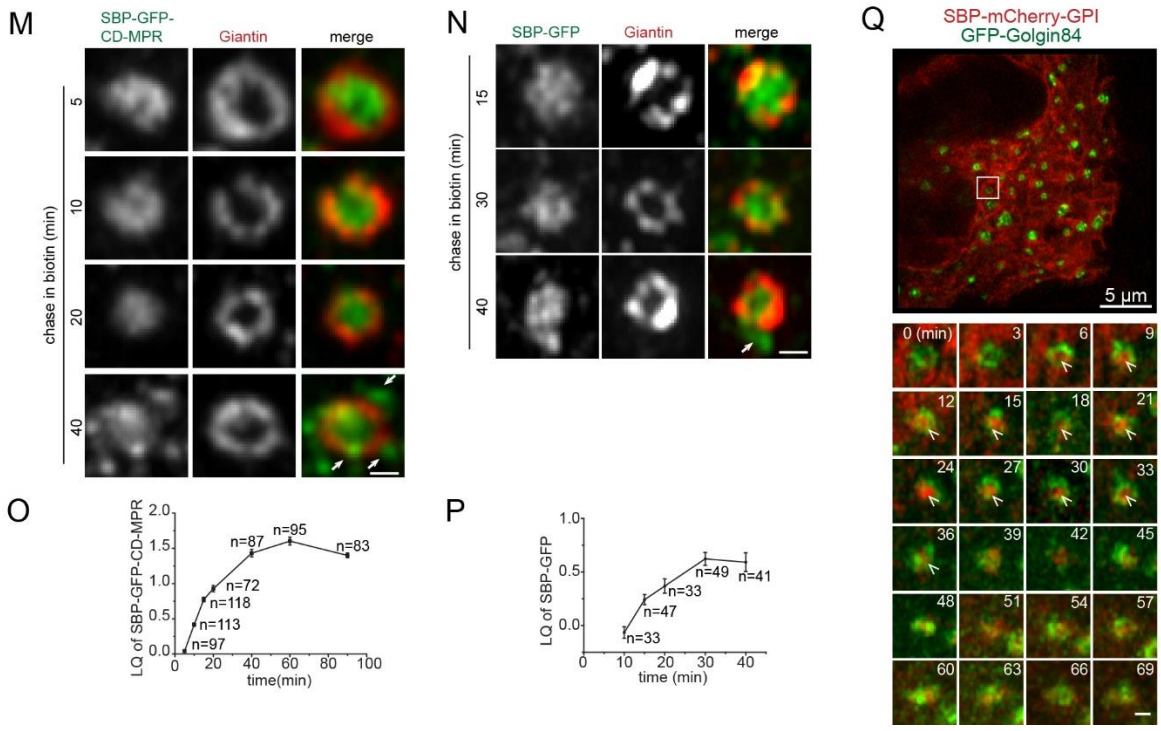

Figure 32: Conventional or small secretory cargos localize to the cisternal interior during intra-Golgi trafficking.
(A-P) HeLa cells singly transfected with a secretory cargo or co-transfected with a secretory cargo and GalT-mCherry were treated with nocodazole and chased in the presence of biotin and cycloheximide at indicated times. (A-C,G-I,M-N) Secretory cargos localize to the cisternal interior during intra-Golgi trafficking. Cells were immuno-stained by the Giantin antibody. Arrows indicate budding transport carriers. Scale bar, 500 nm. (D-F,J-L,O-P) LQ vs time plots were measured from the parallel experiments correspond to (A-C, G-I, M-N). Cells were immuno-stained by the GM130 antibody and imaged by a wide-field fluorescence microscope and images were subjected to GLIM analysis. n, number of analysed Golgi mini-stacks. Error bars, SEMs. (Q) The RUSH reporter SBP-mCherry-GPI demonstrates the cisternal interior localization during its intra-Golgi trafficking in living cells. HeLa cells transiently expressing GFP-Golgin84 and SBP-mCherry-GPI were chased in the presence of biotin and cycloheximide and imaged live under the Airyscan microscope. The boxed region in the full view cell image before the addition of biotin was chosen to display the time series below. Time stamps under the biotin treatment are indicated on top of every micrograph. Arrowheads indicate interior localizations. Scale bar, 500 nm.

6.2 Bulky cargos preferentially localize to the cisternal rim

Previously, it was reported that large secretory protein aggregates were found at the cisternal rim when transitioning through the Golgi (Lavieu et al., 2013; Volchuk et al., 2000). In order to investigate whether bulky cargos in general preferentially partition to the cisternal rim, a soluble RUSH reporter, collagenX, was used as the model for

study. Collagens are one of the major components of extracellular matrix (ECM). There are at least 28 different collagens in vertebrates (Frantz et al., 2010). Most of them, including collagenX, can form triple-stranded helices. They are then able to assemble into macromolecules (Frantz et al., 2010; Kwan et al., 1991). Under Airyscan imaging, collagenX exhibited punctate and diffuse patterns (Figure 33A, arrows). These could represent high and low multimeric states of collagenX, respectively. During intra-Golgi trafficking, both diffuse and punctate collagenX were partitioned to the cisternal rim, while the co-expressed mCherry-GPI resided in the cisternal interior (Figure 33A, arrowheads). At later time points, puncta outside Giantin rings were observed. These were likely post-Golgi exocytic carriers.

Furthermore, two secretory FM4-chimeras, soluble FM4-moxGFP and transmembrane FM4-CD8a, were tested. Similar chimeras were described in a previous report (Lavieu et al., 2013). Their aggregated states can be controlled by a small molecule, D/D solubilizer. By default, in the ER, these two FM4-chimeras can form protein aggregates that are too large to be accommodated in COPII vesicles. Therefore, they are arrested in the ER. However, the administration of D/D solubilizer can reverse their aggregated states. Once aggregates are dissolved, monomeric or low multimeric forms of FM4-chimeras can be exported from the ER into the secretory pathway. After incubating NRK cells expressing FM4-chimeras at 20°C in the presence of D/D solubilizer for 2 hrs, de-aggregated chimeras were accumulated and arrested in the Golgi. We then kept cells under the same conditions for another 2 hrs in the absence of D/D solubilizer to re-introduce the aggregation.

Under the Airyscan microscope, both FM4-chimeras appeared at the cisternal interior (Figure 33D-E, arrowheads) within the Giantin ring when they were in de-aggregated states. In contrast, after the D/D solubilizer washout, re-aggregated FM4-chimeric

puncta were formed and partitioned to the cisternal rim (Figure 33D-E, arrows), coinciding with Giantin rings.

Collectively, the lateral localization study of various secretory cargos suggests that bulky and conventional or small secretory cargos might preferentially localize to the cisternal rim and interior, respectively, during intra-Golgi trafficking.

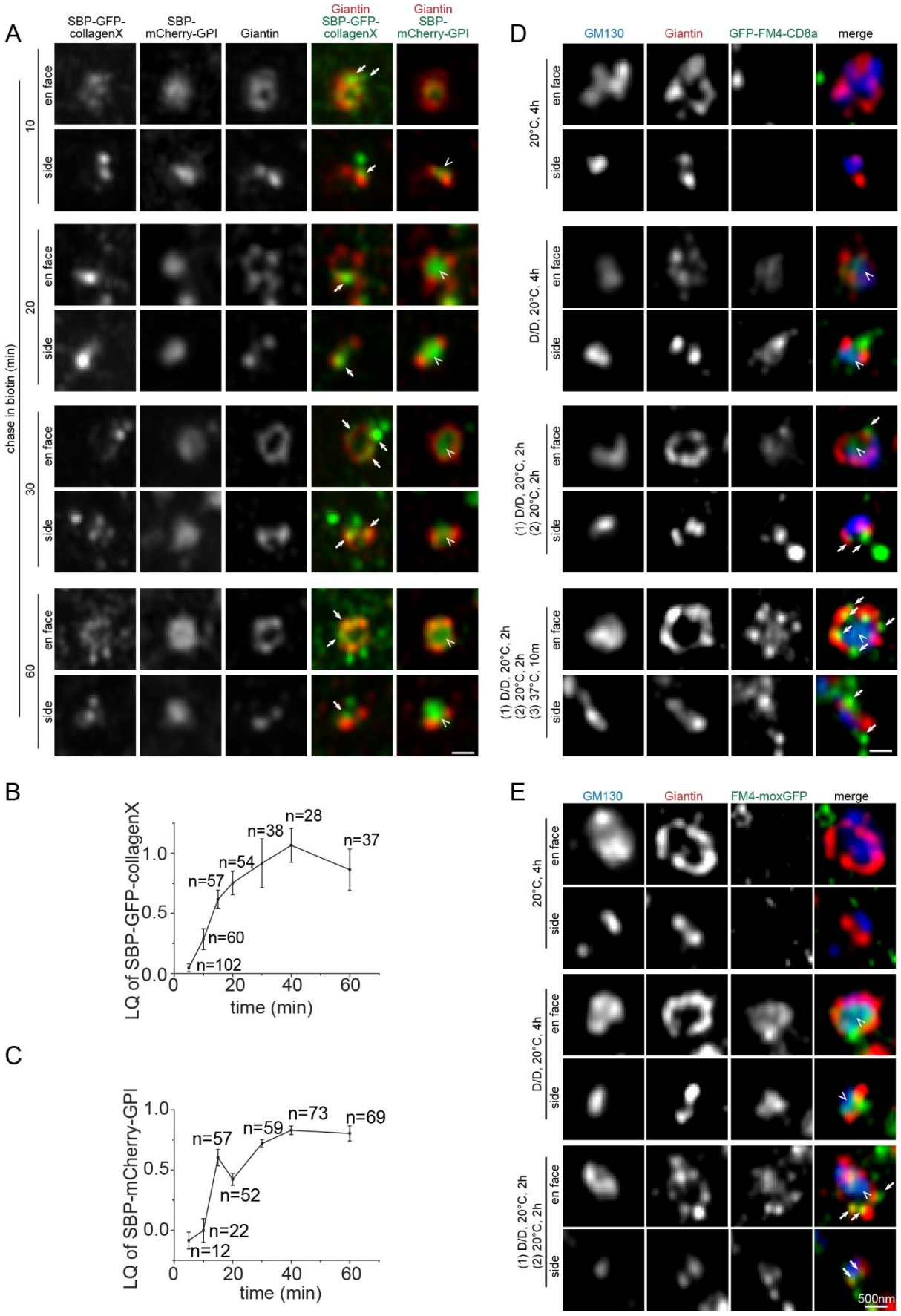

Figure 33: Bulky cargos localize to cisternal rims during their intra-Golgi trafficking.

(A) The partition of mCherry-GPI and collagenX to the cisternal interior and rim, respectively, during their intra-Golgi trafficking. HeLa cells transiently expressing SBP-mCherry-GPI and SBP-GFP-collagenX were treated with nocodazole and chased in the presence of biotin and cycloheximide. Cells were immuno-stained by the Giantin antibody. (B-C) The LQ vs time plots for collagenX and mCherry-GPI. Experiments were performed as described in Figure 32(D-F, J-L, O-P). n, number of analysed Golgi mini-stacks. Error bars, SEMs. (D-E) The aggregated FM4-moxGFP and FM4-CD8a localize to the cisternal rim, whereas their de-aggregated forms localize in the cisternal interior. NRK cells transiently expressing FM4-CD8a or FM4-moxGFP were subjected to incubation conditions as indicated. Cells were immuno-stained by GM130 and Giantin antibodies. Note that the first sets of images were absent of any FM4-fusions signal in Golgi mini-stacks and this was due to the aggregated FM4-fusions failed to be exported from the ER. They served as negative controls for these transport assays. (A,D-E) Arrows and arrowheads indicate the cisternal rim and interior, respectively. Scale bar, 500 nm.

6.3 Estimating the stoichiometry of collagenX and FM4 aggregates

Protein aggregates of collagenX and FM4 chimeras are assumed to appear as distinct puncta *in vivo*. In order to estimate the stoichiometry of these protein aggregates, an imaging-based approach was adopted as described below.

The nuclear pore complex (NPC) consists of ~30 different component proteins, called nucleoporins (Nups) (Cronshaw et al., 2002). The NPC is organized into an 8-fold rotational symmetry surrounding the nucleocytoplasmic axis (Beck et al., 2004). Previously, in our laboratory, a shRNA-based gene-replacement imaging assay was developed to estimate the stoichiometry of Nups in the NPC. The endogenous Nups of HeLa cells were individually knocked down by their corresponding shRNAs, followed by the expression of shRNA-resistant GFP-tagged Nups. Utilizing TIRF microscopy, the intensity of a single GFP molecule was measured based on the intensity difference before and after photobleaching. By comparing the fluorescence intensity of a single GFP molecule and that of shRNA-resistant GFP-tagged Nups in the Nup knockdown cells, the stoichiometry of several Nups, including Nup133, was successfully measured. It was found that 16 copies of Nup133 are present in an NPC (Tie et al., 2016b).

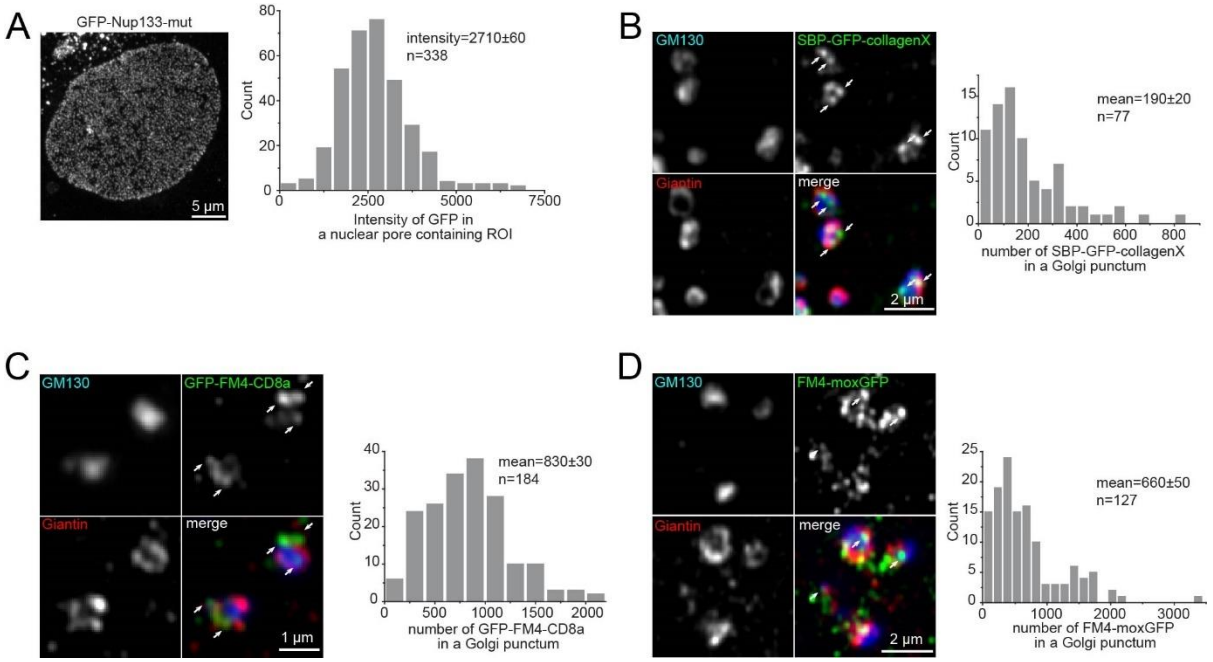

Figure 34: The estimation of the stoichiometry of fluorescent protein aggregates. (A) The expression of GFP-Nup133-mut and the estimation of total fluorescence intensity of individual GFP-Nup133-mut substituted NPC. Cells were first depleted of their endogenous Nup133 by the shRNA, followed by transiently expressing the shRNA-resistant GFP-Nup133-mut. The distribution of total fluorescence intensity of NPCs is shown in the histogram. n, number of analysed NPC. (B-D) The estimation of stoichiometry of SBP-GFP-collagenX, GFP-FM4-CD8a and FM4-moxGFP aggregates. Cells transiently expressing either one of these proteins were immuno-stained by GM130 and Giantin antibodies. The histogram beside each set of images displays the distribution of estimated stoichiometry of corresponding protein aggregates (puncta indicated by arrows) that are associated with Golgi mini-stacks. n, number of analysed Golgi puncta. Scale bars, as indicated in images. (A-D) Statistics, mean±SEM.

Using the shRNA-resistant GFP-tagged Nup133 as an *in vivo* GFP fluorescence standard (Figure 34A), a GFP-collagenX punctum was estimated to contain 190±20 copies (n=77) of constituent molecules (Figure 34B). In addition, aggregated FM4-moxGFP and FM4-CD8a puncta that appeared associated with the Golgi were estimated to contain 660±50 (n=127) and 830±30 (n=184) copies of their respective constituent molecules (Figure 34C-D). Furthermore, the MWs of the individual puncta of collagenX, FM4-moxGFP and FM4-CD8a were estimated to be 20,000 kDa, 50,000 kDa and 81,000 kDa, respectively. The MWs were calculated by multiplying the copy

numbers per aggregate by the MW per molecule. This provided evidence that these molecules were highly aggregated.

6.4 The lateral localization of ST6GAL1 did not change in the presence of synchronous transiting cargos

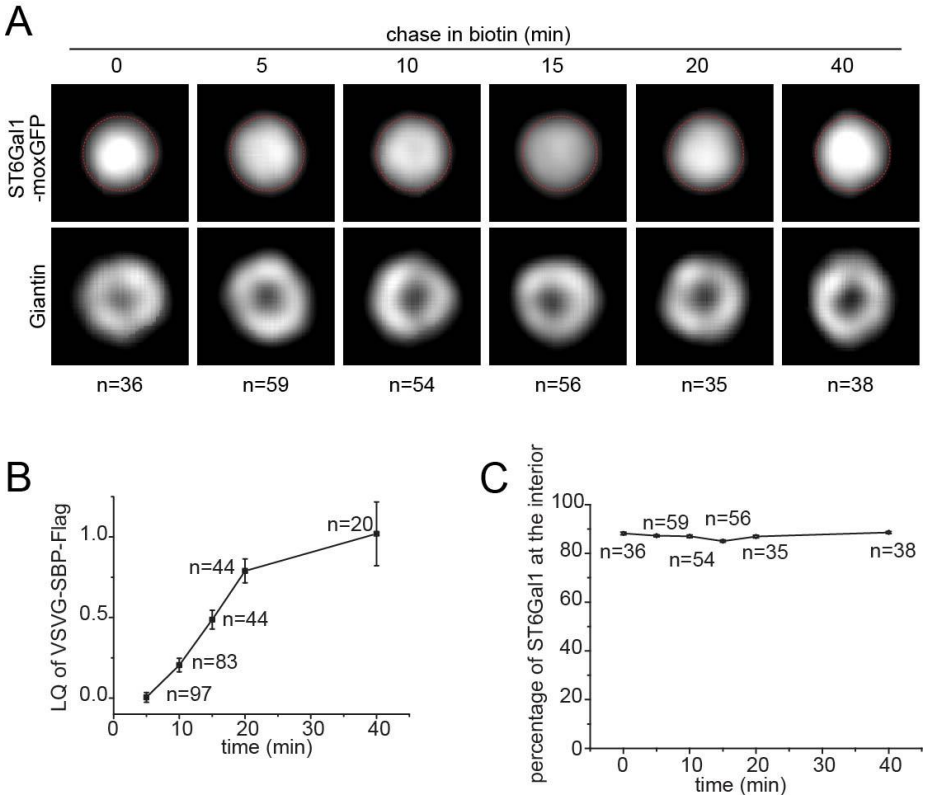

Figure 35: ST6Gal1 mainly remains in the cisternal interior when VSVG is transiting across the Golgi mini-stack.
(A, C) The lateral localization of ST6Gal1 does not change during the intra-Golgi transport of VSVG. HeLa cells transiently expressing VSVG-SBP-Flag (a RUSH reporter) and ST6Gal1-moxGFP were treated with nocodazole and chased in the presence of biotin and cycloheximide at different times as indicated. Cells were immuno-stained by the Giantin antibody. n, number of averaged Golgi mini-stacks. (A) The averaged en face views of ST6Gal1 and Giantin from different biotin chase times. Red dotted circle indicates the interior region of interest. The circle indicates the steady state lateral distribution of ST6Gal1. (C) The percentage of ST6Gal1-moxGFP within red dotted circles were plotted against the time of intra-Golgi trafficking of VSVG-SBP-Flag. (B) The LQ vs time plot for VSVG. The experiment was performed as described in Figure 32(D-F, J-L, O-P). n, number of analysed Golgi mini-stacks.

Golgi enzymes are expected to maintain their axial localizations amid intensive traffic in the Golgi so that the polarity of the Golgi is preserved. This hypothesis was tested

by investigating the lateral distribution of ST6Gal1 upon a surge of transiting secretory cargos, using VSVG as a RUSH reporter (Figure 35).

HeLa cells were co-transfected with ST6Gal1 and VSVG. During intra-Golgi trafficking of VSVG (Figure 35B), the majority of ST6Gal1 remained in the cisternal interior (Figure 35A, C). Our finding was inconsistent with a previous EM study in which Golgi enzymes were found to shift from the cisternal rim to the cisternal interior in the presence of transiting cargo loads (Kweon et al., 2004).

6.5 The direct visualization of secretory cargo waves during intra-Golgi trafficking

A synchronous cargo wave of VSVG-tso45 in Golgi mini-stacks was observed in a previous EM study (Trucco et al., 2004). However, Patterson et al. reported that VSVG-tso45 was homogenously distributed across all Golgi cisternae within 5 mins of incubation at the permissive temperature, 32°C. Hence, the group proposed the rapid partitioning model (Patterson et al., 2008). Patterson et al. suggested that the temperature shifts involved in Trucco's experiment could induce a change in the ratio of sphingolipids to glycerophospholipids in Golgi cisternae. This would in turn affect the distribution and kinetics of VSVG-tso45 across the Golgi stack, eventually creating the cargo waves observed by Trucco et al.

In this section, the nature of the cargo wave during intra-Golgi trafficking was re-examined. The study was conducted using a RUSH reporter, VSVG, thereby avoiding the potential influences of temperature shifts. Hence, our experimental condition is more likely to mimic physiological trafficking in the Golgi stack.

Under different biotin chase times, the averaged side views of VSVG appeared as a single-peak compact wave that progressively and axially moved from a position close to GM130 toward GalT (Figure 36A). Similarly, the progressive movement of cargo

waves was also observed in the averaged side views of another RUSH reporter, TfR (Figure 36E).

For the first time, under physiological temperature, we provide LM imaging evidence to demonstrate the existence of synchronous traffic waves that traverse the Golgi mini-stack over time. This is consistent with the previous EM study (Trucco et al., 2004) but contradictory to the results reported by Patterson et al. (Patterson et al., 2008).

In addition, VSVG and TfR displayed disk-like cisternal interior localization in their en face views (Figure 36C,G). Intriguingly, the radius of VSVG appeared the smallest at the *cis*-Golgi and became the largest when it reached the medial/*trans*-Golgi (15 mins post-biotin chase). After that, the radius of VSVG decreased. A similar trend of change in radius was demonstrated by TfR (Figure 36G). This observation could indicate a gradual increase in the lateral size of cisternae from the *cis*- to the *trans*-Golgi, with secretory cargos resided transiently as they traversed the Golgi mini-stack.

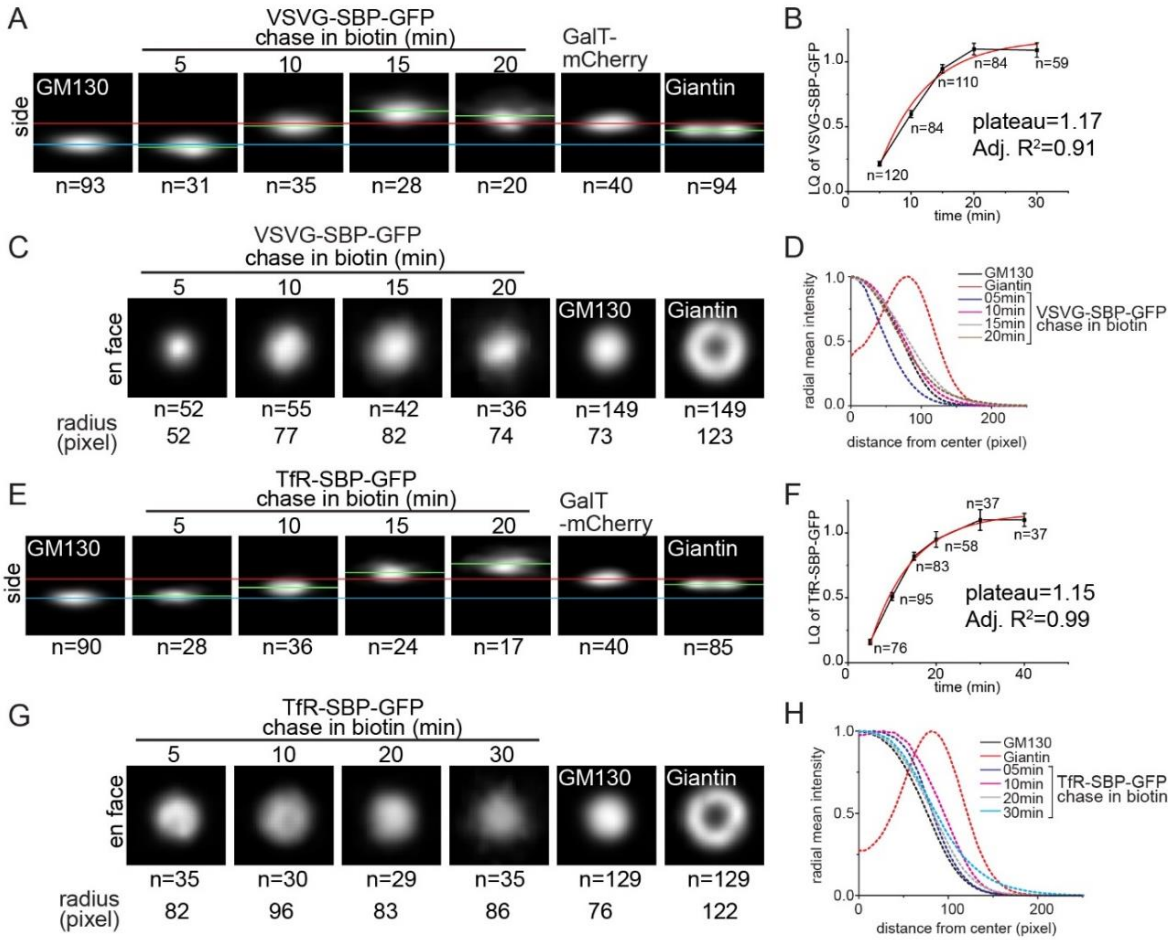

Figure 36: VSVG and TfR appear as single-peak cargo waves during intra-Golgi trafficking.

(A,C-D,E,G-H) HeLa cells transiently expressing VSVG-SBP-GFP or TfR-SBP-GFP were treated with nocodazole and chased in the presence of biotin and cycloheximide at different times as indicated. Cells were fixed and immuno-stained by GM130 and Giantin antibodies. The averaged en face and side views of Golgi resident proteins and secretory cargos are shown. n, number of averaged Golgi mini-stacks. (A, E) The averaged side views of VSVG and TfR display single-peak cargo waves that progressively transit from the *cis*- to *trans*-face. The averaged side view of GalT-mCherry was obtained from Figure 24J. The Ycenter^{mass}s of GM130 (blue), GalT-mCherry (red), VSVG-SBP-GFP, TfR-SBP-GFP and Giantin (green) were marked by color-coded lines. The Ycenter^{mass}s of all side view images were translated by 3-fold along the Y-axis with respect to that of GM130. (C-D,G-H) The radii of averaged en face views of VSVG and TfR change during intra-Golgi trafficking. Radial mean intensity profiles were plotted in (D,H). The radius of each averaged en face view image is indicated. (B,F) LQ vs time plots demonstrate the axial localization of VSVG and TfR corresponding to (A,C,E,G). Experiments were performed as described in Figure 32(D-F, J-L, O-P). The adjusted R^2 (adj. R^2) and plateau of fitted curve are indicated in each plot. n, number of analysed Golgi mini-stacks.

6.6 20°C incubation accumulates the cargo wave at the medial-Golgi

15°C and 20°C incubations have been widely adopted to accumulate secretory cargos in the ERGIC and TGN, respectively (Griffiths et al., 1985; Matlin and Simons, 1983; Saraste and Kuismanen, 1984). However, using GLIM, VSVG-tso45-GFP was observed to be blocked at the medial-Golgi at 20°C (Tie et al., 2016a). The discrepancy was addressed by investigating the side view of a RUSH reporter, CD-MPR.

The LQ of CD-MPR was measured in the presence of biotin and cycloheximide. Under the incubation conditions used (15°C for 1.5 hrs, 20°C for 2 hrs and 37°C for 18 hrs), the LQs of CD-MPR were measured to be -0.04±0.05, 0.38±0.02 and 1.87±0.08, corresponding to the *cis*-Golgi (LQ=0.00±0.25), the medial-Golgi (LQ=0.50±0.25) and the TGN (LQ>1.25), respectively (mean±SEM, Figure 37C). The 37°C incubation for 18 hrs was used to mimic the TGN localization of CD-MPR at the steady state. Its LQ and averaged side view suggested its localization at the TGN (Figure 37A, third row; Figure 37C).

The localization of CD-MPR in the 15°C incubation is predicted to be at the ERGIC (LQ<-0.25). Although its LQ corresponds to the *cis*-Golgi, it is similar to that of an ERGIC marker, ERGIC53 (LQ=-0.16; Table 6). Notably, the averaged side view of CD-MPR at 15°C showed a slight shift toward the preceding region of GM130 (Figure 37A, first row), which may correspond to the closely adjacent ERGIC.

The LQ of CD-MPR at 20°C was consistent with the findings of our previous study of VSVG-tso45-GFP (Tie et al., 2016a). Both experiments indicated that 20°C could accumulate cargos in the medial-Golgi, but not the TGN (Figure 37C). Moreover, the averaged side view of CD-MPR at 20°C incubation showed that it localized between

GM130 and GalT-mCherry (Figure 37A, middle row), supporting its localization at the medial-Golgi but not the TGN.

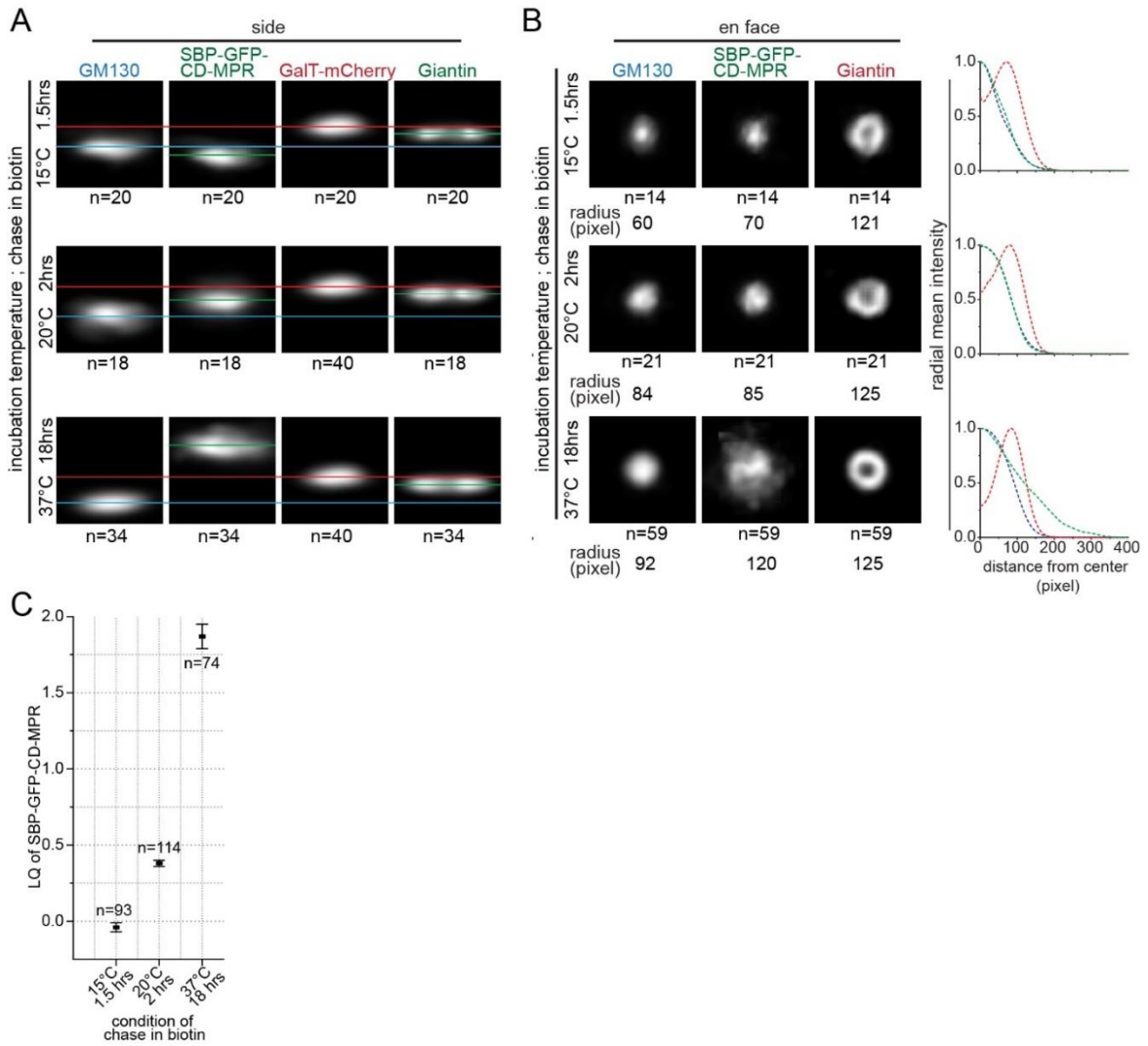

Figure 37: 15°C and 20°C block CD-MPR at the ERGIC/*cis*-Golgi and medial-Golgi, respectively.

HeLa cells singly transfected with SBP-GFP-CD-MPR or co-transfected with SBP-GFP-CD-MPR and GalT-mCherry were treated with nocodazole and chased in the presence of biotin and cycloheximide at indicated temperatures and times. The averaged (A) en face and (B) side views of Golgi resident proteins and secretory cargos are shown. (A) 15°C and 20°C block CD-MPR at the ERGIC/*cis*- and medial-Golgi, respectively. The averaged side view of GalT-mCherry was obtained from Figure 24J. Ycenter^{mass}s of GM130 (blue), GalT-mCherry (red), SBP-GFP-CD-MPR and Giantin (green) are indicated by color-coded lines. Ycenter^{mass}s of proteins were translated as described in Figure 36. (B) The radius of GM130 decrease at 15°C. Radial mean intensity profiles were plotted and color-coded according to colours assigned to different proteins. The radius of averaged en face view images is indicated. (A-B) n, number of averaged Golgi mini-stacks. (C) The LQ vs time plot for SBP-GFP-CD-MPR indicates its axial localization corresponding to (A-B) at indicated conditions. n, number of analysed Golgi mini-stacks. Error bars, SEMs.

Notably, the radius of the GM130 disk, measured by the radial mean intensity profile, was smaller at 15°C than at 37°C (Figure 37B). Unravelling the potential effect of temperatures on the lateral size of Golgi cisternae would require a systematic study.

6.7 The *trans*-Golgi can function as the Golgi exit site

The TGN is commonly regarded as the cargo sorting and exit site of the Golgi (Griffiths and Simons, 1986). However, alternative Golgi exit sites have been suggested in the literature (see Section 1.3.4). Using GLIM, the LQs of various RUSH reporters were measured during their intra-Golgi trafficking. Assuming that a cargo would accumulate at its exit site for a prolonged time, the plateau of the LQ vs. time plot should represent the cargo exit site in the Golgi. Our group reported that RUSH reporters, including E-cadherin, CD59 and TNFα, left the Golgi at the *trans*-Golgi. In contrast, the CD8a chimera CD8a-Furin, which contains the cytosolic tail of Furin, exited the Golgi at the TGN (Tie et al., 2016a). Therefore, we proposed that, like the TGN, the *trans*-Golgi could function as a Golgi exit site. In order to further probe our hypothesis, additional RUSH reporters were analysed.

In non-polarized HeLa cells, it was found that different RUSH reporters plateaued at different Golgi subcompartments. Soluble collagenX (plateau=0.99); mCherry-GPI (plateau=0.86), VSVG (plateau=1.17) and TfR (plateau=1.15) plateaued at the *trans*-Golgi; while Lamp1 (plateau=1.56), CD-MPR (plateau=1.53) and Vamp4 (plateau=1.46) plateaued at the TGN (Figure 38H). Combine with our previous findings (Tie et al., 2016a), these data suggest that constitutive secretory cargos, such as collagenX, CD59, mCherry-GPI, E-cadherin, VSVG, TNFα and TfR, exit the Golgi at the *trans*-region, whereas the TGN or endolysosome-targeted proteins, such as CD8a-Furin, Lamp1, CD-MPR and Vamp4, exit the Golgi at the TGN (Figure 38).

Collectively, our data suggest that both the *trans*-Golgi and the TGN could function as Golgi exit sites. We propose that cargos with TGN targeting signal(s) can exit at the TGN. Otherwise, cargos exit at the *trans*-Golgi by default. The validity of this hypothesis is further investigated in the next section.

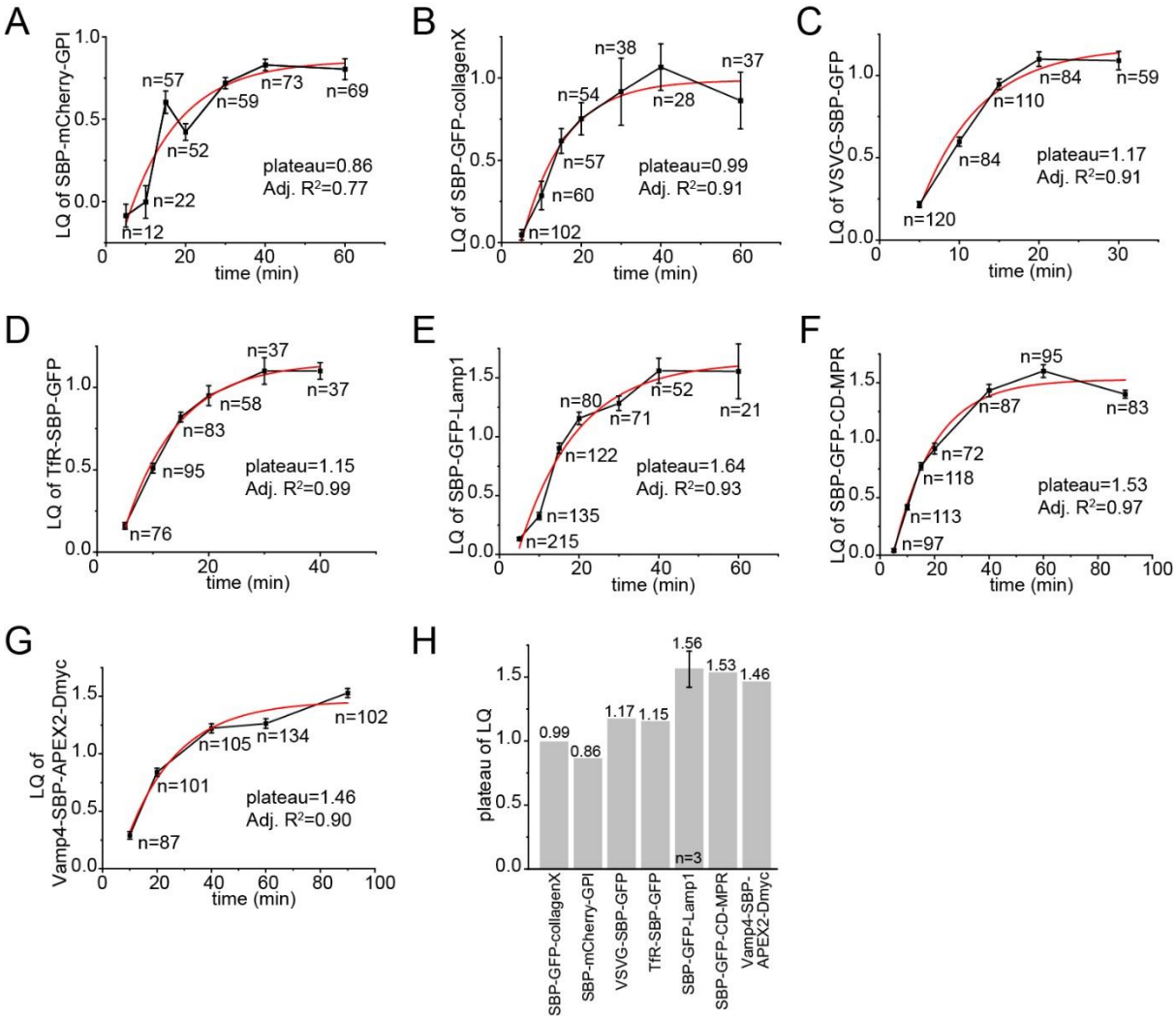

Figure 38: The Golgi exit sites of various RUSH secretory cargos.
(A-G) LQ vs time plots of various RUSH secretory cargos indicate that they could exit the Golgi at either the *trans*-Golgi or the TGN. Experiments were performed as described in Figure 32(D-F, J-L, O-P). The adjusted R^2 (Adj. R^2) and plateau of fitted curve are indicated in each plot. Error bars, SEMs. N, number of analysed Golgi mini-stacks. Note that A-B, D-E and F were shown in Figure 32-33. (H) The comparison of plateaus of secretory cargos. The LQ of the plateau is indicated on top of each bar. For Lamp1, the mean of LQs of 3 independent experiments was shown. Error bar, SD.

6.8 Secretory cargos access and exit at the TGN in a signal-dependent manner

Previously, CD8a-Furin was reported to exit the Golgi at the TGN (Tie et al., 2016a). However, after the tyrosine motif and acidic clusters in the Furin cytosolic tail were mutated, the mutant CD8a-Furin(Y+AC) changed its exit site to the *trans*-Golgi (Tie et al., 2016a). This suggested that either the tyrosine motif or the acidic clusters is sufficient for Furin to access and exit at the TGN. In this section, a few pairs of reporters, including VSVG-tso45 vs. VSVG-tso45-Furin, Lamp1 vs. Lamp1^{Y404A} and CD-MPR vs. CDMPR$^{LL/AA}$ (Figure 31,39), were investigated for the potential role of their cytosolic signal(s) in determining their Golgi exit sites.

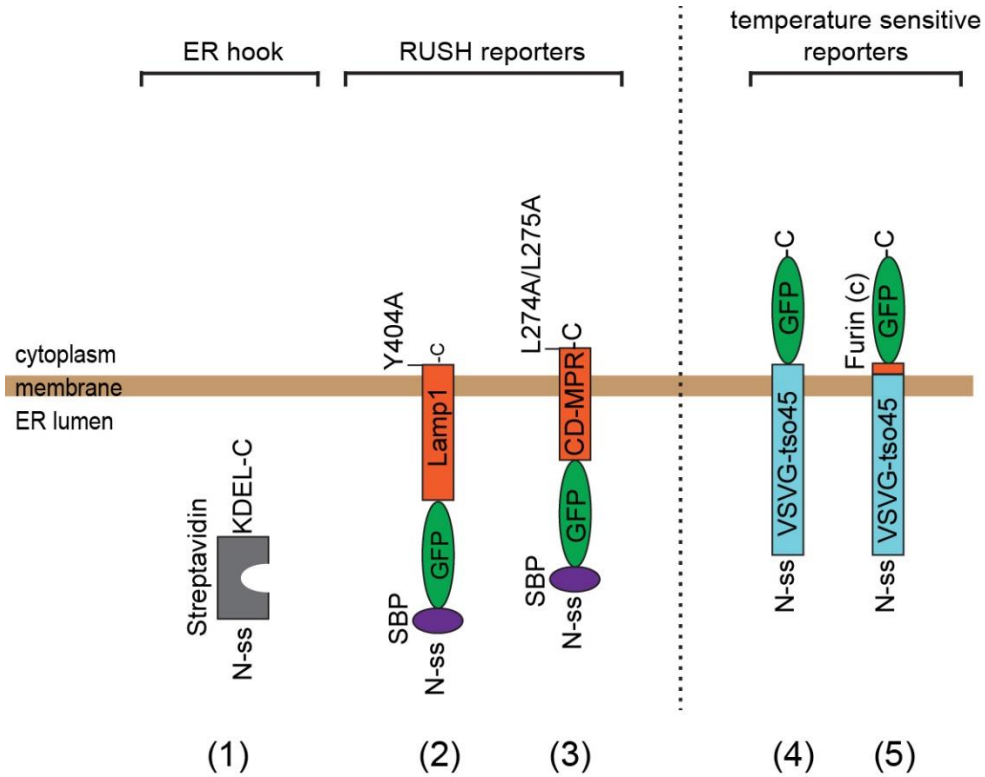

Figure 39: ER hook, Lamp1^{Y404A}, CD-MPR$^{LL/AA}$, VSVG-tso45 and VSVG-tso45-Furin.

The schematic diagram shows ER hooks and secretory reporters that are used in Figure 40-41: 1) Strep-KDEL (soluble hook), 2) ss-SBP-GFP-Lamp1^{Y404A}, 3) ss-SBP-GFP-CD-MPR$^{LL/AA}$, 4) VSVG-tso45-GFP, 5) VSVG-tso45-Furin-GFP. ss-SBP-GFP-Lamp1^{Y404A} contains Y404A mutation. ss-SBP-GFP-CD-MPR$^{LL/AA}$ contains LL274-275AA mutations. VSVG-tso45-Furin, the cytosolic tail of VSVG-tso45 is substituted by that of Furin. KDEL, an ER-retention signal; ss, signal sequence; SBP, streptavidin-binding peptide.

6.8.1 The cytosolic tail of Furin enables VSVG-tso45 to access and exit at the TGN

Previously, VSVG-tso45-GFP was observed to plateau at the *trans*-Golgi (plateau=0.86; Figure 40A) (Tie et al., 2016a, Figure 6D). In contrast, VSVG-tso45-Furin-GFP, in which the cytosolic domain of VSVG-tso45 was substituted by that of Furin, plateaued at the TGN (plateau=1.59; Figure 40B). These results were consistent with our previous findings on CD8a-Furin and CD8a-Furin(Y+AC) (Tie et al., 2016a). Collectively, the results suggest that either the tyrosine motif or the acidic clusters is sufficient for Furin to access and exit at the TGN.

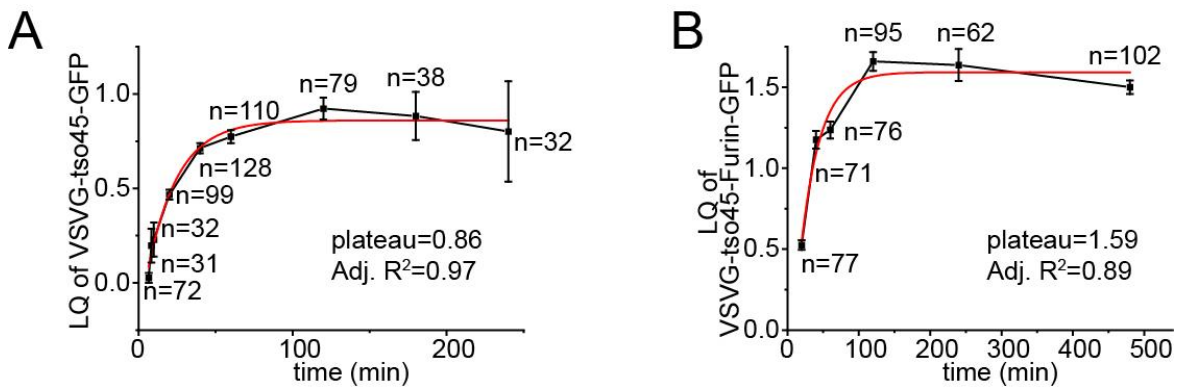

Figure 40: The cytosolic tail of Furin enables VSVG-tso45 to exit the Golgi at the TGN.
(A-B) VSVG-tso45 and VSVG-tso45-Furin exit the Golgi at the *trans*-Golgi and TGN, respectively. HeLa cells transiently expressing GalT-mCherry and either one of the temperature sensitive reporters were incubated at 40°C. Cells were then incubated at 32°C for different times in the presence of cycloheximide. Cells were fixed and immuno-stained by the GM130 antibody. They were imaged by a wide-field fluorescence microscope and GLIM was performed to obtain the axial localization of reporters. The adjusted R^2 (Adj. R^2) and plateau of fitted curve are indicated in each plot. Error bars, SEMs. n, number of analysed Golgi mini-stacks. Note that (A) is from our previous report (Tie et al., 2016a, Figure6D).

6.8.2 The tyrosine motif in the cytosolic tail of Lamp1 determines its Golgi exit site

In order to assess whether the cytosolic signal(s) in other cargos plays a similar role to that suggested by the data for Furin, two TGN-exiting RUSH reporters, Lamp1 and CD-MPR, were investigated.

In the cytosolic tail of Lamp1, the only known sorting signal, a tyrosine motif, was mutated from Y^{404}QTI to A^{404}QTI. Subsequently, the LQs of the mutant during the biotin chase were measured. The LQ vs. time plot indicated that the mutant plateaued at the *trans*-Golgi (plateau=1.17), which is different from the plateau of the wild-type protein (plateau=1.65, corresponding to the TGN; Figure 41A-B). This result suggests that the tyrosine motif of Lamp1 could function as the TGN-targeting signal and determine the Golgi exit site of Lamp1.

CD-MPR possesses two cytosolic signals, a tyrosine-based and a dileucine-based motif (Bonifacino and Traub, 2003). The dileucine-based motif can interact with GGAs, a class of clathrin-associated monomeric adaptors (Puertollano et al., 2001a). The dileucine motif mutant, CD-$MPR^{LL/AA}$ (Chen et al., 2017), was investigated to determine the role of its cytosolic signals in the location of Golgi exit. Both CD-MPR (plateau=1.53) and CD-$MPR^{LL/AA}$ (plateau=1.46) were found to plateau at the TGN (Figure 41C-D), suggesting that the tyrosine motif might be sufficient for TGN targeting. Notably, the CD-$MPR^{LL/AA}$ was prohibited from exiting the Golgi (Chen et al., 2017). It would be interesting to look into the Golgi exit site of tyrosine-motif and dual-motif mutants of CD-MPR in the future.

Collectively, our results suggest that the *trans*-Golgi and the TGN can both function as Golgi exit sites. The necessity and the nature of cytosolic signal(s) on secretory cargos could determine their Golgi exit sites.

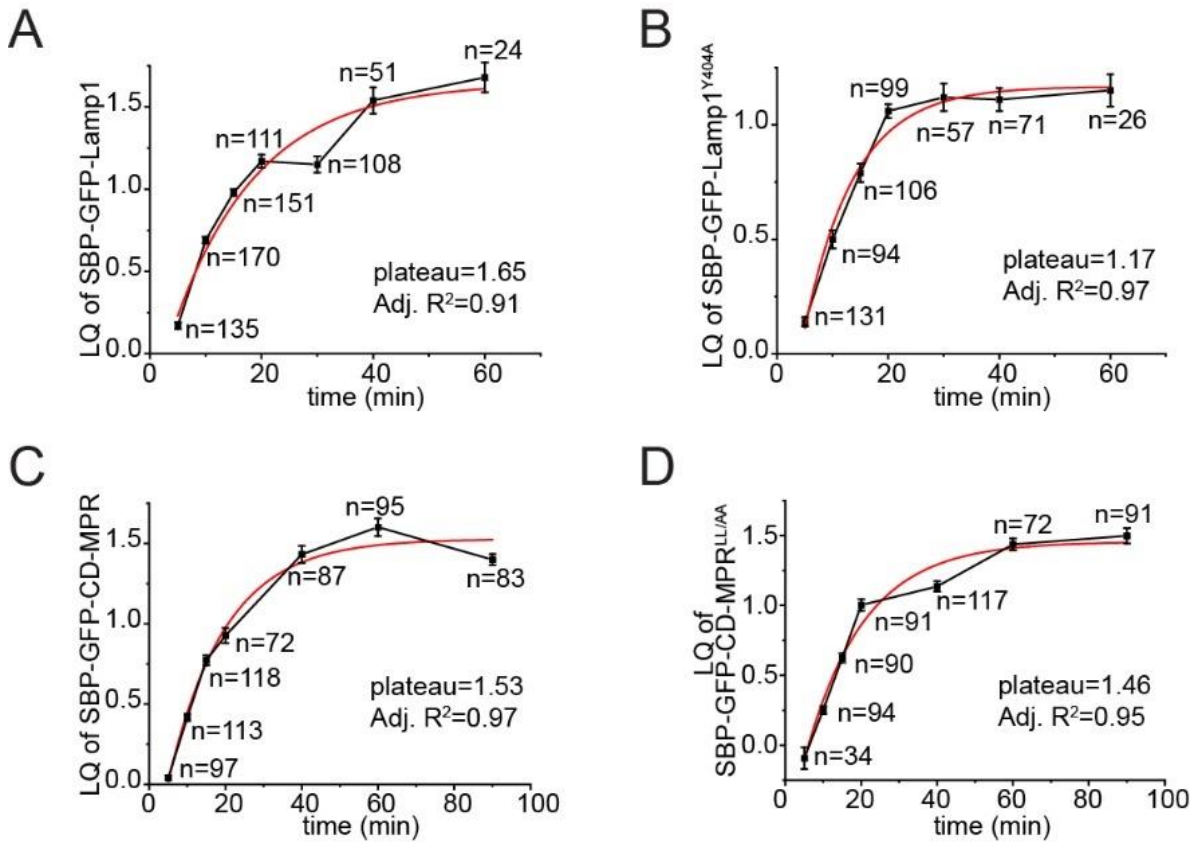

Figure 41: The tyrosine motif of Lamp1 determines its access and exit at the TGN, whereas the dileucine motif of CD-MPR does not affect its access to the TGN.

(A-B) Lamp1 and Lamp1^{Y404A} exit the Golgi at the TGN and *trans*-Golgi, respectively. (C-D) Both CD-MPR and CD-MPR$^{LL/AA}$ can access the TGN. (A-D) Experiments were performed as described in Figure 32(D-F, J-L, O-P). The adjusted R^2 (Adj. R^2) and plateau of fitted curve are indicated in each plot. n, number of analysed Golgi mini-stacks. Error bars, SEMs.

Chapter 7: Discussion

7.1 LQs, en face views and side views of Golgi proteins reveal the spatial and molecular organization of the Golgi mini-stack

The LM study of the localization of Golgi proteins has been challenging, mainly due to the complicated architecture of the Golgi and the resolution limit of LM.

By analysing the structurally simplified nocodazole-induced Golgi mini-stacks using our previously developed method, GLIM, we investigated the axial localization of Golgi proteins by mapping their LQs (Tie et al., 2016a). In principle, the LQs of all Golgi proteins can be accurately measured using GLIM, provided that the SNR of the fluorescence signals is high enough (Waters, 2009). A mini-stack is accepted for GLIM analysis only when the SNRs of the fluorescence signals in three channels are high enough. This is because the center^{mass} of a protein could be skewed if the SNR of the image is low, and the accuracy of GLIM relies heavily on the measurement of the center^{mass} of individual proteins. In GLIM, the center^{mass} is determined by the distribution/concentration of the protein in 2D space. Theoretically, the fluorescence intensity is proportional to the concentration of a fluorescently labelled protein. As long as the fluorescence signal of the protein does not saturate the detector (e.g. SCMOS camera), the center^{mass} can accurately reflect the distribution/concentration of the protein. This, in turn, results in accurate and reproducible LQs.

One must be cautious when investigating exogenous Golgi proteins, as they might introduce undesirable biological effects on the Golgi organization (Cosson et al., 2005). Ideally, endogenous Golgi proteins would be imaged, either by antibody staining or gene tagging. As an alternative good practice, cells with moderate or low expression of exogenous protein(s) were chosen for our imaging. By expanding the LQ database,

we hope to generate a comprehensive axial localization map of Golgi proteins, which could be a useful resource for Golgi research.

The lateral localization of Golgi proteins, on the other hand, can best be demonstrated from their en face and side views. Using cisternal rim-localized proteins, such as Golgin84, GCC185, Giantin and GPP130, a method was developed to discern the en face and side views of Golgi mini-stacks (Figure 7B). The ring and double-punctum staining patterns demonstrated by cisternal rim-localized proteins were validated to represent the en face and side views of Golgi mini-stacks, respectively. The method is applicable not only to nocodazole-induced Golgi mini-stacks, but also to the less-dense region of a native Golgi (Figure 27). The method was further developed by averaging the en face and side views of Golgi proteins (Figure 13-14), which aims to enhance common features and suppress random ones.

A limitation of GLIM is that it cannot visually reveal the cisternal distribution of Golgi proteins. The lateral localization study has successfully uncovered such information. Thus, using GLIM and our newly established analytical methods to determine lateral localization, we provided imaging data for the molecular organization of the Golgi mini-stack.

Golgi enzymes that appear as either disks or inner-rings were found to mainly localize in the interior of medial- and *trans*-Golgi cisternae (Figure 23-25). This is consistent with a recent cryo-ET study on algal Golgi that revealed the zipper-like intra- and inter-cisternal protein arrays localized to the interior of medial- and *trans*-cisternae (Engel et al., 2015). The protein arrays were suggested to mainly comprise Golgi enzymes. These enzymes might be organized into an ‘enzyme matrix’, and we speculate that the ‘enzyme matrix’ could have three functional roles: 1) to stack cisternal membrane,

2) to create a favourable environment for the localization of Golgi enzymes or other proteins and 3) to exclude components of trafficking machinery to cisternal rims.

Indeed, components of trafficking machinery were found to localize at the rim of the medial- and *trans*-Golgi, the entire *cis*- and *trans*-Golgi and the TGN (Figure 16-21), thereby complementing the localization of Golgi enzymes (Figure 23-24,30). The Golgi was proposed to contain many processing and export subdomains that distribute throughout the Golgi stack (Patterson et al., 2008). This study has provided the imaging evidence to demonstrate the spatial separation of processing and transport domains to the interior and rim of the Golgi stack, respectively (Figure 30).

GLIM and the lateral localization study were together exploited to generate two quantitative maps of the molecular organization of the Golgi mini-stack (Figure 28-29). The stacked region of the Golgi is spindle-shaped, with medial-cisternae having the largest diameter. The diameter of cisternae is smaller toward the *cis*- and *trans*-poles (Figure 28-29). This description is supported by our measurement of the lateral size of GM130 and Giantin (Figure 14D). Consistently, during the transition from the *cis*- to *trans*-cisternae, the averaged en face views of RUSH reporters, including VSVG and TfR, demonstrated a similar trend in radius size (Figure 36). Of note, the smaller diameter of the *cis*-cisternae has been observed in multiple studies (Bykov et al., 2017; Donohoe et al., 2013; Engel et al., 2015; Henderson et al., 2007; Staehelin and Kang, 2008).

In the non-stacked region of the Golgi (i.e. the ERES, the ERGIC and the TGN), the lateral localization of proteins is generally expansive, and their radii could be >50% larger than that of Giantin, as exemplified by γ-Adaptin (normalized radius=1.69) and others (Figure 28-29, Table 8-9). This could be explained by the pleiomorphic nature

of the structure of non-stack regions. For instance, the TGN is portrayed as a region with anastomosed tubules originating from the rims of *trans*-cisternae (Ladinsky et al., 1994; Ladinsky et al., 1999). Tubular domains and budding carriers at the TGN could extend into a wide space and result in the relatively large radii and lateral sizes of TGN-localized proteins.

The TGN structure could vary significantly across cell types. A comparison of EM studies on the TGN from 14 different mammalian cell types reported extensive and multi-layered TGNs in cell types that do not possess large secretory granules (Clermont et al., 1995). In our study, the multi-tier organization of the TGN was observed in HeLa cells. Each tier seemed to be characterized by a different molecular composition, as suggested by the averaged side view images of different TGN proteins (Figure 22D). To our knowledge, such TGN organization has never been reported using LM imaging. In addition, two distinct localization patterns were observed in the TGN: compact lumps and scattered puncta (Figure 20-21, 22A-B). Although the membrane architecture corresponds to the compact lump or the tier-like organization remains unclear, the non-layered zone might be occupied mainly by dissociative transport carriers, as suggested by the localization of proteins associated with CCVs (e.g. GGA2, CI-MPR, GGA1, γ-Adaptin and CLCB), which are either clathrin adaptors or clathrin-dependent cargos.

7.2 Size-dependent lateral partitioning of molecules in the Golgi mini-stack

Almost one-third of the eukaryotic proteome traverses the secretory pathway. Most of these proteins can undergo post-translational modifications, such as glycosylation, in the Golgi (Ghaemmaghami et al., 2003). Since our results revealed the preferential localization of components of trafficking machinery and Golgi enzymes to the rim and

interior of the Golgi mini-stack, respectively, secretory proteins are expected to localize to the cisternal interior in order to access Golgi enzymes for modification during intra-Golgi trafficking. Indeed, synchronous RUSH reporters, including GFP, CD59, mCherry-GPI, VSVG, E-cadherin, CD8a-Furin, Lamp1, TfR and CD-MPR, were observed to reside at the cisternal interior. Budding profiles can be observed from these reporters at later time points, and these could represent the post-Golgi exocytic transport carriers (Figure 32). Notably, these reporters were not obviously concentrated at cisternal rims where components of transport machinery localize. This could be due to the relatively short residence time of secretory cargos at the rim, where they can quickly transit to subsequent cisternae or be retrieved to the interior, possibly to ensure complete modifications. Hence, as a result of the net movement between transition and retrieval, they mainly localize to the cisternal interior kinetically. The retrieval of molecules into the cisternal interior could occur by default and might be independent of modifications, as GFP, which is not post-translationally modified, was also found predominantly in the cisternal interior (Figure 32N).

In contrast, several cargos that form protein aggregates, including collagenX, FM4-CD8a and FM4-moxGFP, were clearly partitioned to the cisternal rim during their intra-Golgi trafficking. This could be due to the incompatibility of these cargos within the interior environment of cisternae, which is occupied by the ‘enzyme matrix’. For example, bulky cargos might not be well accommodated in the tightly-packed cisternal interior environment, in which the intracisternal and intercisternal spaces were reported to be around 10–20 nm (Engel et al., 2015; Klumperman, 2011). The phenomenon of rim-partitioning of bulky cargos in the Golgi was also noted in several EM studies (Bonfanti et al., 1998; Engel et al., 2015; Lavieu et al., 2013; Volchuk et al., 2000).

Collectively, the lateral localization study of secretory cargos demonstrates that small cargos (<115 kDa) and large protein aggregates, including collagenX (~20,000 kDa), GFP-FM4-CD8a (~81,000 kDa) and FM4-moxGFP (~50,000 kDa), preferentially localize to the cisternal interior and rim, respectively. Hence, our imaging data from various cargos provide LM evidence to support the size-dependent lateral partitioning of secretory cargos in Golgi cisternae.

Of note, the rim-partitioning based on the size of molecules could indirectly account for the preferential interior localization of most Golgi enzymes. In general, Golgi enzymes are type II transmembrane proteins that share the common feature of having a short N-terminus cytosolic tail (Lairson et al., 2008). Therefore, they are compatible with cisternal interiors, which have tightly packed intercisternal spaces of ~10 nm (Engel et al., 2015). In contrast, Golgins, such as Giantin, Golgin84 and GCC185, that have long (yet flexible) coiled-coil cytosolic domains, are mainly found at the cisternal rim. This may be due to the incompatibility of their extended coiled-coil domains with the small intercisternal space. In line with this hypothesis, the mScarlet-Giantin-C129, which contains only 129 aa of the Giantin C-terminus, demonstrated substantial interior localization (Figure 9C). Hence, these observations further support a size-dependent lateral partitioning mechanism.

7.3 Secretory cargos could exit the Golgi at the *trans*-Golgi by default, whereas the access to and exit at the TGN might be signal-dependent

Although the TGN is regarded as the hub for cargo sorting and exit (Griffiths and Simons, 1986), the notion that the *trans*-Golgi functions as the alternative Golgi exit site was documented previously (Chen et al., 2017; Ladinsky et al., 1999; Ladinsky et al., 2002; Mogelsvang et al., 2004; Storrie et al., 2012; Tie et al., 2016a). In this study, the Golgi exit site of various secretory cargos was examined by measuring their LQs

during intra-Golgi trafficking. Most of them, including mCherry-GPI, collagenX, VSVG, TfR and the previously reported E-cadherin and CD59, were found to leave the Golgi at the *trans*-Golgi. As the boundary between the *trans*-Golgi and TGN is not definitive, one could alternatively interpret the exit site of these cargos as the TGN, but in a region proximal to the *trans*-cisternae. Nonetheless, in contrast, Lamp1, CD-MPR, Vamp4 and the previously reported CD8a-Furin could access and exit at the TGN (Tie et al., 2016a) (Figure 38).

What decides a cargo's exit site? It was noted that all of our tested TGN-exit cargos, but not the *trans*-Golgi-exit cargos, possess cytosolic signals that could potentially interact with TGN-localized adaptor proteins. Hence, we hypothesize that a cargo that possesses a sorting signal(s) that interacts with TGN-localized adaptor protein(s) can access and exit at the TGN, whereas a cargo without such a signal exits at the *trans*-Golgi by default.

Of note, in polarized epithelial cells, E-cadherin, VSVG and TfR were reported to leave the Golgi in AP-1B-associated CCVs via direct or indirect interaction with the μ1B subunit (Fölsch et al., 1999; Fölsch et al., 2003; Gravotta et al., 2012; Ling et al., 2007). However, nonpolarized cells, such as HeLa cells, express only μ1A, not μ1B. Hence, these three molecules are unlikely to be sorted into CCVs in nonpolarized HeLa cells, which were used in our study, therefore leading to their exits at the *trans*-Golgi. Moreover, detailed EM studies of the Golgi export of VSVG demonstrated that non-coated pleiomorphic transport carriers might facilitate its Golgi exit (Polishchuk et al., 2003; Polishchuk et al., 2000). This suggests that the origin of VSVG-containing transport carriers might not be the TGN. In addition, a comparison between E-cadherin and VSVG using LM demonstrated that they shared similar transport carriers and kinetics in HeLa cells (Lock et al., 2005).

Collectively, these observations suggest that a secretory cargo lacking the signal that interacts with a TGN-localized clathrin adaptor can exit at the *trans*-Golgi by default. In support of this idea, GPI-anchored (e.g. mCherry-GPI and CD59) and soluble proteins (e.g. collagenX) were also observed to exit at the *trans*-Golgi (Figure 38B).

In contrast, proteins that exit at the TGN, such as CD-MPR, Furin, Lamp1 and Vamp4, are known to interact with clathrin-associated adaptors via their cytosolic signals. In brief, the YXXΦ and acidic clusters-DXXLL of CD-MPR interact with AP-1 and GGAs, respectively (Höning et al., 1997; Puertollano et al., 2001a); the YXXΦ and acidic clusters of Furin interact with AP-1 and Mint3, respectively (Han et al., 2008; Teuchert et al., 1999); the YXXΦ of Lamp1 interacts with AP-1 (Höning et al., 1996); and the [DE]XXX[LI] and acidic clusters of Vamp4 interact with AP-1 (Hinners et al., 2003; Peden et al., 2001).

Additionally, the three following experimental observations from our laboratory support our hypothesis that a sorting signal is required for the TGN exit. First, the cytosolic tail of Furin is sufficient for VSVG-tso45 to exit the Golgi at the TGN (Figure 40). Second, the tyrosine motif mutant of Lamp1, Lamp1^{Y404A}, exits the Golgi at the *trans*-Golgi (Figure 41A-B). Third, we reported previously that the tyrosine motif and acidic clusters mutant of CD8a-Furin, CD8a-Furin(Y+AC), exits the Golgi at the *trans*-Golgi (Tie et al., 2016a).

Cytosolic signals play crucial roles in anterograde and retrograde trafficking pathways (Bonifacino and Traub, 2003; De Matteis and Luini, 2008; Guo et al., 2014; Mancias and Goldberg, 2005). For instance, the internalization of Furin at the PM is mediated by its cytosolic tyrosine motif and AP2-associated CCVs (Teuchert et al., 1999), the interaction between phosphofurin acidic cluster sorting protein 1 (PACS1) and the

cytosolic acidic clusters of Furin mediates the latter's recycling from endosomes to the Golgi (Crump et al., 2001) and the cytosolic tyrosine motif of Lamp1 can mediate its lysosomal targeting either directly or indirectly via the PM (Höning and Hunziker, 1995; Janvier and Bonifacino, 2005). However, the role of cytosolic sorting signals in determining a cargo's Golgi exit site is not well established. In this study, we proposed and demonstrated that the cytosolic signal is required to guide a secretory cargo to access and exit at the TGN. In contrast, cargos that do not possess a TGN-targeting cytosolic signal exit at the *trans*-Golgi by default.

Notably, in this study, all membrane cargos that exit at the *trans*-Golgi are targeted to the PM. In contrast, cargos that exit at the TGN are predominantly targeted to subcellular compartments, such as lysosomes and endosomes. Hence, our findings suggest that cargos destined for the PM and endolysosomes might predominantly exit at the *trans*-Golgi and TGN, respectively.

7.4 Secretory cargos can traverse the Golgi stack in synchronous cargo waves

The mechanism by which secretory cargos traverse Golgi cisternae is still under debate, although the cisternal maturation model is generally most well-received among the current models (Glick and Luini, 2011). By using GLIM to quantitatively localize synchronous RUSH reporters, I successfully measured the progressive movements of various secretory cargos from the *cis*- to *trans*-face of the Golgi in the current and previous studies (Tie et al., 2016a). However, the cisternal distributions of cargos remain unclear because GLIM does not provide visual evidence. For instance, if the LQ of a transiting cargo is 0.5, its cisternal distribution could indicate either of the following scenarios: the cargos are concentrated in the medial-Golgi or they are homogenously distributed throughout the entire Golgi stack. This puzzle has been

solved using observations from the averaged side view images of two RUSH reporters, VSVG and TfR. During intra-Golgi trafficking, these synchronous cargos clearly demonstrated single-peak transiting cargo waves (Figure 36).

However, such observations might be insufficient to distinguish between the three prevalent intra-Golgi trafficking models (see Section 1.4). Although we observed neither COPI-like vesicular profiles nor intercisternal continuities, our findings don't rule out the stable compartment and intercisternal continuities trafficking models for several reasons. First, vesicular profiles, such as COPI vesicles, might not be detectable under our sample preparation conditions. Small vesicles might not be well preserved in the cytoplasm once cells are permeabilized, which is necessary for IF protocols. Second, even if cargos are concentrated in COPI vesicles, these signals might be too weak to be detected. Third, given the resolution limit of Airyscan microscopy (140 nm in the x-y plane), we cannot resolve COPI vesicles and intercisternal continuities, which were estimated to be in the range of 50 nm and 20–80 nm in diameter, respectively (Beznoussenko et al., 2014; Bykov et al., 2017; Marsh et al., 2004; Trucco et al., 2004). Fourth, the intra-Golgi trafficking via intercisternal continuities might occur for only certain groups of secretory cargos. For example, it has been reported that albumin, but not VSVG and procollagen I, was found in intercisternal tubules under EM (Beznoussenko et al., 2014). Therefore, it is possible that only small and soluble cargos can access these tubules to traverse the Golgi.

Nonetheless, the observation of cargo waves under physiological temperature is direct evidence against the rapid partitioning trafficking model (Patterson et al., 2008), which predicts that the Golgi behaves like a single mixed compartment in which any new arrivals can mix within the compartment stochastically. According to this model, cargos are predicted to equilibrate in the Golgi within a short time of arrival and not

demonstrate synchronous compact cargo waves. Therefore, our observations from the averaged side views of VSVG and TfR do not support this model.

In fact, the observation of the spatial separation of processing and transport domains into the cisternal interior and rim, respectively, agrees with the rim progression model (to a certain extent) (Lavieu et al., 2013). This model predicts that a Golgi cisterna consists of two domains, an immobile central domain and mobile rim domain. Secretory cargos are assumed to access the mobile rim domain to traverse the Golgi, while the central domain remains stationary. This model satisfactorily accounts for our observation of the rim partitioning of bulky cargos, including collagenX and FM4-chimeras, but fails to account for the lack of concentration of most conventional or small cargos at cisternal rims.

Altogether, the Golgi might adopt multiple mechanisms to facilitate efficient intra-Golgi trafficking of various secretory cargos. Our current results only resolve the lateral localization of cargos (i.e. cisternal rim and interior) during intra-Golgi trafficking. It might be important to investigate Golgi enzymes' localization pattern in the presence of synchronous cargo waves in order to distinguish different intra-Golgi trafficking models. Although we did not observe any significant change in the lateral distribution of ST6Gal1 in the presence of VSVG cargo waves (Figure 35), a more detailed and systematic effort would be needed to resolve the question in the future.

Nonetheless, the successful observation of cargo waves prompted us to re-examine some biological events pertaining to Golgi trafficking. For example, it is widely accepted that 15°C and 20°C incubations arrest proteins at the ERGIC and the TGN, respectively (Griffiths et al., 1985; Matlin and Simons, 1983; Saraste and Kuismanen, 1984). However, using GLIM, CD-MPR was found to be accumulated in the

ERGIC/*cis*-Golgi and the medial-Golgi at 15°C and 20°C incubations, respectively. Similar observations were also obtained for VSVG-tso45 in our previous study (Tie et al., 2016a). Importantly, by inspecting the averaged side view of synchronous CD-MPR, we directly visualized its localization at the medial-Golgi, but not the TGN, at 20°C (Figure 37).

Although studies in the early 1980s reported that 20°C incubation arrested secretory cargos at *trans*-cisternae (Griffiths et al., 1985; Saraste and Kuismanen, 1984), these results might be ambiguous. For example, Griffith et al. reported that VSVG was commonly observed not only at the *trans*-most cisterna, but also at several preceding cisternae under 20°C incubation in their EM study (Griffiths et al., 1985). Given the limitations of conventional EM techniques and the potential under-sampling of EM thin sections, the effect of 20°C incubation on Golgi trafficking might need to be re-examined using cutting-edge techniques, such as cryo-FIB and cryo-ET.

Chapter 8: Conclusions and future perspectives

The main findings from this study are as follows:

1. Based on the Airyscan imaging of Golgi rim markers, including Golgin84, Giantin, GCC185 and GPP130, a method was developed to discern Golgi mini-stack orientations (i.e. en face and side views).
2. The averaged en face and side view images of Golgi proteins were exploited to study their lateral localizations. Combining the results obtained using GLIM and from the lateral localization study, a quantitative map of the molecular organization of the Golgi mini-stack was generated.
3. The TGN could adopt a multi-tier architecture axially and two molecular localization patterns laterally (i.e. compact lump and scattered puncta).
4. The processing and transport domains, which are mainly occupied by Golgi enzymes and components of trafficking machinery, respectively, are spatially separated into the cisternal interior and rim, respectively.
5. Bulky and small secretory cargos preferentially localize to the cisternal rim and interior, respectively, during their intra-Golgi trafficking.
6. Synchronous secretory cargos appear in cargo waves during their intra-Golgi trafficking.
7. Secretory cargos could exit the Golgi mini-stack at the *trans*-Golgi by default, whereas their access and exit at the TGN could be signal-dependent.

This study combined the previously developed method GLIM and the lateral localization study of Golgi proteins to construct the molecular organization of the Golgi mini-stack. Airyscan microscopy was chosen for the imaging of Golgi proteins because it is compatible with conventional fixation protocols and fluorophores. In practice, Airyscan microscopy can reach a resolution of 140 nm in the x-y plane (Huff, 2015). By coupling more advanced super-resolution microscopy with our methods of analysing en face and side views of Golgi proteins, it would be possible to resolve the molecular organization of the Golgi mini-stack in greater detail. A potential candidate is STED microscopy, which can reach a resolution of <50 nm in the x-y plane. In addition, it does not involve extensive post-acquisition image reconstruction, thereby reducing the potential introduction of computational artefacts into final images (Wegel et al., 2016).

Alternatively, diffraction-limited Golgi features could be resolved using expansion microscopy (ExM). The Golgi structure could be expanded isotropically using chemical processing procedures. Thereafter, the physically expanded Golgi could be resolved satisfactorily even by conventional wide-field fluorescence microscopy (Wassie et al., 2019). It was reported that with ExM, the achievable resolution could reach ~25-70 nm (Chang et al., 2017; Truckenbrodt et al., 2018), depending on the expansion factor, which ranges from 4.5- to 10-fold. Ideally, the molecular organization of the Golgi could be deciphered to an unprecedented detail by combining ExM and a super-resolution LM technique, such as STED.

In addition, it would be interesting to investigate the Golgi exit of various secretory cargos in polarized epithelial cells. The Golgi exit could be more complicated in these cells because additional sorting and transport machinery are expected to sort proteins destined for apical or basolateral domains, in addition to endo-lysosomes. We propose that our methods, which include GLIM and the lateral localization analysis of resident proteins and secretory cargos, could be useful in deciphering potential Golgi exit domains or subcompartments and their spatial relationships. Moreover, important signals that guide secretory cargos to their corresponding exit sites could be identified.

Lastly, it is known that virus strains, including the coronavirus strains, assemble in the ERGIC and then traverse the Golgi to be secreted from infected cells (Klumperman et al., 1994; Siu et al., 2008; Stertz et al., 2007). Our observation that bulky cargos transit the Golgi mini-stack through cisternal rims might suggest that some large viral strains could traverse the Golgi in a similar manner. Hence, we hope to visualize and investigate the intra-Golgi trafficking routes of viral particles by examining their lateral localization. Such fundamental research could serve as the basis for the development of measures to constrain viral export from infected cells at the Golgi.

Bibliography

Ang, A.L., T. Taguchi, S. Francis, H. Fölsch, L.J. Murrells, M. Pypaert, G. Warren, and I. Mellman. 2004. Recycling endosomes can serve as intermediates during transport from the Golgi to the plasma membrane of MDCK cells. *The Journal of cell biology*. 167:531-543.

Baeuerle, P.A., and W.B. Huttner. 1987. Tyrosine sulfation is a trans-Golgi-specific protein modification. *The Journal of cell biology*. 105:2655-2664.

Bai, X., D. Zhou, J.R. Brown, B.E. Crawford, T. Hennet, and J.D. Esko. 2001. Biosynthesis of the linkage region of Glycosaminoglycans cloning and activity of galactosyltransferase ii, the sixth member of the β1, 3-galactosyltransferase family (β3GalT6). *Journal of Biological Chemistry*. 276:48189-48195.

Banfield, D.K. 2011. Mechanisms of protein retention in the Golgi. *Cold Spring Harbor perspectives in biology*. 3:a005264.

Bannykh, S.I., T. Rowe, and W.E. Balch. 1996. The organization of endoplasmic reticulum export complexes. *The Journal of cell biology*. 135:19-35.

Barlowe, C., and A. Helenius. 2016. Cargo capture and bulk flow in the early secretory pathway. *Annual review of cell and developmental biology*. 32:197-222.

Barr, F.A., M. Puype, J. Vandekerckhove, and G. Warren. 1997. GRASP65, a protein involved in the stacking of Golgi cisternae. *Cell*. 91:253-262.

Bascom, R.A., S. Srinivasan, and R.L. Nussbaum. 1999. Identification and characterization of golgin-84, a novel Golgi integral membrane protein with a cytoplasmic coiled-coil domain. *Journal of Biological Chemistry*. 274:2953-2962.

Beck, M., F. Förster, M. Ecke, J.M. Plitzko, F. Melchior, G. Gerisch, W. Baumeister, and O. Medalia. 2004. Nuclear pore complex structure and dynamics revealed by cryoelectron tomography. *Science*. 306:1387-1390.

Becker, B., B. Bölinger, and M. Melkonian. 1995. Anterograde transport of algal scales through the Golgi complex is not mediated by vesicles. *Trends in cell biology*. 5:305-307.

Ben-Tekaya, H., K. Miura, R. Pepperkok, and H.-P. Hauri. 2005. Live imaging of bidirectional traffic from the ERGIC. *Journal of cell science*. 118:357-367.

Beznoussenko, G.V., V.V. Dolgikh, E.V. Seliverstova, P.B. Semenov, Y.S. Tokarev, A. Trucco, M. Micaroni, D. Di Giandomenico, P. Auinger, and I.V. Senderskiy. 2007. Analogs of the Golgi complex in microsporidia: structure and avesicular mechanisms of function. *Journal of cell science*. 120:1288-1298.

Beznoussenko, G.V., S. Parashuraman, R. Rizzo, R. Polishchuk, O. Martella, D. Di Giandomenico, A. Fusella, A. Spaar, M. Sallese, and M.G. Capestrano. 2014. Transport of soluble proteins through the Golgi occurs by diffusion via continuities across cisternae. *Elife*. 3:e02009.

Bindels, D.S., L. Haarbosch, L. Van Weeren, M. Postma, K.E. Wiese, M. Mastop, S. Aumonier, G. Gotthard, A. Royant, and M.A. Hink. 2017. mScarlet: a bright monomeric red fluorescent protein for cellular imaging. *Nature methods*. 14:53.

Bock, J., J. Klumperman, S. Davanger, and R. Scheller. 1997. Syntaxin 6 functions in trans-Golgi network vesicle trafficking. *Molecular biology of the cell*. 8:1261-1271.

Boncompain, G., S. Divoux, N. Gareil, H. De Forges, A. Lescure, L. Latreche, V. Mercanti, F. Jollivet, G. Raposo, and F. Perez. 2012. Synchronization of secretory protein traffic in populations of cells. *Nature methods*. 9:493.

Boncompain, G., and F. Perez. 2013. Fluorescence-based analysis of trafficking in mammalian cells. *In* Methods in cell biology. Vol. 118. Elsevier. 179-194.

Bonfanti, L., A.A. Mironov, J.A. Martínez-Menárguez, O. Martella, A. Fusella, M. Baldassarre, R. Buccione, H.J. Geuze, and A. Luini. 1998. Procollagen traverses the Golgi stack without leaving the lumen of cisternae: evidence for cisternal maturation. *Cell*. 95:993-1003.

Bonifacino, J.S., and L.M. Traub. 2003. Signals for sorting of transmembrane proteins to endosomes and lysosomes. *Annual review of biochemistry*. 72:395-447.

Boos, W., and A.L. Stachelin. 1981. Ultrastructural localization of the maltose-binding protein within the cell envelope of Escherichia coli. *Archives of microbiology*. 129:240-246.

Borgese, N. 2016. Getting membrane proteins on and off the shuttle bus between the endoplasmic reticulum and the Golgi complex. *Journal of cell science*. 129:1537-1545.

Brockhausen, I., H. Schachter, and P. Stanley. 2009. O-GalNAc glycans. *In* Essentials of Glycobiology. 2nd edition. Cold Spring Harbor Laboratory Press.

Brown, D.L., K. Heimann, J. Lock, L. Kjer‐Nielsen, C. van Vliet, J.L. Stow, and P.A. Gleeson. 2001. The GRIP domain is a specific targeting sequence for a population of trans‐Golgi network derived tubulo‐vesicular carriers. *Traffic*. 2:336-344.

Brown, F.C., C.H. Schindelhaim, and S.R. Pfeffer. 2011. GCC185 plays independent roles in Golgi structure maintenance and AP-1–mediated vesicle tethering. *Journal of Cell Biology*. 194:779-787.

Brown, W. 1990. Cation-independent mannose 6-phosphate receptors are concentrated in trans Golgi elements in normal human and I-cell disease fibroblasts. *European journal of cell biology*. 51:201-210.

Bykov, Y.S., M. Schaffer, S.O. Dodonova, S. Albert, J.M. Plitzko, W. Baumeister, B.D. Engel, and J.A. Briggs. 2017. The structure of the COPI coat determined within the cell. *eLife*. 6.

Cantarel, B.L., P.M. Coutinho, C. Rancurel, T. Bernard, V. Lombard, and B. Henrissat. 2009. The Carbohydrate-Active EnZymes database (CAZy): an expert resource for glycogenomics. *Nucleic acids research*. 37:D233-D238.

Casler, J.C., E. Papanikou, J.J. Barrero, and B.S. Glick. 2019. Maturation-driven transport and AP-1–dependent recycling of a secretory cargo in the Golgi. *Journal of Cell Biology*. 218:1582-1601.

Chang, J.-B., F. Chen, Y.-G. Yoon, E.E. Jung, H. Babcock, J.S. Kang, S. Asano, H.-J. Suk, N. Pak, and P.W. Tillberg. 2017. Iterative expansion microscopy. *Nature methods*. 14:593-599.

Chen, Y., D.C. Gershlick, S.Y. Park, and J.S. Bonifacino. 2017. Segregation in the Golgi complex precedes export of endolysosomal proteins in distinct transport carriers. *Journal of Cell Biology*. 216:4141-4151.

Cheung, P.-y.P., C. Limouse, H. Mabuchi, and S.R. Pfeffer. 2015. Protein flexibility is required for vesicle tethering at the Golgi. *Elife*. 4:e12790.

Chun, J., Z. Shapovalova, S.Y. Dejgaard, J.F. Presley, and P. Melançon. 2008. Characterization of class I and II ADP-ribosylation factors (Arfs) in live cells: GDP-bound class II Arfs associate with the ER-Golgi intermediate compartment independently of GBF1. *Molecular biology of the cell*. 19:3488-3500.

Clermont, Y., A. Rambourg, and L. Hermo. 1995. Trans-Golgi network (TGN) of different cell types: Three-dimensional structural characteristics and variability. *The Anatomical Record*. 242:289-301.

Cole, N.B., N. Sciaky, A. Marotta, J. Song, and J. Lippincott-Schwartz. 1996. Golgi dispersal during microtubule disruption: regeneration of Golgi stacks at peripheral endoplasmic reticulum exit sites. *Molecular biology of the cell*. 7:631-650.

Cosson, P., M. Amherdt, J.E. Rothman, and L. Orci. 2002. A resident Golgi protein is excluded from peri-Golgi vesicles in NRK cells. *Proceedings of the National Academy of Sciences*. 99:12831-12834.

Cosson, P., M. Ravazzola, O. Varlamov, T.H. Söllner, M. Di Liberto, A. Volchuk, J.E. Rothman, and L. Orci. 2005. Dynamic transport of SNARE proteins in the Golgi apparatus. *Proceedings of the National Academy of Sciences*. 102:14647-14652.

Crevenna, A.H., B. Blank, A. Maiser, D. Emin, J. Prescher, G. Beck, C. Kienzle, K. Bartnik, B. Habermann, and M. Pakdel. 2016. Secretory cargo sorting by Ca2+-dependent Cab45 oligomerization at the trans-Golgi network. *Journal of Cell Biology*. 213:305-314.

Cronshaw, J.M., A.N. Krutchinsky, W. Zhang, B.T. Chait, and M.J. Matunis. 2002. Proteomic analysis of the mammalian nuclear pore complex. *The Journal of cell biology*. 158:915-927.

Crottet, P., D.M. Meyer, J. Rohrer, and M. Spiess. 2002. ARF1· GTP, tyrosine-based signals, and phosphatidylinositol 4, 5-bisphosphate constitute a minimal machinery

to recruit the AP-1 clathrin adaptor to membranes. *Molecular biology of the cell*. 13:3672-3682.

Crump, C.M., Y. Xiang, L. Thomas, F. Gu, C. Austin, S.A. Tooze, and G. Thomas. 2001. PACS-1 binding to adaptors is required for acidic cluster motif-mediated protein traffic. *The EMBO journal*. 20:2191-2201.

Dalton, A.J., and M.D. Felix. 1954. Cytologic and cytochemical characteristics of the Golgi substance of epithelial cells of the epididymis–in situ, in homogenates and after isolation. *American Journal of Anatomy*. 94:171-207.

De Matteis, M.A., and A. Luini. 2008. Exiting the Golgi complex. *Nature reviews Molecular cell biology*. 9:273-284.

Dell'Angelica, E.C., R. Puertollano, C. Mullins, R.C. Aguilar, J.D. Vargas, L.M. Hartnell, and J.S. Bonifacino. 2000. GGAsa family of ADP ribosylation factor-binding proteins related to adaptors and associated with the Golgi complex. *The Journal of cell biology*. 149:81-94.

Derby, M.C., C. van Vliet, D. Brown, M.R. Luke, L. Lu, W. Hong, J.L. Stow, and P.A. Gleeson. 2004. Mammalian GRIP domain proteins differ in their membrane binding properties and are recruited to distinct domains of the TGN. *Journal of cell science*. 117:5865-5874.

Diao, A., D. Rahman, D.J. Pappin, J. Lucocq, and M. Lowe. 2003. The coiled-coil membrane protein golgin-84 is a novel rab effector required for Golgi ribbon formation. *The Journal of cell biology*. 160:201-212.

Donohoe, B.S., B.H. Kang, M.J. Gerl, Z.R. Gergely, C.M. McMichael, S.Y. Bednarek, and L.A. Staehelin. 2013. Cis-Golgi cisternal assembly and biosynthetic activation occur sequentially in plants and algae. *Traffic*. 14:551-567.

Doray, B., P. Ghosh, J. Griffith, H.J. Geuze, and S. Kornfeld. 2002. Cooperation of GGAs and AP-1 in packaging MPRs at the trans-Golgi network. *Science*. 297:1700-1703.

Dunphy, W.G., R. Brands, and J.E. Rothman. 1985. Attachment of terminal N-acetylglucosamine to asparagine-linked oligosaccharides occurs in central cisternae of the Golgi stack. *Cell*. 40:463-472.

Dunphy, W.G., E. Fries, L.J. Urbani, and J.E. Rothman. 1981. Early and late functions associated with the Golgi apparatus reside in distinct compartments. *Proceedings of the National Academy of Sciences*. 78:7453-7457.

Dunphy, W.G., and J.E. Rothman. 1983. Compartmentation of asparagine-linked oligosaccharide processing in the Golgi apparatus. *The Journal of Cell Biology*. 97:270-275.

Dunphy, W.G., and J.E. Rothman. 1985. Compartmental organization of the Golgi stack. *Cell*. 42:13-21.

Eckert, E.S., I. Reckmann, A. Hellwig, S. Röhling, A. El-Battari, F.T. Wieland, and V. Popoff. 2014. Golgi phosphoprotein 3 triggers signal-mediated incorporation of glycosyltransferases into coatomer-coated (COPI) vesicles. *Journal of Biological Chemistry*. 289:31319-31329.

Engel, B.D., M. Schaffer, S. Albert, S. Asano, J.M. Plitzko, and W. Baumeister. 2015. In situ structural analysis of Golgi intracisternal protein arrays. *Proceedings of the National Academy of Sciences*. 112:11264-11269.

Ernst, A.M., S.A. Syed, O. Zaki, F. Bottanelli, H. Zheng, M. Hacke, Z. Xi, F. Rivera-Molina, M. Graham, and A.A. Rebane. 2018. S-Palmitoylation sorts membrane cargo for anterograde transport in the golgi. *Developmental cell*. 47:479-493. e477.

Farquhar, M., and H.-P. Hauri. 1997. Protein sorting and vesicular traffic in the Golgi apparatus. *In* The Golgi Apparatus. Springer. 63-129.

Farquhar, M.G., and J.F. Rinehart. 1954. Cytologic alterations in the anterior pituitary gland following thyroidectomy: an electron microscope study. *Endocrinology*. 55:857-876.

Fölsch, H., H. Ohno, J.S. Bonifacino, and I. Mellman. 1999. A novel clathrin adaptor complex mediates basolateral targeting in polarized epithelial cells. *Cell*. 99:189-198.

Fölsch, H., M. Pypaert, S. Maday, L. Pelletier, and I. Mellman. 2003. The AP-1A and AP-1B clathrin adaptor complexes define biochemically and functionally distinct membrane domains. *The Journal of cell biology*. 163:351-362.

Frantz, C., K.M. Stewart, and V.M. Weaver. 2010. The extracellular matrix at a glance. *Journal of cell science*. 123:4195-4200.

Freeze, H.H., and A.D. Elbein. 2009. Glycosylation precursors. *In* Essentials of Glycobiology. 2nd edition. Cold Spring Harbor Laboratory Press.

Fullekrug, J., P. Scheiffele, and K. Simons. 1999. VIP36 localisation to the early secretory pathway. *Journal of Cell Science*. 112:2813-2821.

Galbraith, C.G., and J.A. Galbraith. 2011. Super-resolution microscopy at a glance. *Journal of cell science*. 124:1607-1611.

Gannon, J., J.J. Bergeron, and T. Nilsson. 2011. Golgi and related vesicle proteomics: simplify to identify. *Cold Spring Harbor perspectives in biology*. 3:a005421.

Ghaemmaghami, S., W.-K. Huh, K. Bower, R.W. Howson, A. Belle, N. Dephoure, E.K. O'Shea, and J.S. Weissman. 2003. Global analysis of protein expression in yeast. *Nature*. 425:737-741.

Gilchrist, A., C.E. Au, J. Hiding, A.W. Bell, J. Fernandez-Rodriguez, S. Lesimple, H. Nagaya, L. Roy, S.J. Gosline, and M. Hallett. 2006. Quantitative proteomics analysis of the secretory pathway. *Cell*. 127:1265-1281.

Gilkey, J.C., and L.A. Staehelin. 1986. Advances in ultrarapid freezing for the preservation of cellular ultrastructure. *Journal of electron microscopy technique*. 3:177-210.

Gill, D.J., K.M. Tham, J. Chia, S.C. Wang, C. Steentoft, H. Clausen, E.A. Bard-Chapeau, and F.A. Bard. 2013. Initiation of GalNAc-type O-glycosylation in the endoplasmic reticulum promotes cancer cell invasiveness. *Proceedings of the National Academy of Sciences*. 110:E3152-E3161.

Gillingham, A.K., and S. Munro. 2007. The small G proteins of the Arf family and their regulators. *Annu. Rev. Cell Dev. Biol.* 23:579-611.

Gleeson, P.A., J.G. Lock, M.R. Luke, and J.L. Stow. 2004. Domains of the TGN: coats, tethers and G proteins. *Traffic*. 5:315-326.

Glick, B.S., and A. Luini. 2011. Models for Golgi traffic: a critical assessment. *Cold Spring Harbor perspectives in biology*. 3:a005215.

Goldberg, D.E., and S. Kornfeld. 1983. Evidence for extensive subcellular organization of asparagine-linked oligosaccharide processing and lysosomal enzyme phosphorylation. *Journal of Biological Chemistry*. 258:3159-3165.

Golgi, C. 1898. Sur la structure des cellules nerveuses (1). *Arch. ital. biol.* 30:60-71.

Gonzalez, A., and E. Rodriguez-Boulan. 2009. Clathrin and AP1B: key roles in basolateral trafficking through trans-endosomal routes. *FEBS letters*. 583:3784-3795.

Goud, B., A. Zahraoui, A. Tavitian, and J. Saraste. 1990. Small GTP-binding protein associated with Golgi cisternae. *Nature*. 345:553.

Gravotta, D., J.M. Carvajal-Gonzalez, R. Mattera, S. Deborde, J.R. Banfelder, J.S. Bonifacino, and E. Rodriguez-Boulan. 2012. The clathrin adaptor AP-1A mediates basolateral polarity. *Developmental cell*. 22:811-823.

Griffiths, G., M. Ericsson, J. Krijnse-Locker, T. Nilsson, B. Goud, H.-D. Söling, B.L. Tang, S.H. Wong, and W. Hong. 1994. Localization of the Lys, Asp, Glu, Leu tetrapeptide receptor to the Golgi complex and the intermediate compartment in mammalian cells. *The Journal of Cell Biology*. 127:1557-1574.

Griffiths, G., S. Pfeiffer, K. Simons, and K. Matlin. 1985. Exit of newly synthesized membrane proteins from the trans cisterna of the Golgi complex to the plasma membrane. *The Journal of cell biology*. 101:949-964.

Griffiths, G., and K. Simons. 1986. The trans Golgi network: sorting at the exit site of the Golgi complex. *Science*. 234:438-443.

Grigoriev, I., D. Splinter, N. Keijzer, P.S. Wulf, J. Demmers, T. Ohtsuka, M. Modesti, I.V. Maly, F. Grosveld, and C.C. Hoogenraad. 2007. Rab6 regulates transport and targeting of exocytotic carriers. *Developmental cell*. 13:305-314.

Guo, Y., D.W. Sirkis, and R. Schekman. 2014. Protein sorting at the trans-Golgi network. *Annual review of cell and developmental biology*. 30:169-206.

Halter, D., S. Neumann, S.M. van Dijk, J. Wolthoorn, A.M. De Maziere, O.V. Vieira, P. Mattjus, J. Klumperman, G. van Meer, and H. Sprong. 2007. Pre-and post-Golgi translocation of glucosylceramide in glycosphingolipid synthesis. *The Journal of cell biology*. 179:101-115.

Han, H.-M., C. Bouchet-Marquis, J. Huebinger, and M. Grabenbauer. 2013. Golgi apparatus analyzed by cryo-electron microscopy. *Histochemistry and cell biology*. 140:369-381.

Han, J., Y. Wang, S. Wang, and C. Chi. 2008. Interaction of Mint3 with Furin regulates the localization of Furin in the trans-Golgi network. *Journal of cell science*. 121:2217-2223.

Hara-Kuge, S., T. Ohkura, A. Seko, and K. Yamashita. 1999. Vesicular-integral membrane protein, VIP36, recognizes high-mannose type glycans containing $\alpha 1 \rightarrow 2$ mannosyl residues in MDCK cells. *Glycobiology*. 9:833-839.

Hauri, H.-P., F. Kappeler, H. Andersson, and C. Appenzeller. 2000. ERGIC-53 and traffic in the secretory pathway. *J Cell Sci*. 113:587-596.

Hay, J.C., J. Klumperman, V. Oorschot, M. Steegmaier, C.S. Kuo, and R.H. Scheller. 1998. Localization, dynamics, and protein interactions reveal distinct roles for ER and Golgi SNAREs. *The Journal of cell biology*. 141:1489-1502.

Henderson, G.P., L. Gan, and G.J. Jensen. 2007. 3-D ultrastructure of O. tauri: electron cryotomography of an entire eukaryotic cell. *PloS one*. 2:e749.

Herzig, Y., H.J. Sharpe, Y. Elbaz, S. Munro, and M. Schuldiner. 2012. A systematic approach to pair secretory cargo receptors with their cargo suggests a mechanism for cargo selection by Erv14. *PLoS biology*. 10.

Hinners, I., F. Wendler, H. Fei, L. Thomas, G. Thomas, and S.A. Tooze. 2003. AP-1 recruitment to VAMP4 is modulated by phosphorylation-dependent binding of PACS-1. *EMBO reports*. 4:1182-1189.

Hirschberg, K., C.M. Miller, J. Ellenberg, J.F. Presley, E.D. Siggia, R.D. Phair, and J. Lippincott-Schwartz. 1998. Kinetic analysis of secretory protein traffic and characterization of Golgi to plasma membrane transport intermediates in living cells. *The Journal of cell biology*. 143:1485-1503.

Hirst, J., W.W. Lui, N.A. Bright, N. Totty, M.N. Seaman, and M.S. Robinson. 2000. A family of proteins with γ-adaptin and VHS domains that facilitate trafficking between the trans-Golgi network and the vacuole/lysosome. *The Journal of cell biology*. 149:67-80.

Höning, S., J. Griffith, H. Geuze, and W. Hunziker. 1996. The tyrosine-based lysosomal targeting signal in lamp-1 mediates sorting into Golgi-derived clathrin-coated vesicles. *The EMBO journal*. 15:5230-5239.

Höning, S., and W. Hunziker. 1995. Cytoplasmic determinants involved in direct lysosomal sorting, endocytosis, and basolateral targeting of rat lgp120 (lamp-I) in MDCK cells. *The Journal of Cell Biology*. 128:321-332.

Höning, S., M. Sosa, A. Hille-Rehfeld, and K. von Figura. 1997. The 46-kDa mannose 6-phosphate receptor contains multiple binding sites for clathrin adaptors. *Journal of Biological Chemistry*. 272:19884-19890.

Howarth, M., D.J. Chinnapen, K. Gerrow, P.C. Dorrestein, M.R. Grandy, N.L. Kelleher, A. El-Husseini, and A.Y. Ting. 2006. A monovalent streptavidin with a single femtomolar biotin binding site. *Nature methods*. 3:267-273.

Huff, J. 2015. The Airyscan detector from ZEISS: confocal imaging with improved signal-to-noise ratio and super-resolution. *Nature methods*. 12:i-ii.

Huff, J., A. Bergter, J. Birkenbeil, I. Kleppe, R. Engelmann, and U. Krzic. 2017. The new 2D Superresolution mode for ZEISS Airyscan. *Nature Methods*. 14:1223.

Janvier, K., and J.S. Bonifacino. 2005. Role of the endocytic machinery in the sorting of lysosome-associated membrane proteins. *Molecular biology of the cell*. 16:4231-4242.

Kaiser, H.-J., A. Orłowski, T. Róg, T.K. Nyholm, W. Chai, T. Feizi, D. Lingwood, I. Vattulainen, and K. Simons. 2011. Lateral sorting in model membranes by cholesterol-mediated hydrophobic matching. *Proceedings of the National Academy of Sciences*. 108:16628-16633.

Kelleher, D.J., and R. Gilmore. 2006. An evolving view of the eukaryotic oligosaccharyltransferase. *Glycobiology*. 16:47R-62R.

Kellokumpu, S. 2019. Golgi pH, ion and redox homeostasis: How much do they really matter? *Frontiers in cell and developmental biology*. 7:93.

Klumperman, J. 2011. Architecture of the mammalian Golgi. *Cold Spring Harbor perspectives in biology*. 3:a005181.

Klumperman, J., A. Hille, T. Veenendaal, V. Oorschot, W. Stoorvogel, K. Von Figura, and H.J. Geuze. 1993. Differences in the endosomal distributions of the two mannose 6-phosphate receptors. *The Journal of cell biology*. 121:997-1010.

Klumperman, J., J.K. Locker, A. Meijer, M.C. Horzinek, H.J. Geuze, and P. Rottier. 1994. Coronavirus M proteins accumulate in the Golgi complex beyond the site of virion budding. *Journal of virology*. 68:6523-6534.

Klute, M.J., P. Melançon, and J.B. Dacks. 2011. Evolution and diversity of the Golgi. *Cold Spring Harbor perspectives in biology*. 3:a007849.

Kondylis, V., and C. Rabouille. 2009. The Golgi apparatus: lessons from Drosophila. *FEBS letters*. 583:3827-3838.

Kondylis, V., H.E.v.N. tot Pannerden, B. Herpers, F. Friggi-Grelin, and C. Rabouille. 2007. The golgi comprises a paired stack that is separated at G2 by modulation of the actin cytoskeleton through Abi and Scar/WAVE. *Developmental cell*. 12:901-915.

Koreishi, M., T.J. Gniadek, S. Yu, J. Masuda, Y. Honjo, and A. Satoh. 2013. The golgin tether giantin regulates the secretory pathway by controlling stack organization within Golgi apparatus. *PloS one*. 8.

Kreis, T.E., and H.F. Lodish. 1986. Oligomerization is essential for transport of vesicular stomatitis viral glycoprotein to the cell surface. *Cell*. 46:929-937.

Kreykenbohm, V., D. Wenzel, W. Antonin, V. Atlachkine, and G.F. von Mollard. 2002. The SNAREs vti1a and vti1b have distinct localization and SNARE complex partners. *European journal of cell biology*. 81:273-280.

Kurokawa, K., H. Osakada, T. Kojidani, M. Waga, Y. Suda, H. Asakawa, T. Haraguchi, and A. Nakano. 2019. Visualization of secretory cargo transport within the Golgi apparatus. *Journal of Cell Biology*. 218:1602-1618.

Kwan, A., C.E. Cummings, J.A. Chapman, and M.E. Grant. 1991. Macromolecular organization of chicken type X collagen in vitro. *The Journal of Cell Biology*. 114:597-604.

Kweon, H.-S., G.V. Beznoussenko, M. Micaroni, R.S. Polishchuk, A. Trucco, O. Martella, D. Di Giandomenico, P. Marra, A. Fusella, and A. Di Pentima. 2004. Golgi enzymes are enriched in perforated zones of Golgi cisternae but are depleted in COPI vesicles. *Molecular biology of the cell*. 15:4710-4724.

Ladinsky, M.S., J.R. Kremer, P.S. Furcinitti, J.R. McIntosh, and K.E. Howell. 1994. HVEM tomography of the trans-Golgi network: structural insights and identification of a lace-like vesicle coat. *The Journal of cell biology*. 127:29-38.

Ladinsky, M.S., D.N. Mastronarde, J.R. McIntosh, K.E. Howell, and L.A. Staehelin. 1999. Golgi structure in three dimensions: functional insights from the normal rat kidney cell. *The Journal of cell biology*. 144:1135-1149.

Ladinsky, M.S., C.C. Wu, S. McIntosh, J.R. McIntosh, and K.E. Howell. 2002. Structure of the Golgi and distribution of reporter molecules at 20 C reveals the complexity of the exit compartments. *Molecular biology of the cell*. 13:2810-2825.

Lafay, F. 1974. Envelope proteins of vesicular stomatitis virus: effect of temperature-sensitive mutations in complementation groups III and V. *Journal of virology*. 14:1220-1228.

Lairson, L., B. Henrissat, G. Davies, and S. Withers. 2008. Glycosyltransferases: structures, functions, and mechanisms. *Annu. Rev. Biochem.* 77:521-555.

Lam, S.S., J.D. Martell, K.J. Kamer, T.J. Deerinck, M.H. Ellisman, V.K. Mootha, and A.Y. Ting. 2015. Directed evolution of APEX2 for electron microscopy and proximity labeling. *Nature methods*. 12:51.

Lavieu, G., M.H. Dunlop, A. Lerich, H. Zheng, F. Bottanelli, and J.E. Rothman. 2014. The Golgi ribbon structure facilitates anterograde transport of large cargoes. *Molecular biology of the cell*. 25:3028-3036.

Lavieu, G., H. Zheng, and J.E. Rothman. 2013. Stapled Golgi cisternae remain in place as cargo passes through the stack. *Elife*. 2:e00558.

Lesa, G.M., J. Seemann, J. Shorter, J. Vandekerckhove, and G. Warren. 2000. The amino-terminal domain of the Golgi protein giantin interacts directly with the vesicle-tethering protein p115. *Journal of Biological Chemistry*. 275:2831-2836.

Ling, K., S.F. Bairstow, C. Carbonara, D.A. Turbin, D.G. Huntsman, and R.A. Anderson. 2007. Type Iγ phosphatidylinositol phosphate kinase modulates adherens junction and E-cadherin trafficking via a direct interaction with μ1B adaptin. *The Journal of cell biology*. 176:343-353.

Linstedt, A., M. Foguet, M. Renz, H. Seelig, B. Glick, and H. Hauri. 1995. A C-terminally-anchored Golgi protein is inserted into the endoplasmic reticulum and then transported to the Golgi apparatus. *Proceedings of the National Academy of Sciences*. 92:5102-5105.

Linstedt, A., A. Mehta, J. Suhan, H. Reggio, and H. Hauri. 1997. Sequence and overexpression of GPP130/GIMPc: evidence for saturable pH-sensitive targeting of a type II early Golgi membrane protein. *Molecular biology of the cell*. 8:1073-1087.

Lock, J.G., L.A. Hammond, F. Houghton, P.A. Gleeson, and J.L. Stow. 2005. E-cadherin transport from the trans-Golgi network in tubulovesicular carriers is selectively regulated by golgin-97. *Traffic*. 6:1142-1156.

Lock, J.G., and J.L. Stow. 2005. Rab11 in recycling endosomes regulates the sorting and basolateral transport of E-cadherin. *Molecular biology of the cell*. 16:1744-1755.

Loh, E., and W. Hong. 2002. Sec34 is implicated in traffic from the endoplasmic reticulum to the Golgi and exists in a complex with GTC-90 and ldlBp. *Journal of Biological Chemistry*. 277:21955-21961.

Losev, E., C.A. Reinke, J. Jellen, D.E. Strongin, B.J. Bevis, and B.S. Glick. 2006. Golgi maturation visualized in living yeast. *Nature*. 441:1002-1006.

Lu, L., and W. Hong. 2003. Interaction of Arl1-GTP with GRIP domains recruits autoantigens Golgin-97 and Golgin-245/p230 onto the Golgi. *Molecular biology of the cell*. 14:3767-3781.

Lu, L., and W. Hong. 2014. From endosomes to the trans-Golgi network. *In* Seminars in cell & developmental biology. Vol. 31. Elsevier. 30-39.

Lu, L., H. Horstmann, C. Ng, and W. Hong. 2001. Regulation of Golgi structure and function by ARF-like protein 1 (Arl1). *Journal of cell science*. 114:4543-4555.

Lu, L., G. Tai, and W. Hong. 2004. Autoantigen Golgin-97, an effector of Arl1 GTPase, participates in traffic from the endosome to the trans-golgi network. *Molecular biology of the cell*. 15:4426-4443.

Ludwig, A., B.J. Nichols, and S. Sandin. 2016. Architecture of the caveolar coat complex. *Journal of cell science*. 129:3077-3083.

Luke, M.R., L. Kjer-Nielsen, D.L. Brown, J.L. Stow, and P.A. Gleeson. 2003. GRIP domain-mediated targeting of two new coiled-coil proteins, GCC88 and GCC185, to subcompartments of the trans-Golgi network. *Journal of Biological Chemistry*. 278:4216-4226.

Luzio, J., B. Brake, G. Banting, K. Howell, P. Braghetta, and K. Stanley. 1990. Identification, sequencing and expression of an integral membrane protein of the trans-Golgi network (TGN38). *Biochemical Journal*. 270:97-102.

Mahajan, D., B.K. Boh, Y. Zhou, L. Chen, T.C. Cornvik, W. Hong, and L. Lu. 2013. Mammalian Mon2/Ysl2 regulates endosome-to-Golgi trafficking but possesses no guanine nucleotide exchange activity toward Arl1 GTPase. *Scientific reports*. 3:3362.

Mahajan, D., H.C. Tie, B. Chen, and L. Lu. 2019. Dopey1-Mon2 complex binds to dual-lipids and recruits kinesin-1 for membrane trafficking. *Nature communications*. 10:1-19.

Mancias, J.D., and J. Goldberg. 2005. Exiting the endoplasmic reticulum. *Traffic*. 6:278-285.

Marra, P., T. Maffucci, T. Daniele, G. Di Tullio, Y. Ikehara, E.K. Chan, A. Luini, G. Beznoussenko, A. Mironov, and M.A. De Matteis. 2001. The GM130 and GRASP65 Golgi proteins cycle through and define a subdomain of the intermediate compartment. *Nature cell biology*. 3:1101.

Marsh, B.J., N. Volkmann, J.R. McIntosh, and K.E. Howell. 2004. Direct continuities between cisternae at different levels of the Golgi complex in glucose-stimulated mouse islet beta cells. *Proceedings of the National Academy of Sciences*. 101:5565-5570.

Martínez-Menárguez, J.A., R. Prekeris, V.M. Oorschot, R. Scheller, J.W. Slot, H.J. Geuze, and J. Klumperman. 2001. Peri-Golgi vesicles contain retrograde but not anterograde proteins consistent with the cisternal progression model of intra-Golgi transport. *J Cell Biol*. 155:1213-1224.

Matlin, K.S., and K. Simons. 1983. Reduced temperature prevents transfer of a membrane glycoprotein to the cell surface but does not prevent terminal glycosylation. *Cell*. 34:233-243.

Matsuoka, K., L. Orci, M. Amherdt, S.Y. Bednarek, S. Hamamoto, R. Schekman, and T. Yeung. 1998. COPII-coated vesicle formation reconstituted with purified coat proteins and chemically defined liposomes. *Cell*. 93:263-275.

Matsuura-Tokita, K., M. Takeuchi, A. Ichihara, K. Mikuriya, and A. Nakano. 2006. Live imaging of yeast Golgi cisternal maturation. *Nature*. 441:1007-1010.

Mellman, I., and K. Simons. 1992. The Golgi complex: In vitro veritas? *Cell*. 68:829-840.

Mironov, A.A., G.V. Beznoussenko, P. Nicoziani, O. Martella, A. Trucco, H.-S. Kweon, D. Di Giandomenico, R.S. Polishchuk, A. Fusella, and P. Lupetti. 2001. Small cargo proteins and large aggregates can traverse the Golgi by a common mechanism without leaving the lumen of cisternae. *The Journal of cell biology*. 155:1225-1238.

Moelleken, J., J. Malsam, M.J. Betts, A. Movafeghi, I. Reckmann, I. Meissner, A. Hellwig, R.B. Russell, T. Söllner, and B. Brügger. 2007. Differential localization of coatomer complex isoforms within the Golgi apparatus. *Proceedings of the National Academy of Sciences*. 104:4425-4430.

Mogelsvang, S., N. Gomez-Ospina, J. Soderholm, B.S. Glick, and L.A. Staehelin. 2003. Tomographic evidence for continuous turnover of Golgi cisternae in Pichia pastoris. *Molecular biology of the cell*. 14:2277-2291.

Mogelsvang, S., B.J. Marsh, M.S. Ladinsky, and K.E. Howell. 2004. Predicting function from structure: 3D structure studies of the mammalian Golgi complex. *Traffic*. 5:338-345.

Molloy, S., L. Thomas, J. VanSlyke, P. Stenberg, and G. Thomas. 1994. Intracellular trafficking and activation of the furin proprotein convertase: localization to the TGN and recycling from the cell surface. *The EMBO journal*. 13:18-33.

Munro, S. 2011. The golgin coiled-coil proteins of the Golgi apparatus. *Cold Spring Harbor perspectives in biology*. 3:a005256.

Muschalik, N., and S. Munro. 2018. Golgins. *Current Biology*. 28:R374-R376.

Nakamura, N., C. Rabouille, R. Watson, T. Nilsson, N. Hui, P. Slusarewicz, T.E. Kreis, and G. Warren. 1995. Characterization of a cis-Golgi matrix protein, GM130. *The Journal of cell biology*. 131:1715-1726.

Nakano, A., and A. Luini. 2010. Passage through the Golgi. *Current opinion in cell biology*. 22:471-478.

Nilsson, T., C.E. Au, and J.J. Bergeron. 2009. Sorting out glycosylation enzymes in the Golgi apparatus. *FEBS letters*. 583:3764-3769.

Nilsson, T., M. Pypaert, M.H. Hoe, P. Slusarewicz, E.G. Berger, and G. Warren. 1993. Overlapping distribution of two glycosyltransferases in the Golgi apparatus of HeLa cells. *The Journal of Cell Biology*. 120:5-13.

Niu, X., C. Gao, L.J. Lo, Y. Luo, C. Meng, J. Hong, W. Hong, and J. Peng. 2012. Sec13 safeguards the integrity of the endoplasmic reticulum and organogenesis of the digestive system in zebrafish. *Developmental biology*. 367:197-207.

Odorizzi, G., and I.S. Trowbridge. 1997. Structural requirements for basolateral sorting of the human transferrin receptor in the biosynthetic and endocytic pathways of Madin-Darby canine kidney cells. *The Journal of cell biology*. 137:1255-1264.

Opat, A.S., F. Houghton, and P.A. Gleeson. 2000. Medial Golgi but Not Late Golgi Glycosyltransferases Exist as High Molecular Weight Complexes ROLE OF LUMINAL DOMAIN IN COMPLEX FORMATION AND LOCALIZATION. *Journal of Biological Chemistry*. 275:11836-11845.

Opat, A.S., C. van Vliet, and P.A. Gleeson. 2001. Trafficking and localisation of resident Golgi glycosylation enzymes. *Biochimie*. 83:763-773.

Oprins, A., R. Duden, T.E. Kreis, H.J. Geuze, and J.W. Slot. 1993. Beta-COP localizes mainly to the cis-Golgi side in exocrine pancreas. *The Journal of cell biology*. 121:49-59.

Orci, L., M. Ravazzola, A. Volchuk, T. Engel, M. Gmachl, M. Amherdt, A. Perrelet, T.H. Söllner, and J.E. Rothman. 2000. Anterograde flow of cargo across the Golgi stack potentially mediated via bidirectional “percolating” COPI vesicles. *Proceedings of the National Academy of Sciences*. 97:10400-10405.

Paccaud, J.-P., W. Reith, J.-L. Carpentier, M. Ravazzola, M. Amherdt, R. Schekman, and L. Orci. 1996. Cloning and functional characterization of mammalian homologues of the COPII component Sec23. *Molecular Biology of the Cell*. 7:1535-1546.

Patterson, G.H., K. Hirschberg, R.S. Polishchuk, D. Gerlich, R.D. Phair, and J. Lippincott-Schwartz. 2008. Transport through the Golgi apparatus by rapid partitioning within a two-phase membrane system. *Cell*. 133:1055-1067.

Peden, A.A., G.Y. Park, and R.H. Scheller. 2001. The Di-leucine motif of vesicle-associated membrane protein 4 is required for its localization and AP-1 binding. *Journal of Biological Chemistry*. 276:49183-49187.

Pelham, H.R., and S. Munro. 1993. Sorting of membrane proteins in the secretory pathway. *Cell*. 75:603-605.

Pelletier, L., C.A. Stern, M. Pypaert, D. Sheff, H.M. Ngô, N. Roper, C.Y. He, K. Hu, D. Toomre, and I. Coppens. 2002. Golgi biogenesis in Toxoplasma gondii. *Nature*. 418:548-552.

Pereira, N.A., H.X. Pu, H. Goh, and Z. Song. 2014. Golgi phosphoprotein 3 mediates the Golgi localization and function of protein O-linked mannose β-1, 2-N-acetlyglucosaminyltransferase 1. *Journal of Biological Chemistry*. 289:14762-14770.

Pfeffer, S.R. 2010. How the Golgi works: a cisternal progenitor model. *Proceedings of the National Academy of Sciences*. 107:19614-19618.

Pinhal, M.A., B. Smith, S. Olson, J.-i. Aikawa, K. Kimata, and J.D. Esko. 2001. Enzyme interactions in heparan sulfate biosynthesis: uronosyl 5-epimerase and 2-O-sulfotransferase interact in vivo. *Proceedings of the National Academy of Sciences*. 98:12984-12989.

Polishchuk, E.V., A. Di Pentima, A. Luini, and R.S. Polishchuk. 2003. Mechanism of constitutive export from the golgi: bulk flow via the formation, protrusion, and en bloc

cleavage of large trans-golgi network tubular domains. *Molecular biology of the cell*. 14:4470-4485.

Polishchuk, R.S., E.V. Polishchuk, P. Marra, S. Alberti, R. Buccione, A. Luini, and A.A. Mironov. 2000. Correlative light-electron microscopy reveals the tubular-saccular ultrastructure of carriers operating between Golgi apparatus and plasma membrane. *J Cell Biol*. 148:45-58.

Pols, M.S., E. Van Meel, V. Oorschot, C. Ten Brink, M. Fukuda, M. Swetha, S. Mayor, and J. Klumperman. 2013. hVps41 and VAMP7 function in direct TGN to late endosome transport of lysosomal membrane proteins. *Nature communications*. 4:1-12.

Presley, J.F., N.B. Cole, T.A. Schroer, K. Hirschberg, K.J. Zaal, and J. Lippincott-Schwartz. 1997. ER-to-Golgi transport visualized in living cells. *Nature*. 389:81.

Preuss, D., J. Mulholland, A. Franzusoff, N. Segev, and D. Botstein. 1992. Characterization of the Saccharomyces Golgi complex through the cell cycle by immunoelectron microscopy. *Molecular biology of the cell*. 3:789-803.

Puertollano, R., R.C. Aguilar, I. Gorshkova, R.J. Crouch, and J.S. Bonifacino. 2001a. Sorting of mannose 6-phosphate receptors mediated by the GGAs. *Science*. 292:1712-1716.

Puertollano, R., P.A. Randazzo, J.F. Presley, L.M. Hartnell, and J.S. Bonifacino. 2001b. The GGAs promote ARF-dependent recruitment of clathrin to the TGN. *Cell*. 105:93-102.

Puri, S., C. Bachert, C.J. Fimmel, and A.D. Linstedt. 2002. Cycling of early Golgi proteins via the cell surface and endosomes upon lumenal pH disruption. *Traffic*. 3:641-653.

Rabouille, C., N. Hui, F. Hunte, R. Kieckbusch, E.G. Berger, G. Warren, and T. Nilsson. 1995a. Mapping the distribution of Golgi enzymes involved in the construction of complex oligosaccharides. *Journal of cell science*. 108:1617-1627.

Rabouille, C., and J. Klumperman. 2005. The maturing role of COPI vesicles in intra-Golgi transport. *Nature Reviews Molecular Cell Biology*. 6:812-817.

Rabouille, C., T. Misteli, R. Watson, and G. Warren. 1995b. Reassembly of Golgi stacks from mitotic Golgi fragments in a cell-free system. *The Journal of cell biology*. 129:605-618.

Rambourg, A., and Y. Clermont. 1990. Three-dimensional electron microscopy: structure of the Golgi apparatus. *European journal of cell biology*. 51:189-200.

Rambourg, A., and Y. Clermont. 1997. Three-dimensional structure of the Golgi apparatus in mammalian cells. *In* The Golgi Apparatus. Springer. 37-61.

Rivera, V.M., X. Wang, S. Wardwell, N.L. Courage, A. Volchuk, T. Keenan, D.A. Holt, M. Gilman, L. Orci, and F. Cerasoli. 2000. Regulation of protein secretion through controlled aggregation in the endoplasmic reticulum. *Science*. 287:826-830.

Rizzo, R., S. Parashuraman, P. Mirabelli, C. Puri, J. Lucocq, and A. Luini. 2013. The dynamics of engineered resident proteins in the mammalian Golgi complex relies on cisternal maturation. *J Cell Biol*:jcb. 201211147.

Rocha, N., F. Payne, I. Huang-Doran, A. Sleigh, K. Fawcett, C. Adams, A. Stears, V. Saudek, S. O'Rahilly, and I. Barroso. 2017. The metabolic syndrome-associated small G protein ARL15 plays a role in adipocyte differentiation and adiponectin secretion. *Scientific reports*. 7:17593.

Roth, J. 2002. Protein N-glycosylation along the secretory pathway: relationship to organelle topography and function, protein quality control, and cell interactions. *Chemical reviews*. 102:285-304.

Roth, J., and E.G. Berger. 1982. Immunocytochemical localization of galactosyltransferase in HeLa cells: codistribution with thiamine pyrophosphatase in trans-Golgi cisternae. *The Journal of Cell Biology*. 93:223-229.

Rottger, S., J. White, H.H. Wandall, J.-C. Olivo, A. Stark, E.P. Bennett, C. Whitehouse, E.G. Berger, H. Clausen, and T. Nilsson. 1998. Localization of three human polypeptide GalNAc-transferases in HeLa cells suggests initiation of O-linked glycosylation throughout the Golgi apparatus. *Journal of Cell Science*. 111:45-60.

Roux, A., G. Cappello, J. Cartaud, J. Prost, B. Goud, and P. Bassereau. 2002. A minimal system allowing tubulation with molecular motors pulling on giant liposomes. *Proceedings of the National Academy of Sciences*. 99:5394-5399.

Saraste, J., and E. Kuismanen. 1984. Pre-and post-Golgi vacuoles operate in the transport of Semliki Forest virus membrane glycoproteins to the cell surface. *Cell*. 38:535-549.

Saraste, J., U. Lahtinen, and B. Goud. 1995. Localization of the small GTP-binding protein rab1p to early compartments of the secretory pathway. *Journal of cell science*. 108:1541-1552.

Satoh, A., Y. Wang, J. Malsam, M.B. Beard, and G. Warren. 2003. Golgin-84 is a rab1 binding partner involved in Golgi structure. *Traffic*. 4:153-161.

Serafini, T., L. Orci, M. Amherdt, M. Brunner, R.A. Kahn, and J.E. Rothmant. 1991. ADP-ribosylation factor is a subunit of the coat of Golgi-derived COP-coated vesicles: a novel role for a GTP-binding protein. *Cell*. 67:239-253.

Sharpe, H.J., T.J. Stevens, and S. Munro. 2010. A comprehensive comparison of transmembrane domains reveals organelle-specific properties. *Cell*. 142:158-169.

Shaywitz, D.A., L. Orci, M. Ravazzola, A. Swaroop, and C.A. Kaiser. 1995. Human SEC13Rp functions in yeast and is located on transport vesicles budding from the endoplasmic reticulum. *The Journal of Cell Biology*. 128:769-777.

Shental-Bechor, D., and Y. Levy. 2008. Effect of glycosylation on protein folding: a close look at thermodynamic stabilization. *Proceedings of the National Academy of Sciences*. 105:8256-8261.

Short, B., C. Preisinger, R. Körner, R. Kopajtich, O. Byron, and F.A. Barr. 2001. A GRASP55-rab2 effector complex linking Golgi structure to membrane traffic. *J Cell Biol*. 155:877-884.

Siu, Y., K. Teoh, J. Lo, C. Chan, F. Kien, N. Escriou, S. Tsao, J. Nicholls, R. Altmeyer, and J. Peiris. 2008. The M, E, and N structural proteins of the severe acute respiratory syndrome coronavirus are required for efficient assembly, trafficking, and release of virus-like particles. *Journal of virology*. 82:11318-11330.

Skrincosky, D., R. Kain, A. El-Battari, M. Exner, D. Kerjaschki, and M. Fukuda. 1997. Altered Golgi localization of core 2 β-1, 6-N-acetylglucosaminyltransferase leads to decreased synthesis of branched O-glycans. *Journal of Biological Chemistry*. 272:22695-22702.

Smith, R.D., and V.V. Lupashin. 2008. Role of the conserved oligomeric Golgi (COG) complex in protein glycosylation. *Carbohydrate research*. 343:2024-2031.

Snyder, C.M., G.A. Mardones, M.S. Ladinsky, and K.E. Howell. 2006. GMx33 associates with the trans-Golgi matrix in a dynamic manner and sorts within tubules exiting the Golgi. *Molecular biology of the cell*. 17:511-524.

Sohda, M., Y. Misumi, A. Yamamoto, A. Yano, N. Nakamura, and Y. Ikehara. 2001. Identification and characterization of a novel Golgi protein, GCP60, that interacts with the integral membrane protein giantin. *Journal of Biological Chemistry*. 276:45298-45306.

Spooner, R.A., P. Watson, D.C. Smith, F. Boal, M. Amessou, L. Johannes, G.J. Clarkson, J.M. Lord, D.J. Stephens, and L.M. Roberts. 2008. The secretion inhibitor Exo2 perturbs trafficking of Shiga toxin between endosomes and the trans-Golgi network. *Biochemical Journal*. 414:471-484.

Staehelin, L.A., and B.-H. Kang. 2008. Nanoscale architecture of endoplasmic reticulum export sites and of Golgi membranes as determined by electron tomography. *Plant Physiology*. 147:1454-1468.

Staehelin, L.A., and I. Moore. 1995. The plant Golgi apparatus: structure, functional organization and trafficking mechanisms. *Annual review of plant biology*. 46:261-288.

Stamnes, M.A., and J.E. Rothman. 1993. The binding of AP-1 clathrin adaptor particles to Golgi membranes requires ADP-ribosylation factor, a small GTP-binding protein. *Cell*. 73:999-1005.

Stanley, P. 2011. Golgi glycosylation. *Cold Spring Harbor perspectives in biology*. 3:a005199.

Steegmaier, M., J. Klumperman, D.L. Foletti, J.-S. Yoo, and R.H. Scheller. 1999. Vesicle-associated Membrane Protein 4 is Implicated inTrans-Golgi Network Vesicle Trafficking. *Molecular biology of the cell*. 10:1957-1972.

Stertz, S., M. Reichelt, M. Spiegel, T. Kuri, L. Martínez-Sobrido, A. García-Sastre, F. Weber, and G. Kochs. 2007. The intracellular sites of early replication and budding of SARS-coronavirus. *Virology*. 361:304-315.

Storrie, B., M. Micaroni, G.P. Morgan, N. Jones, J.A. Kamykowski, N. Wilkins, T.H. Pan, and B.J. Marsh. 2012. Electron T omography R eveals R ab6 I s E ssential to the T rafficking of trans-G olgi C lathrin and COPI-C oated V esicles and the M aintenance of G olgi C isternal N umber. *Traffic*. 13:727-744.

Stow, J., and R. Murray. 2015. Post-golgi transport-cargo, carriers, and pathways.

Subramaniam, V.N., F. Peter, R. Philp, S.H. Wong, and W. Hong. 1996. GS28, a 28-kilodalton Golgi SNARE that participates in ER-Golgi transport. *Science*. 272:1161-1163.

Sullivan, L.H. 1922. The tall office building artistically considered.

Suvorova, E.S., R. Duden, and V.V. Lupashin. 2002. The Sec34/Sec35p complex, a Ypt1p effector required for retrograde intra-Golgi trafficking, interacts with Golgi SNAREs and COPI vesicle coat proteins. *The Journal of cell biology*. 157:631-643.

Suvorova, E.S., R.C. Kurten, and V.V. Lupashin. 2001. Identification of a human orthologue of Sec34p as a component of the cis-Golgi vesicle tethering machinery. *Journal of Biological Chemistry*. 276:22810-22818.

Tanaka, M., T. Izawa, J. Yamate, R.J. Franklin, T. Kuramoto, T. Serikawa, and M. Kuwamura. 2014. The VF rat with abnormal myelinogenesis has a mutation in Dopey1. *Glia*. 62:1530-1542.

Tang, B.L., T. Zhang, D.Y. Low, E.T. Wong, H. Horstmann, and W. Hong. 2000. Mammalian homologues of yeast sec31p An ubiquitously expressed form is localized to endoplasmic reticulum (ER) exit sites and is essential for ER-Golgi transport. *Journal of Biological Chemistry*. 275:13597-13604.

Teuchert, M., S. Berghöfer, H.-D. Klenk, and W. Garten. 1999. Recycling of Furin from the Plasma Membrane FUNCTIONAL IMPORTANCE OF THE CYTOPLASMIC TAIL SORTING SIGNALS AND INTERACTION WITH THE AP-2 ADAPTOR MEDIUM CHAIN SUBUNIT. *Journal of Biological Chemistry*. 274:36781-36789.

Thorley, J.A., J. Pike, and J.Z. Rappoport. 2014. Super-resolution microscopy: a comparison of commercially available options. *In* Fluorescence Microscopy. Elsevier. 199-212.

Tie, H., B. Chen, X. Sun, L. Cheng, and L. Lu. 2017. Quantitative Localization of a Golgi Protein by Imaging Its Center of Fluorescence Mass. *Journal of visualized experiments: JoVE*.

Tie, H., D. Mahajan, B. Chen, L. Cheng, A. VanDongen, and L. Lu. 2016a. A novel imaging method for quantitative Golgi localization reveals differential intra-Golgi trafficking of secretory cargoes. *Molecular biology of the cell*. 27:848.

Tie, H.C., V. Madugula, and L. Lu. 2016b. The development of a single molecule fluorescence standard and its application in estimating the stoichiometry of the nuclear pore complex. *Biochem Biophys Res Commun*. 478:1694-1699.

Tran, T.H.T., Q. Zeng, and W. Hong. 2007. VAMP4 cycles from the cell surface to the trans-Golgi network via sorting and recycling endosomes. *Journal of cell science*. 120:1028-1041.

Traub, L.M., and J.S. Bonifacino. 2013. Cargo recognition in clathrin-mediated endocytosis. *Cold Spring Harbor perspectives in biology*. 5:a016790.

Trucco, A., R.S. Polishchuk, O. Martella, A. Di Pentima, A. Fusella, D. Di Giandomenico, E. San Pietro, G.V. Beznoussenko, E.V. Polishchuk, and M. Baldassarre. 2004. Secretory traffic triggers the formation of tubular continuities across Golgi sub-compartments. *Nature cell biology*. 6:1071-1081.

Truckenbrodt, S., M. Maidorn, D. Crzan, H. Wildhagen, S. Kabatas, and S.O. Rizzoli. 2018. X10 expansion microscopy enables 25‐nm resolution on conventional microscopes. *EMBO reports*. 19:e45836.

Van Meer, G., D.R. Voelker, and G.W. Feigenson. 2008. Membrane lipids: where they are and how they behave. *Nature reviews Molecular cell biology*. 9:112-124.

Velasco, A., L. Hendricks, K.W. Moremen, D. Tulsiani, O. Touster, and M.G. Farquhar. 1993. Cell type-dependent variations in the subcellular distribution of alpha-mannosidase I and II. *The Journal of cell biology*. 122:39-51.

Volchuk, A., M. Amherdt, M. Ravazzola, B. Brügger, V.M. Rivera, T. Clackson, A. Perrelet, T.H. Söllner, J.E. Rothman, and L. Orci. 2000. Megavesicles implicated in the rapid transport of intracisternal aggregates across the Golgi stack. *Cell*. 102:335-348.

Volchuk, A., M. Ravazzola, A. Perrelet, W.S. Eng, M. Di Liberto, O. Varlamov, M. Fukasawa, T. Engel, T.H. Söllner, and J.E. Rothman. 2004. Countercurrent distribution of two distinct SNARE complexes mediating transport within the Golgi stack. *Molecular biology of the cell*. 15:1506-1518.

Waguri, S., F. Dewitte, R. Le Borgne, Y. Rouillé, Y. Uchiyama, J.-F. Dubremetz, and B. Hoflack. 2003. Visualization of TGN to endosome trafficking through fluorescently labeled MPR and AP-1 in living cells. *Molecular biology of the cell*. 14:142-155.

Warren, G., and I. Mellman. 1999. Bulk flow redux? *Cell*. 98:125-127.

Wassie, A.T., Y. Zhao, and E.S. Boyden. 2019. Expansion microscopy: principles and uses in biological research. *Nature methods*. 16:33-41.

Waters, J.C. 2009. Accuracy and precision in quantitative fluorescence microscopy. The Rockefeller University Press.

Wegel, E., A. Göhler, B.C. Lagerholm, A. Wainman, S. Uphoff, R. Kaufmann, and I.M. Dobbie. 2016. Imaging cellular structures in super-resolution with SIM, STED and Localisation Microscopy: A practical comparison. *Scientific reports*. 6:1-13.

Weidman, P., R. Roth, and J. Heuser. 1993. Golgi membrane dynamics imaged by freeze-etch electron microscopy: views of different membrane coatings involved in tubulation versus vesiculation. *Cell*. 75:123-133.

Wessels, E., D. Duijsings, T.-K. Niu, S. Neumann, V.M. Oorschot, F. de Lange, K.H. Lanke, J. Klumperman, A. Henke, and C.L. Jackson. 2006. A viral protein that blocks Arf1-mediated COP-I assembly by inhibiting the guanine nucleotide exchange factor GBF1. *Developmental cell*. 11:191-201.

Wildt, S., and T.U. Gerngross. 2005. The humanization of N-glycosylation pathways in yeast. *Nature Reviews Microbiology*. 3:119-128.

Wu, C.C., R.S. Taylor, D.R. Lane, M.S. Ladinsky, J.A. Weisz, and K.E. Howell. 2000. GMx33: a novel family of trans-Golgi proteins identified by proteomics. *Traffic*. 1:963-975.

Xiang, Y., X. Zhang, D.B. Nix, T. Katoh, K. Aoki, M. Tiemeyer, and Y. Wang. 2013. Regulation of protein glycosylation and sorting by the Golgi matrix proteins GRASP55/65. *Nature communications*. 4:1-14.

Xu, Y., S. Martin, D.E. James, and W. Hong. 2002. GS15 forms a SNARE complex with syntaxin 5, GS28, and Ykt6 and is implicated in traffic in the early cisternae of the Golgi apparatus. *Molecular biology of the cell*. 13:3493-3507.

Zanetti, G., S. Prinz, S. Daum, A. Meister, R. Schekman, K. Bacia, and J.A. Briggs. 2013. The structure of the COPII transport-vesicle coat assembled on membranes. *Elife*. 2:e00951.

Zhang, P., R. Haryadi, K.F. Chan, G. Teo, J. Goh, N.A. Pereira, H. Feng, and Z. Song. 2012. Identification of functional elements of the GDP-fucose transporter SLC35C1 using a novel Chinese hamster ovary mutant. *Glycobiology*. 22:897-911.

Appendix 1

```
macro " Normalization and Giantin alignment for en face Golgi mini-stacks "
{
folder_path=getDirectory("Choose a Directory");
run("Clear Results");
title=getTitle;
selectWindow(title);
run("Properties...", "channels=3 slices=1 frames=1 unit=pixel pixel_width=1
pixel_height=1 voxel_depth=1");
Image_h=getHeight();
Qx=0;
Qy=0;
Total_Intensity=0;
for (i=0; i<Image_h;  i++ )
{       for (j=0;  j<Image_h; j++)
                {Intensity=getPixel(i, j);

                        {Total_Intensity=Total_Intensity+Intensity;
                        Qx=Qx+i*Intensity;
                        Qy=Qy+j*Intensity;}
                }
}
mx=Qx/Total_Intensity;          //center of mass along the x-axis
my=Qy/Total_Intensity;          //center of mass along the y-axis

Q=0;
Total_Intensity=0;
for (i=0; i<Image_h; i++)
{       for (j=0;  j<Image_h; j++)
                {Intensity=getPixel(i,j);
```

```
                    {Total_Intensity=Total_Intensity+Intensity;
                    Q=Q+((i-mx)*(i-mx)+(j-my)*(j-my))*Intensity;}
            }
}
gyradius=sqrt(Q/Total_Intensity);
print("image=", title);
selectWindow(title);
Image_h=getHeight();
New_h=Image_h*100/gyradius;
run("Size...", "width=&New_h height=&New_h depth=3 constrain average
interpolation=Bilinear");
run("Canvas Size...", "width=701 height=701 position=Center zero");
run("Set Measurements...", "center redirect=None decimal=4");
run("Clear Results");
run("Measure");
mx=getResult("XM", nResults-1);          //nResults-1 is the last row of results;
nResults is the numbe of rows in the Results window.
my=getResult("YM", nResults-1);
x_shift=350-mx;
y_shift=350-my;
run("Translate...", "x=&x_shift y=&y_shift interpolation=Bilinear stack"); //"stack"
means the operation applies to all slices; "slice" means the operation is restricted to
the current slice.
getDimensions(width1, height1, channels, slice1, frame1);
for (channel_i=1; channel_i<=channels; channel_i++)
{
Stack.setChannel(channel_i);
run("Translate...", "x=&x_shift y=&y_shift interpolation=Bilinear");
run("Set Measurements...", "integrated redirect=None decimal=4");
run("Select All");
run("Measure");
Integrated_intensity=getResult("IntDen", nResults-1);
```

```
I_factor=200000000/Integrated_intensity;
run("Multiply...", "value=&I_factor slice");
}
getDimensions(width1, height1, channels, slice1, frame1);
run("Split Channels");
for (channel_i=1; channel_i<=channels; channel_i++)
{selectWindow("C"+channel_i+"-"+title);
saveAs("Tiff", folder_path+"C"+channel_i+"-"+title);  //string concatenation
}
print("files are saved at= ", folder_path);
print("-----------------------------------------------------------------------------------------------------------------");
run("Clear Results");
}
```

Appendix 2

```
macro "radial mean intensity profile"
{
run("Clear Results");
xm=349.5;
ym=349.5;
for (k=0; k<=499; k++)
{
        setResult("total intensity", k, 0);
        setResult("No. pixels", k, 0);
        setResult("mean intensity", k, 0);
}
for (i=0;i<=700;i++)
{       for (j=0; j<=700; j++)
        {       radius=sqrt((i-xm)*(i-xm)+(j-ym)*(j-ym));
                n=floor(radius);
                intensity=getPixel(i,j);
                cumulative_intensity=getResult("total intensity", n)+intensity;
                setResult("total intensity", n, cumulative_intensity);
                cumulative_pixel=getResult("No. pixels", n)+1;
                setResult("No. pixels", n, cumulative_pixel);
        }
}
for (i=0; i<nResults; i++)
{
                cumulative_pixel=getResult("No. pixels", i);
                cumulative_intensity=getResult("total intensity", i);
                if (cumulative_pixel!=0)
                        {
                                average_intensity=cumulative_intensity/cumulative_pixel;
```

```
                    setResult("mean intensity", i, average_intensity);
                }
            else
            {
                    setResult("mean intensity", i, 0);
            }

}
}
```

Appendix 3

```
macro "rotation resize normalization for side view averaging"
{
folder_path=getDirectory("Choose a Directory")
run("Clear Results");
title=getTitle;
selectWindow(title);
run("Properties...", "channels=3 slices=1 frames=1 unit=pixel pixel_width=1
pixel_height=1 voxel_depth=1");
run("Set Measurements...", "center redirect=None decimal=4");
roiManager("Deselect");
roiManager("Measure");
x1=getResult("XM", 0);
y1=getResult("YM", 0);
x2=getResult("XM", 1);
y2=getResult("YM", 1);
print("x1= ", x1, "; y1= ", y1, "; x2= ", x2, "; y2= ", y2);
run("Clear Results");
run("Set Measurements...", "center redirect=None decimal=4");
run("Select All");
run("Measure");
xc=getResult("XM", 0);
yc=getResult("YM", 0);
print("xc= ", xc, "; yc= ", yc);
Image_h=getHeight();
x_shift=(Image_h/2)-xc;
y_shift=(Image_h/2)-yc;
run("Translate...", "x=&x_shift y=&y_shift interpolation=Bilinear");
print("x_shift= ", x_shift, "; y_shift= ", y_shift);
Angle=0-(57.2958*atan((y2-yc)/(x2-xc)));
run("Rotate... ", "angle=&Angle grid=2 interpolation=Bilinear");
```

```
print("Rotation angle (degree) = ", Angle);
d=(sqrt((x2-x1)*(x2-x1)+(y2-y1)*(y2-y1)))/2;
print("The radius of the Giantin puncta = ", d);
selectWindow(title);
Image_wh=getHeight();
New_w=Image_wh*80/d;
New_h=Image_wh*8;
run("Size...", "width=&New_w height=&New_h interpolation=Bilinear");
run("Canvas Size...", "width=701 height=701 position=Center zero");
getDimensions(width1, height1, channels, slice1, frame1);
for (channel_i=1; channel_i<=channels; channel_i++)
{
Stack.setChannel(channel_i);
run("Set Measurements...", "integrated redirect=None decimal=4");
run("Select All");
run("Measure");
Integrated_intensity=getResult("IntDen", nResults-1);
I_factor=50000000/Integrated_intensity;
run("Multiply...", "value=&I_factor slice");
}
getDimensions(width1, height1, channels, slice1, frame1);
run("Split Channels");
for (channel_i=1; channel_i<=channels; channel_i++)
{selectWindow("C"+channel_i+"-"+title);
saveAs("Tiff", folder_path+"C"+channel_i+"-"+title);  //string concatenation
}
print("The image file:  ", title);
print("Processed files are saved at= ", folder_path);
print("----------------------------------------------------------------------------------------------------
----------");
roiManager("Delete");}
```